

# MÉMOIRE D'HABILITATION À DIRIGER DES RECHERCHES

Spécialité Physique

## Single-Particle Modeling of X-ray Absorption Near-Edge Structure: Theoretical Development and Applications

Delphine Cabaret

*Université Pierre et Marie Curie (UPMC)*

*Institut de Minéralogie et de Physique des Milieux Condensés (IMPMC)*

Soutenue le 29 novembre 2012 devant le jury composé de :

Christian Bonhomme	président
Frank de Groot	rapporteur
Lucia Reining	rapporteur
Odile Stéphan	rapporteur
Yves Joly	examineur
François Farges	examineur



# Table des matières

<b>1</b>	<b>Mémoire</b>	<b>5</b>
1.1	General introduction . . . . .	6
1.2	Modeling XANES using single-particle methods . . . . .	7
1.2.1	Real-space approaches . . . . .	7
1.2.2	Band structure approaches . . . . .	9
1.2.3	XANES modeling within a pseudopotential scheme . . . . .	10
1.3	Probing structural properties . . . . .	12
1.3.1	The local structure of $3d$ impurities in allochromatic minerals . . . . .	13
1.3.2	The local structure of Ge and Mg in model compounds and glasses . . . . .	16
1.4	Probing the $3d$ empty states of transition metals at the $K$ pre-edge . . . . .	21
1.4.1	Introduction . . . . .	21
1.4.2	The Ti $K$ edge in $\text{TiO}_2$ . . . . .	25
1.4.3	The low-spin $\text{Fe}^{2+}$ $K$ -edge in $\text{FeS}_2$ and $\text{MnCO}$ . . . . .	28
1.4.4	The $\text{Cr}^{3+}$ $K$ edge in allochromatic minerals . . . . .	32
1.4.5	The V $K$ edge in tsavorite and the Fe $K$ edge in $\text{MnCN}$ . . . . .	36
1.4.6	Conclusion . . . . .	39
1.5	Forthcoming studies . . . . .	41
1.5.1	The impact of nuclear motion on XANES spectra and NMR parameters . . . . .	41
1.5.2	The modeling of ELNES spectra . . . . .	45
1.6	and what else?... <i>beyond DFT</i> . . . . .	48
	Appendix: Technical details of the calculations . . . . .	51
	A1- Structure of the studied compounds . . . . .	51
	A2- Pseudopotentials . . . . .	53
	A3- XANES calculation parameters . . . . .	53
	Bibliographie . . . . .	56
<b>2</b>	<b>Sélection d'articles</b>	<b>69</b>



# 1 Mémoire

## 1.1 General introduction

I conduct my research activity at the *Institut de Minéralogie et de Physique des Milieux Condensés* (IMPMC),<sup>1</sup> within the group of Quantum-Theory of Materials, led by Francesco Mauri. The group is composed of 7 permanent members, 3 *directeurs de recherche* CNRS (Francesco Mauri, Christian Brouder, Matteo Calandra), 2 *chargés de recherche* CNRS (Michele Lazzeri, Michele Casula), 1 *ingénieur de recherche* CNRS (Lorenzo Paulatto) and 1 *maître de conférences* UPMC (me). My research activity is focused on the X-ray Absorption Spectroscopy (XAS) and its modeling by first-principles calculations based on Density Functional Theory (DFT). This research theme is stimulated by the pluridisciplinarity that characterizes our laboratory, since XAS is commonly used by at least 6 over the 10 groups that constitute the IMPMC (notably in condensed-matter physics, molecular magnetism, environmental mineralogy and geomicrobiology).

XAS is a powerful tool to study electronic and structural properties of a given element in a material, like impurities in minerals and major component elements of crystalline or non-crystalline systems. Indeed, contrary to X-ray diffraction, XAS is a structural probe that does not require long-range order, and is suitable to investigate the structure of amorphous materials such as glasses. In addition to its element selectivity, XAS is orbital selective: as the binding energies of the core levels are distinct, one can choose the level where the electron is excited and consequently which empty states are probed. Therefore, since electric-dipole transitions prevail in XAS, the  $p$ -empty states of the absorbing atom are probed at the  $K$  (or  $L_1$ ) edge, the  $d$ - (and potentially the  $s$ ) empty states of the absorbing atom are probed at the  $L_{2,3}$  (or  $M_{2,3}$ ) edges, and the  $f$ -empty states can be reached at the  $M_{4,5}$  edges. My research activity is focused on  $K$  edges.

A XAS spectrum at the  $K$  edge includes the near-edge region (typically the first 50 eV), called XANES for X-Ray Absorption Near-Edge Structure, and the extended region (typically 500-1000 eV), called EXAFS for Extended X-ray Absorption Fine Structure. Apart from the distinction about the energy range, only the type of the analysis applied to the experimental data basically distinguishes XANES and EXAFS. The EXAFS data treatment is based on Fourier-transform procedures that lead to quantitative information about the local structure of the absorbing atom. Hence, coordination number and distances between the absorber and atoms belonging to its first (even second) neighboring shell, can be provided by EXAFS analysis. On the contrary, XANES is sensi-

tive to the geometry of the local structure. As Georges Calas likes to say, “when EXAFS tells us that the absorber is in fourfold coordination, XANES tells us whether the neighbors are distributed in a square planar or in a tetrahedron.” Moreover, due to the large mean free path of the ejected electron (the so-called photoelectron) in the XANES region, XANES contains information about the structural organization over distances up to about 7-8 Å. Finally, a XANES spectrum (at the  $K$ -edge) provides an experimental picture of the  $p$ -empty Density Of States (DOS) of the absorber, when one core-hole is present on its  $1s$  level. Hence, a XANES spectrum contains a tremendous amount of information, whose extraction is a challenging task. This constitutes the crucial part of my job.

Since the analysis of a XANES spectrum is not straightforward, theoretical tools are often required to access the information contained in the spectral features. During my PhD (1994-1997) supervised by Philippe Sainctavit, I have used the Multiple-Scattering (MS) theory to model XANES at the  $K$ -edge of low- $Z$  elements (Mg, Al) in geomaterials [46, 47]. Fairly soon, the limitations of the MS method appeared to me as a serious issue. Thus, during my postdoc with Rino Natoli in Frascati, thanks to a collaboration with Yves Joly, I turned out to other numerical techniques, such as the finite-difference method and the Full-Potential Linearized-Augmented-Plane-Wave method [120, 44]. After my recruitment at the UPMC, Francesco Mauri encouraged me to implement XANES calculations within a plane-wave band-structure code, in which he and Chris Pickard had just developed the Gauge-Including-Projector-Augmented-Wave (GIPAW) method for the calculation of Nuclear Magnetic Resonance (NMR) chemical shifts [181]. The efficiency of this implementation [211] was a turning point of my research activity. For instance, it enabled me to investigate increasingly precise effects observable in XANES or XAS-related techniques, such as X-ray Natural Linear Dichroism (XNLD) [42, 124, 38, 41], Resonant X-ray Scattering (RXS) [133, 134] or the impact of vibrations [39, 32, 153].

All the methods I used, or still use, are single-particle methods based on DFT, and treat the exchange and correlation between electrons within mean-field theory, for instance in the local density approximation (LDA). However DFT fundamentally is not appropriate to the theoretical description of electronic excitations, thus the calculation of XAS. By definition, DFT is a theory able to determine the ground-state properties of a material, only. In practice, most of the XANES calculations published in the literature ignore this matter of fact, and there is a kind of general consensus stating that DFT-based approaches are acceptable for core-level spectroscopies. This point will be discussed at the end of this thesis.

<sup>1</sup>The IMPMC was created in 2004 from the union of the *Laboratoire de Minéralogie-Cristallographie de Paris* (LMCP, UMR 7590) and the laboratory of *Physique des Milieux Condensés* (PMC, UMR 7602).

Theoretical developments and calculations are research activities intimately connected to experiment. Therefore I regularly participate to experimental campaigns in synchrotron facilities.<sup>2</sup> For instance, I participated to several measurements on the ID12 beamline of ESRF (European Synchrotron Radiation Facility), where our purpose was to record the angular dependence of XANES on orientated single-crystal samples: the Ti *K* pre-edge in SrTiO<sub>3</sub>, the Fe *K* pre-edge in pyrite (FeS<sub>2</sub>) [40], the Cr, Fe and Ti *K*-edges in doped corundum ( $\alpha$ -Al<sub>2</sub>O<sub>3</sub>) [33, 91], the Ca *K*-edge in calcite CaCO<sub>3</sub> and the superconductor CaC<sub>6</sub> [41]. In the early 2000s, within collaboration with Claire Levelut (Université de Montpellier), Stéphanie Rossano and François Farges (Université de Marne-la-vallée), we synthesized oxide glasses in the Na<sub>2</sub>O-SiO<sub>2</sub> system, and measured using different detection modes, the XANES spectra at the Na, Si and O *K*-edge (LURE, SA32 and SA22 beamlines) [58]. In the framework of a collaboration with the laboratories of Le Louvre (with Ina Reiche and Sandrine Pagès-Camagna), I had the opportunity to participate to Cu *K*-edge XANES and EXAFS measurements on archaeological Egyptian blue and green samples (beamline KMC2 at Bessy) [178]. Finally, for two years, I have been the project leader of temperature-dependent XANES measurements on the LUCIA beamline of SOLEIL. To my opinion, the participation to experiments is crucial even for a theoretician. That permits to be aware to the various experimental difficulties (sample preparation, alignments, detection, quality of the signal, etc.), on the one hand, and to the needs of the experimentalists in terms of modeling, on the other hand.

The following is organized in four sections (1.2, 1.3, 1.4, 1.5 and 1.6).

- Section 1.2 is devoted to the single-particle methods used for XANES modeling. After a historical overview of real-space and band-structure approaches, I report the main ingredients of our pseudopotential-plane-wave scheme.
- Section 1.3 is dedicated to the structural information provided by XANES simulations. Two kinds of applications are presented. The first one deals with 3*d* impurities in substitution for aluminum in a series of minerals. The second one is concerned with glass structural properties as probed by XANES. Calculations performed on several model compounds and on a glass are shown.
- Section 1.4 is dedicated to the electronic information that can be extracted from the *K* pre-edge region of transition metal elements. The pre-edge structure, probing the 3*d* empty states, is intimately connected to

<sup>2</sup>XAS measurements require X-rays with high brilliance and are then carried out on synchrotron facilities, after the approval of experimental proposals by a specific program committee.

the electronic properties of the metal (valence, chemical bond) in the material. I first present the different approaches used to access this kind of information. Then I introduce the compounds I studied, according to the difficulty of modeling their pre-edge structure using single-particle DFT-based methods. I start with the case Ti *K*-edge in titanium oxides, where *a priori* the 3*d* states are empty, to finish with the case of V<sup>3+</sup> impurities in a grossular garnet, with 3*d*<sup>2</sup> configuration. I point out the inherent drawbacks of conventional DFT methods to perfectly model the pre-edge region, so introducing the necessity to go beyond DFT in order to improve the agreement with experiment.

- Section 1.5 is devoted to the two main forthcoming studies that I will carry out in the next five years. The first one deals with the electron-phonon interaction observable in XANES and Nuclear Magnetic Resonance (NMR). The second one consists of extending the QUANTUM-ESPRESSO suite of codes to the calculation of electron Energy-Loss Near-Edge Structure (ELNES spectra).

- Section 1.6 gives the concluding remarks, which are focused on the interest of going beyond DFT.

## 1.2 Modeling XANES using single-particle methods

### 1.2.1 Real-space approaches

The method historically used to model XANES spectra is the multiple scattering theory. To my knowledge, the earliest applications of multiple-scattering theory to the modeling of *K*-edge spectra were performed by Dehmer and Dill in the seventies and concern the N<sub>2</sub> molecule [60, 61]. In 1980, Natoli and coworkers employed an extension of the method used by Dehmer and Dill, and published a comparison between experimental and theoretical Ge *K*-edge spectra in GeCl<sub>4</sub> [169]. This paper is known as the first reference to the CONTINUUM code developed by Rino Natoli and his group. The general theoretical scheme of CONTINUUM was presented first by Natoli and Benfatto at the *fourth International Conference on EXAFS and near-edge structure* held in Fontevraud in 1986 [165], and later by Tyson *et al.* in a paper published in 1992 [219].<sup>3</sup> In the same time, John Rehr and his group conceived the FEFF project, which is probably the code

<sup>3</sup>During my PhD, I used CONTINUUM to model XANES at the Al and Mg *K* edges in minerals [46, 47]. In 2006, Ph. Sainctavit, V. Briois and I published a book chapter that describes multiple-scattering theory using a wave-function formalism. [194]. The goal of this chapter is also to show, through applications at the metal *K*-edge of three M(H<sub>2</sub>O)<sub>6</sub><sup>2+</sup> (M=V, Fe, Cu), the influence of the main parameters (potentials, cluster size, structure) of multiple-scattering codes in general, and CONTINUUM in particular.

the most used in the X-ray absorption community. Since the reference work of Rehr and Albers in 1990 [185], the code has been continuously developed.<sup>4</sup> The latest version, FEFF9, presented by Rehr and coworkers in 2009 and 2010 Ref. [187, 188], is defined as a code dedicated to the calculation of spectroscopic properties, based on an *ab initio* real space multiple scattering approach written in a relativistic Green's function formalism that uses self-consistent spherical *muffin-tin* scattering potentials. The spectroscopic properties are EXAFS, XANES, XNCD (X-ray natural circular dichroism), XMCD (X-ray magnetic circular dichroism), Compton scattering, non-resonant XES (X-ray emission), NRIXS (Non-Resonant Inelastic X-ray Scattering), local DOS, X-ray elastic scattering amplitude  $f = f_0 + f' + if''$  including Thomson and anomalous parts, and EELS (Electron Energy Loss Spectroscopy). Besides, FEFF9 includes many-body effects (see Sec. 1.6), which notably allows the calculation of optical constants from the UV to X-ray energies. The CONTINUUM code of Rino Natoli did not benefit from the same development as FEFF. However, the CONTINUUM formalism was used by some collaborators of Natoli to conceive several multiple-scattering codes, such as the powerful GNXAS software dedicated to EXAFS analysis [81, 80, 235], the MXAN procedure that performs full spectral fitting of the XANES energy region (up to  $\approx 200$  eV above the edge) [19, 167], the multiple scattering part of the FDMNES code [119], the multichannel multiple-scattering code developed by Peter Krüger initially applied to the calculation of Ca  $L_{2,3}$ -edges [137, 138], and the MSSPEC1.0 package recently proposed for the modeling of electron spec-

<sup>4</sup>The first versions of FEFF were dedicated to the calculation of single-scattering EXAFS and, from FEFF4, they incorporated inelastic losses and self-energy shifts with use of a Hedin-Lundqvist self-energy [164]. In 1992 higher order of scattering were included and used to calculate EXAFS of Cu and near-edge structure of molecules O<sub>2</sub> and N<sub>2</sub> (version FEFF5 [186]). Then the path-by-path approach introduced in Ref. [186] was improved in the FEFF6 version [243], notably including the calculation of Debye-Waller factors. FEFF6 was widely used thanks to its weak computational cost. Indeed it is based on an expansion of the full multiple-scattering matrix that avoids its diagonalization (although it is theoretically required at least for the first 10-20 eV of the spectrum). In 1997 Ankudinov implemented the calculation of XMCD (X-ray Magnetic Circular Dichroism) by including relativistic effects, spin and spin-orbit interactions in the FEFF7 version [6]. The subsequent versions of FEFF incorporate full multiple scattering via matrix diagonalization, as in the CONTINUUM code, together with many other features. For instance, the FEFF8 series [5] allows the calculation of self-consistent potentials, density of states, Fermi level, charge transfer, X-ray elastic scattering amplitudes [7], non-resonant X-ray emission spectra and XANES electric quadrupole transitions. Moreover, Nesvizhskii added routines for sum rules applications and for time-dependent local density approximation (TDLDA) calculations in order to take dynamic screening effects into account [4].

troscopies including XANES [197]. On the other side of the Iron Curtain, at the Rostov State University, multiple-scattering theory was also extensively studied for XANES modeling [225]. Indeed, from the seventies [225], the group of Vedrinskii established its own multiple-scattering code. Applications were published in international journals as early as 1982 ( $K$  and  $L_{2,3}$  edges of K and Cl in KCl [225]). The code is still used, known as the XKDQ program package [135]. Besides, in United Kingdom, the group of Vvedensky also developed his multiple-scattering code, ICXANES, in 1986 [228], and later, in the nineties, another italian multiple-scattering code emerged under the name G4XANES [65].

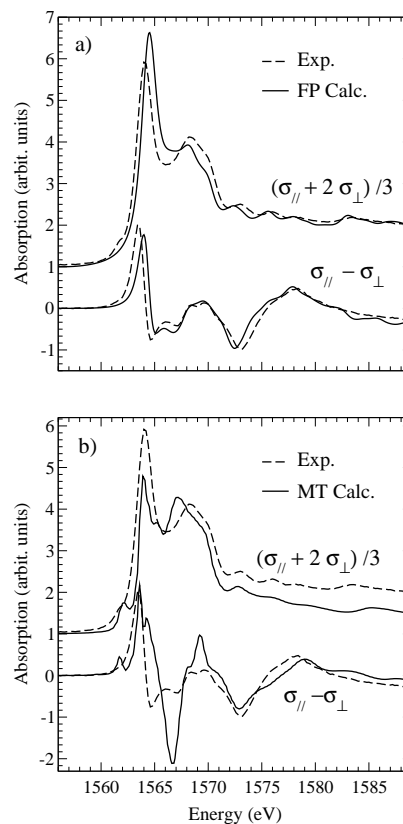


Figure 1.1: Experimental polarized Al  $K$ -edge XANES spectra in corundum ( $\alpha$ -Al<sub>2</sub>O<sub>3</sub>), compared with full potential (FP) calculation (a) and *muffin-tin* (MT) calculation (b). The  $\sigma_{\parallel}$  and  $\sigma_{\perp}$  contributions correspond to the X-ray polarization parallel and perpendicular to the three-fold symmetry axis of the single-crystal sample of corundum, respectively. The difference spectrum,  $\sigma_{\parallel} - \sigma_{\perp}$ , is called XNLD, for X-ray natural linear dichroism, by analogy with XMCD. The *muffin-tin* calculation was performed using CONTINUUM during my PhD. The FP calculation was obtained using the method detailed in the next subsection. Figure extracted from [42].

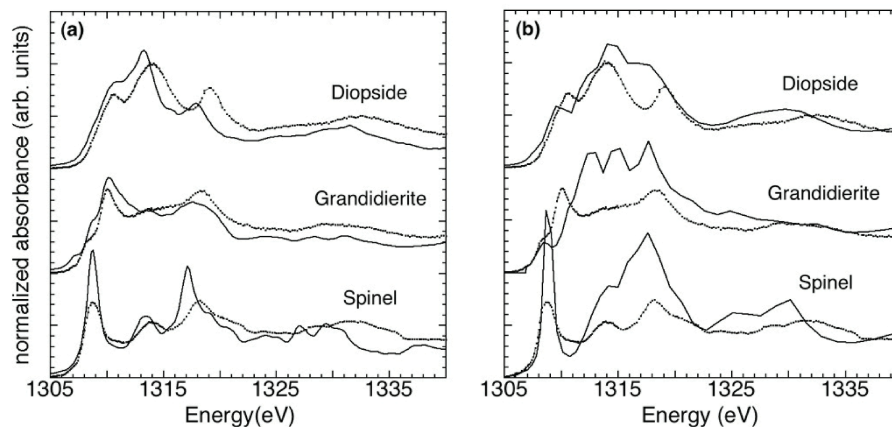


Figure 1.2: Experimental Mg  $K$ -edge XANES in spinel ( $\text{MgAl}_2\text{O}_4$ ), grandierite ( $(\text{Mg,Fe})\text{Al}_3\text{SiBO}_9$ ) and diopside ( $\text{CaMgSi}_2\text{O}_6$ ), compared with full potential (FP) calculation (a) and *muffin-tin* (MT) calculation (b). The MT calculations were performed using FEFF8.2 and the FP calculations, using the method detailed in the next subsection (PhD thesis of N. Trcera [214]). For the three minerals, the experimental-theoretical agreement is satisfactory with the FP approach. In contrast, the *muffin-tin* approach fails to reproduce the XANES spectrum of grandierite. Figure extracted from [215].

The multiple-scattering-theory approach, although quite successful in many applications, suffers from the restriction to potentials of the *muffin-tin* type, i.e., to potentials which are spherically symmetric inside the atomic spheres and constant in the interstitial region. Figures 1.1 and 1.2 illustrate this point by comparing experimental and calculated XANES spectra, which were obtained by using either *muffin-tin* potential (within multiple-scattering framework) or full potential (within the formalism detailed in Sec. 1.2.3). To go beyond the *muffin-tin* approximation, many efforts have been done within the framework of multiple-scattering theory [168, 166, 83, 8, 105, 106]. Even so the prevalent FEFF code still does not use full potential.

At the end of the nineties, the *muffin-tin* approximation was overtaken by using the finite difference method in a real space approach [120], which allows completely free potential shape. This technical advance is due to Yves Joly who developed the FDMNES package [119] (finite-difference-method near-edge structure) under a free and open source distribution. As the FEFF project, FDMNES has been continuously improved and completed. The code calculates XANES, RXS and XMCD spectra, in a tensorial algebra description. The cross-sections can be calculated either using FDM, or multiple-scattering theory in the *muffin-tin* approximation. Due to the recent contributions of O. Bunau, the code includes self-consistency [34] and time dependent density functional theory (TDDFT) calculations [36, 35]. Although this full-potential code is now undoubtedly powerful, in the early 2000s it still required significant computing power and the applications were restricted to small clusters (around 50 atoms without any sym-

metry, at maximum). In this context, we decided to put aside real-space approaches and develop our own full-potential scheme, which allows the treatment of complex systems in a reasonable computing time.

However, it should be mentioned that, as early as the middle of the nineties, the theoretical-chemistry community already had access to full-potential modeling of NEXAFS<sup>5</sup> spectra [3]. Indeed, the earliest versions of the STOBE-DEMON (StockolmBerlin) DFT code,<sup>6</sup> developed by L. G. M. Pettersson (Stockolm University) and K. Hermann (FHI, Berlin) and based on the Linear-Combination of Atomic Orbitals (LCAO) method, are dated from 1996. STOBE permits the calculation of NEXAFS and XES spectra for molecules and atom clusters. In addition, the quantum-chemistry code, named ORCA, developed by F. Neese and his group in Bonn (Germany), is emerging in the XAFS community as a powerful tool for XANES modeling.<sup>7</sup> But, as being solid-state physicists, in the early 2000s we understandably turned towards band-structure approaches.

## 1.2.2 Band structure approaches

The XANES calculation methods are not restricted to real-space approaches. With regards to band structure calculations, local projected densities of empty

<sup>5</sup>In chemistry, the NEXAFS acronym is preferred to the XANES one. NEXAFS stands for Near-Edge X-ray Absorption Fine Structure, not to be confused with EXAFS.

<sup>6</sup>Full information about the STOBE code is available at [www.fhi-berlin.mpg.de/KHsoftware/StoBe/index.html](http://www.fhi-berlin.mpg.de/KHsoftware/StoBe/index.html)

<sup>7</sup>The full documentation of ORCA, defined as an *ab initio*, DFT and semiempirical Self-Consistent-Field-Molecular-Orbital package, is available at [www.thch.uni-bonn.de/tc/orca](http://www.thch.uni-bonn.de/tc/orca).

states (commonly called LDOS) were often used to interpret XANES spectra [233, 53, 57, 13], and in the late nineties, several band structure codes incorporated the radial matrix elements to properly calculate XANES or ELNES (electron energy-loss near-edge structure). It is notably the case of WIEN97 [23], which is based on the full-potential linearized augmented plane wave method [170],<sup>8</sup> the orthogonalized-LCAO program developed by Mo and Ching [158, 159] and CASTEP, whose ELNES part has been developed by Pickard [180, 118, 208]. CASTEP uses pseudopotentials and plane-wave basis set, and reconstructs *all electron* wave functions within the projector augmented wave (PAW) method of Blöchl [24].<sup>9</sup> Within these *ab initio* schemes the treatment of core-hole-electron interaction is usually achieved by including an excited atom into a supercell, typically containing 100-200 atoms. The charge density for such large supercell is easy to calculate self-consistently by using pseudopotentials. On the other hand, the computation of the cross section can be limited by the diagonalization of the Hamiltonian for several empty states at many  $\mathbf{k}$ -points in the Brillouin zone. Indeed in Refs.[180, 118] pseudopotential calculations of ELNES spectra in diamond and *c*-BN were performed with a small 16-atom supercell. In the early 2000s, F. Mauri suggested me to use the recursion method of Haydock, Heine and Kelly [109, 110, 108] to make the calculation of the cross section computationally tractable for larger supercells. Thanks to this iterative technique, the calculation time of XANES becomes negligible compared with the calculation of the self-consistent charge density in large systems. With Mathieu Taillefumier, student of Licence-3 (Bsc) /Master-1 (Msc), we incorporated the recursion method into a pseudopotential scheme (PARATEC) [211]. The efficiency of the method so developed, which definitely avoids the *muffin-tin* approximation, has opened new fields of application. The accuracy of the calculated spectra has enabled us to extract, from the experimental spectra, fine structural and electronic information of the materials under study (see Secs. 1.3 and 1.4). Then the method has been implemented in the open source integrated suite of codes, QUANTUM-ESPRESSO [95], within a package called XSPECTRA [99]. This work has been done at the IMPMC by Ch. Gougoussis during his PhD supervised by M. Calandra [101]. Unlike PARATEC, XSPECTRA allows the use of ultrasoft pseudopotentials. Another advantage of the method

<sup>8</sup>WIEN97 became WIEN2K in 2001.

<sup>9</sup>Band structure codes using *muffin-tin*-type potentials also exist, and some of them incorporate XANES calculations. This is the case of the SPRKKR band structure program package (Spin Polarized Relativistic Korringa-Kohn-Rostoker), based on multiple-scattering theory, developed by H. Ebert and his group, and the `pyLMT0` code based on the Linear-Muffin-Tin-Orbital method, developed by A. Yaresko and coworkers, particularly suited to XMCD modeling [9].

is the fact that it is integrated within an widespread electronic structure code, which optimizes the structure, includes Hubbard parameter (self-consistently calculated), computes bands, DOS, phonons, electron-phonon coupling, Nuclear Magnetic Resonance (NMR) parameters, etc.

In the next subsection, I report the derivation of the x-ray absorption cross-section as presented in our papers [211, 42].

### 1.2.3 XANES modeling within a pseudopotential scheme

XANES modeling requires, for each value  $\hbar\omega$  of the incident x-ray beam energy, the computation of the absorption cross-section that is proportional to the sum of squared probabilities, per unit of time, of making a transition from an initial core state,  $|\psi_i\rangle$  with energy  $E_i$ , to an unoccupied final state,  $|\psi_f\rangle$  with energy  $E_f$ . In a single-particle approach, the XANES cross section is written:

$$\sigma(\omega) = 4\pi^2\alpha\hbar\omega \sum_{i,f} |\langle\psi_f|\mathcal{O}|\psi_i\rangle|^2 \delta(E_f - E_i - \hbar\omega), \quad (1.1)$$

where  $\alpha$  is the fine structure constant and  $\mathcal{O}$  is a transition operator coupling the initial states and the final states. In the electric quadrupole approximation,  $\mathcal{O}$  is given by

$$\mathcal{O} = \underbrace{\hat{\mathbf{e}} \cdot \mathbf{r}}_{\text{electric dipole E1}} + \underbrace{\frac{i}{2} \hat{\mathbf{e}} \cdot \mathbf{r} \mathbf{k} \cdot \mathbf{r}}_{\text{electric quadrupole E2}} \quad (1.2)$$

where  $\hat{\mathbf{e}}$  and  $\mathbf{k}$  are the polarization-vector direction and the wave vector of the photon beam, respectively [31]. Within the frozen core approximation,  $|\psi_i\rangle$  is a core state localized on the atomic site  $\mathbf{R}_0$  that can be taken from an *all electron* ground state atomic calculation. In the impurity model,  $|\psi_f\rangle$  is an excited empty state that is solution of the Schrödinger equation for a potential that includes a core-hole on the absorbing atom. Our scheme uses pseudopotentials in a plane wave basis set and the *all electron*  $|\psi_f\rangle$  is not directly computed. The PAW formalism permits the reconstruction of *all electron* wave function,  $\langle\mathbf{r}|\psi_f\rangle$ , from the corresponding pseudo-wave function,  $\langle\mathbf{r}|\tilde{\psi}_f\rangle$  by using a linear operator  $\mathcal{T}$ :

$$|\psi_f\rangle = \mathcal{T}|\tilde{\psi}_f\rangle. \quad (1.3)$$

$\mathcal{T}$  differs from identity by a sum of local atom-centered contributions, that act only within spherical core regions centered on each atomic site  $\mathbf{R}$ , called augmentation regions and noted  $\Omega_{\mathbf{R}}$ :

$$\mathcal{T} = \mathbf{1} + \sum_{\mathbf{R},n} \left[ |\phi_{\mathbf{R},n}\rangle - |\tilde{\phi}_{\mathbf{R},n}\rangle \right] \langle\tilde{p}_{\mathbf{R},n}|. \quad (1.4)$$

Here  $|\phi_{\mathbf{R},n}\rangle$  and  $|\tilde{\phi}_{\mathbf{R},n}\rangle$  are the *all electron* and pseudo partial waves, respectively, which coincide outside  $\Omega_{\mathbf{R}}$ . The vectors  $\langle\tilde{p}_{\mathbf{R},n}|$ , called projector functions [24], are equal to zero outside  $\Omega_{\mathbf{R}}$  and satisfy the condition  $\langle\tilde{p}_{\mathbf{R},n}|\tilde{\phi}_{\mathbf{R},n'}\rangle = \delta_{\mathbf{R}\mathbf{R}'}\delta_{nn'}$ . The index  $n$  refers to the angular momentum quantum numbers  $(\ell, m)$  and to an additional number  $\nu$ , used if there is more than one projector per angular momentum channel. The  $|\phi_{\mathbf{R},n}\rangle$  form a complete basis for any physical non-core *all electron* wave function within  $\Omega_{\mathbf{R}}$ <sup>10</sup>. Therefore the  $|\tilde{\phi}_{\mathbf{R},n}\rangle$  are also a complete basis for any physical pseudo wave function  $|\tilde{\psi}\rangle$  within  $\Omega_{\mathbf{R}}$ , i.e. for any  $\langle\mathbf{r}|\chi_{\mathbf{R}}\rangle$  function centered on an atomic site  $\mathbf{R}$  and equal to zero outside  $\Omega_{\mathbf{R}}$ ,

$$\sum_n \langle\tilde{\psi}|\tilde{p}_{\mathbf{R},n}\rangle \langle\tilde{\phi}_{\mathbf{R},n}|\chi_{\mathbf{R}}\rangle = \langle\tilde{\psi}|\chi_{\mathbf{R}}\rangle. \quad (1.5)$$

Substituting Eq. (1.4) in Eq. (1.3) and then Eq. (1.3) in the transition matrix element of Eq. (1.1), we obtain

$$\begin{aligned} \langle\psi_f|\mathcal{O}|\psi_i\rangle &= \langle\tilde{\psi}_f|\mathcal{O}|\psi_i\rangle \\ &+ \sum_{\mathbf{R},n} \langle\tilde{\psi}_f|\tilde{p}_{\mathbf{R},n}\rangle \langle\phi_{\mathbf{R},n}|\mathcal{O}|\psi_i\rangle \\ &- \sum_{\mathbf{R},n} \langle\tilde{\psi}_f|\tilde{p}_{\mathbf{R},n}\rangle \langle\tilde{\phi}_{\mathbf{R},n}|\mathcal{O}|\psi_i\rangle. \end{aligned} \quad (1.6)$$

In Eq.1.6, the initial wave function  $\langle\mathbf{r}|\psi_i\rangle$  is localized on the site of the absorbing atom,  $\mathbf{R}_0$ , thus only the  $\mathbf{R}_0$  term has to be considered in each sum. Furthermore it should be noticed that  $\langle\mathbf{r}|\mathcal{O}|\psi_i\rangle$  is zero outside the  $\Omega_{\mathbf{R}_0}$  region. Therefore we can make use of Eq.(1.5) for the third term of Eq.(1.6), which thus vanishes with the first term. Now, introducing

$$|\tilde{\varphi}_{\mathbf{R}_0}^i\rangle = \sum_n |\tilde{p}_{\mathbf{R}_0,n}\rangle \langle\phi_{\mathbf{R}_0,n}|\mathcal{O}|\psi_i\rangle, \quad (1.7)$$

we obtain the following simple expression for the X-ray absorption cross section

$$\sigma(\omega) = 4\pi^2\alpha_0\hbar\omega \sum_{i,f} |\langle\tilde{\psi}_f|\tilde{\varphi}_{\mathbf{R}_0}^i\rangle|^2 \delta(E_f - E_i - \hbar\omega). \quad (1.8)$$

In a reciprocal space approach, the index  $f$  refers to two indexes: the number of empty bands and the number of  $\mathbf{k}$ -points that mesh the irreducible Brillouin zone of the reciprocal lattice. The calculation of XANES from Eq. (1.8) requires the computation of many empty states, that is computationally expensive.

To avoid this drawback, we use the recursion method of Haydock, Heine and Kelly [109, 110, 108], that contains a powerful algorithm to transform a Hermitian matrix into a tridiagonal form, and permits to rewrite the cross-section as a continued fraction. By doing so, only the occupied bands have to be calculated.

<sup>10</sup>A natural choice for the *all electron* partial waves is the solutions of the radial Schrödinger equation for the isolated atom.

To use the recursion method in our scheme, we shall introduce the Green's operator into Eq.(1.8) by making the substitution

$$\sum_f |\tilde{\psi}_f\rangle \delta(E_f - E_i - \hbar\omega) \langle\tilde{\psi}_f| = -\frac{1}{\pi} \Im[\tilde{G}(E)], \quad (1.9)$$

with

$$\tilde{G}(E) = (E - \tilde{H} + i\gamma)^{-1}. \quad (1.10)$$

In Eq.(1.10)  $\tilde{G}(E)$  is the Green's operator associated with the pseudo-Hamiltonian  $\tilde{H} = \mathcal{T}^\dagger H \mathcal{T}$ , which is Hermitian. The energy  $E$  is given by  $E = E_i + \hbar\omega$  and  $\gamma$  is an infinitesimal positive number. The cross section (Eq. 1.8) can be rewritten as

$$\sigma(\omega) = -4\pi\alpha\hbar\omega \sum_i \Im \left[ \langle\tilde{\varphi}_{\mathbf{R}_0}^i|(E - \tilde{H} + i\gamma)^{-1}|\tilde{\varphi}_{\mathbf{R}_0}^i\rangle \right]. \quad (1.11)$$

Following the original work of Lanczos [141, 142], the recursion method sets up a new basis in which the pseudo-Hamiltonian  $\tilde{H}$ , has a tridiagonal representation, from which the matrix elements  $\langle\tilde{\varphi}_{\mathbf{R}_0}^i|(\tilde{H} - E - i\gamma)^{-1}|\tilde{\varphi}_{\mathbf{R}_0}^i\rangle$  are very simply derived. This new basis (Lanczos basis) is obtained by the repeated action of  $\tilde{H}$  onto the normalized initial vector  $|u_0\rangle = |\tilde{\varphi}_{\mathbf{R}_0}^i\rangle / \sqrt{\langle\tilde{\varphi}_{\mathbf{R}_0}^i|\tilde{\varphi}_{\mathbf{R}_0}^i\rangle}$  through the symmetric three-term recurrence relation

$$\tilde{H}|u_i\rangle = a_i|u_i\rangle + b_{i+1}|u_{i+1}\rangle + b_i|u_{i-1}\rangle. \quad (1.12)$$

where  $\{a_i\}$  and  $\{b_i\}$  are two sets of real parameters given by

$$a_i = \langle u_i|\tilde{H}|u_i\rangle \quad (1.13)$$

and

$$b_i = \langle u_i|\tilde{H}|u_{i-1}\rangle = \langle u_{i-1}|\tilde{H}|u_i\rangle. \quad (1.14)$$

The tridiagonal matrix representation of  $\tilde{H}$  in the  $\{|u_i\rangle\}$  basis then permits to rewrite the transition matrix element  $\langle\tilde{\varphi}_{\mathbf{R}_0}^i|(\tilde{H} - E - i\gamma)^{-1}|\tilde{\varphi}_{\mathbf{R}_0}^i\rangle$  as a continued fraction, leading to the following expression for the cross section:

$$\begin{aligned} \sigma(\omega) &= -4\pi\alpha\hbar\omega \times \\ &\sum_i \Im \frac{\langle\tilde{\varphi}_{\mathbf{R}_0}^i|\tilde{\varphi}_{\mathbf{R}_0}^i\rangle}{a_0 - E - i\gamma - \frac{b_1^2}{a_1 - E - i\gamma - \frac{b_2^2}{a_2 - E - i\gamma - \frac{b_3^2}{\ddots}}}} \end{aligned} \quad (1.15)$$

A simple terminator is used to finish the continued fraction [18]. In particular, if  $N$  is the number of iterations required to converge the calculation, we consider that the coefficients  $(a_i, b_i)$  are equal to  $(a_N, b_N)$  for  $i > N$ , this leads to an analytical form of the terminator. It should be noted that the number of iterations  $N$  strongly depends on the broadening parameter  $\gamma$ .

With the iterative technique of Haydock the main part of XANES calculation involves the computation of the Hamiltonian acting on a single vector. This means that the computing time is considerably reduced compared to that can be required by Eq. 1.8 with an explicit diagonalisation.

First the method was implemented in the electric dipole (E1) approximation and restricted to the use of norm-conserving pseudopotential. During her PhD [89], Emilie Gaudry added the electric quadrupole (E2) transitions under my supervising. For a  $K$  edge, the initial state is given by the  $1s$  core wave function,  $\langle \mathbf{r} | \psi_{\mathbf{R}_0}^{1s} \rangle$ , solution of the Schrödinger equation for the isolated absorbing atom (non excited). Then Eq. (1.7) reads:

$$|\tilde{\varphi}_{\mathbf{R}_0}^{1s}\rangle = \sum_{m,\nu} |\tilde{p}_{\mathbf{R}_0,\ell,m,\nu}\rangle \langle \phi_{\mathbf{R}_0,\ell,m,\nu} | \mathcal{O} | \psi_{\mathbf{R}_0}^{1s} \rangle, \quad (1.16)$$

where  $\ell=1$  and  $\mathcal{O} = \hat{\boldsymbol{\varepsilon}} \cdot \mathbf{r}$  in the case of E1 transitions, and  $\ell=2$  and  $\mathcal{O} = \frac{i}{2} \hat{\boldsymbol{\varepsilon}} \cdot \mathbf{r} \hat{\mathbf{k}} \cdot \mathbf{r}$  in the case of E2 transitions. The partial waves  $|\phi_{\mathbf{R}_0,\ell,m,\nu}\rangle$  are valence wave functions, obtained by solving the Schrödinger equation for the isolated excited atom (with one  $1s$  electron). Later, the method was transplanted in QUANTUM-ESPRESSO by Ch. Gougoussis. In 2009, Ch. Gougoussis *et al.* extended the method to ultrasoft pseudopotentials [99].<sup>11</sup>

Our scheme does not calculate absolute transition energies.<sup>12</sup> When the absorber sits in one unique site, i.e., one Wyckoff site in crystals, this problem is not a real drawback. The energy scale of the calculated XANES spectrum is simply shifted by hand in order to match with the experimental spectrum. However, this problem becomes a serious issue in the case of *multisite* compounds, where the absorber occupies more

<sup>11</sup>In the ultrasoft scheme, we define the  $\mathcal{S}$  operator:

$$\mathcal{S} = \mathbf{1} + \sum_{\mathbf{R},n,n'} |\tilde{p}_{\mathbf{R},n}\rangle q_{\mathbf{R},nn'} \langle \tilde{p}_{\mathbf{R},n'}|. \quad (1.17)$$

where the integrated augmentation charge,  $q_{\mathbf{R},nn'}$ , is given by:  $q_{\mathbf{R},nn'} = \langle \phi_{\mathbf{R},n} | \phi_{\mathbf{R},n'} \rangle - \langle \tilde{\phi}_{\mathbf{R},n} | \tilde{\phi}_{\mathbf{R},n'} \rangle$ . The  $\mathcal{S}$  matrix is of the same order as the Hamiltonian (its dimension is given by the number of plane waves).

Then new Lanczos vectors are defined as:

$$|t_i\rangle = \mathcal{S}^{1/2} |u_i\rangle, \quad (1.18)$$

with  $|t_0\rangle = |\tilde{\varphi}_{\mathbf{R}_0}^i\rangle / \sqrt{\langle \tilde{\varphi}_{\mathbf{R}_0}^i | \mathcal{S}^{-1} | \tilde{\varphi}_{\mathbf{R}_0}^i \rangle}$ . The recurrence relation (Eq. 1.12) becomes  $\tilde{H} \mathcal{S}^{-1} |t_i\rangle = a_i |t_i\rangle + b_{i+1} |t_{i+1}\rangle + b_i |t_{i-1}\rangle$ , where the new Lanczos vectors  $|t_i\rangle$  are no longer orthogonal but  $\langle t_i | \mathcal{S}^{-1} | t_j \rangle = \delta_{i,j}$ . During the Lanczos chain, vectors  $|\tilde{t}_i\rangle = \mathcal{S}^{-1} |t_i\rangle$  are stored, so that the  $a_i$  and  $b_i$  coefficients can be defined as  $a_i = \langle \tilde{t}_i | \tilde{H} | \tilde{t}_i \rangle$  and  $b_i = \langle \tilde{t}_i | \tilde{H} | \tilde{t}_{i-1} \rangle$ . Thus, the expression of Eq. (1.15) is unchanged except the numerator of the continued fraction that is replaced by  $\langle \tilde{\varphi}_{\mathbf{R}_0}^i | \mathcal{S}^{-1} | \tilde{\varphi}_{\mathbf{R}_0}^i \rangle$ .

Note that the use of norm-conserving pseudopotentials appears as a specific case of this method with  $\mathcal{S} = \mathbf{1}$ .

<sup>12</sup>Pseudopotential approach uses the frozen-core approximation, i.e., it only considers the valence electrons and the core electron do not contribute to the total energy.

than one symmetrically-inequivalent site. This situation is encountered in amorphous systems such as glasses, where the absorber lies in a distribution of sites, all geometrically inequivalent. It is also often encountered in minerals or crystals with rather complex structures. As an example, in  $\text{K}_2\text{Ge}_8\text{O}_{17}$ , O sits in 11 inequivalent crystallographic sites (see Tab. 1.13) and the resulting theoretical O  $K$ -edge spectrum is the weighted average of eleven individual contributions according to the multiplicity of each oxygen atomic site. At each inequivalent site, the  $K$ -edge energy (the energy required to promote the core  $1s$  electron to the conduction band minimum) is different, because both the  $1s$  energy and the conduction band edge, in presence of the core hole, are site dependent. This is called the core-level shift. One way to estimate the core-level shift is to subtract from the energies of the conduction states, the Kohn and Sham potential,  $V_{KS}(\mathbf{r})$ , averaged on the  $1s$  core region:

$$\langle V_{KS} \rangle = \int V_{KS}(\mathbf{r}) \rho(\mathbf{r}) d^3r, \quad (1.19)$$

where  $\rho(\mathbf{r}) = 0$  outside the core region and  $\int \rho(\mathbf{r}) d^3r = 1$ . In Eq. (1.19), the Kohn-Sham potential is calculated for the supercell including the core-hole. Since the variation of  $V_{KS}(\mathbf{r})$  from one site to another is smooth and uniform in the core region, the variation of  $\langle V_{KS} \rangle$  from one site to another does not depend on the function  $\rho(\mathbf{r})$ . Here  $\rho(\mathbf{r})$  is chosen as:

$$\rho(\mathbf{r}) = \frac{|\langle \mathbf{r} | \tilde{p}_s \rangle|^2}{\int |\langle \mathbf{r} | \tilde{p}_s \rangle|^2 d^3r}, \quad (1.20)$$

where  $|\tilde{p}_s\rangle$  is the first  $s$  projector available in the pseudopotential of the absorbing atom. This method of core-level-shift calculation was successfully used in the XANES calculations at the O  $K$ -edge in  $\text{K}_2\text{Ge}_8\text{O}_{17}$  [45] and at the Mg  $K$ -edge in a silicate glass of  $\text{K}_2\text{O-MgO-3SiO}_2$  composition [217]. Moreover, it was proven to be efficient for the calculation of the relative energy positions of Mg  $K$ -XANES spectra in a selection of reference minerals [216]. At present, in the framework of the PhD thesis of Damien Manuel, this method (for *multisite* compounds only) is confronted to total energy difference calculations, obtained for the supercell without the core-hole and the supercell with the core-hole plus one extra valence electron.

In Secs. 1.3 and 1.4, I present many XANES calculations, which were all performed using this pseudopotential scheme (Sec. 1.2.3), except the case of pyrite ( $\text{FeS}_2$ ) and the Ti  $K$  pre-edge structure in rutile ( $\text{TiO}_2$ ) shown in Fig. 1.13.

Table 1.1: Description of the allochromatic minerals investigated. The compositions were analyzed using the Cameca SX50 electron microprobe at the CAMPARIS facility of Paris (UPMC). Here I give the concentration (in wt ppm) of the various 3d impurities present in the minerals. The amount of the impurity investigated is in boldface. In the case of blue sapphire, we assumed that the low concentration of Ti compared to that of Fe did not affect the site relaxation around iron. In the case of red pyrope, the presence of the large amount of Fe compared to Cr was found to have a very weak impact on the local structure of Cr [123]. The increase of M-O distance in the MO<sub>6</sub> octahedra, where M is the impurity investigated, is given by the distance relaxation evaluated from  $d_{M-O}-d_{Al-O}/d_{Al-O}$ . The Al-O distance is the one in the host structure.

Name, origin	Compound Simplified formula	Concentration of 3d elements (wt ppm)					Dist. relax.	Ref.
		Cr	Fe	Ti	V	Mn		
Blue sapphire <i>synthetic</i>	$\alpha\text{-Al}_2\text{O}_3\text{:Fe-Ti}$		<b>1,500</b>	750			4.9%	[91]
Pink sapphire <i>synthetic</i>	$\alpha\text{-Al}_2\text{O}_3\text{:Ti}^{3+}$			<b>540</b>			5.5%	[91]
Ruby (red) <i>synthetic</i>	$\alpha\text{-Al}_2\text{O}_3\text{:Cr}^{3+}$	<b>10,000</b>					2.6%	[91]
Emerald (green) <i>synthetic</i>	$\text{Be}_3\text{Si}_6\text{Al}_2\text{O}_{18}\text{:Cr}^{3+}$	<b>1,200</b>					3.7%	[90]
Red spinel <i>Mogok, Myanmar (gem-quality)</i>	$\text{MgAl}_2\text{O}_4\text{:Cr}^{3+}$	<b>7,000</b>					3.1%	[125]
Red pyrope <i>Garnet ridge, Arizona</i>	$\text{Mg}_3\text{Al}_2\text{Si}_3\text{O}_{12}\text{:Cr}^{3+}$	<b>14,300</b>	74,500			3,700	3.7%	[126]
Tsavorite (green grossular) <i>natural, unknown location</i>	$\text{Ca}_3\text{Al}_2\text{Si}_3\text{O}_{12}\text{:V}^{3+}$	50	20	110	<b>600</b>	450	3.6%	[28]

## 1.3 Probing structural properties

XANES is much used for local structure determination. The development of the pseudopotential method enables us to investigate structural properties in many systems. In this section, I successively describe the contribution of XANES modeling for local environment studies of 3d impurities in minerals (Sec. 1.3.1), and of germanium and magnesium in oxide glasses (Sec. 1.3.2).

### 1.3.1 The local structure of 3d impurities in allochromatic minerals

During the PhD thesis of Emily Gaudry [89], Amélie Juhin [123] and Amélie Bordage [26], the structural relaxation around substitutional paramagnetic impurities (Cr, Ti, Fe, V) in various allochromatic minerals<sup>13</sup> (corundum, beryl, spinel, silicate garnets) was investigated by combining XANES experiments (and in some cases EXAFS) and first-principles calculations. Color-

<sup>13</sup>An allochromatic mineral is colorless in itself and colored by the presence of impurities.

less corundum ( $\alpha\text{-Al}_2\text{O}_3$ ) becomes red ruby, pink sapphire, or yellow sapphire when a small amount of  $\text{Cr}^{3+}$ ,  $\text{Ti}^{3+}$ , or  $\text{Fe}^{3+}$  incorporates the structure, respectively. The color of blue sapphire is due to the presence of (Fe-Ti) pairs in  $\alpha\text{-Al}_2\text{O}_3$ . Equally,  $\text{Cr}^{3+}$  impurities are responsible for the red color of spinel ( $\text{MgAl}_2\text{O}_4$ ) and pyrope garnet ( $\text{Mg}_3\text{Al}_2\text{Si}_3\text{O}_{12}$ ), and for the green color of emerald (Cr-doped beryl  $\text{Be}_3\text{Si}_6\text{Al}_2\text{O}_{18}$ ). Trivalent vanadium also induces green coloration, notably in the grossular calcic garnet ( $\text{Ca}_3\text{Al}_2\text{Si}_3\text{O}_{12}$ ), also called tsavorite. In all these minerals, the 3d impurity (Cr, Ti, Fe, or V) substitutes for Al, which is sixfold coordinated to oxygen. We studied  $\text{Cr}^{3+}$  in ruby, emerald, red spinel and red pyrope,  $\text{Ti}^{3+}$  in pink sapphire,  $\text{Fe}^{3+}$  in blue sapphire and  $\text{V}^{3+}$  in tsavorite. The samples studied are described in Table 1.1.<sup>14</sup> Since the

<sup>14</sup>In the red pyrope natural sample, a large amount of Fe was detected, as compared to Cr. The  $\text{Fe}^{2+}/\text{Fe}$  ratio was evaluated around 90 %, indicating that Fe mainly substitutes for Mg in the mineral. However, the plausible presence of Fe at around 3.2 Å from Cr has no impact on the Cr *K*-edge spectrum, at least at first glance. Indeed the Cr *K*-edge spectrum of a synthetic red pyrope (with no Fe impurity), *a posteriori* recorded, was found to be almost the same as the one of the natural sample. The differences between both XANES spectra are not salient at all, and concerns the intensity of peak d, and the relative positions

radii of the trivalent  $3d$  ions are larger than the one of  $\text{Al}^{3+}$  ( $r_{\text{Cr}^{3+}}=0.615 \text{ \AA}$ ,  $r_{\text{Fe}^{3+}}=0.645 \text{ \AA}$ ,  $r_{\text{Ti}^{3+}}=0.67 \text{ \AA}$ ,  $r_{\text{V}^{3+}}=0.64 \text{ \AA}$  and  $r_{\text{Al}^{3+}}=0.535 \text{ \AA}$  in an octahedral site [199, 37]), structural modifications of the Al substitutional site are expected.

In order to determine these structural modifications, energy minimization calculations by relaxing the atomic positions were performed for supercells containing one  $3d$  impurity in substitution for Al (see the Appendix for technical details). The main result is that the relaxation is found to be local, mainly related to the distances within the coordination shell of the impurity. The relaxed distances between the impurity and its first oxygen neighbors ( $d_{\text{M-O}}$ ) are very close to those of the fully-substituted systems ( $\text{Cr}_2\text{O}_3$  for ruby,  $\text{MgCr}_2\text{O}_4$  for red spinel,  $\text{Fe}_2\text{O}_3$  for blue sapphire,  $\text{Ti}_2\text{O}_3$  for pink sapphire). An evaluation of the increase of the mean  $d_{\text{M-O}}$  distance is given in the right part of Table 1.1. The spatial relaxation around the dopant is more extended in sapphires than in ruby, slightly affecting the second neighbors [91]. In red pyrope, the second and third shells of neighbors (Mg and Si) relax partially [126]. In tsavorite, the V-Si distance increases during the relaxation process, while the V-Ca distance remains quite the same. The angular relaxation is weak and restricted to the coordination shell of the dopant in the three doped  $\alpha\text{-Al}_2\text{O}_3$  and in emerald (angles  $\leq 0.8^\circ$ ) [91, 90]. The angular relaxation is more significant in red spinel with angular tilts of the Mg-centered tetrahedra around the Cr-centered octahedron [125]. Equally in red pyrope, Cr-site relaxation is accommodated by angular tilts of the Si-centered tetrahedra around the Cr-centered octahedron, and by a deformation of the Mg-centered dodecahedra [126]. An augmentation of the site distortion was observed in red spinel and in the two garnets; the octahedral angular variance, as defined by Robinson [189], increases from  $4.92^\circ$  to  $8.1^\circ$  for red spinel, and from  $2.2^\circ$  to  $5.3^\circ$  for tsavorite. Despite these radial and angular relaxations, the other key result is that the local point symmetry is retained during the substitution for Al.

In order to determine the validity of these theoretical relaxed structures, EXAFS data analysis were performed in the case of ruby [93], blue sapphire [93], emerald [90], red spinel [125] and red pyrope [126], and the experimental and theoretical M-O distances were found in good agreement. However, in diluted samples, EXAFS collection is limited (EXAFS data are indeed not available for tsavorite and pink sapphire). Thus the comparison between experimental and theoretical XANES spectra becomes a valuable approach to get information about the local structure of the dopant. XANES spectra were recorded for all compounds. The samples were single crystals, so that the angular dependence of X-ray absorption was explored. Cubic compounds (spinel and garnets) are isotropic

of peaks c and f (see Fig. 1.4) [123].

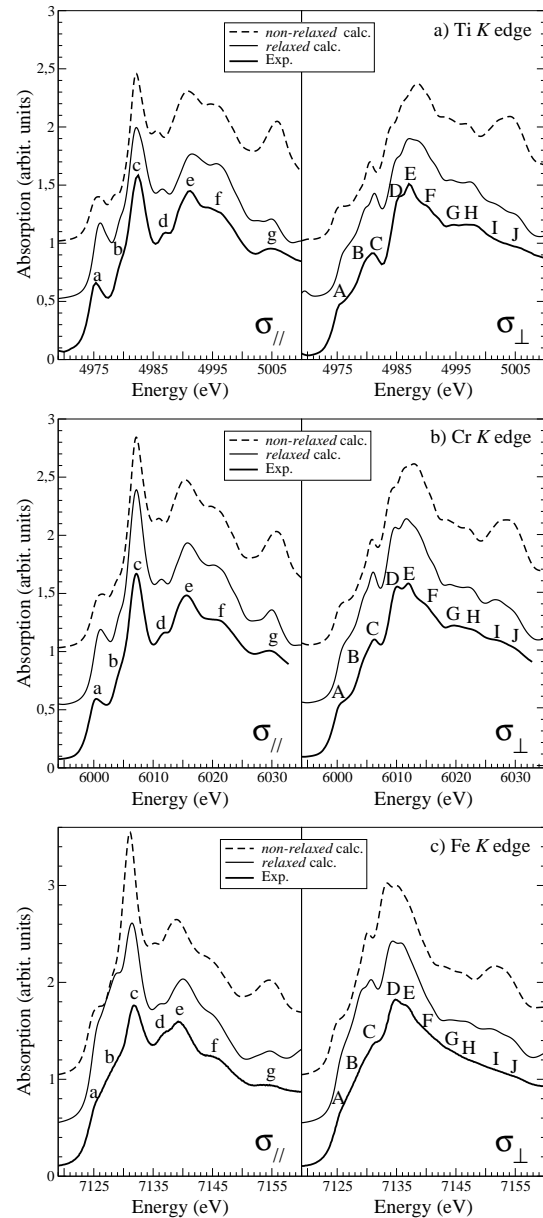


Figure 1.3: Comparison between  $\sigma_{\parallel}$  (left) and  $\sigma_{\perp}$  (right) experimental data (thick lines) and theoretical spectra obtained with the supercells before (dashed lines) and after (thin solid lines) energy-minimization calculation: a) the Ti  $K$  edge in pink sapphire,  $\alpha\text{-Al}_2\text{O}_3\text{:Ti}^{3+}$ ; b) the Cr  $K$  edge in ruby,  $\alpha\text{-Al}_2\text{O}_3\text{:Cr}^{3+}$ ; c) the Fe  $K$  edge in blue sapphire,  $\alpha\text{-Al}_2\text{O}_3\text{:Fe-Ti}$ . Figure extracted from Ref. [91].

regards to electric dipole transitions.<sup>15</sup> For doped  $\alpha\text{-Al}_2\text{O}_3$  and emerald, a strong linear dichroism was observed in the XANES spectra. Consequently, for these minerals, I show either the  $\sigma_{\parallel}$  and  $\sigma_{\perp}$  signals respectively corresponding to the x-ray polarization direction

<sup>15</sup>In cubic crystals, the angular dependence of XAS only concerns the electric quadrupole transitions, that occur in the pre-edge region (see the analysis in Sec. 1.4).

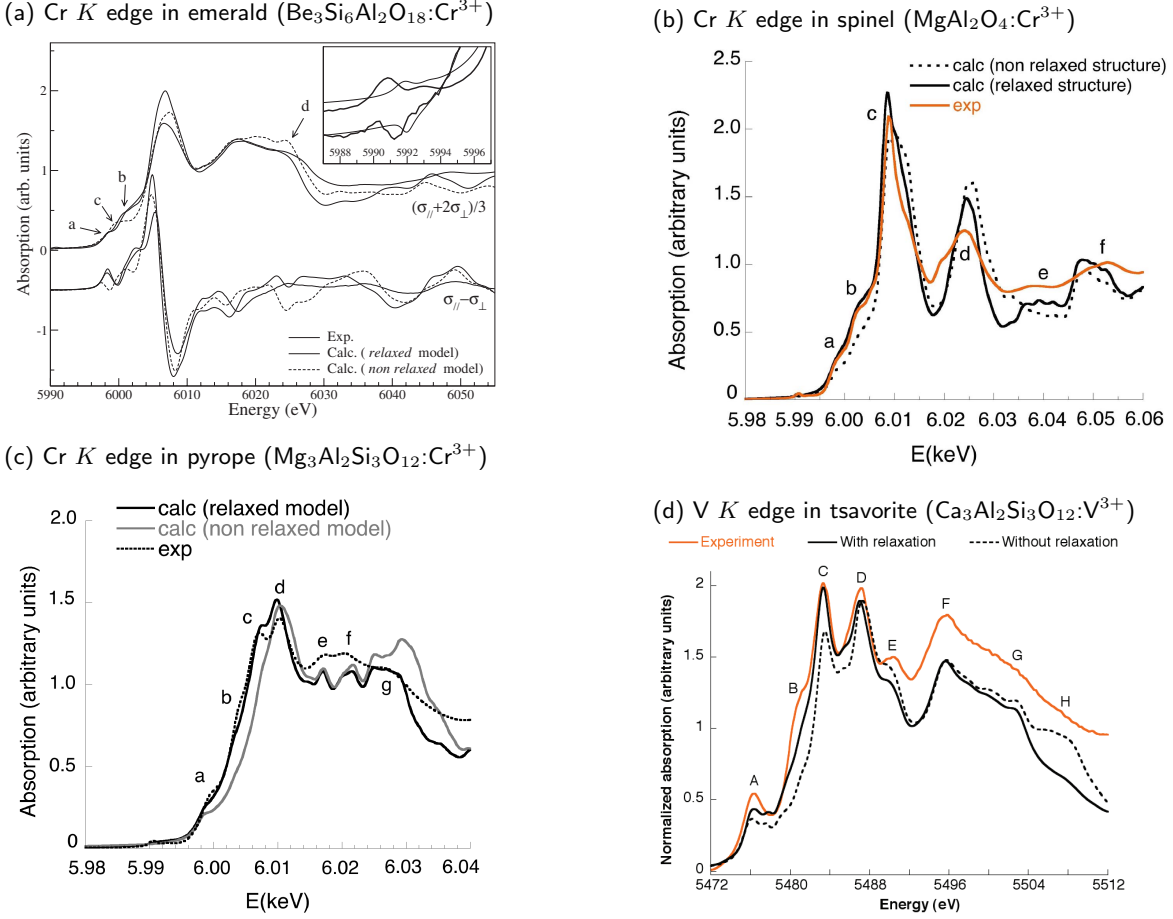


Figure 1.4: Comparison between experimental XANES spectra and calculated absorption cross-sections obtained for the relaxed and non-relaxed structural models: Cr  $K$  edge in emerald (a), spinel (b) and pyrope (c); V  $K$  edge in grossular (tsavorite). Figures (a), (b), (c) and (d) come from Ref. [90, 125, 126, 28], respectively.

( $\hat{\varepsilon}$ ) along and normal to the high-symmetry axis of the crystal, or the isotropic spectrum and XNLD signal (X-ray Natural Linear Dichroism), given by:

$$\sigma_{\text{iso}} = \frac{\sigma_{\parallel} + 2\sigma_{\perp}}{3}, \quad (1.21)$$

$$\sigma_{\text{XNLD}} = \sigma_{\parallel} - \sigma_{\perp}. \quad (1.22)$$

The high-symmetry axis (optical axis) of the doped  $\alpha$ -Al<sub>2</sub>O<sub>3</sub> is of order 3, along the [111] direction of the trigonal cell. For emerald, the high symmetry axis is six-fold and parallel to the  $c$  axis of the hexagonal cell.<sup>16</sup> The sensitivity of XANES to the site structural relaxation was evaluated by computing the XANES spectra for the relaxed supercells and for the non-relaxed supercells, in which one dopant atom replaces an Al atom in its exact position.

Figures 1.3 and 1.4 compare experimental XANES spectra with calculated spectra obtained from the relaxed and non-relaxed structural models. First of all,

<sup>16</sup>For both orientations ( $\sigma_{\parallel}$  and  $\sigma_{\perp}$ ), the X-ray wave-vector  $\mathbf{k}$  is kept perpendicular to the optical axis. This last information is not relevant here, but is used in the pre-edge modeling in Sec. 1.4.

the differences observed between calculated spectra are small but not negligible. The relaxation affects similar XANES regions upon all the series of allochromatic minerals. Indeed, the intensity of the peak located at around 30 eV above the edge is clearly overestimated with the non-relaxed model: peak g of  $\sigma_{\parallel}$  and peak I of  $\sigma_{\perp}$  for ruby and sapphires, peak d of emerald, peak g of red pyrope, peak H of tsavorite, and the small feature located between peaks d and e of red spinel. Moreover peak e of red spinel is only reproduced by the relaxed model. Thus, the XANES features located at around 30 eV above the edge are mainly due to the photoelectron scattering within the coordination shell, so providing a marker of the local character of the relaxation (that is an increase of the bond lengths in the MO<sub>6</sub> octahedron, M=Cr<sup>3+</sup>, Fe<sup>3+</sup>, Ti<sup>3+</sup>, V<sup>3+</sup>). In addition, the edge region (first 10 eV) calculated with the non-relaxed models is clearly not as well reproduced as with the relaxed models. This 10 eV width region appears as another marker of the local relaxation. From these observations, we can conclude that (i) the structural models obtained from our first-principles relaxation procedure are reliable, (ii) XANES is sensitive

to variations in interatomic distances within the coordination shell of the absorbing atom, even if the point symmetry is unchanged.

The Cr-O distances so determined in ruby, emerald and spinel have been used by Moreno and collaborators in order to determine the origin of color of these minerals, which is still a debated in the literature [86, 87, 102, 1].

Besides, similar approaches (combining XANES and first-principles calculations) are now commonly used to investigate the local structure of 3d impurities in oxides (crystals and glasses). For instance, Di Benedetto *et al.* [66] determined the local environment of Fe in natural amethyst (a variety of  $\alpha$ -quartz) by using x-ray absorption spectroscopy (EXAFS and XANES) and DFT+*U* calculations performed with VASP.<sup>17</sup> The analysis of the experimental spectra suggests that Fe is mainly trivalent and replaces Si in its tetrahedral site. This substitution seems to be associated with numerous local distortions due to the presence of Fe<sup>3+</sup> variably compensated by protons and/or alkaline ions, or uncompensated. These results are almost supported by their DFT+*U* simulations (energy minimization) performed on a supercell of  $\alpha$ -quartz including one Fe in substitution for one Si. XANES simulations, missing in their study, would have permit to test the reliability of their relaxation DFT calculations. In a recent paper [29], Bordage *et al.* performed polarized XANES measurements and first-principles relaxation and XANES calculations (with QUANTUM-ESPRESSO), to estimate the proportion of Cr<sup>3+</sup> cations among the two different octahedral sites of the alexandrite structure (Be<sub>3</sub>Al<sub>2</sub>O<sub>4</sub>:Cr<sup>3+</sup>). In another recent paper [213], Tamura *et al.* investigated the local structure of titanium impurities, not in a crystal, but in a glass (Ti-doped SiO<sub>2</sub> glass), by modeling Ti *K*-XANES and O *K*-ELNES spectra using PAW calculations, as implemented in QMAS.<sup>18</sup> It is showed that a Ti atom in substitution for Si in amorphous SiO<sub>2</sub> glass produces a strong pre-edge peak at the Ti *K*-edge and a narrow peak below the threshold at the O *K* edge, in agreement with experimental observations. Besides, the study of Tamura *et al.* makes a nice transition to the following subsection dedicated to the contribution of XANES modeling for structural investigations in amorphous systems.

<sup>17</sup>The full documentation of the VASP code is available at <http://www.vasp.at/>.

<sup>18</sup>Code QMAS, standing for Quantum MAterials Simulator, is based on DFT, uses periodic boundary conditions, plane-wave basis set and full-PAW method (<http://qmas.jp>).

### 1.3.2 The local structure of Ge and Mg in model compounds and glasses

#### Introduction

The physical and chemical properties as well as the durability of a glassy material are intimately related to its composition. The understanding of these properties is thus dependent on the knowledge of the structural environment of the glass components, i.e., the cations. XAS, thanks to its chemical selectivity, is currently used for structural investigation in amorphous materials. However, the analysis of the XANES features of a glass is not straightforward.

Traditionally, XANES spectra of reference model compounds are jointly recorded with those of the glasses under study. Then structural fingerprints are identified in the XANES spectra of the crystalline model compounds, and used to deduce structural information from the spectra of glasses. Usual XANES structural fingerprints are the threshold energy, well-identified specific peaks or pre-edge intensity. For instance, the position of the Mg, Al and Si *K*-XANES threshold is often used as a marker of the coordination number of the probed cation (see for example the Si *K*-edge study of alkali and alkali-CaO silicophosphate glasses performed by Fleet *et al.* [82], the Al *K*-edge study in model compounds and Earth's surface minerals by Ildefonse *et al.* [116] and the Mg *K*-edge study of minerals and silicate glasses by Li *et al.* [150]). Earlier on Li and coworkers [148] had defined the prominent peaks of the B *K*-edge spectra of B<sub>2</sub>O<sub>3</sub> and BPO<sub>4</sub> (clearly separated in energy), as the signatures of <sup>[3]</sup>B and <sup>[4]</sup>B species, respectively. They used this fingerprint method to evaluate the relative proportions of <sup>[3]</sup>B and <sup>[4]</sup>B in K<sub>2</sub>O-SiO<sub>2</sub>-B<sub>2</sub>O<sub>3</sub>-P<sub>2</sub>O<sub>5</sub> glasses. Dingwell *et al.* correlated the Ti *K* pre-edge intensity of minerals to the Ti coordination number, and used this marker to evaluate the Ti coordination state in Ti-bearing silicate glasses [68]. Farges *et al.* also used the Ti *K* pre-edge structure as a marker of Ti coordination number in various crystals and silicate glasses and melts [76, 75], emphasizing its reliability by FEFF6 calculations performed on crystal model compounds [76].

As early shown by François Farges in the nineties (see for instance Ref. [76, 77]), XANES calculations performed on model compounds provide a useful (even essential) contribution to fingerprint-*type* analysis of XANES spectra of glasses. A more direct method to access the glass structure is to simulate the glass XANES spectrum, but this requires realistic structural models. For instance in 2000, Maurizio *et al.*, performed Cu *K*-edge multiple scattering calculations from model clusters, built on the basis of known crystalline structures involving Cu<sup>+</sup> and Cu<sup>2+</sup> ions in silicate matrices, in order to distinguish between Cu<sup>+</sup> and Cu<sup>2+</sup> in silicate glasses [156]. Nearly at the same time, molecular dynamics (MD) simulations on

glass compositions started being performed in order to provide plausible structural model clusters for real-space XANES calculations. For Si  $K$ -edge multiple-scattering calculations in amorphous silica performed with Claire Levelut [146], we used clusters generated by *ab initio* Car-Parrinello MD [50]. In the framework of a thesis dealing with the structure of nuclear-waste glasses [144], I used classical MD simulations in a 5-oxide borosilicate glass to study the impact of the presence of noble metals on the glass structure, which was detectable by Si  $K$ -XANES spectroscopy [43]. Similar method, combining MD and real-space XANES modeling, was used by Farges *et al.* to interpret Fe  $K$ -edge spectra in silicate glasses [78].

As a result, XANES modeling appears as a key step in glass-structure investigations using XANES spectroscopy. In the following, I present two rather recent studies that use plane-wave pseudopotentials XANES calculations. The first one is focused on crystal model compounds based on germanium oxide. Our purpose is to establish relevant XANES marker of five-fold coordinated Ge species. The second one deals with the Mg local environment in reference minerals and silicate glasses. We show that MD simulations are crucial to access the local structure of Mg in glasses.

### Probing fivefold coordinated Ge in germanates using O $K$ -edge XANES

Through experimental studies carried out on Tisilicate glasses [114] and alkali germanate glasses [230, 231], Henderson and collaborators showed the capability of O  $K$ -edge XANES to determine the coordination of the cation bound to oxygen. To support this experimental evidence, I performed a theoretical analysis of O  $K$ -edge XANES spectra of three germanate model compounds:  $\alpha$ -quartz like  $\text{GeO}_2$  (q- $\text{GeO}_2$ ), rutile-type  $\text{GeO}_2$  (r- $\text{GeO}_2$ ) and  $\text{K}_2\text{Ge}_8\text{O}_{17}$ . This work was achieved within a collaboration with Prof. Henderson of the University of Toronto [45]. Here, I have chosen to focus on the meaningful case of  $\text{K}_2\text{Ge}_8\text{O}_{17}$  only, using another point of view than that of our paper (Ref. [45]), in order to emphasize the key results that were used in subsequent studies [232, 145].

In  $\text{K}_2\text{Ge}_8\text{O}_{17}$ , Ge and O atoms occupy 4 and 11 inequivalent crystallographic sites, respectively. Of the four Ge sites, one is in fivefold coordination ( $^{[5]}\text{Ge}$ ) and the other three are in tetrahedral coordination ( $^{[4]}\text{Ge}$ ). The fivefold Ge site has a distorted trigonal bipyramid geometry with one of the oxygen atoms pointing into the center of the small four-membered rings (see Fig. 1.5). The  $\text{K}_2\text{Ge}_8\text{O}_{17}$  structure presents a large variety of Ge-O-Ge angles ranging from  $91^\circ$  to  $133^\circ$ . Angles formed by one O and two  $^{[5]}\text{Ge}$  are smaller ( $\simeq 92^\circ$ - $103^\circ$ ) than those formed by one O and two  $^{[4]}\text{Ge}$  ( $\simeq 120^\circ$ - $132^\circ$ ), thus establishing a relationship between the Ge-O-Ge angle and the Ge coordination number.

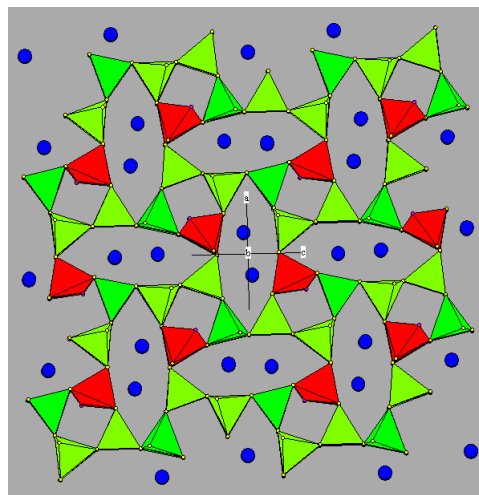


Figure 1.5: Structure of  $\text{K}_2\text{Ge}_8\text{O}_{17}$  viewed down the direction  $[010]$  of the orthorhombic unit cell. The K atoms (blue circles) are inside the eight-membered rings made up of six  $\text{GeO}_4$  tetrahedra (green) and two  $\text{GeO}_5$  polyhedra (red).

Since O  $K$ -edge XANES spectroscopy probes the geometry around oxygen, it is sensitive to variation of the Ge-O-Ge angle, and thus indirectly to Ge coordination.

The experimental O  $K$ -edge XANES spectrum of  $\text{K}_2\text{Ge}_8\text{O}_{17}$  is the average of the signals coming from the 11 inequivalent sites. Taking the site multiplicity into account, it yields the mean average of the environment around 17 oxygen atoms, i.e., two O bound to two  $^{[5]}\text{Ge}$ , six O bound to one  $^{[5]}\text{Ge}$  and one  $^{[4]}\text{Ge}$ , nine O bound to two  $^{[4]}\text{Ge}$ . The crucial advantage of the calculation is that it permits to determine the spectral signature of all individual site.

Fig. 1.6 displays the experimental and calculated XANES spectra of  $\text{K}_2\text{Ge}_8\text{O}_{17}$  (in black), together with theoretical spectra providing the spectral signatures of oxygen connected to  $^{[5]}\text{Ge}$  only (in red), oxygen connected to one  $^{[5]}\text{Ge}$  and  $^{[4]}\text{Ge}$  (in red+green) and oxygen connected to  $^{[4]}\text{Ge}$  only (in green). To complete the figure, the experimental and calculated spectra of q- $\text{GeO}_2$ , the usual crystal reference of  $^{[4]}\text{Ge}$ , has been added at the bottom. The two relevant results of these simulations are the following:

(i) The position of peak c undergoes a shift to higher energy when the Ge-O-Ge angle increases. This shift is about 2 eV from  $97.7^\circ$  to  $130^\circ$  (see Fig. 1.6). Therefore the peak c position can be used as a marker of the presence of fivefold Ge. This result was found in agreement with the interpretation of O  $K$ -edge spectra of  $\text{Na}_2\text{O-GeO}_2$  and  $\text{K}_2\text{O-GeO}_2$  glasses [230, 231]. Moreover this marker was subsequently used by Wang and Henderson to identify the formation of fivefold Ge in alkali germanophosphate glasses when increasing alkali content and at various Ge to P ratios [232].

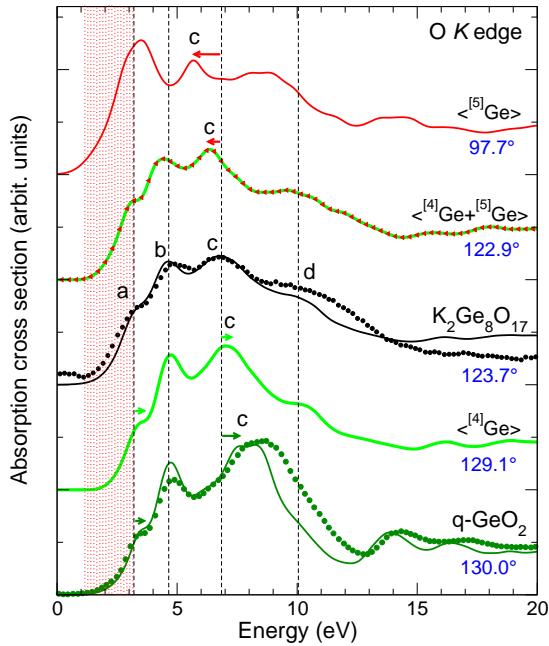


Figure 1.6: **Black curves:** comparison between the calculated (solid) and experimental (dotted) O  $K$ -edge XANES spectra of  $K_2Ge_8O_{17}$ . The theoretical spectrum is the weighted average of the 11 eleven individual contributions according to the multiplicity of each oxygen Wyckoff site. Each individual contribution corresponds to the absorbing O atom located in one of the 11 inequivalent sites. **Red and light-green curves:** theoretical O  $K$ -edge XANES spectra built from the individual spectra.  $\langle^{[5]}Ge\rangle$  is the mean averaged of the two individual spectra corresponding to absorbing O bound to 2  $^{[5]}Ge$ .  $\langle^{[4]}Ge+^{[5]}Ge\rangle$  is the mean-averaged spectrum of the three individual spectra corresponding to absorbing O bound to 1  $^{[4]}Ge$  and 1  $^{[5]}Ge$ .  $\langle^{[4]}Ge\rangle$  is the mean-averaged of five individual spectra corresponding to absorbing O bound to 2  $^{[4]}Ge$ . **Dark green curves:** comparison between the calculated (solid) and experimental (dotted) O  $K$ -edge XANES spectra of  $q-GeO_2$ , where Ge is in tetrahedral coordination. The mean Ge-O-Ge angle is indicated below each spectrum. Vertical dashed lines indicates the positions of the four main features of the experimental spectrum. The arrows point out the relevant effects of Ge-O-Ge angles and then to Ge coordination number. The parameters used for the calculation are given in the Appendix.

(ii) Another useful marker of fivefold Ge (albeit less salient at first glance) is the presence of a significant absorption signal in the region of 2 eV width colored in red in Fig. 1.6, located at the beginning of the spectrum (more or less around the edge jump). Indeed the absorption signal becomes greater in this region (with the appearance of low-energy spectral fea-

tures/shoulders), when the mean Ge-O-Ge angle decreases from  $130^\circ$  to  $97.7^\circ$ . This can be explained by empty DOS considerations. Local DOS calculations performed on  $q-GeO_2$  showed that the first features (in the first 5 eV) of the XANES spectrum are due to the overlap between O- $p$  empty states and Ge empty states [45]. This overlap increases when the Ge-O-Ge angle decreases, resulting in a stronger density of O  $p$  empty states in this region, which can lead to the formation of features or shoulders in the red-colored region. Since small values of the Ge-O-Ge angle are associated to  $^{[5]}Ge$  species, this observation was recently used by Lelong *et al.* to evaluate the amount of fivefold Ge in amorphous  $GeO_2$  under high pressure using *in situ* O  $K$ -edge inelastic X-ray scattering (IXS) measurements [145].

Besides, these two  $^{[5]}Ge$  signatures appear to be clearly different from those of sixfold Ge [45, 145], making the O  $K$ -edge spectroscopy an promising probe of  $^{[5]}Ge$  species in germanate glasses and amorphous germania. A forthcoming study will be the analysis of theoretical individual spectra of amorphous  $GeO_2$  (at ambient and under pressure) calculated for 150 atom cells obtained from MD simulations. These structural models provide a large variety of  $^{[4]}Ge$  and  $^{[5]}Ge$  environments, together with a useful distribution of Ge-O-Ge angles, that will be exploited to confirm the reliability of the two fivefold-Ge markers cited above.

### Probing the local environment of Mg in silicate glasses

Among the various cations entering a glass composition, magnesium is one of the more abundant elements in natural glasses. In synthetic glasses, it has been shown that even a small quantity of magnesium influences the physical and chemical properties of the glass, such as viscosity, durability and the glass transition temperature [67]. However, in spite of its influence on the glass properties, the structural environment of magnesium in silicate glasses has rarely been investigated and the few existing studies led to controversial results. The coordination number of magnesium in  $CaMgSi_2O_6$  glass was found to be 4, 5 or 6 depending on the method of investigation (extended energy-loss fine structure spectroscopy [210], XAS [117, 150], or nuclear magnetic resonance spectroscopy (NMR) [136], respectively). In the case of  $MgO-SiO_2$  glass systems, Kubicki and Lasaga showed by MD simulations that Mg is fourfold coordinated [139] while Wilding and coworkers reported a Mg coordination number around 4.5, combining x-ray and neutron diffraction with reverse Monte Carlo simulation [237]. Later, Shimoda *et al.* concluded that Mg is six-fold coordinated to oxygen in distorted sites [200]. These experimental and numerical controversies on the Mg coordination number contribute to the difficulty in having an accurate picture of the structure of Mg-bearing silicate glasses.

In this context was initiated the PhD thesis of Nicolas Trcera, supervised by Prof. Stéphanie Rossano (Université de Marne-la-Vallée) [214]. The purpose of the thesis was the investigation of the Mg environment in synthetic magnesio-silicate glasses, using Raman spectroscopy, XAS and first-principles calculations.

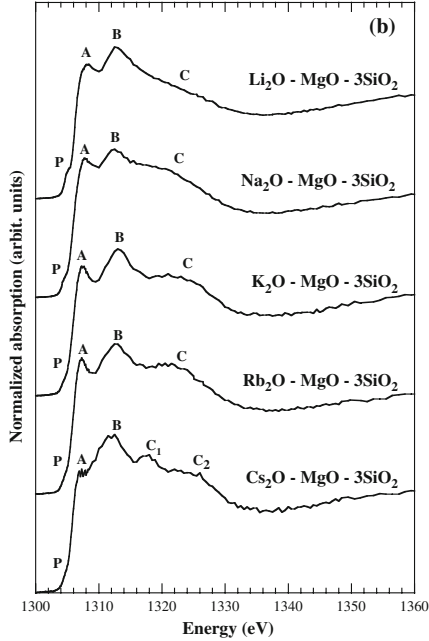


Figure 1.7: Experimental Mg  $K$ -edge XANES spectra of the synthetic XMS3 glasses where  $X = \text{Li, Na, K, Rb}$  and  $\text{Cs}$ . Figure extracted from Ref. [216].

XANES measurements were carried out on various glass compositions and on a large selection of reference minerals (see Table 1.2). For instance, Fig. 1.7 exhibits the experimental Mg  $K$ -XANES spectra of XMS3 glasses with  $X_2\text{O-MgO-3SiO}_2$  composition ( $X = \text{Li, Na, K, Rb, Cs}$ ). To ensure the interpretation of the Mg  $K$ -edge spectra of glasses, the selected minerals present a wide variety of Mg environments, with coordination number ranging from 4 to 8. One notices that the mean Mg-O distance increases with the Mg coordination number.

In a first paper [216], our purpose was to derive from the calculation some relationship between pertinent structural parameters and the variations observed between XANES spectra of a selection of minerals. Fig. 1.8 compares theoretical and experimental XANES spectra in the case of spinel, grandidierite, farringtonite, diopside, enstatite, forsterite and pyrope. An overall good agreement between experimental and calculated spectra is observed. Core-level shift calculations enabled us to reproduce the relative energy positions between the different Mg  $K$ -XANES spectra. Considering the peak-A energy of spinel as reference, the discrepancy between the peak-A position in theo-

Table 1.2: List of the reference Mg-bearing minerals studied during the PhD thesis of N. Trcera. For each of them, I give the Mg coordination number (CN) and the mean Mg-O distance  $\langle d_{\text{Mg-O}} \rangle$ . Four of them contain two inequivalent crystallographic sites for Mg.

Mineral	Formula	CN	$\langle d_{\text{Mg-O}} \rangle$
pyrope	$\text{Mg}_3\text{Al}_2\text{Si}_3\text{O}_{12}$	8	2.27 Å
cordierite	$\text{Mg}_2\text{Al}_4\text{Si}_5\text{O}_{18}$	6	2.11 Å
forsterite	$\text{Mg}_2\text{SiO}_4$	6	2.10 Å
		6	2.13 Å
monticellite	$\text{CaMgSiO}_4$	6	2.13 Å
enstatite	$\text{Mg}_2\text{Si}_2\text{O}_6$	6	2.08 Å
		6	2.15 Å
diopside	$\text{CaMgSi}_2\text{O}_6$	6	2.08 Å
talc	talc	6	2.07 Å
		6	2.07 Å
farringtonite	$\text{Mg}_3\text{P}_2\text{O}_8$	6	2.13 Å
		5	2.05 Å
grandidierite	$(\text{Mg,Fe})\text{Al}_3\text{SiBO}_9$	5	2.04 Å
spinel	$\text{MgAl}_2\text{O}_4$	4	1.92 Å

retical and experimental spectra is  $\leq 0.2$  eV.<sup>19</sup> Fig. 1.8 confirms the trend previously observed by Ildefonse *et al.* [117] and Dien Li *et al.* [150], i.e., that the Mg  $K$ -XANES undergoes a global shift to higher energy with increasing Mg coordination. As referred to the case of spinel ( $^{44}\text{Mg}$ ), the maximum shift (2.5 eV) of the first main feature (peak A) is observed for pyrope ( $^{88}\text{Mg}$ ). Consequently, assuming that the use of this fingerprint is reliable, the XANES spectra of Fig. 1.7 suggest that in the CsMS3, RbMS3 and KMS3 glasses, with shift between -0.3 eV and +0.3 eV, Mg would be mainly fourfold coordinated to oxygen. For NaMS3 and LiMS3, with shift equal to 0.7 eV and 1.0 eV, respectively, the mean coordination number of Mg would be greater than four (and probably lower than 8). The distinction between  $^{55}\text{Mg}$  and  $^{60}\text{Mg}$  is undecipherable. Indeed, the shift of  $^{55}\text{Mg}$  in our selected minerals would be contained between 1.3 eV and 1.9 eV, and the  $^{60}\text{Mg}$ -bearing compounds exhibit shifts ranging from 0.8 eV (forsterite) to 2.1 eV (theoretical individual spectrum of the M2 site of enstatite), and even to 2.5 eV (theoretical individual spectrum of farringtonite). This dispersion of peak-A positions for  $^{60}\text{Mg}$  was found to be related to the distortion of the  $\text{MgO}_6$  octahedron. In Fig. 1.9 are plotted the peak-

<sup>19</sup>Nevertheless, in all cases, peaks B, C and D are at too low energies as compared with experiment. Such mismatch between theory and experiment is often observed within DFT-LDA framework, which is known to underestimate conduction band energies. Similar discrepancies in the peak relative positions, between theory and experiment, is noticeable at the O  $K$ -edge in Fig. 1.6 and at the Al  $K$ -edge in Fig. 1.1.

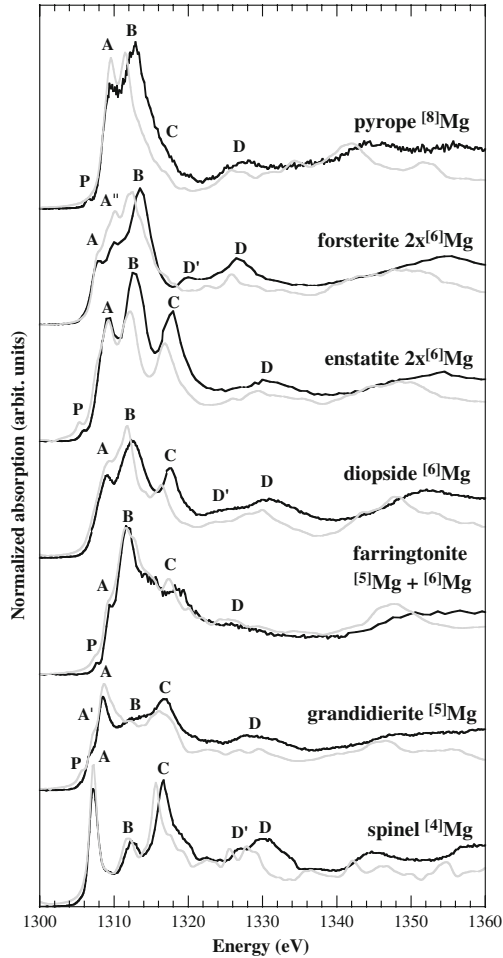


Figure 1.8: Comparison between calculated (grey line) and experimental (black line) Mg  $K$ -edge XANES spectra for seven of the ten reference minerals studied. Figure extracted from Ref. [216].

A position for the  $^{6}\text{Mg}$  spectra as a function of the quadratic elongation of the octahedron.<sup>20</sup> Excluding the farringtonite point, two sets of data are noticeable: a shift of about 2 eV from spinel is associated to weakly-distorted octahedra, while a shift around 0.8 eV corresponds to a substantial distortion of the octahedron.

In a second paper [217], our purpose was to inves-

<sup>20</sup>A convenient and quantitative measure of the octahedron distortion is the quadratic elongation (QE), that is found to be linearly correlated to the angular variance (AV) [189]:

$$\text{QE} = \frac{1}{6} \sum_{i=1}^6 \left( \frac{l_i}{l_0} \right)^2,$$

$$\text{AV} = \frac{1}{11} \sum_{i=1}^{12} (\theta_i - 90^\circ)^2,$$

where  $l_i$  corresponds to the Mg-O distance within the octahedron,  $l_0$  is the Mg-O distance in an octahedron with  $O_h$  symmetry whose volume is equal to that of the distorted octahedron, and where  $\theta_i$  is the octahedral angle.

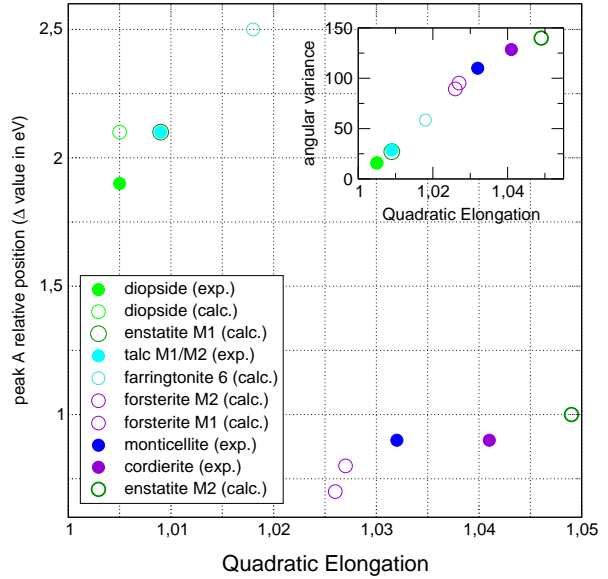


Figure 1.9: Peak-A position (as referred to spinel) as a function of the quadratic elongation of the  $\text{MgO}_6$  octahedron. The inset shows the fairly linear correlation between the quadratic elongation and the angular variance as suggested by Robinson *et al.* [189]. The data point relative to the six-fold Mg site of farringtonite is not exactly within the first set. This may come from the fact that farringtonite is a phosphate while all the other minerals are silicates. Figure extracted from Ref. [216].

tigate the Mg environment in a glass of composition  $\text{K}_2\text{O-MgO-3SiO}_2$  (KMS3), by modeling the Mg  $K$ -edge XANES spectrum from a structural model, which was determined using classical MD simulation coupled with first-principles structural relaxation (see the appendix for details). The structural model so obtained is characterized by five distinct sites of Mg, located in distorted tetrahedra with quadratic elongation ranging from 1.027 to 1.162. Figure 1.10 compares the experimental Mg  $K$ -edge spectrum of KMS3 with the theoretical one, which is the mean average of the five individual contributions. The good agreement between theory and experiment led us to the conclusion that Mg is fourfold coordinated to oxygen in KMS3. This result corroborates the conclusions drawn on the basis of the comparison of XANES spectra of glasses with crystalline references considering the peak-A shift (referred to spinel).

Dien Li *et al.* [150] further utilized the relation between peak-A position and Mg local structure in order to extract quantitative information from the spectra: they established a polynomial correlation function between the energy position of peak A and the Mg-O bond mean distance, that they then used to estimate the average Mg-O distance and thus the Mg coordination number in  $\text{CaMgSi}_2\text{O}_6\text{-NaAlSi}_3\text{O}_8$  glasses [150].

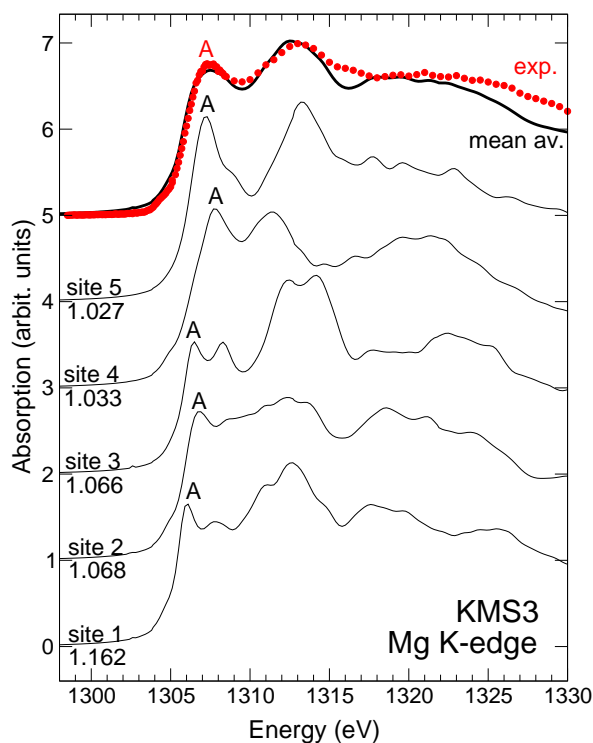


Figure 1.10: Experimental (red points) and theoretical (black line) XANES spectra of KMS3 glass. The theoretical spectrum is the average of the individual spectra obtained for Mg absorbing atoms fourfold coordinated to oxygen atoms. The quadratic elongation of the absorbing-atom tetrahedral geometry is indicated above each curve. Data extracted from Ref. [217].

However, our study shows that (i) the use of such a correlation function to determine the mean Mg-O distance in amorphous materials has to be ruled out, (ii) the peak-A position is not a reliable marker of the Mg-site geometry, especially when considering single-site Mg *K*-edge spectra. Figure 1.11 reports our experimental and theoretical values of peak-A position (referred to spinel) as a function of the mean Mg-O bond length. The XANES calculations permit to increase the number of data points since they yield the values for the two Mg sites of farringtonite, enstatite and forsterite, and for the five Mg sites of the KMS3 glass. Figure 1.11 also incorporates the experimental peak-A positions of Dien Li *et al.* together with their correlation function. Concerning point (i), the salient result of Fig. 1.11 is that numerous data points do not coincide with the polynomial function, and that no obvious correlation can be established. By some happy coincidence, the data point corresponding to the mean average theoretical spectrum of KMS3, with its error bar estimated to 0.2 eV, is located near the correlation function. Further calculations on glasses would be necessary to confirm the accidental nature of this result.

Concerning point (ii), Fig. 1.11 shows that single-site data points are widely dispersed for a given coordination state of Mg. For instance, the use of peak-A position is useless to discriminate, on the one hand, between  $^{[6]}\text{Mg}$  in strongly-distorted octahedra and  $^{[5]}\text{Mg}$  and, on the other hand, between  $^{[5]}\text{Mg}$  and  $^{[6]}\text{Mg}$  in weakly-distorted octahedra, assuming that such distinctions are meaningful in a glass.

To conclude on this part, according to me, the fingerprint method based on the comparison with crystalline references is able to only give a vague idea of the mean number of Mg first neighbors in Mg-bearing oxide materials. Moreover, it is extremely awkward to extract Mg-O mean distances in glasses, from XANES experimental spectra, without using MD structural models. Manifestly, these results are not shared by Seuthe *et al.*, who recently published a structural analysis of Mg *K*-edge XANES spectra of KMS3 modified or ablated by a femtosecond-laser [198]. Indeed, despite the fact that their XANES spectrum of non-irradiated KMS3 is strongly different from ours, Seuthe *et al.* used the peak-A positions of minerals published by Dien Li *et al.* [150] to empirically establish a linear relation between the Mg *K*-edge position and the average Mg-O bond distance. By doing so, they estimate the mean Mg-O distance (with three decimals!) equal to 2.084 Å (for the non-irradiated KMS3). Moreover, the fact that they did not measure their own crystalline reference spectra is a real issue (they used those published by other authors 13 years ago). Even if energy-calibration of the monochromator is supposed to be carefully checked, variation of around 1-2 eV of threshold energy is currently observed for a same compound. For instance, the peak-A position of spinel was found at 1307.2 eV in our measurements [216], at 1308.7 eV in Ref. [171] and at 1309.2 eV in Ref. [150].

## Conclusion

Probing the local structure of cations in oxide glasses by using XANES spectroscopy is a challenging task. Although O *K*-XANES spectroscopy was found to be a promising tool to determine the Ge coordinence in GeO<sub>2</sub>-based materials, O *K*-edge spectra self-evidently become less informative in the case of glasses containing more than one network-former cation. In such cases, the use of XANES at the cation *K*-edge is a natural choice. However, a reliable analysis of the spectra definitely requires MD simulations, which now are easy available due the constant progress of computing power. This is what I learn from our Mg *K*-edge study, the paper on dense silica glass published in Scientific Report by Min Wu *et al.* [240] is one of the recent studies that support this point of view.

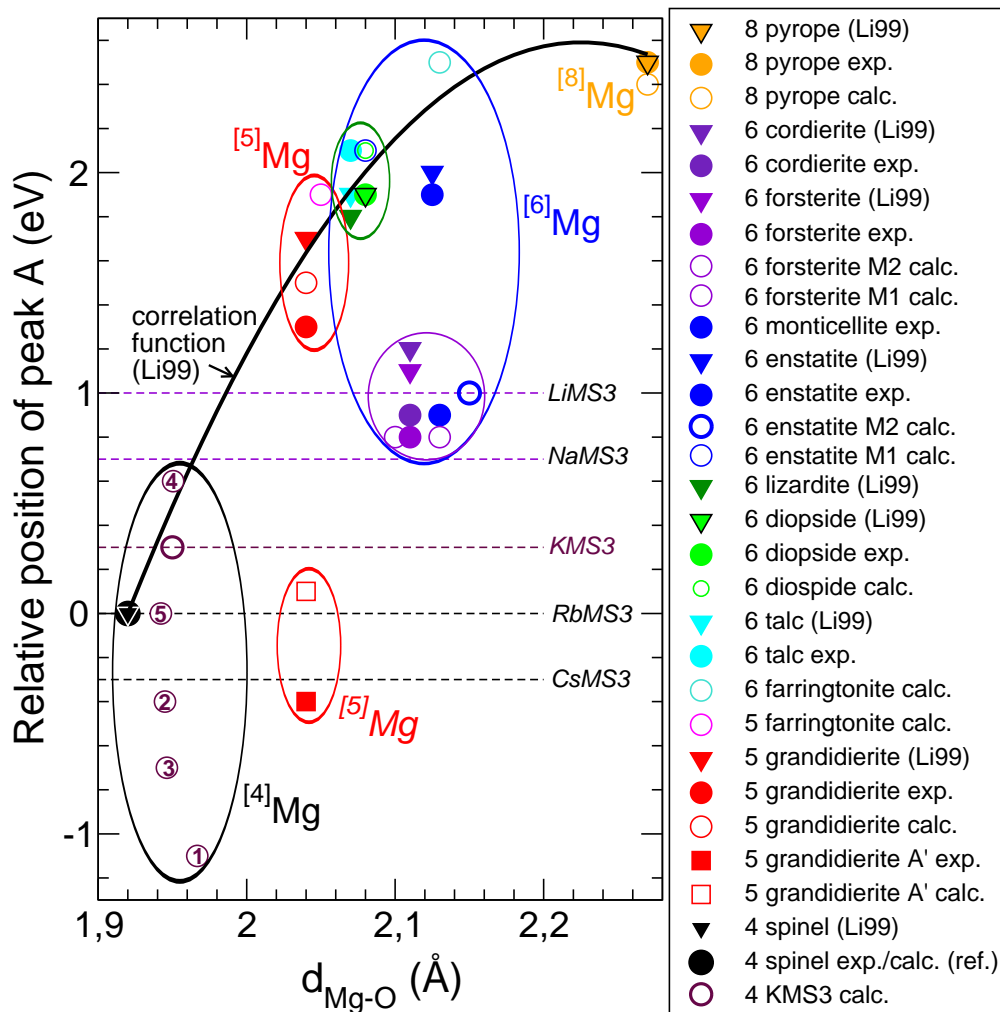


Figure 1.11: Relative peak A position as a function of the mean Mg-O interatomic distance  $\langle d_{\text{Mg-O}} \rangle$  (spinel is taken as reference). The empty and filled circles are our calculated and experimental values, respectively. For the KMS3 glass, I plotted the data points corresponding to the 5 individual spectra shown in Fig. 1.10, as well as the point corresponding to mean average spectrum. The filled triangles are those of Ref. [150]. Two triangles (forsterite and cordierite) are much below the correlation function, in contrast to the analogous Fig. 4 of Ref. [150]. Indeed, Dien Li *et al.* considered the mean energy position of peaks A' and A for cordierite and forsterite to determine the polynomial correlation function (black line). The blue ellipse gathers all the data points corresponding to  $^{[6]}\text{Mg}$ . The data points surrounded by the green ellipse correspond to  $^{[6]}\text{Mg}$  in weakly-distorted octahedra ( $1 < \text{QE} < 1.01$ ). The data points surrounded by the violet ellipse correspond to  $^{[6]}\text{Mg}$  in strongly-distorted octahedra ( $1.025 < \text{QE} < 1.05$ ). The sixfold site of the farringtonite phosphate appears far apart from the others (all the other  $^{[6]}\text{Mg}$ -bearing minerals are silicates). The black ellipse gathers the  $^{[4]}\text{Mg}$  values, i.e. spinel and the theoretical KMS3. For  $^{[5]}\text{Mg}$ , two red ellipses are displayed, according to the choice for the first peak of the grandidierite spectrum, i.e., A (top ellipse) or A' (bottom ellipse). Finally, the peak-A positions of the XMS3 glass series are represented as horizontal dashed lines.

## 1.4 Probing the 3d empty states of transition metals at the K pre-edge

*Note: This section of my HDR thesis was written in autumn 2009. Afterwards it was partly published in 2010, as an invited paper in a special issue of Physical Chemistry Chemical Physics [38]. The current text has been updated with the recent bibliography.*

### 1.4.1 Introduction

In the case of XANES spectra recorded at the K edge of transition metal elements, some features arise in the pre-edge region and are related to the 3d empty orbitals of the probed element. Thus, the pre-edge features of transition metals are related to the coordination number, oxidation state and spin state of the absorbing atom, and to the point symmetry of the absorbing atom site (see the review paper of Yamamoto, dated 2008 [241]). The latter point concerning the site symmetry is crucial in the sense that the pre-edge features can be interpreted using group theory. Indeed, the analyses of the pre-edge features usually make use of the character table of the irreducible representations of the absorbing-atom site-symmetry point group (the most often  $O_h$  and  $T_d$  point symmetries are considered for sixfold and fourfold coordinated absorbing atom, respectively, even if the absorbing atom site polyhedron is not regular). The various methods used for pre-edge analyses can be classified into two groups: the fingerprint approach and the calculations. The fingerprint approach consists of a comparison between the pre-edge spectrum of the material under study with the ones of reference model compounds, including eventually fitting procedures of the spectra by pseudo-voigt functions. The most often, a subtraction of a baseline is first applied to the spectrum in order to extract the pre-edge features [84, 238, 74, 21]. Three kinds of theoretical approaches to calculate the K pre-edge are distinguished: the multielectronic approach based on the Ligand Field Multiplet theory (LFM), the single-particle (or mono-electronic) approach based on DFT, and the many-body Green's function methods. This section is focused on single-particle calculations of the K pre-edge structure for 3d transition metal bearing compounds. Before presenting the outline of the paper, we first draw up an overview of various pre-edge analyses using the methods mentioned above.

In Earth and environmental sciences for instance, the fingerprint approach is widely used to determine the oxidation state of the probed 3d element in complex minerals or natural/synthetic glasses. For instance, in 2001 Galois *et al.* investigated the redox of Fe in synthetic and volcanic glasses, by fitting the corresponding Fe K pre-edge spectra with those of ref-

erence compounds [84]. Such an analysis is based on the 2 eV chemical shift existing between the pre-edge structure of the ferrous and ferric ions in the chosen reference compounds. According to Wilke *et al.* (2001), the most useful characteristics of the Fe K pre-edge for determining Fe oxidation state and coordination number are the position of its centroid and its integrated intensity [238]. By measuring the Fe K pre-edge of 30 model compounds (including natural minerals and synthetic compounds with Fe coordination environments ranging from 4 to 12 oxygen atoms for  $Fe^{2+}$ , and from 4 to 6 oxygen atoms for  $Fe^{3+}$ ), Wilke *et al.* established that the separation between the average pre-edge centroid positions for  $Fe^{2+}$  and  $Fe^{3+}$  is  $1.4 \pm 0.1$  eV. Then the authors used this result to measure the average Fe-redox state for mixed  $Fe^{2+}$ - $Fe^{3+}$  compounds, the pre-edge structure arising between the positions of that of  $Fe^{2+}$  and  $Fe^{3+}$ . In such a way, they have estimated the  $Fe^{3+}/Fe^{2+}$  ratio in more than ten minerals, containing variable/unknown amounts of  $Fe^{2+}/Fe^{3+}$ . The accuracy in redox determination is found to be  $\pm 10$  mol% provided that the site geometry for each redox state is known [238]. More recently, Farges (2009) reported an experimental XANES study of the oxidation state of chromium in a variety of Cr-bearing model compounds containing  $Cr^{2+}$ ,  $Cr^{3+}$ ,  $Cr^{4+}$ ,  $Cr^{5+}$  and  $Cr^{6+}$ , in which the Cr-site symmetry is  $D_{4h}$ ,  $O_h$  and/or  $T_d$  [74]. In particular, it is shown that the centroid position of the pre-edge feature is a better indicator of the Cr valence than the edge position. As chromium, vanadium occurs in nature under various oxidation states (i.e.,  $V^{2+}$ ,  $V^{3+}$ ,  $V^{4+}$  and  $V^{5+}$ ), and vanadium K pre-edge XANES spectra vary systematically with valence state and site symmetry. Sutton *et al.* (2005) illustrated this point by plotting the maximum of the pre-edge intensity as a function of the pre-edge centroid energy for about 50 V-bearing crystalline and glass compounds [209]. In the resulting graph appear distinct regions corresponding to  $[VI]V^{3+}$ ,  $[V]V^{4+}$ ,  $[VI]V^{4+}$ ,  $[IV]V^{5+}$  and  $[V]V^{5+}$ . Balan *et al.* (2006) used these vanadium K pre-edge properties to determine the valence state of vanadium in natural vanadiferous titanomagnetites, and to calculate the proportion of vanadium occurring as  $V^{4+}$  was calculated by comparison with octahedral  $V^{3+}$  and  $V^{4+}$  references [14, 27].

All the examples cited above attest to the interest of the fingerprint approach for the analysis of the pre-edge, at least in Earth and environmental sciences. However, the pre-edge region contains much more precise information, the extraction of which requires calculations. Before introducing the calculation methods used to model the pre-edge, the different electronic transitions, which may occur in the K pre-edge region of transition metal elements, have to be established. There are three kinds of electronic transitions used to describe the pre-edge features, as recalled by de Groot (2007) [56]: (i) local electric quadrupole transitions

(E2),  $1s \rightarrow 3d$ ; (ii) non-local electric dipole transition (E1),  $1s \rightarrow p$ , where the empty  $p$  states of the absorbing atom are hybridized with the empty  $3d$  states of the nearest metal neighbors *via* the  $p$  empty states of the ligands; (iii) local electric dipole transition (E1),  $1s \rightarrow p$ , where the empty  $p$  states of the absorbing atom are hybridized with the empty  $3d$  states of the absorbing atom. In the latter, the  $p$ - $d$  mixing is possible only if the absorbing atom site is not centrosymmetric or if the absorbing atom site centrosymmetry is broken by the atom vibrations. The use of calculation tools enables to determine the contribution of each kind of electronic transitions to the pre-edge features. In any case, the  $3d$  empty states of the transition metal elements of the compound under study are probed in the pre-edge region, either directly through E2 transitions, or indirectly through E1 transitions. The latter can be either local or non-local.<sup>21</sup> Therefore, the final states probed in the pre-edge are rather localized states, where the electron-electron repulsion is supposed to be important. In such cases, the appropriate method to calculate the pre-edge is *a priori* the Ligand Field Multiplet (LFM) one. For instance, the remarkable work by Westre *et al.* [236] shows that the  $K$  pre-edge features of iron ions can be interpreted in the LFM approach. In this study, a fitting procedure was first used to identify the pre-edge features. The allowed multielectronic final states were then determined using the LFM theory, and the relative energies and intensities of the pre-edge features were simulated using molecular orbitals calculations based on DFT. Thanks to this methodology, a detailed understanding of the Fe  $K$  pre-edge features of ferrous and ferric model complexes (comprising tetrahedral, octahedral, and square pyramidal Fe environment, as well as low/high spin states of Fe) was obtained. However in Ref. [236], the transition matrix elements are not calculated in the LFM framework. This was done (for the first time) in the case of the Fe  $K$  pre-edge by Arrio *et al.* in 2000 [12]. More precisely, the eigenstates of the ions and the absolute intensities of the E2 and E1 transitions involved in the  $K$  pre-edge of  $\text{Fe}^{2+}$  and  $\text{Fe}^{3+}$  in minerals, where the iron ions are either in octahedral or tetrahedral sites, have been calculated. Moreover, Arrio *et al.* developed a new model for  $p$ - $d$  hybridization that occurs for ions in tetrahedral site. This model enables to quantify that  $p$ - $d$  hybridization, and to derive the local structure parameters (crystal field, bond covalence) [12]. In 2009, de Groot and co-workers reported LFM calculated spectra of the  $3d^n \rightarrow 1s^1 3d^{n+1}$  E2 transitions with a crystal field value  $10Dq$  of 1.2 eV for  $n = 0, \dots, 9$ , and showed that charge-transfer effects have a weak influence on the  $1s \rightarrow 3d$  pre-edge spectral shapes [55].

<sup>21</sup>Note that local transitions are also called intrasite or in-site, and that non-local transitions are equally called intersite or off-site.

Single-particle methods are quite widely used to calculate  $3d$  element  $K$  pre-edge spectra, although they are in principle not fully appropriate for such applications. The analysis of the pre-edge features can be carried out by both cross-section and local density of states calculations. Single-particle calculations are performed either in a cluster approach, or using periodic boundary conditions. In 2005, Farges used the cluster approach of the FEFF code to calculate Mn  $K$  pre-edge, in order to distinguish the signature of  $\text{Mn}^{2+}$  from the one of  $\text{Mn}^{3+}$  in Mn-bearing oxides [73]. Calculations are also useful to determine the E1 contribution arising from the metal-metal pairs, as previously described in point (ii), in order to include it in the baseline that is used to extract the pre-edge features. Indeed, as explained by Farges, such E1 contributions complicate the determination of the absorbing atom oxidation state and symmetry when using fitting procedures [73]. Similarly, Farges (2009) used FEFF single-particle calculations at the Cr  $K$  edge to support the experimental analysis carried out on a large series of pre-edge spectra in Cr-bearing oxide minerals [74]. Next to cluster approaches, band structure codes are often used to interpret the pre-edge features. Several band structure codes now include the explicit calculation of the absorption cross-section in the electric dipole and quadrupole approximations. As an example, a DFT calculation of the Ni  $K$  pre-edge features using the GGA+ $U$  formalism successfully reproduces the experimental polarized spectra [98]. I do not want to cite further examples using single-particle DFT theory to calculate pre-edge features in this introduction, since it is the subject of the next subsections.

Since single-particle methods are formally dedicated to ground state calculations, many body Green's function approaches have been developed in order to model electronic excitations [176]. These approaches include time-dependent DFT (TDDFT),  $GW$  calculations and the Bethe-Salpeter equation. TDDFT calculations were performed at the V  $K$  edge of  $\text{V}_2\text{O}_5$  [54], at the Fe  $K$  edge of a series of ten iron model complexes [59], and at the Mn  $K$  edge of manganese coordination compounds [190], giving a correct agreement with experiment in the pre-edge region. The Bethe-Salpeter approach was applied to the calculation of the Ti  $K$  pre-edge structure in rutile [202] and in  $\text{SrTiO}_3$  [239]. Although promising, such methodologies still remain quite too challenging to be applied to complex materials.

In the following, I recall all the single-particle theoretical studies of the  $K$  pre-edge of  $3d$  elements, which I carried out or to which I collaborated. These DFT applications are compared to similar work extracted from the literature. I have chosen to present these results using an ascending order of electronic interaction complexity. In the compounds studied, the  $3d$  elements all sit in a distorted octahedral environment. However, a regular octahedron with  $O_h$  symmetry is considered

in a first approximation, so that the 3d levels are split into two groups: the  $t_{2g}$  and the  $e_g$  orbitals. The various cases of 3d shell occupations that I encountered are illustrated in Fig. 1.12.

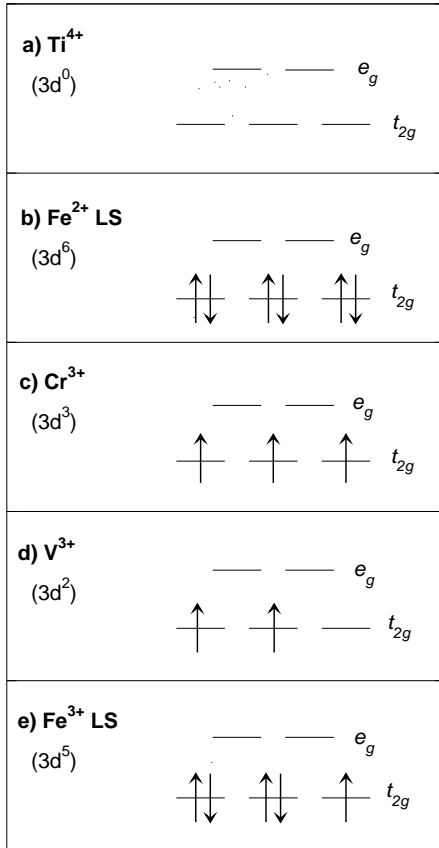


Figure 1.12: Representation of the 3d levels electronic occupation (in  $O_h$  symmetry) of the transition metal ions investigated. Figure reproduced in Ref. [38].

In subsection 1.4.2, the simplest case of the Ti K pre-edge in titanium oxides (rutile and anatase) is presented. Indeed, since the formal charge of Ti in  $\text{TiO}_2$  is +IV, there are no 3d electrons (fig. 1.12a), what provides an ideal situation for single-particle calculations.

In subsection 1.4.3, two examples of Fe K pre-edge where Fe is divalent in a low-spin state are described. In this case, the  $t_{2g}$  orbitals are fully occupied and the  $e_g$  ones are empty (see Fig. 1.12b). Thus, the 3d states, probed by XAS, are the  $e_g$  ones only. In such a case the photoelectron is excited to a level where the multielectronic effects are expected to be weak enough, to be treated within a single-particle framework. The compounds studied are pyrite, a mineral with formula  $\text{FeS}_2$ , and a model molecule, which represents the environment of iron in carbonmonoxy-myoglobin (MbCO).

In subsection 1.4.4, Cr K pre-edge single-particle calculations are presented for three insulating materials ( $\alpha\text{-Al}_2\text{O}_3\text{:Cr}^{3+}$ ,  $\text{Be}_3\text{Si}_6\text{Al}_2\text{O}_{18}\text{:Cr}^{3+}$  and

$\text{MgAl}_2\text{O}_4\text{:Cr}^{3+}$ ), in which Cr occurs as an impurity and has a +III oxidation state ( $3d^3$ ). Here the single-particle calculations need to be spin-polarized since, in an octahedral environment, the  $3d\text{-}t_{2g}$  orbitals of  $\text{Cr}^{3+}$  are occupied by three electrons with parallel spins (see Fig. 1.12c). In spin-polarized calculations, spin-up and spin-down transition matrix elements are separately calculated. Consequently, for spin-up transitions, the situation is quite similar to that of  $\text{Fe}^{2+}$  in low-spin states, in the sense that the transitions towards 3d states only occur towards  $e_g$  states (directly for E2 transitions or indirectly for local E1 transitions). Therefore the electron-electron interaction is supposed to be weak enough to be treated in a single-particle framework. Equally, for spin-down transitions, the situation looks equivalent to the case of the Ti K pre-edge since both the  $t_{2g}$  and  $e_g$  levels are empty and can be probed by XAS.

In subsection 1.4.5, I present two examples that can be considered as limit cases to be treated within a single-particle approach:  $\text{V}^{3+}$  impurity in the garnet-grossular structure, and low-spin  $\text{Fe}^{3+}$  in a molecule, which represents the Fe environment in the cyanomet-myoglobin protein (MbCN). In the case of  $\text{V}^{3+}$ , the  $t_{2g}$  states are occupied by two parallel spins, leaving vacant one of the three mono-electronic orbital (see Fig. 1.12d). Thus, for the majority spin, the electron-electron repulsion is expected to play a significant role in the electronic structure of vanadium, what *a priori* makes the single-particle approximation too strong to be used for the transition matrix element calculation. On the contrary, for the minority spin, since both the  $t_{2g}$  and  $e_g$  orbitals are empty, the calculation of the transition matrix elements for the minority spins is *a priori* equivalent to the previous situation (Fig. 1.12c). The last case, corresponding to high-spin  $\text{Fe}^{3+}$  in MbCN, combines the difficulties of  $\text{Cr}^{3+}$  for the majority spin and of  $\text{V}^{3+}$  for the minority spin (Fig. 1.12e). Hence, this last application of single-particle calculation appears to be the most critical case among all the examples treated in this section.

For each compound, I first give the electronic transitions expected in the pre-edge region. Then, I compare the theoretical spectra with the experimental ones. Finally, I give the assignment of the pre-edge features. Technical details of the calculations are summarized in Appendix A1.

## 1.4.2 The Ti K edge in $\text{TiO}_2$

Three polymorphs of  $\text{TiO}_2$  exist in nature: rutile, anatase and brookite.<sup>22</sup> In this subsection, the Ti K pre-edge spectra of rutile and anatase are investigated.

<sup>22</sup>The most common form is rutile, which is also the stable phase, still above 700°C. Anatase and brookite both convert to rutile upon heating. Anatase is the stable form at low temperature.

### The electronic transitions expected in the pre-edge region

Rutile and anatase both crystallize in the tetragonal system. The point group of rutile is  $4/mmm$  ( $D_{4h}$ ), which yields a dichroic behaviour of XAS in the electric-dipole approximation [31]. The point symmetry of the Ti site,  $mmm$  ( $D_{2h}$ ), is centrosymmetric. Consequently, local E2 transitions and non-local E1 transitions are expected to contribute to the Ti  $K$  pre-edge features of rutile.<sup>23</sup> The point group of anatase is the same as that of rutile (although anatase and rutile space groups are different). The Ti site symmetry is  $\bar{4}m2$  ( $D_{2d}$ ), thus not centrosymmetric. Consequently, in addition to E2 and non-local E1 transitions, local E1 transitions are expected in the Ti  $K$  pre-edge region of anatase.

### Analysis of the polarized Ti $K$ pre-edge of rutile

At the end of the nineties, within a tight collaboration with Yves Joly (CNRS, Grenoble, France) and Rino Natoli (INFN, Frascati, Italy), I theoretically investigated the angular dependence of the Ti  $K$  pre-edge features by using both cluster and band structure full-potential approaches [120, 44]. The former was the finite difference method of the FDMNES program developed by Yves Joly [119]. It was used to calculate the absorption cross-section for the E1 and E2 transitions, for a 6.9 Å radius cluster including core-hole effects. The latter was the WIEN97 electronic structure code, based on the FP-LAPW method [23]. It was used to calculate local and partial density of states of rutile in its ground state (no core-hole was considered).

Figure 1.13 shows the comparison of the calculated FDMNES spectra with the experimental ones of Poulenc *et al.* [182], for  $\epsilon$  parallel and perpendicular to the 4-fold symmetry axis (i.e., the  $z$  axis of the tetragonal cell), the wave vector being along the direction [110]. For both polarizations, the pre-edge region exhibits three well defined features, labeled  $A_1$ ,  $A_2$  and  $A_3$ , which are reproduced by the single-particle calculations:

- For  $\epsilon \parallel z$ , the E2 calculation displays two peaks that contributes to  $A_1$  and  $A_2$ . The E1 calculation also displays two peaks, but contributing to  $A_2$  and  $A_3$ . Therefore,  $A_1$  is a purely E2 peak, originating from  $1s \rightarrow 3d$  local transition. Peak  $A_3$  is a purely E1 non-local peak, originating from  $1s \rightarrow p$  transitions, where the  $p$  empty states of the absorbing atom are hybridized with empty  $3d$  states of the Ti second neighbors. This hybridization is achieved *via* the empty  $p$  orbitals of the O first neighbors. Peak  $A_2$  originates from both kinds of transition (local E2 and non local E1), the E2 contribution representing around 10% of

<sup>23</sup>Note that local E1 transitions due to the atom vibrations are not formally excluded. This point will not be investigated here.

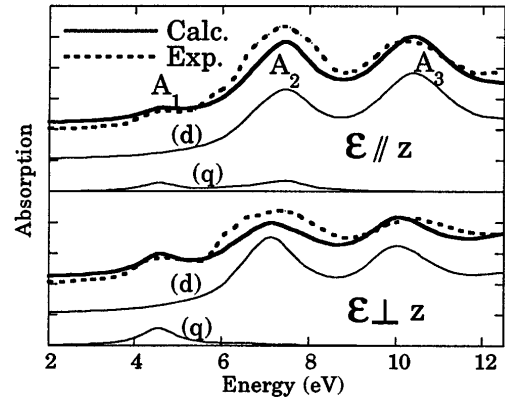


Figure 1.13: Comparison between experimental (dotted line) and calculated (solid line) Ti  $K$  pre-edge spectra of rutile, for the  $\epsilon \parallel z$  (top) and  $\epsilon \perp z$  (bottom) experimental configurations. The calculated spectra are the sum of E2 and E1 contributions, labeled (q) and (d), respectively. Figure extracted from Ref. [120].

the sum E1+E2.

- For  $\epsilon \perp z$ , the E1 contribution also exhibits two peaks, explaining the origin of peaks  $A_2$  and  $A_3$ , while the E2 contribution only displays one peak, giving the origin of peak  $A_1$ .

Now the question is why the E2 contribution is characterized by two peaks for  $\epsilon \parallel z$  and only one for  $\epsilon \perp z$ , the wave vector  $\mathbf{k}$  being parallel to [110]. To answer this question, one should consider the crystallographic structure of rutile. The tetragonal unit cell of rutile comprises two  $\text{TiO}_6$  octahedra, which are crystallographically equivalent but are differently orientated with respect to the photon beam (see Fig. 1.14). When both  $\mathbf{k}$  and  $\epsilon$  are between the Ti-O bonds, the E2 transition probes the local  $e_g$ -like orbital. This happens for  $\epsilon \parallel z$  when Ti in site 1 is excited. On the contrary, when vector  $\mathbf{k}$  (resp.  $\epsilon$ ) is between Ti-O bonds and vector  $\epsilon$  (resp.  $\mathbf{k}$ ) is along a Ti-O bond, the electronic transition probes a local orbital between the bonds, which is mainly  $t_{2g}$ -like. This case is encountered for  $\epsilon \parallel z$  when Ti in site 2 is excited, and for  $\epsilon \perp z$  when both Ti sites are excited. Therefore, when  $\epsilon \parallel z$  (and  $\mathbf{k} \parallel [110]$ ), as the  $d_{xz}$  and  $d_{yz}$  states of the crystal are probed, the first E2 peak corresponds to a transition from the  $1s$  level to the  $t_{2g}$ -like orbital belonging to the Ti site 2, and the second E2 peak to a transition to the  $e_g$ -like orbital belonging to the Ti site 1. When  $\epsilon \perp z$  (and  $\mathbf{k} \parallel [110]$ ), as the  $d_{x^2-y^2}$  states of the crystal are probed, the E2 peak corresponds to transitions from the  $1s$  orbitals to  $t_{2g}$ -like orbitals of both Ti sites. Following similar geometrical arguments, we can show that for the non-local E1 contributions, the  $t_{2g}$  and  $e_g$  orbitals of the Ti neighbors are indirectly

probed at the energy positions of  $A_2$  and  $A_3$  peaks, respectively. The energy position of the  $t_{2g}$  and  $e_g$  orbitals is different for the Ti absorbing atom and for the Ti non-excited neighbors because the  $1s$  core-hole attracts the  $3d$  levels of the Ti absorbing atom. The corresponding energy shift is about 2 eV. Table 1.3 summarizes the assignment of the three Ti  $K$  pre-edge features of rutile for both  $\varepsilon$  orientations.

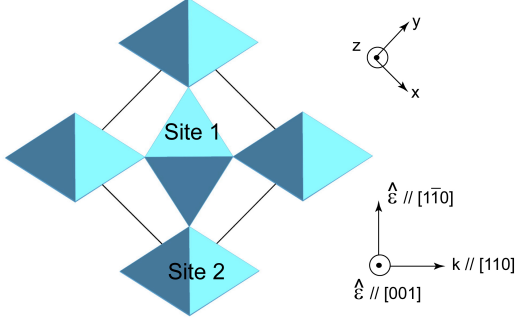


Figure 1.14: Crystallographic structure of rutile, showing the orientation of the two equivalent  $\text{TiO}_6$  octahedra in the unit cell with respect to the polarization and wave vectors for the two experimental setups. Figure reproduced in Ref. [38].

Table 1.3: Assignment of the three Ti  $K$  pre-edge features of rutile for two distinct orientations of the incident photon beam polarization ( $\hat{\varepsilon}$ ).

Peak	Assignment for $\varepsilon \parallel z$
$A_1$	E2: $1s \rightarrow 3d-t_{2g}$ of Ti absorber
$A_2$	E1: $1s \rightarrow p_z$ hybrid. $3d-t_{2g}$ of Ti neighb. + E2: $1s \rightarrow 3d-e_g$ of Ti absorber
$A_3$	E1: $1s \rightarrow p_z$ hybrid. $3d-e_g$ of Ti neighb.
Peak	Assignment for $\varepsilon \perp z$
$A_1$	E2: $1s \rightarrow 3d-t_{2g}$ of Ti absorber
$A_2$	E1: $1s \rightarrow (p_x, p_y)$ hybrid. $3d-t_{2g}$ of Ti neighb.

The good agreement between the experimental and calculated spectra presented in Fig. 1.13 was achieved by considering the following electronic parameters in the FDMNES program:<sup>24</sup> the  $3d$  orbital occupation number of the absorbing atom is  $n_d^* = 1.91$ , the  $3d$  orbital occupation number of the non-excited Ti (Ti neighbors) is  $n_d = 1.0$ , the Ti  $4s$  occupation number being set to zero, and the oxygen  $2p$  occupation being equal to  $6 - n_d/2$  (for neutrality). The parameter  $n_d^*$  includes the amount of screening charge on the Ti absorbing atom. Since the E2 transitions are extremely

<sup>24</sup>The original purpose of the FDMNES program is to fit the experimental XANES spectra in order to provide an electron population analysis [120].

sensitive to the value of  $n_d^*$ , the evaluation of  $n_d^*$  was obtained with high accuracy by fitting the energy position of  $A_1$ . The parameter  $n_d$  was optimized especially with the energy positions of peaks  $A_2$  and  $A_3$  with respect to the XANES features located at around 20 eV above the edge. Note also that the energy position of  $A_2$  and  $A_3$  was quite sensitive to the amount of charge transfer between Ti and O.

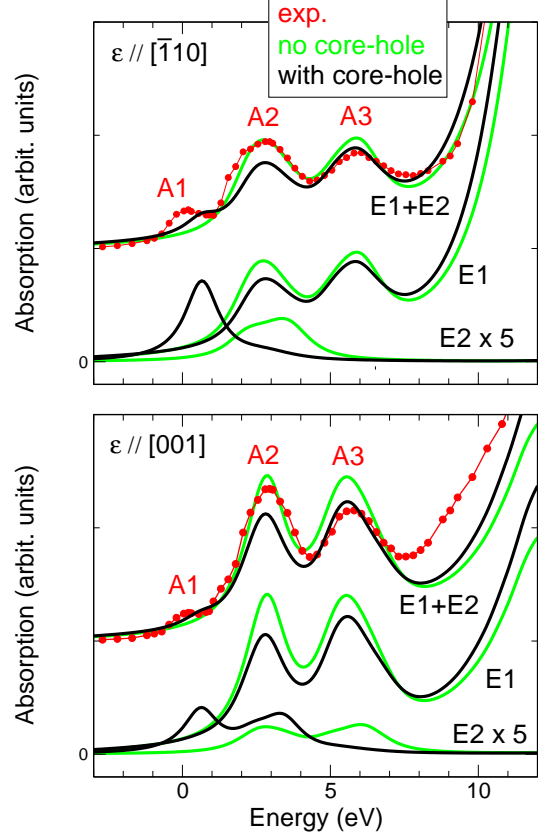


Figure 1.15: Comparison between experimental (red line with circles) and calculated (solid line) Ti  $K$  pre-edge spectra of rutile, for the  $\varepsilon \parallel z$  (bottom) and  $\varepsilon \perp z$  (top) experimental configurations. The calculated spectra were carried out with the XSPECTRA package of QUANTUM-ESPRESSO suite of codes, for a supercell including a core-hole (black line) or not (green lines), so showing the effects of the presence of the  $1s$  core-hole. The zero energy corresponds to the highest occupied state of the calculation including the core-hole effects. Note that the E2 contribution has been multiplied by 5 for clarity. Figure reproduced in Ref. [38].

Within a first-principles Self-Consistent-Field (SCF) approach, like the QUANTUM-ESPRESSO suite of codes, the agreement with experiment is less satisfactory since no fitting parameter is used, as can be seen in Fig. 1.15. Three kinds of discrepancy are noticeable. First, the calculated  $A_1$  peak is located at too high energy (about 0.6 eV), when compared to experiments. This disagreement represents the main drawback of the

SCF approach, compared to the fitting one adopted in the FDMNES code. In the SCF approach, the core-hole effects (including the screening charge on the Ti absorbing atom) are taken into account within the SCF calculation of the charge density for a supercell including a  $1s$  core-hole on one of the Ti atoms. When no core-hole is present in the calculation (green lines), one observes that the E1 contribution is not much modified. Only the relative intensities of peaks  $A_2$  and  $A_3$  are changed. On the contrary, as already mentioned in the study performed with FDMNES [120], the E2 contribution is very sensitive to the core-hole effects. The presence of the core-hole especially affects the energy positions of the two local transitions  $1s \rightarrow 3d-t_{2g}$  and  $1s \rightarrow 3d-e_g$  by attracting them to lower energy. Without the core-hole, peak  $A_1$  is not reproduced. Nevertheless this attractive effect does not seem sufficient to provide a total agreement with experiment. But, it also appears that if the attraction was more important, the  $3d-t_{2g}$  states of the excited atom could fall into the occupied states. Indeed, the presence of the core-hole dramatically affects the value of the gap, which decreases from 1.82 eV to 0.36 eV (at the  $\Gamma$  point) when taking into account the core-hole. Consequently, the fact that E2 peaks are at too high energy in the SCF approach is globally related to the use of a LDA-based DFT method, which (i) is known to underestimate the gap of insulating materials, (ii) is not fully appropriate to the modeling of the core-hole-electron interaction. In 2004, Shirley calculated the Ti  $K$  pre-edge of rutile using a Bethe-Salpeter approach (BS) [202]. He obtained an overall good agreement with experiment, notably with peak  $A_1$  at nearly the right position. Thus the BS approach adopted by Shirley provides a better description of the XAS core-hole effects than DFT-LDA methods.

The second discrepancy concerns the shape of the  $A_2$  peak which seems to include two components in the experimental data. According to the measurements of Le Fèvre *et al.* (2005) [79], the first component would be an E2 one ( $1s \rightarrow 3d-e_g$ ) and the second component, an E1 one ( $1s \rightarrow p$  hybridized with the  $t_{2g}$  shell of the Ti neighbors). In the calculations presented here, these two contributions are not resolved in energy, due again to the difficulty of single-electron approach to fully account for the core-hole-electron interaction. The third discrepancy is related to the intensity of peak  $A_2$ , which is not high enough with respect to the experimental one, whatever the method is employed. Thermal fluctuations of nuclei were found to be at the origin of this discrepancy [70, 32].

### Analysis of the isotropic Ti $K$ pre-edge of anatase

In the framework of the PhD thesis of Amélie Bordage (2009) [26], the Ti  $K$  pre-edge isotropic spectrum was calculated using QUANTUM-ESPRESSO, and compared

to the experimental data of Ref. [193]. The results are shown in Fig. 1.16. The Ti  $K$  pre-edge of anatase is characterized by three peaks ( $A_1$ ,  $A_2$  and  $A_3$ ), like in rutile. However, unlike the case of rutile, the E1 contribution exhibits three peaks, due to the fact that local E1 transitions also occur. The E2 contribution displays two features: a  $1s \rightarrow 3d-t_{2g}$  well-resolved peak followed by a broad and weak  $1s \rightarrow 3d-e_g$  peak. The first E2 peak represents 22% of the total intensity of peak  $A_1$  and the second 2% of the total intensity of peak  $A_2$ . The quadrupole contribution is therefore weak compared to the dipole one, as expected in a non-centrosymmetric site. The assignment of the three pre-edge peaks is given in Table 1.4.

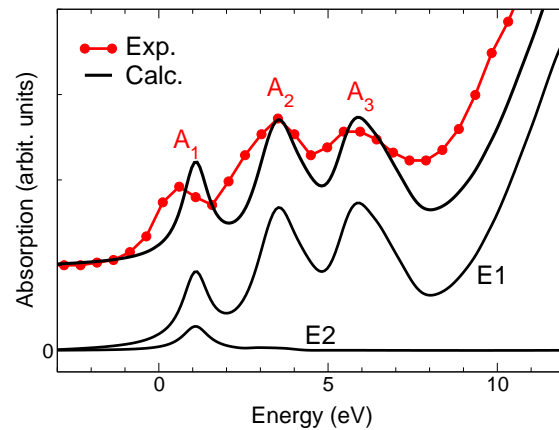


Figure 1.16: Comparison between experimental (red line with circles) and calculated (black solid line) Ti  $K$  pre-edge isotropic spectra of anatase. The calculated spectrum is the sum of the E1 and E2 contributions, which are also shown. Figure reproduced in Ref. [38].

Table 1.4: Assignment of the three Ti  $K$  pre-edge features of anatase.

Peak	Assignment
$A_1$	E1: $1s \rightarrow p-t_{2g}$ of Ti absorber + E2: $1s \rightarrow 3d-t_{2g}$ of Ti absorber
$A_2$	E1: $1s \rightarrow p-e_g$ of Ti absorber + E1: $1s \rightarrow p$ hybrid. $3d-t_{2g}$ of Ti neighb. + E2: $1s \rightarrow 3d-e_g$ of Ti absorber
$A_3$	E1: $1s \rightarrow p_z$ hybrid. $3d-e_g$ of Ti neighb.

The agreement between theory and experiment obtained for anatase is equivalent to the one of rutile, i.e., it has at least two main drawbacks. First, the calculated  $A_1$  peak is at too high energy (of about 0.5 eV). Second, the  $A_2$  may contain two components, as suggested by Glatzel *et al.* [96], which are not distinguishable in the simulation. These two drawbacks

may have the same origin, i.e., the lack of DFT-LDA to properly model the core-hole-electron interaction. Indeed the second peak involves local and non-local transitions. The local ones are E1 and E2, thus involving the  $3d-e_g$  shell of the Ti absorbing atom. Due to the misplacement of the  $3d$  levels of the excited Ti, the  $3d$  states of the absorbing Ti are located at too high energy (the core-hole is not attractive enough).

### 1.4.3 The low-spin $\text{Fe}^{2+}$ K-edge in $\text{FeS}_2$ and MbCO

The Fe K pre-edge in compounds where Fe is in six-fold coordination, divalent and low spin, also constitutes a favorable case for single-particle calculations, as we will see below. Indeed, electronic transitions can only involve the empty  $e_g$  states (see Fig. 1.12b). Two compounds are investigated: pyrite ( $\text{FeS}_2$ ) and the carbonmonoxy-myoglobin (MbCO).

#### The electronic transitions expected in the pre-edge region

As pyrite crystallizes in the cubic system, the electric dipole transitions are isotropic [31]. In the cubic cell, iron atoms are octahedrally coordinated to sulphur atoms and sit in four equivalent sites with point symmetry  $\bar{3}$  ( $C_{3i}$ ). Thus the iron site contains an inversion center, that means that local  $p-d$  hybridization are forbidden: local E1 transitions are not expected in the pre-edge region. Consequently, only E2 transitions and non local E1 transitions are expected in the pre-edge region (as in the case of rutile). Note that in the cubic cell, the four  $\text{FeS}_6$  octahedra are tilted from the cubic crystallographic axis by about  $23^\circ$  [206].

Myoglobin (Mb) is a single-chain globular protein of 153 amino acids, which contains a heme, i.e., an iron-bearing porphyrin. A proximal histidine (H93) group is attached directly to the iron center. When a CO molecule is linked to Fe on the opposite side of the heme plane, iron Fe is in divalent low spin state. Then the six coordination positions of Fe are occupied, i.e., the four nitrogen atoms in the heme plane (labeled  $N_p$ ), the nitrogen atom belonging to the distal histidine (H93), and the carbon atom of the CO molecule (see Fig. 1.17). The protein is then called carbonmonoxy-myoglobin (MbCO). MbCO crystallizes in a monoclinic lattice (space group  $P2_1$ ), with two molecules (about 1500 atoms) per unit cell [128, 227]. The two Fe atoms contained in the unit cell obviously are too far from each other to interact. Therefore, since the Fe site is non-centrosymmetric in an approximate  $4mm$  ( $C_{4v}$ ) symmetry, two kinds of transitions are expected in the pre-edge: E2 and local E1.

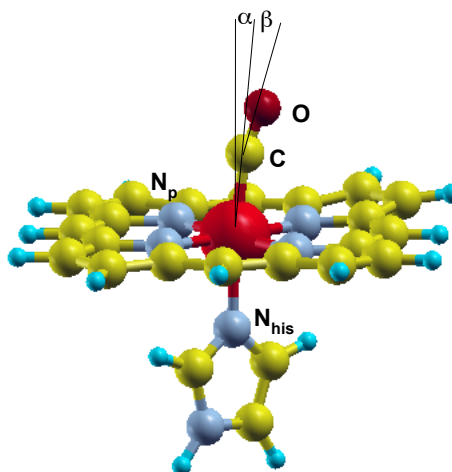


Figure 1.17: Local environment of Fe in MbCO, within the cluster used for XANES calculation. It contains 48 atoms, including additional hydrogen atoms introduced to ensure the neutrality of the system. The nitrogen first neighbors of iron are labeled  $N_p$  for the four belonging to the heme plane and  $N_{his}$  for the one belonging to the H93 histidine residue. The angle  $\alpha$  and  $\beta$  are introduced to characterize the angular geometry of the chain Fe-C-O (or Fe-C-N). Figure generated by XCrysDen [132] and reproduced in Ref. [38].

#### Angular dependence of the Fe K pre-edge of pyrite

In 2001, we measured the angular dependence of the pre-edge region in order to reveal the E2 transitions [40]. Indeed, since the system is cubic, only the E2 transitions depend on the orientation of the crystal towards the X-ray beam, the E1 ones being isotropic. The XNLD (linear dichroism) was found to be around 0.5 % of the edge jump. Experimental results were compared with single-particle calculations, which were performed for a 51 atom cluster by using FDMNES and considering two kinds of electronic full-potential: one non self-consistent calculated within FDMNES,<sup>25</sup> one self-consistent (SCF) generated using the WIEN2K FLAPW code.<sup>26</sup>

<sup>25</sup>The non self-consistent potential consists of the solution of the Poisson equation for a simple superposition of neutral atomic electronic densities. To the Coulomb potential so obtained, was added an exchange and correlation potential of Hedin-Lundqvist type. The  $Z+1$  approximation is used to simulate the core-hole and screening effects. No fitting parameter were determined as in the case of rutile.

<sup>26</sup>The FDMNES code can use as input SCF full-potential generated by the WIEN2K (or the older version named WIEN97). For pyrite, I used WIEN97 and the SCF full-potential by minimizing the total energy of a  $2 \times 2 \times 2$  cubic supercell, including a  $1s$  core-hole on one of the 32 Fe atoms. The other parameters of the code were set to the default values.

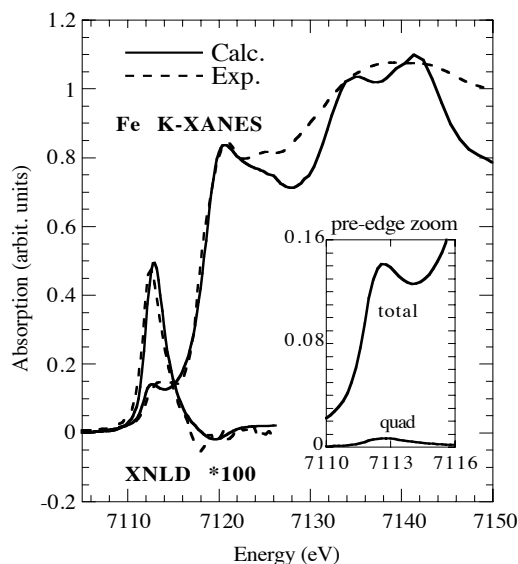


Figure 1.18: Experimental (dashed line) and calculated (solid line) Fe  $K$ -edge spectra in pyrite. The XNLD signal is multiplied by a factor 100. The calculated XANES and XNLD were obtained with the non-SCF potential. Inset: zoom of the pre-edge region, where both total and E2 cross sections are plotted. The experimental spectra were recorded on the ID12 beam line of ESRF. Figure extracted from Ref. [40].

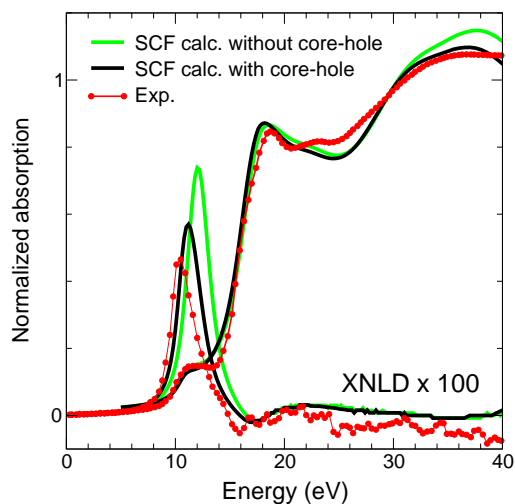


Figure 1.19: Comparison between the experimental (red line with circles) XANES and XNLD spectra with the corresponding calculated spectra obtained with WIEN2K SCF potentials used as input in the FDMNES code (in black, the potential including the  $1s$  core-hole, and in green, the ground state potential).

Figs. 1.18 and 1.19 show the results obtained with the non-SCF potential and the SCF potential, respec-

tively, and compare them to the experimental spectra. A good agreement is obtained with both kinds of potential. The isotropic part of the E2 transitions were determined from the calculations (see the inset of Fig. 1.18). The isotropic E2 cross section (labeled quad) corresponds to transitions  $1s \rightarrow 3d-e_g$  of the Fe absorbing atom; it is about 4 % of the pre-edge intensity and 0.7 % of the edge jump. The pre-edge mainly results from E1 transitions, which are non-local (i.e.  $1s \rightarrow p$  hybridized with  $3d-e_g$  of the neighboring Fe via the empty  $p$ -states of the S neighbors). Figure 1.19 shows the core-hole effects, that are found to be weak in the XANES region. From the observation of the calculated dichroic signals, the same phenomenon as for rutile is noticed, that is the shift of the E2 transitions towards lower energy when the core-hole is taken into account. Also the strength of the XNLD signal decreases with the presence of the core hole, improving the agreement with experiment.

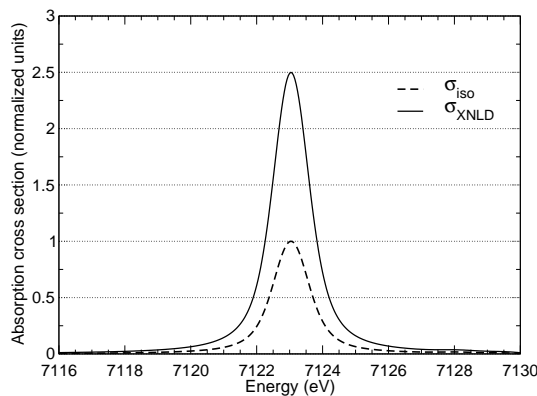


Figure 1.20: LFM-calculated E2 transitions for a  $\text{Fe}^{2+}$  ion in  $O_h$  point symmetry: comparison between the isotropic cross section ( $\sigma_{\text{iso}}$ ) and the dichroic cross section ( $\sigma_{\text{XNLD}}$ ).

Parallel to single-particle calculations, LFM calculations were performed by Marie-Anne Arrio, in order to get more insight into the origin of the dichroic signal. The calculation was first carried out for a low spin divalent iron in a regular octahedron with the fourfold axis parallel to the  $z$  axis of the crystal. For such a geometry, the XNLD signal is 2.5 times larger than the E2 isotropic signal (see Fig. 1.20). In order to stick to experiment, one needs to take into account the orientation of the octahedron in the crystal as well as the multiplicity of the iron sites in the unit cell. When this is done, one finds that for a  $23^\circ$ -tilted octahedron<sup>27</sup> the dichroism is strongly reduced and the ratio  $\sigma_{\text{XNLD}}/\sigma_{\text{iso}}$  is then equal to 0.75 (see Fig. 1.21). This value is in good agreement with the single-particle calculations, for which it was found equal to 0.9.

<sup>27</sup>The tilt angle is between the fourfold axis of the octahedron and the  $z$  axis of the crystal.

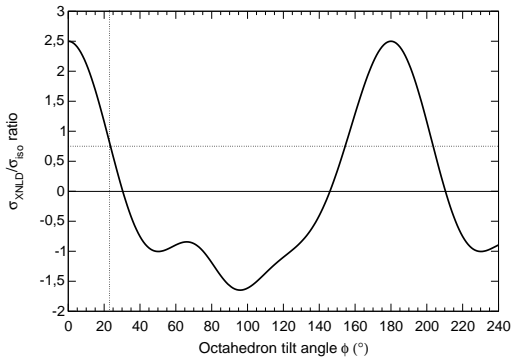


Figure 1.21: Theoretical  $\sigma_{\text{XNLD}}/\sigma_{\text{iso}}$  intensity ratio as a function of the octahedron tilt angle,  $\Phi$ , as derived from LFM calculations. For  $\Phi = 0$ , the ratio is equal to 2.5. When tilting the octahedron, the ratio decreases and becomes negative when  $\Phi \geq 30^\circ$ . In pyrite,  $\Phi = 23^\circ$  that reduces the ratio to 0.75. Note that if the angle was about  $30^\circ$ , no angular dependence could have been observed. Calculations performed by Philippe Sainctavit.

### Angular dependence of the Fe K pre-edge of MbCO

In 1999, Della Longa *et al.* recorded angular-dependent spectra at the Fe K-edge of a single crystal of MbCO [64]. By neglecting the anisotropy in the heme plane, they deduced from their measurements two polarized spectra, corresponding to the x-ray polarization parallel and normal to the heme plane. In the framework of the PhD thesis of Mounir Arfaoui [11], the spectra were calculated using our DFT-plane-wave scheme. Here, only the results in the pre-edge region for both polarization are shown (Fig. 1.22). The calculations were performed using the 48-atom cluster shown in Fig. 1.17, which was embedded in a large cubic supercell. In such a way that the Fe- $N_p$  bonds are along the  $x$  and  $y$  axis, and the Fe- $N_{\text{his}}$  along the  $z$  axis. The atomic positions are those deduced from the MXAN refinement given in Ref. [152], and reported in the Appendix.

For both polarizations, the Fe K pre-edge region is characterized by two features  $A_1$  and  $A_2$ , which are reproduced by the calculations (see Fig. 1.22). The E1 and E2 decomposition indicates that, in the case of  $\hat{\varepsilon} \perp \text{heme}$ , the two peaks essentially come from E1 transitions (the E2 transitions represent 5% of the total intensity of the  $A_2$  peak) and, in the case of  $\hat{\varepsilon} \parallel \text{heme}$ , peak  $A_1$  and peak  $A_2$  originate from E2 transitions and local E1 transitions, respectively. While the energy separation between  $A_1$  and  $A_2$  is satisfactorily reproduced (with an error of about 0.2 eV), the theoretical pre-edge is at too high energy as regards to the experimental one: the shift is about 1.4 eV for the  $\hat{\varepsilon} \parallel \text{heme}$  configuration and 0.9 eV for the  $\hat{\varepsilon} \perp \text{heme}$  configuration. Again, we observe that when the 3d

orbitals of the absorbing atom are involved in the origin of the pre-edge features, these latter occur at too high energy, when calculated in a single-particle DFT approach. The discrepancy is here more pronounced than in the case of pyrite. The Fe-S bond in pyrite is strongly covalent, thus the Fe 3d orbitals are not too localized to be quite accurately modeled using a single-particle DFT-LDA approach [40].

In order to further analyze the origin of the two features, the local and partial density of states (lp-DOS) are also shown in Fig. 1.22 (bottom panels). The lp-DOS, which take into account the 1s core-hole on Fe, were calculated using Löwdin projections and a Gaussian broadening of 0.07 eV (with  $\beta = 14^\circ$ ). The lp-DOS plots enable to visualize the reason why the E2 transitions are negligible when  $\varepsilon \perp \text{heme}$  and significant when  $\varepsilon \parallel \text{heme}$ . Indeed, when  $\varepsilon \perp \text{heme}$  (i.e.  $\varepsilon \parallel [001]$  and  $\mathbf{k} \parallel [\bar{1}10]$ ), only the  $t_{2g}$  orbitals can be probed. Since they are mostly occupied, the resulting E2 absorption cross-section is found very weak. On the contrary, when  $\varepsilon \parallel \text{heme}$  (i.e.  $\varepsilon \parallel [110]$  and  $\mathbf{k} \parallel [\bar{1}10]$ ), the empty  $e_g-3d_{x^2-y^2}$  is probed, thus leading to one peak in the E2 absorption cross section. The lp-DOS plots also enable to reveal the various hybridizations between the orbitals, which are involved in the pre-edge. Since MbCO is a molecule, these hybridizations can be described in terms of molecular orbitals (MO). Let us first define the MO of the iron ligands, which are involved in the pre-edge. There are two axial ligands: the carbon atom of the CO molecule and the nitrogen atom of the H93 histidine group. The unoccupied MO orbitals of the CO molecule are  $\pi^*$  and  $\sigma^*$ , partially defined by the C  $2p_x, p_y$  empty states and the C  $2p_z$  empty states, respectively. One of the antibonding  $\sigma^*$  MO ( $sp^2$ ) of the histidine cycle is notably defined by the  $N_{\text{his}}-2p_z$  empty states. In the heme plane, the four ligands are the  $N_p$  atoms, and it is the  $\sigma^*$  MO of the porphyrine that participate in the pre-edge feature. This latter MO is partially described by the four  $N_p-(2p_x, 2p_y)$  empty states. Then the ligand MOs are hybridized with the 3d empty states of iron to form other antibonding MOs, that are at the origin of the pre-edge features. In particular, it can be seen in Fig. 1.22 (left) that the  $A_2$  peak of the  $\hat{\varepsilon} \perp \text{heme}$  configuration is due to E1 transitions  $1s \rightarrow 4p_z$  where the Fe- $4p_z$  empty states are hybridized with the MOs formed by the  $t_{2g}$   $3d_{xz}$  and  $3d_{yz}$  and the  $\pi^*$  coming from CO. Consequently, the more the CO bond is tilted, i.e. the greater is the  $\beta$  angle, the more efficient is the hybridization. This explains why peak  $A_2$  is more intense for  $\beta=14^\circ$  than for  $\beta=10^\circ$ . Note that the  $10^\circ$  match better with experiment. This result suggests that the  $14^\circ$ , resulting from the fitting procedure of the XANES spectrum performed by Della Longa *et al.* [152] is overestimated. The assignment of the pre-edge features for both orientations of the polarization vector in terms of unoccupied MO is given in Table 1.5. The lp-DOS calculations presented here

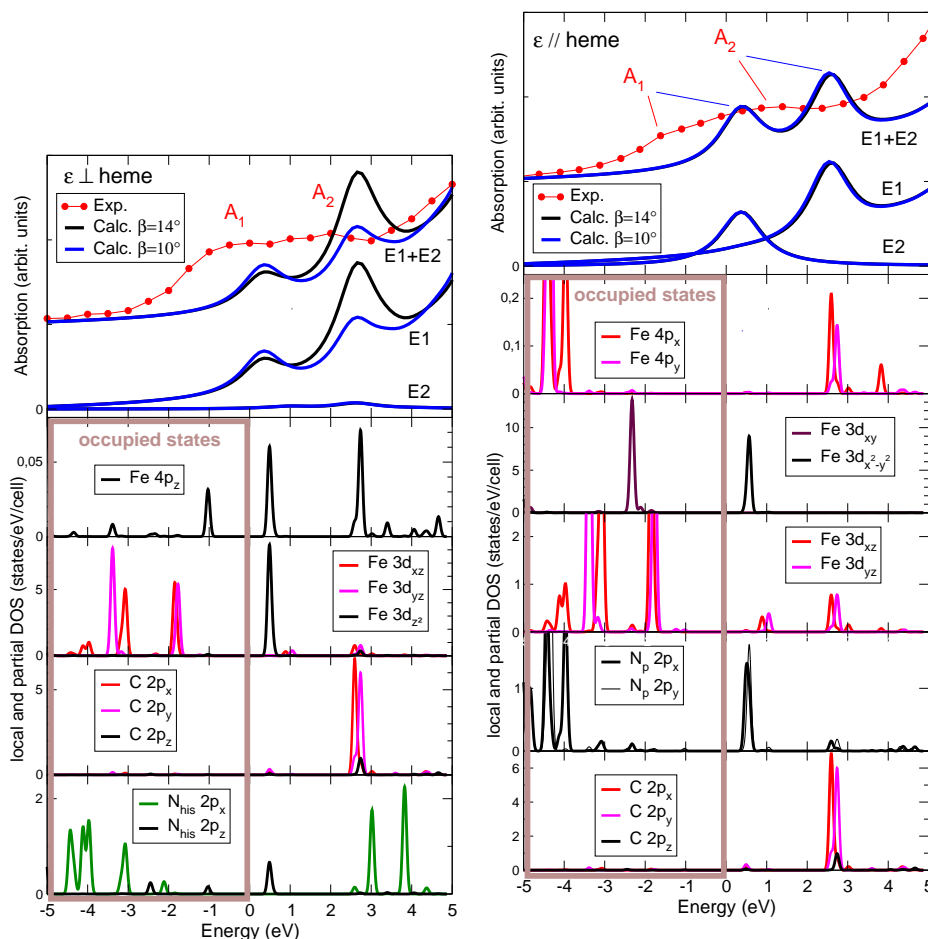


Figure 1.22: Analysis of the MbCO pre-edge transitions for  $\varepsilon$  normal to the heme plane (left) and in the heme plane (right),  $\mathbf{k}$  being kept fixed in the heme plane. Top panel: Experimental and calculated pre-edge spectra for two values of the  $\beta$  angle (including the decomposition into E1 and E2 transitions). Bottom panels: local and partial DOS involved in the pre-edge region. The experimental spectra have been shifted in energy in order to make the main peak of the normal-polarized XANES experimental and theoretical spectra coincide. Figure reproduced in Ref. [38].

partially confirm and complete the tentative MO assignments given by Della Longa *et al.* in 1999 [64].

Through the two examples of pyrite and MbCO, it was shown that single-particle calculations work pretty well to reproduce the Fe  $K$ -pre-edge structure when Fe is in ferrous low-spin state and in sixfold coordination. Moreover such calculations enable to give a detailed assignment of the pre-edge peaks.

#### 1.4.4 The $\text{Cr}^{3+}$ $K$ edge in allochromatic minerals

In the framework of the PhD thesis of Emilie Gaudry (2004) [89] and of Amélie Juhin (2008) [123], the angular dependence of the pre-edge features at the Cr  $K$ -edge in three allochromatic minerals was studied: ruby[92] and emerald [90], and spinel [124].

Table 1.5: Main MO assignment of the pre-edge peaks of the Fe  $K$ -XANES spectra of MbCO for two distinct orientations of the incident photon beam polarization ( $\hat{\varepsilon}$ ).

Peak	Assignment for $\varepsilon \perp \text{heme}$
A <sub>1</sub>	E1: $1s \rightarrow 4p_z$ hybrid. with MO $[3d_z^2 + \sigma^*(\text{H93})]^*$ and with MO $[3d_z^2 + \sigma^*(\text{CO})]^*$
A <sub>2</sub>	E1: $1s \rightarrow 4p_z$ hybrid. with MO $[3d_{yz}-3d_{xz} + \pi^*(\text{CO})]^*$
Peak	Assignment for $\varepsilon \parallel \text{heme}$
A <sub>1</sub>	E2: $1s \rightarrow \text{MO } [3d_{x^2-y^2} + \sigma_{\text{porph.}}^*]^*$
A <sub>2</sub>	E1: $1s \rightarrow 4p_x, 4p_y$ hybrid. with MO $[3d_{xz}, 3d_{yz} + \pi^*(\text{CO})]^*$

The local crystallographic structure of Cr in the three minerals was detailed in Sec. 1.3.1. The most important result to remember here is that the point symmetry of the Cr site is the same as the one the Al host site.

### The electronic transitions expected in the pre-edge region

The amount of chromium being very low in the three compounds (below a few atomic-percent), the probability to have chromium atoms in neighboring sites is also low. This permits to exclude the contribution of non-local E1 transitions. The number of the expected E2 transitions can be predicted for a  $d^3$  configuration in octahedral environment, as can be seen from Fig. 1.23. The ground state of  $\text{Cr}^{3+}$  corresponds to a configuration where the three lowest  $d$ -orbitals (the  $t_{2g}$ -like) are occupied by the majority spin. In the excited state, the photoelectron can probe, on the one hand, the empty  $t_{2g}$  orbitals for minority spin (case B in Fig. 1.23) and, on the other hand, the empty  $e_g$  ones, for both majority and minority spins (cases A and C in Fig. 1.23, respectively). Therefore, three spin-polarized E2 transitions can be expected at the Cr K pre-edge. The sequence from spinel to ruby via emerald corresponds to a decreasing symmetry of the Cr-site, starting from the  $D_{3d}$  symmetry point group in Cr-doped spinel, to  $D_3$  in emerald and finally  $C_3$  in ruby. As will be shown, the degree of admixture between the empty  $p$  states and the empty  $3d$  states of the absorbing atom is consequently increasing, which affects the intensity of the local E1 transitions contributing to the pre-edge. In spinel, the Cr site is centrosymmetric. Thus no E1 local transitions are expected and only E2 transitions should arise in the Cr K pre-edge structure. On the contrary, in emerald and in ruby the Cr site is not centrosymmetric, meaning that local E1 transitions are expected in the pre-edge, in addition to the E2 ones.

### Angular dependence of the Cr K pre-edge in red spinel

The full angular dependence of the Cr K pre-edge in red spinel was measured and modeled by Juhin *et al.*, in order to reveal quantitative information on the crystallographic and electronic structure of  $\text{Cr}^{3+}$  [124]. The experimental spectra measured for two different orientations are shown in Figure 1.24 (left and right). For each of them, the upper panel shows the experimental spectrum and the theoretical one, with the E1 and E2 contributions plotted separately. Both panels show that the Cr K pre-edge has a pure electric quadrupole character, as expected, since the E1 contribution contributes only to the edge tail without showing any features. For the two orientations ( $\epsilon_a=[010]$ ,  $\mathbf{k}_a=[\bar{1}00]$  and  $\epsilon_b=[1,1,\sqrt{2}]$ ,  $\mathbf{k}_b=[-$

$1,-1,\sqrt{2}]$ , respectively), the correct number of peaks (one and two, respectively) is well reproduced by the single-particle calculation. For the first configuration (Fig. 1.24, left), the experimental spectrum shows a single peak labeled A1. The electric quadrupole operator, expressed as  $xy$ , enables to probe the empty  $d$  electronic density, projected on Cr, in the  $xy$  direction, i.e., between the Cr-O bonds. The corresponding empty  $d$  states have almost a pure  $t_{2g}$  character, and thus they can be reached only by a photoelectron with spin  $\downarrow$  (Fig. 1.23, case B). This prediction is consistent with the calculation. For the second configuration (Fig. 1.24, right), two peaks A1 and A2 are obtained in the experimental pre-edge spectrum. For this orientation, the electric quadrupole operator is expressed as  $\frac{3z^2-r^2}{4} - \frac{xy}{2}$ , which enables to probe the  $3d$  electronic density both in the  $xy$  and  $3z^2-r^2$  directions. The corresponding  $d$  empty states are thus respectively  $t_{2g}$  and  $e_g$  ones. For the  $t_{2g}$  component, one peak is expected for spin  $\downarrow$ , as in the first configuration; for the  $e_g$  component, two peaks are expected, one for spin  $\downarrow$  and one for spin  $\uparrow$  (cases A and C in Fig. 1.23).

These predictions are in line with the theoretical spectrum, which shows that peak A1 arises from transitions towards  $e_g^\uparrow$  and  $t_{2g}^\downarrow$  states, while peak A2 corresponds to transitions towards  $e_g^\downarrow$  states. Furthermore, although the symmetry of the Cr site is  $D_{3d}$ , no splitting between the empty  $t_{2g}$  orbitals is visible, which is an indication that the trigonal distortion is very small. The peak assignment is given in Tab. 1.6.

Although the agreement between theory and experiment is satisfactory enough to provide a clear vision of the assignment of the  $1s$ - $3d$  transitions occurring in the pre-edge, there are two main drawbacks. First, we observe again that in the calculation, the E2 pre-edge features occur at too high energy with respect to the edge, due to the modeling of the core-hole effects. Second, the absolute and the relative intensities are not perfectly reproduced using the single-particle approach, as well as the splitting of the two peaks, which is underestimated. This was attributed to the fact that the interelectronic repulsion on the  $3d$  levels of the Cr ion cannot fully be described in the LDA framework [124].

### Angular dependence of the Cr K pre-edge in ruby

In the framework of the PhD thesis of Emilie Gaudry [89], the angular dependence of the Cr K pre-edge structure in ruby was also measured and interpreted in a single-particle point of view. Figure 1.25 compares the experimental and calculated isotropic ( $\sigma_1$ ) and dichroic ( $\sigma_2$ ) spectra, together with a zoom on the pre-edge region. The pre-edge is defined by two main peaks, here called A<sub>1</sub> and A<sub>2</sub>. They are well reproduced by the calculations as well as their angular dependence, but their positions are 2 eV too high as

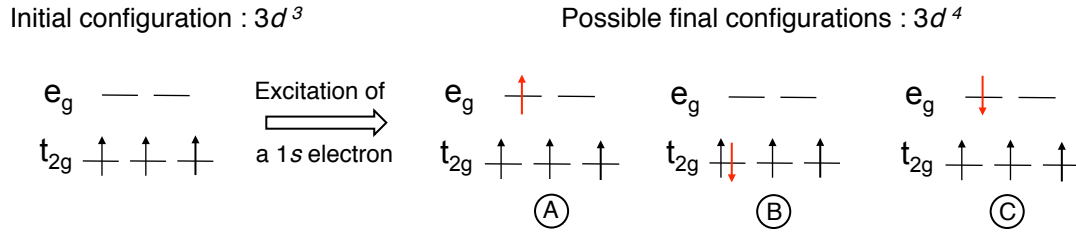


Figure 1.23: Schematic single-electron representation of the  $3d$  orbitals of  $\text{Cr}^{3+}$  in  $O_h$  symmetry for the ground state and the possible final states for the E2 transitions. Figure reproduced in Ref. [38].

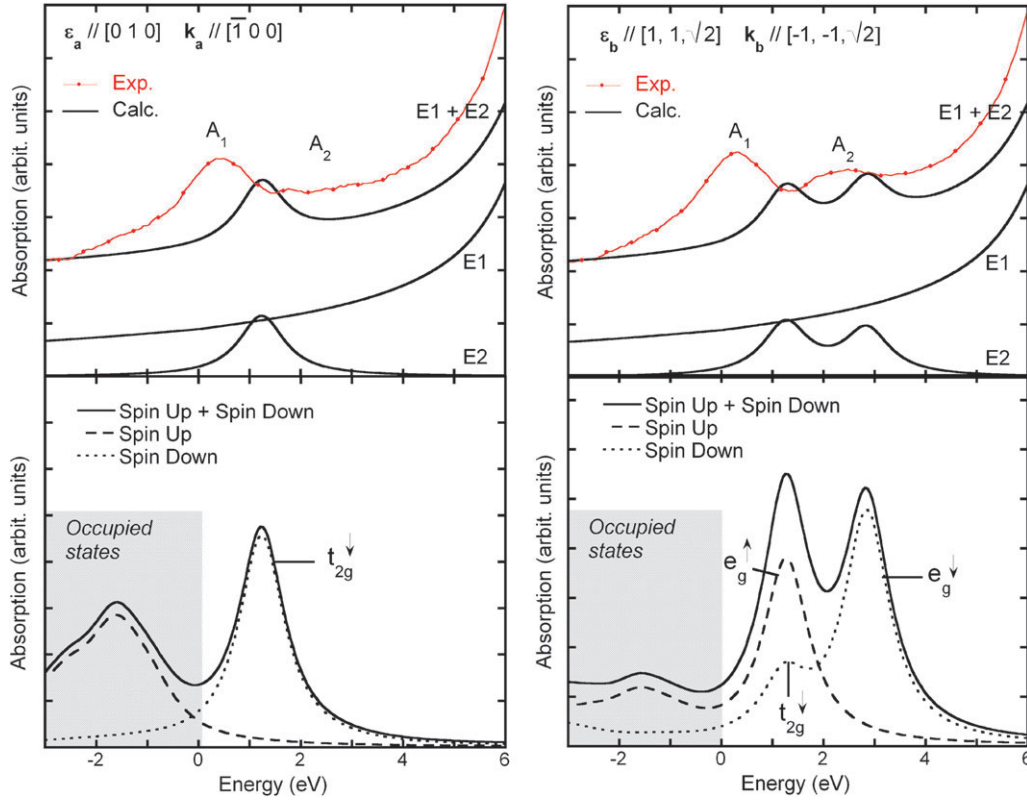


Figure 1.24: Analysis of the  $K$  pre-edge transitions of  $\text{Cr}^{3+}$  in spinel, for the  $(\epsilon_a=[010]; \mathbf{k}_a=[\bar{1}00])$  orientation (left), and for the  $(\epsilon_b=[1, 1, \sqrt{2}]; \mathbf{k}_b=[-1, -1, \sqrt{2}])$  orientation (right). Top panels: experimental and calculated pre-edge spectra, with the decomposition into E1 and E2 transitions. Bottom panels: spin-polarized calculations of the E2 cross-section. The zero energy is the Fermi energy. The grey region corresponds to the virtual transitions towards the occupied states. The experimental spectra were shifted in energy in order to make the main peak of the edge coincide with the theoretical data. Figure reproduced in Ref. [38].

compared with experiment.

Figure 1.26 shows the decomposition into E1 and E2 spin-polarized contributions of the pre-edge peaks for the two angular-dependent  $\sigma_{\parallel}$  and  $\sigma_{\perp}$  pre-edge spectra. While the Cr  $K$  pre-edge of spinel, with the Cr-O bonds along its cubic crystallographic axes, was quite easy to interpret, the one of ruby is more complicated to analyze in detail. We have to take into account the orientation of  $\epsilon$  and  $\mathbf{k}$  within the  $\text{Cr-O}_6$  octahedron the 3-fold axis ( $C_3$ ) of which is along the  $[111]$  direction of the trigonal cell. Moreover the analysis

of the E1 transitions in the polarized calculated spectra is possible using group theory, only if symmetry point group lower than  $O_h$  is considered. We use the  $C_{3v}$  character table although the symmetry of the Cr site in  $\alpha\text{-Al}_2\text{O}_3:\text{Cr}^{3+}$  is  $C_3$  [92]. The electronic transitions are associated with the irreducible representation  $\Gamma$  given by:

$$\Gamma = \Gamma_f \otimes \Gamma_{\mathcal{O}} \otimes \Gamma_{1s},$$

where  $\Gamma_{1s}=a_1$  is the irreducible representation of the  $1s$  initial state, which is totally symmetric,  $\Gamma_{\mathcal{O}}$  is the one of the transition operator, which is either E1 or

Table 1.6: Assignment of the pre-edge features of the Cr  $K$ -XANES spectra in Cr-doped spinel for the two experimental orientations, which lead to the maximum XNLD.

Peak	Assignment for $\epsilon \parallel [010]$ and $\mathbf{k} \parallel [\bar{1}00]$	
	Spin $\uparrow$	Spin $\downarrow$
A <sub>1</sub>	/	E2: $1s \rightarrow 3d-t_{2g}^{\downarrow}$
Peak	Assignment for $\epsilon \parallel [1,1,\sqrt{2}]$ and $\mathbf{k} \parallel [-1,-1,\sqrt{2}]$	
	Spin $\uparrow$	Spin $\downarrow$
A <sub>1</sub>	E2: $1s \rightarrow 3d-e_g^{\uparrow}$	E2: $1s \rightarrow 3d-t_{2g}^{\downarrow}$
A <sub>2</sub>	/	E2: $1s \rightarrow 3d-e_g^{\downarrow}$

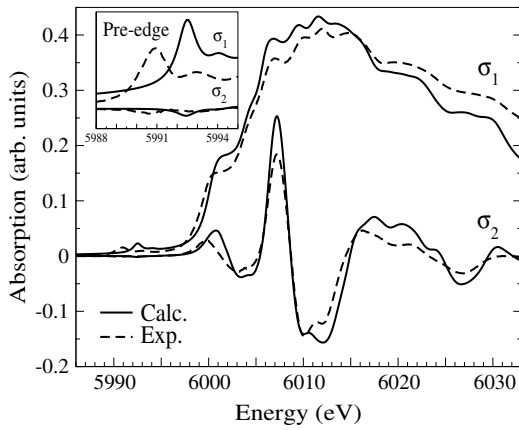


Figure 1.25: Comparison between the experimental (dashed line) and calculated (solid line) isotropic ( $\sigma_1$ ) and XNLD ( $\sigma_2$ ) spectra at the Cr  $K$ -edge in ruby. Inset: zoom on the pre-edge region. Figure extracted from Ref. [92].

E2, and  $\Gamma_f$  is the one of the final state, which is of symmetry  $p$  and  $d$ , respectively. A transition is allowed if it has the symmetry of a scalar, i.e., if it transforms like the totally symmetric irreducible representation. As summarized in Table 1.7, the irreducible representation  $t_{1u}(O_h)$  of the  $p$  orbitals is split into two ones,  $a_1(C_{3v})$  and  $e(C_{3v})$ , for the components  $p_{\parallel C_3}$  and  $p_{\perp C_3}$ , respectively. For the  $d$  orbitals,  $t_{2g}(O_h)$  is split into  $a_1(C_{3v})$  and  $e(C_{3v})$ , and  $e_g(O_h)$  becomes  $e(C_{3v})$ .

For the E2 transitions, and whatever the orientation of  $\epsilon$  is, the operator  $\mathcal{O}$  belongs to the  $e(C_{3v})$  irreducible representation, corresponding to both  $t_{2g}(O_h)$  and  $e_g(O_h)$  (see p.131 of Ref. [89] for the correspondance between the  $O_h$  symmetry axes and the  $C_{3v}$  symmetry axes). This leads to one peak for majority spin (case A in Fig. 1.23) and two peaks for minority spin (cases B and C in Fig. 1.23). Note that, as in spinel, the  $t_{2g}^{\downarrow}$  and  $e_g^{\uparrow}$  states of Cr in ruby almost arise at the same energy.

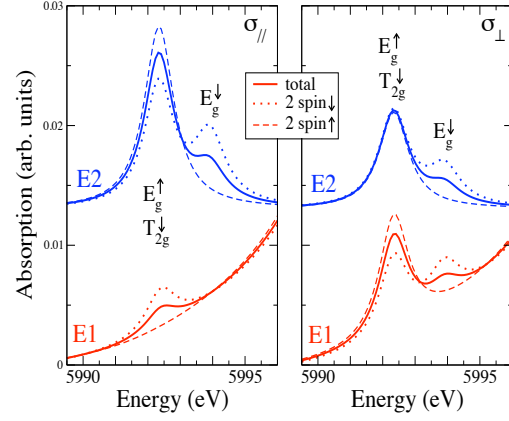


Figure 1.26: E1 and E2 spin-dependent absorption cross-sections calculated for  $\epsilon \parallel C_3$  (left) and  $\epsilon \perp C_3$  (right) at the Cr  $K$ -pre-edge in ruby. The wave-vector  $\mathbf{k}$  is kept fixed perpendicular to the  $C_3$  axis for both  $\epsilon$  orientations. Figure extracted from Ref. [92].

Table 1.7: Irreducible representations of the  $O_h$  and  $C_{3v}$  symmetry point groups for the  $p$  and  $d$  states, used for the interpretation of Cr  $K$  pre-edge in ruby. The directions  $x$ ,  $y$  and  $z$  refer to the octahedron axes (and not the cell axis of ruby).

Final state symmetry	Irreducible representation	
	$O_h$	$C_{3v}$
$p$	$t_{1u}$ for $p_x, p_y, p_z$	$a_1$ for $p_{\parallel C_3}$ $e$ for $p_{\perp C_3}$
$d$	$t_{2g}$	$a_1$ $e$
	$e_g$	$e$

Unlike the E2 transitions, the E1 transitions depend on the direction of  $\epsilon$ . When  $\epsilon \parallel C_3$  (Fig. 1.26-left), the operator  $\mathcal{O}$  belongs to  $a_1(C_{3v})$ . The corresponding  $p_{\parallel C_3}$  states can only hybridize with  $d$  state belonging to the same  $a_1(C_{3v})$  irreducible representation, coming from  $t_{2g}(O_h)$ . For  $\text{Cr}^{3+}$ , this leads to only one E1 peak illustrating the hybridization of  $p_{\parallel C_3}$  with the  $t_{2g}^{\downarrow}$  states. When  $\epsilon \perp C_3$  (Fig. 1.26-right), the operator  $\mathcal{O}$  belongs to  $e(C_{3v})$ . The corresponding  $p_{\perp C_3}$  states hybridize with  $t_{2g}$  and  $e_g$  states, leading to one E1 peak for majority spin and two E1 peaks for minority spin. A summary of the peak assignment is given in Table 1.8.

Table 1.8: Assignment of the Cr  $K$  pre-edge features in ruby for two distinct orientations of the incident photon beam polarization ( $\varepsilon$ ). For emerald, the assignment is almost the same. The unique difference is that no E1 transition can occur for  $\varepsilon \parallel C_3$ .

Peak	Assignment for $\varepsilon \parallel C_3$	
	Spin $\uparrow$	Spin $\downarrow$
A <sub>1</sub>	E2: $1s \rightarrow 3d-e_g^\uparrow$	E2: $1s \rightarrow 3d-t_{2g}^\downarrow$
		E1: $1s \rightarrow p_{\parallel C_3}$ hybrid. with $3d-t_{2g}^\downarrow$
A <sub>2</sub>		E2: $1s \rightarrow 3d-e_g^\downarrow$
Peak	Assignment for $\varepsilon \perp C_3$	
	Spin $\uparrow$	Spin $\downarrow$
A <sub>1</sub>	E2: $1s \rightarrow 3d-e_g^\uparrow$	E2: $1s \rightarrow 3d-t_{2g}^\downarrow$
	E1: $1s \rightarrow p_{\perp C_3}$ hybrid. with $3d-e_g^\uparrow$	E1: $1s \rightarrow p_{\perp C_3}$ hybrid. with $3d-t_{2g}^\downarrow$
A <sub>2</sub>		E2: $1s \rightarrow 3d-e_g^\downarrow$
		E1: $1s \rightarrow p_{\perp C_3}$ hybrid. with $3d-e_g^\downarrow$

### Angular dependence of the Cr $K$ pre-edge of emerald

Still in the framework of the PhD thesis of Emilie Gaudry [89], the angular dependence of the Cr  $K$  pre-edge structure in emerald was measured and interpreted in a single-particle picture. Figure 1.27 compares the experimental and calculated spectra in the pre-edge region for two orientations of  $\varepsilon$ , i.e. parallel and normal to the optical axis of emerald (the 6-fold symmetry axis). Fig. 1.27 also shows the decomposition into E1 and E2 spin-polarized contributions. As in ruby, the pre-edge exhibit two features for both orientations of the polarization vector. In the following, the features are labeled A<sub>1</sub> and A<sub>2</sub>.

Table 1.9: Irreducible representations of the  $O_h$  and  $D_3$  symmetry point groups for the  $p$  and  $d$  states, used for the interpretation of Cr  $K$  pre-edge in emerald. The directions  $x$ ,  $y$  and  $z$  refer to the octahedron axes (and not the cell axis of emerald).

Final state symmetry	Irreducible representation	
	$O_h$	$D_3$
$p$	$t_{1u}$ for $p_x, p_y, p_z$	$a_2$ for $p_{\parallel C_3}$ $e$ for $p_{\perp C_3}$
$d$	$t_{2g}$	$a_1$
		$e$
	$e_g$	$e$

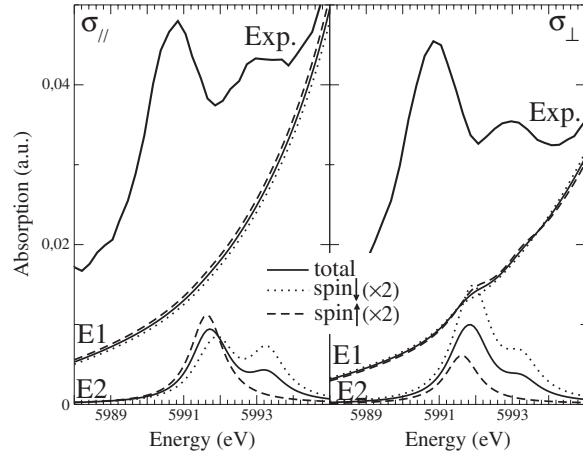


Figure 1.27: Comparison between the experimental and calculated Cr  $K$  pre-edge absorption spectra of emerald, for  $\varepsilon \parallel$  (left) and  $\perp$  (right) to the 6-fold symmetry axis (the direction of  $\mathbf{k}$  is kept fixed normal to the 6-fold axis). Figure extracted from Ref. [90].

The irreducible representations of  $D_3$ , which is the symmetry point group of Cr in emerald, differ from those of  $C_{3v}$  for the  $p$  states only (see Table 1.9). Consequently, the calculated E2 transitions at the Cr  $K$  pre-edge of emerald have exactly the same assignment as the ones of ruby. Now let us consider the E1 transitions. When  $\varepsilon$  is parallel to the 6-fold axis (along the  $C_3$  axis of the  $D_3$  point group), the transition operator  $\mathcal{O}$  belongs to the  $a_2(D_3)$  irreducible representation. Therefore, no hybridization between the  $p_{\parallel C_6}$  and  $d$  states are possible, and the calculated E1 spectrum does not exhibit any feature. When  $\varepsilon$  is perpendicular to the 6-fold axis, the transition operator  $\mathcal{O}$  to the  $e(D_3)$  irreducible representation. The corresponding  $p_{\perp C_3}$  (or  $p_{\perp C_6}$ ) states can hybridize with  $d$  states of symmetry  $e(D_3)$ , and the situation is analogous to that of ruby. However, the calculated E1 peaks are very weak. That would mean that the hybridization between the  $p$  and  $d$  states of chromium in emerald is small. Indeed, since the distortion of the chromium site in ruby is larger than in emerald, it favors the  $p$ - $d$  hybridization.

In the case of emerald too, the DFT calculations enable to give an assignment of the pre-edge peak in a single-particle point of view. The experimental features are quite well reproduced even if the problem of energy position is still present. Indeed, the calculated pre-edge arises at too high energy and the theoretical energy separation between the two A<sub>1</sub> and A<sub>2</sub> features is underestimated.

### 1.4.5 The V K edge in tsavorite and the Fe K edge in MbCN

In this last scenario of pre-edge single-particle calculations, one of the two spin-polarized  $t_{2g}$  levels is partially occupied, suggesting strong electron-electron repulsion. Without an LDA+ $U$  approach, this situation is challenging to be modeled using a DFT-LDA single-particle method. The two examples treated below are the  $V^{3+}$  K edge in  $Ca_3Al_2Si_3O_{12}:V^{3+}$  and the  $Fe^{3+}$  K edge in cyanomet-myoglobin (MbCN), where  $Fe^{3+}$  is in the low-spin state.

#### The electronic transitions expected in the pre-edge region

In the framework of the PhD thesis of Amélie Bordage [26], in addition to anatase, the V K pre-edge structure of tsavorite ( $Ca_3Al_2Si_3O_{12}:V^{3+}$ ) was studied in detail. In tsavorite (V-bearing calcic silicate garnet), which crystallizes in the cubic system as all garnets, vanadium is present as a substituted minor element in the Al site, with  $\bar{3}$  ( $C_{3i}$ ) point symmetry (see Sec. 1.3.1). Hence, no local E1 transitions are expected in the pre-edge. Moreover, non-local E1 transitions are not expected neither, assuming that the other 3d impurities present in the natural samples (Mn, Ti, Cr, Fe) are assumed to not interact with the V main impurities (see Tab. 1.1). Consequently, the electronic transitions expected in the pre-edge region only are E2 transitions, which can probe the  $t_{2g}$  and  $e_g$  states whatever the spin is (up or down).

While Fe is in a low-spin ferrous state in MbCO, it is in a low-spin ferric state in MbCN. Hence the MbCN protein has a spin momentum  $S = 1/2$ . However, the atomic arrangements around Fe in MbCO and in MbCN are quite similar (see Tab. 1.14 in the Appendix). Consequently, as in MbCO, local E1 and E2 transitions are expected in the pre-edge region. For the majority spin, only the  $e_g$  can be probed while for the minority spin, both the  $t_{2g}$  and  $e_g$  orbitals are accessible in XAS.

#### Angular dependence of the V K pre-edge in tsavorite

Polarized XANES spectra at the V K-edge were recorded on an oriented single-crystal by Bordage *et al.* [28] (see Fig. 1.28). The recorded orientations are identical to those measured for Cr-bearing spinel (red spinel). The upper panels of Figure 1.28 (left and right) compare the experimental and theoretical spectra obtained for the two orientations  $\epsilon_a=[010]$ ;  $\mathbf{k}_a=[\bar{1}00]$  and  $\epsilon_b=[1,1,\sqrt{2}]$ ;  $\mathbf{k}_b=[-1,-1,\sqrt{2}]$ . For both orientations, the pre-edge exhibits three features, which are well reproduced by the single-particle calculations, but again at too high energy. The pure

electric quadrupole character of the pre-edge is well-observed (transitions E1 do not contribute to the pre-edge structure, except in the edge tail). When the polarized spectra are displayed in the same graph (not shown), one can notice that the angular dependence of the pre-edge is satisfactorily reproduced by the calculations, in the sense that both the relative energies and intensities are correctly simulated.

The lower panels of Figure 1.28 (left and right) show the spin-polarized calculations of the E2 cross section performed for each experimental orientation. An assignment of the E2 transitions involved in the experimental peaks, labeled  $A_1$ ,  $A_2$  and  $A_3$ , can be done within a single-particle picture of the transitions from the 1s states to the empty 3d ones. Peak  $A_1$  is thus attributed to transitions towards the  $t_{2g}^\uparrow$  states. Peak  $A_2$  arises from two contributions: transitions towards the  $t_{2g}^\downarrow$  and  $e_g^\uparrow$  states. Peak  $A_3$  is attributed to transitions towards the  $e_g^\downarrow$  states. However, a more detailed attention must be paid to peak  $A_1$  since it is situated astride the occupied and empty states. This is due to the  $3d^2$  electronic configuration of  $V^{3+}$ : two  $t_{2g}$  orbitals are occupied and one is empty. Hence, when looking at lower panels of Fig. 1.28, which represent both the virtual transitions to occupied state and the actual transitions to the empty states, one should observe two separated features, below and above the Fermi energy. In fact, the single-particle calculations are not able to reproduce the energy splitting of empty and occupied  $t_{2g}$  orbitals, which was expected by the irreducible representations of the  $C_{3i}$  vanadium site point group. Consequently, even if the agreement between experiment and calculation is quite satisfactory when the occupied states are cut, standard plane-wave DFT approach fails to properly model 3d incomplete spin-polarized levels. This drawback will be again illustrated with the next and last compound.

#### Angular dependence of the Fe K pre-edge in MbCN

The top panels of Figure 1.29 (left and right) compare the experimental Fe K pre-edge polarized spectra of MbCN with cross-section calculations (for  $\epsilon \perp heme$  and  $\epsilon \parallel heme$ , respectively). The spectra were recorded by Arcovito *et al.* [10] applying a protocol similar to that used for MbCO [64]. While the pre-edge spectra MbCO show two features, the experimental pre-edge spectra of MbCN are characterized by one main peak, labelled A, which is twice as more intense for  $\epsilon \perp heme$  than for  $\epsilon \parallel heme$ . The shape and the anisotropy of the Fe K pre-edge of MbCN is well reproduced by the single-particle calculations (the fact that the calculated pre-edges are too intense with respect to experiment is essentially due to a too weak  $\gamma$  broadening parameter used in the cross-section calculation). The decomposition into E1 and E2 contributions shows that peak A is due to E1 transitions for  $\epsilon \perp heme$  and

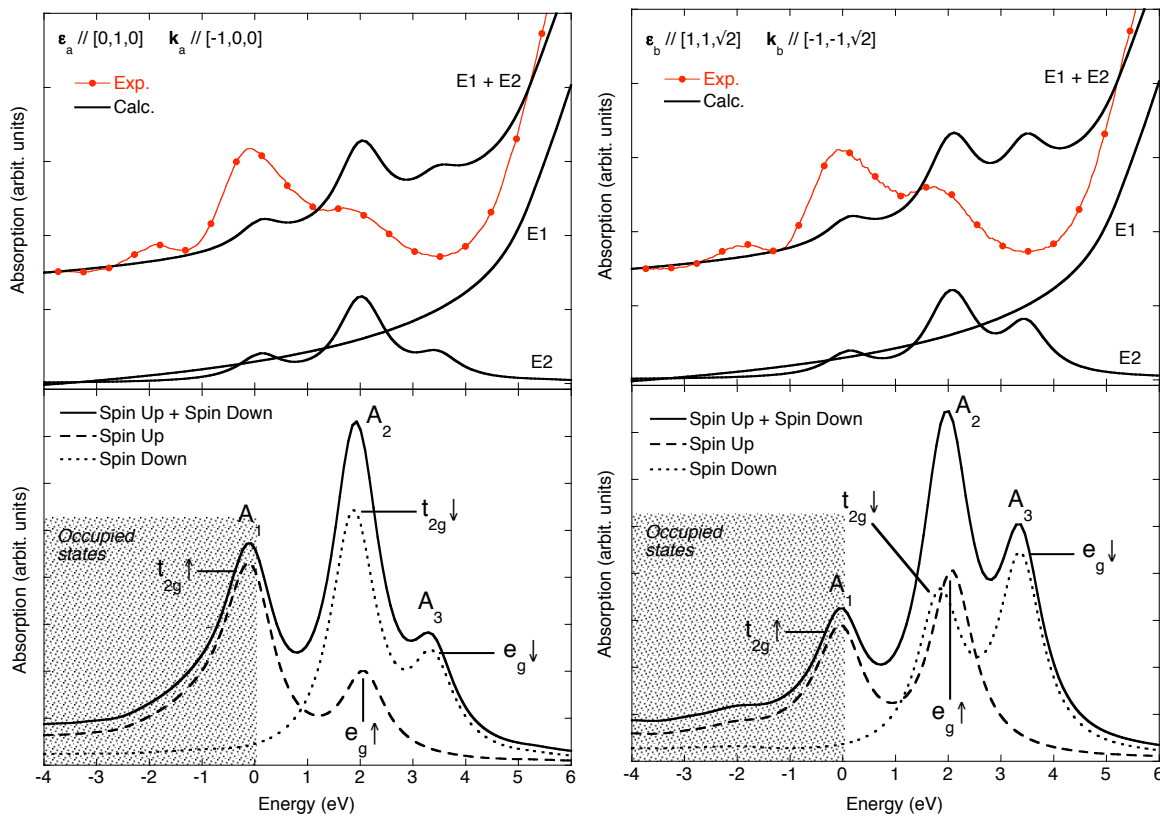


Figure 1.28: Analysis of the  $K$  pre-edge transitions of  $V^{3+}$  in tsavorite, for the  $(\epsilon_a=[010]; \mathbf{k}_a=[\bar{1}00])$  orientation (left) and for the  $(\epsilon_b=[1, 1, \sqrt{2}]; \mathbf{k}_b=[-1, -1, \sqrt{2}])$  orientation (right). Top panels: experimental and calculated pre-edge spectra, with the decomposition into E1 and E2 transitions. Bottom panel: spin-polarized calculations of the E2 cross-section. The grey region corresponds to the virtual transitions towards the occupied states. The experimental spectra have been shifted in energy in order to make the main peak of the edge coincide with the theoretical data. Figure reproduced in Ref. [38].

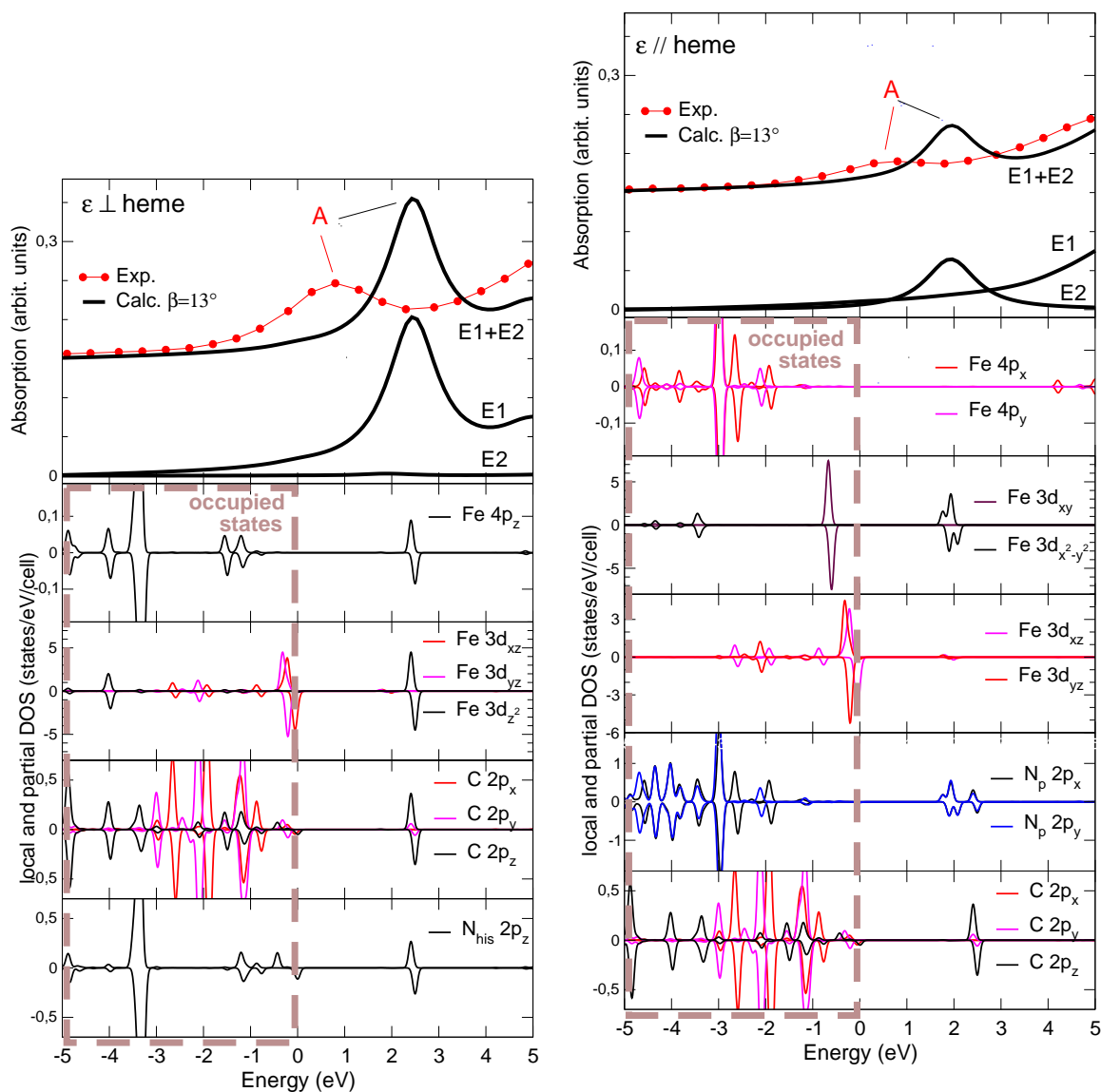


Figure 1.29: Analysis of the MbCN pre-edge transitions for  $\varepsilon$  normal to the heme plane (left) and in the heme plane (right). Top panel: Experimental and calculated pre-edge spectra (including the decomposition into E1 and E2 transitions). Bottom panels: local and partial spin-polarized DOS involved in the pre-edge region. The experimental spectra have been shifted in energy in order to make the main peak of the normal-polarized XANES experimental and theoretical spectra coincide.

to E2 transitions for  $\varepsilon \parallel heme$ . The same decomposition was observed for peak A<sub>1</sub> of MbCO. Since Fe lies in a nearly centrosymmetric environment within the heme plane, the absence of local E1 transitions for  $\varepsilon \parallel heme$  makes sense.

Although the expected number of pre-edge components is four (three E2 and one E1), one observes only one single broad feature in the XANES spectrum, which can be explained by the spin-polarized lp-DOS of Fe and of its neighbors (lower panels of Figure 1.29). This is due to several reasons. First, because of the experimental set up (orientation of beam with respect to the single-crystal sample), the transitions towards

the partially empty  $t_{2g}$  states were not probed. Second, as can be seen from the lp-DOS, no significant energy splitting is observed between minority and majority spins: the transitions to the empty  $e_g$  states thus occur at a similar energy for both spins. Third, for  $\varepsilon \perp heme$  the weak E2 transitions is masked by the strong local-E1 peak.

The lp-DOS show that peak A has the same assignment as peak A<sub>1</sub> of MbCO for both orientations. Indeed, the same MOs are involved at the energy of the calculated A peak plotted in the top panels. Hence, for the  $\varepsilon \perp heme$  orientation, peak A is due to transitions  $1s \rightarrow 4p_z$  where the  $4p_z$  orbital is hybridized

with the MOs  $[3d_{z^2} + \sigma^*(\text{CN})]^*$  and  $[3d_{z^2} + \sigma^*(\text{H93})]^*$  (the  $\sigma^*(\text{CN})$  and  $\sigma^*(\text{H93})$  ( $sp^2$ ) MO being displayed by the C  $2p_z$  lp-DOS and the N<sub>his</sub>  $2p_z$  lp-DOS). For the  $\varepsilon \parallel \text{heme}$  orientation, peak A is due to transitions  $1s \rightarrow 3d_{x^2-y^2}$  where the Fe  $3d_{x^2-y^2}$  orbital participates in the MO  $[3d_{x^2-y^2} + \sigma^*_{\text{porph}}]$  (the  $\sigma^*_{\text{porph}}$  MO is illustrated by the  $2p_x$  and  $2p_y$  partial DOS of the N atoms belonging to the heme plane). Table 1.10 summarizes the assignment of the pre-edge peak in MbCN.

Table 1.10: Main MO assignment of the Fe  $K$  pre-edge feature of MbCN for two distinct orientations of the incident photon beam polarization ( $\varepsilon$ ), as deduced from single-particle lp-DOS and absorption cross-section spin-polarized calculations.

Peak	Assignment for $\varepsilon \perp \text{heme}$
A	E1: $1s \rightarrow 4p_z$ hybrid. with MO $[3d_{z^2} + \sigma^*(\text{CN})]^*$ and with MO $[3d_{z^2} + \sigma^*(\text{H93})]^*$
Peak	Assignment for $\varepsilon \parallel \text{heme}$
A	E2: $1s \rightarrow \text{MO } [3d_{x^2-y^2} + \sigma^*_{\text{porph}}]^*$

Apart from the now well-known energy position problem of single-particle calculations, the pre-edge of MbCN appears not so critical to model (as initially expected). Nevertheless, these calculations reveal a failure similar to that observed in the case of tsavorite, i.e., the absence of energy splitting of the spin  $\downarrow$  partially filled  $t_{2g}$  shell. Indeed the Fermi energy, as calculated by the plane-wave DFT code, is found to be at the middle of the main peak of the spin  $\downarrow$  Fe  $3d_{xz}$  density of states (see the corresponding panels of Fig. 1.29). Fortunately, this problem has no incidence on the cross-section calculations because the Fe  $3d_{xz}$  states are not probed in the orientation chosen in the experimental setup.

### 1.4.6 Conclusion

Through the examples presented in this section, the issue of coupling closely experiment and theory to extract electronic and structural information was emphasized. In the entire compounds investigated, single-particle calculations were able to reproduce satisfactorily the experimental pre-edge: the number of peaks was well reproduced, and the relative energy positions and relative intensities were in good agreement with the experimental data. This allowed the interpretation of the experimental features within a monoelectronic view of the transitions involved in the  $K$  pre-edge. The information that can be directly inferred from such an assignment are the electric-dipole or electric-quadrupole character of the transitions, as well as the degree of local and non-local orbital hybridization. By

taking advantage of XNLD to probe specific empty orbitals, it is possible to draw a picture orientated in space. In all cases, the angular dependence of the  $K$  pre-edge was indeed reproduced in a level, which was good enough to allow its interpretation. Moreover, if some  $[\varepsilon, \mathbf{k}]$  orientations of the crystal with respect to the x-ray beam are not accessible experimentally, calculations are the only way to probe the corresponding empty levels. Within such a detailed analysis, the electronic structure of a transition metal ion in a given local environment can be well understood and therefore, its spectral signature well characterized.

However, single-particle calculations show some limitations. In the case of spin-polarized calculations for transition metal ions with incomplete  $d$  shells ( $V^{3+}$  and LS  $\text{Fe}^{3+}$ ), occupied and empty states are not well separated in the calculation. Such systems represent a real challenge for DFT. However, we point out that the assignment of the XANES features in terms of one-electron transitions still remains possible, provided that one keeps in mind that the  $3d$  shells are incomplete. In all the compounds investigated, the calculation of  $K$  pre-edge spectra within DFT suffers from two main drawbacks, i.e., the modeling of the core-hole interaction, on the one hand, and the  $3d$  electron-electron repulsion, on the other hand.

First, for all the compounds presented in this paper, we found out that the E2 and local E1 transitions are systematically calculated at too high energy with respect to the edge. This effect is due to the modeling of the  $1s$  core-hole-electron interaction, which leads to an overestimation of the screening of the  $1s$  core-hole. The relative energy positions of the pre-edge features can be improved mainly by two means. The simplest way consists of considering a core-hole with a positive charge superior to one, in order to increase artificially its attraction on the  $3d$  empty states. Nevertheless, such calculations cannot be considered as *ab initio* anymore, since the value of the core-hole is a fitted parameter. An alternative, more elegant way is to consider a dynamic core-hole, instead of a static one as in the calculations presented here. This requires the Bethe-Salpeter formalism, which treats electron and hole dynamics *ab initio*, as well as electron-hole interactions [201]. However, such calculations are nowadays still time-consuming, and complex systems like doped minerals and proteins are definitely challenging.

Second, the other main drawback of single-particle calculations is the modeling of electronic interaction: LDA and GGA approximations give indeed a description of these interactions in a mean-field way, which is not therefore completely satisfactory and which can be responsible for the possible differences in relative peak positions and intensities, compared to experiment. However, keeping in mind that the pre-edge features correspond to localized empty states where  $3d$ - $3d$  interactions are relevant, one must admit that DFT-LDA or DFT-GGA approaches already enable a

good modeling of the angular dependence of the pre-edge. In the case of tsavorite, XNLD was very well-reproduced quantitatively. The less satisfactory agreement was observed for Cr-doped spinel, but it did not hamper the interpretation of the pre-edge. In certain cases, the description of  $3d$ - $3d$  electronic repulsion can be improved by performing LDA+ $U$  (or GGA+ $U$ ) calculations. The Hubbard parameter  $U(3d)$  corresponds to the  $3d$  Coulombian “on-site” repulsion and measures the spurious curvature of the energy functional as a function of occupation. The Hubbard parameter can be determined self-consistently using QUANTUM-ESPRESSO, as an intrinsic linear-response property of the system [52, 140]. Nevertheless, DFT+ $U$  calculations cannot be performed for all systems, since the number of spins up and spins down needs to be non-zero [52]. Few XANES calculations performed in DFT+ $U$  are reported in the literature, for instance at the Ni  $K$  edge in NiO [98], the Cu  $K$  edge in CuO and La<sub>2</sub>CuO<sub>4</sub> [99] and in Ca<sub>2- $x$</sub> CuO<sub>2</sub>Cl<sub>2</sub> [100], the Co  $K$ -edge in LiCoO<sub>2</sub> [127] and the Mn  $K$  edge in Li<sub>2</sub>MnO<sub>3</sub> [212]. In these compounds, the addition of  $U$ , combined to the core-hole effects, enabled to shift the local E2 transitions from the non-local E1 ones in the pre-edge, yielding a better agreement between calculations and experiments.

The way to take into account the many-body interactions lacking in DFT-LDA (i.e., the multi-Slater determinant nature of the electronic states) is to use the multiplet approach. For example, in the case of Cr-doped spinel, it has been shown that the angular dependence of the  $K$  pre-edge could be better modeled [124]. However, this approach has also some drawbacks: (i) it uses a local approach, where a single transition metal ion is considered as embedded in a ligand field. Therefore, non-local E1 transitions occurring in the pre-edge cannot be calculated, (ii) because the calculation includes multiplet effects, a simple atomic picture is no longer possible to assign the transitions in terms of one-electron transitions, (iii) it uses some empirical parameters, which may not be available for all the systems. Hence, multiplet and single-particle methods must be considered as highly complementary. The development of approaches that go beyond DFT, such as DFT-CI (Configuration Interaction), TDDFT and Bethe-Salpeter opens new prospects to draw a fully *ab initio* picture of the pre-edge structure. A nice success of TDDFT is already illustrated by the case of  $K$  pre-edge of Fe<sup>2+</sup> and Fe<sup>3+</sup> in molecular model complexes [59]. Applications of these methods to more complex systems such as doped-crystals remain challenging.

## 1.5 Forthcoming studies

In the next few years, I will mainly focus my research activity on the two following topics: (i) probing the

quantum thermal fluctuations of nuclei by XANES and nuclear magnetic resonance (NMR) spectroscopies, (ii) the modeling of electron-energy-loss near-edge structure (ELNES) spectra. Both studies imply the use and development of the QUANTUM-ESPRESSO suite of codes.

### 1.5.1 The impact of nuclear motion on XANES spectra and NMR parameters

#### Scientific context and aim of the project

XANES and NMR spectroscopies have several specificities in common. They both are chemically selective and probe the local structure around a given element in condensed matter. The analysis of the NMR and XANES spectral data often requires theoretical tools, which are often based on DFT. In particular, the QUANTUM-ESPRESSO open source integrated suite of codes includes packages that calculate XANES spectra (code XSPECTRA) and the NMR parameters (code

GIPAW).<sup>28</sup>

Until now, electronic structure calculations in solids, including XANES and NMR calculations, consider fixed atomic positions, whereas atoms are actually subjected to quantum thermal fluctuations, which reduce to zero point motion at  $T=0\text{K}$ . However, nuclear motion may have significant impact on the chemical shift and the electric field gradient (for quadrupole nuclei) measured by NMR and on XANES spectra, notably in the  $K$  pre-edge structure.

In the case of NMR, rovibrational effects contribute significantly to the chemical shift,  $\delta_{\text{iso}}$  [222]. For instance in MgO, it was shown that the vibrational cor-

<sup>28</sup>The GIPAW code is based on the gauge-including projector-augmented-wave method developed by Pickard and Mauri in 2001 [181], which permits the calculation of NMR parameters within a pseudopotential approach. The GIPAW code generates the NMR shielding tensor,  $\sigma$ , also called chemical shift anisotropy (CSA) tensor and the electric field gradient (EFG) tensor,  $\mathbf{G}$ , in the crystal frame.

- The CSA tensor is defined as the ratio between  $\mathbf{B}_{\text{in}}(\mathbf{r})$  and  $\mathbf{B}$ , where the non-uniform magnetic field  $\mathbf{B}_{\text{in}}(\mathbf{r})$  is induced by the applied external uniform magnetic field  $\mathbf{B}$ :

$$\mathbf{B}_{\text{in}}(\mathbf{r}) = -\sigma(\mathbf{r})\mathbf{B}.$$

The induced magnetic field is produced by the first-order-induced current,  $\mathbf{j}^{(1)}(\mathbf{r}')$ :

$$\mathbf{B}_{\text{in}}(\mathbf{r}) = \frac{1}{c} \int d^3r' \mathbf{j}^{(1)}(\mathbf{r}') \times \frac{\mathbf{r} - \mathbf{r}'}{|\mathbf{r} - \mathbf{r}'|^3}.$$

The GIPAW method uses the perturbation theory and the PAW formalism to compute the all-electron induced current  $\mathbf{j}^{(1)}(\mathbf{r}')$ . The NMR isotropic chemical shift,  $\delta_{\text{iso}}$ , is the given by

$$\delta_{\text{iso}}(\mathbf{r}) = -[\sigma_{\text{iso}}(\mathbf{r}) - \sigma_{\text{ref}}],$$

where  $\sigma_{\text{iso}}(\mathbf{r})$ , the isotropic shielding, is given by

$$\sigma_{\text{iso}}(\mathbf{r}) = \frac{1}{3} \text{Tr}\{\sigma(\mathbf{r})\},$$

and  $\sigma_{\text{ref}}$  is the isotropic shielding of the same nucleus in a reference system.

- In the case of quadrupole nuclei (nuclear spin  $\geq 1$ ), the NMR spectral resonances are shifted and their shape are strongly modified by the quadrupole interaction, which is due to the anisotropic charge distribution inside the nucleus. The resonance shape is defined by  $C_q$ , the quadrupole coupling constant, and  $\eta$ , the asymmetry of the quadrupole interaction. Both quantities are computed from the eigenvalues,  $V_{xx}$ ,  $V_{yy}$  and  $V_{zz}$  of the EFG tensor:

$$C_q = \frac{eQV_{zz}}{h},$$

where  $e$ ,  $Q$  and  $h$  are the absolute value of the electron charge, the nuclear quadrupole momentum and the Planck constant, respectively, and

$$\eta = \frac{V_{xx} - V_{yy}}{V_{zz}}.$$

The components of the EFG tensor are computed from the charge density of the system,  $\rho(\mathbf{r}')$ , [184]:

$$G_{\alpha\beta}(\mathbf{r}) = \int d^3r' \frac{\rho(\mathbf{r}')}{|\mathbf{r} - \mathbf{r}'|^3} \left[ \delta_{\alpha\beta} - 3 \frac{(r_\alpha - r'_\alpha)(r_\beta - r'_\beta)}{|\mathbf{r} - \mathbf{r}'|^2} \right].$$

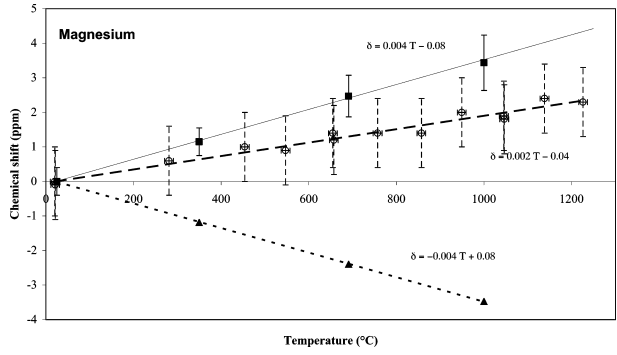


Figure 1.30: Temperature dependence of  $\delta_{\text{iso}}(T)$ - $\delta_{\text{iso}}(25^\circ\text{C})$  for  $^{25}\text{Mg}$  in MgO. The experimental data (open circles) show a linear variation of about 2ppm between  $1200^\circ$  and room temperature. The calculation that only takes the MgO thermal expansion into account (full triangles) leads to a temperature dependence with a negative slope, in total disagreement with experiment. In contrast, the experimental data are quite well reproduced by the calculation that takes both the thermal expansion and the nuclear motion into account (full square). Figure extracted from Ref. [192].

rections related to fluctuations of atoms around their equilibrium position are essential to reproduce the temperature dependence of  $\delta_{\text{iso}}$  observed experimentally [192] (see Fig. 1.30 that compares experimental and theoretical  $^{25}\text{Mg}$   $\delta_{\text{iso}}$ ). The electric field gradient tensor is also very sensitive to temperature and nuclear quadrupole resonance experiments (NQR)<sup>29</sup> show a variation of the resonances  $\nu_+$ ,  $\nu_0$  and  $\nu_-$  up to  $-0.2$  kHz/K [25]. Fig. 1.31, for example, exhibits the temperature dependence of the NQR frequencies of  $^{14}\text{N}$  in the RDX explosive compound. As emphasized by Bonhomme *et al.* [25], NQR spectroscopy offers a real opportunity to monitor the explicit effect of temperature in theoretical first-principles developments. According to the Bayer theory [16], the temperature dependence of the  $\nu$  frequencies can be empirically determined from:

$$\nu(T) = a - \frac{b}{\exp\left(\frac{c}{T}\right) - 1} \quad (1.23)$$

where  $a$ ,  $b$  and  $c$  are fitted on the experimental data ( $a$  is the NQR frequency extrapolated to 0K in the rigid lattice case,  $b$  and  $c$  are functions dependent on the moment of inertia and on the frequency of libration motions of a molecule, respectively). Such a fit was performed in the case of RDX [177]. Eq. (1.23)

<sup>29</sup>NQR spectroscopy only concerns nuclei with spin  $\geq 1$ . NQR is sometimes called “zero field NMR” since NQR measurements are carried out without an external uniform magnetic field. The GIPAW-calculated  $C_q$  and  $\eta$  values can be used for the calculation of NQR resonances, which are considered as limits at 0 K of low-temperature NQR data.

is useful to evaluate the frequencies at temperature out of the experimental range. However it is obviously not able to predict the resonance frequencies when no temperature-dependent experimental data are available. Therefore first-principles modeling of the NQR temperature effects are of first importance to predict the order of magnitude of a given NQR resonance at finite temperature for any sample under study.

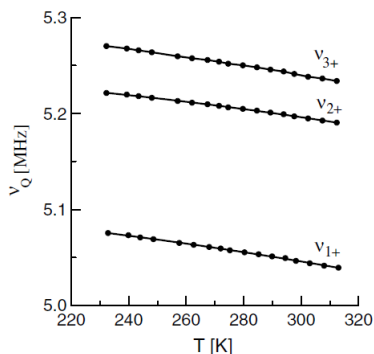


Figure 1.31: Temperature dependence of the NQR  $\nu_+$  frequencies of  $^{14}\text{N}$  in the RDX explosive, also known as cyclotrimethylene-trinitramine ( $\text{C}_3\text{H}_6\text{N}_6\text{O}_6$ ). The three frequencies correspond to the three nitrogen of the  $\text{C}_3\text{N}_3$  cycle of the  $\text{C}_3\text{H}_6\text{N}_6\text{O}_6$  molecule. The 0K extrapolated experimental values are in good agreement with the GIPAW calculated frequencies. Figure extracted from Ref. [177].

In the case of XANES spectroscopy, we have theoretically shown that vibrations could have a spectacular effect at the Al  $K$  edge, allowing  $1s$  to  $3s$  electric dipole transitions [39, 32]. Fig. 1.32 exhibits the Al  $K$ -edge XANES spectrum of corundum ( $\alpha\text{-Al}_2\text{O}_3$ ) and compares it to first-principles calculations performed in the electric-dipole approximation. The calculated spectrum labeled ‘equil.’ was obtained with the atoms at their equilibrium positions. All the experimental XANES features are satisfactorily reproduced by the ‘equil.’ spectrum except pre-edge peak P. Fig. 1.33 shows that the  $3s$  empty states of the absorbing atom arise exactly at the energy position of P. Thus the electronic states involved in the pre-edge region are not the  $3p$  but the  $3s$  empty states of the absorbing atom. The  $3s$  states of the absorber cannot be reached without the participation of nuclear motion. In 2009, Christian Brouder and I developed a theory in order to include vibrations in the computation of the XANES cross-section [39, 32], which allows electric-dipole transitions from the  $1s$  initial state to  $3s$  final states.<sup>30</sup> The

<sup>30</sup>The method presented in Refs. [39, 32] uses several approximations. First, vibrational energies are considered to be small with respect to the experimental resolution. In other words, this approximation accounts for the fact that the absorption process is much faster than atomic vibrations. Second, the strongly lo-

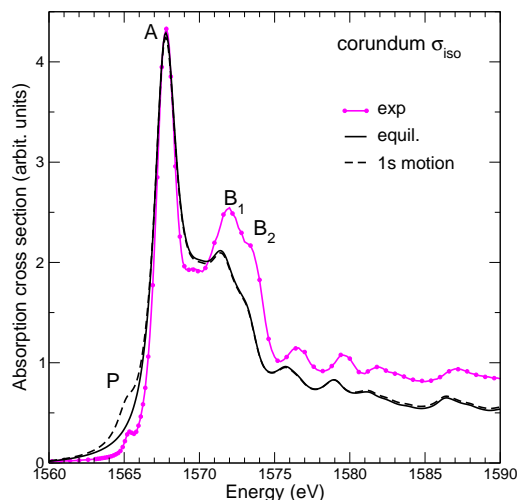


Figure 1.32: Al  $K$ -edge XANES in corundum ( $\alpha\text{-Al}_2\text{O}_3$ ). Comparison between experiment (pink line with full circles) and two theoretical spectra: a standard cross-section calculation performed with the atoms at their equilibrium positions (black solid line) and a cross-section calculation using the method presented in Refs. [39, 32] that allows  $1s \rightarrow 3s$  transitions (black dashed line).

corresponding calculated spectrum, labeled ‘1s motion’ in Fig. 1.32, exhibits a theoretical pre-edge peak in good agreement with experiment. From this preliminary work, we show that quantum thermal fluctuations can result in a violation of symmetry, which allows forbidden electronic transitions. Such forbidden transitions were previously invoked to be responsible for the pre-edge feature that occurs at the Al  $K$  edge in several aluminosilicate minerals [147] and at the Si  $K$  edge in silicon diphosphate [149]. Moreover, Ankudinov and Rehr stated that atomic displacements of order of typical Debye-Waller factors could reveal some forbidden transitions [8]. Consequently, the fact that vibrations may be able to induce additional peaks (in the pre-edge or at higher energies) suggests that XANES could be considered as a relevant probe of quantum thermal fluctuations. In or-

calized character of the  $1s$  initial wave function is used to restrict vibrations in the initial state to the absorbing atom motion only. Third, the crude Born-Oppenheimer approximation is made for the final state, which assumes that atomic motions do not significantly change the final electronic states. Consequently, the final states are determined for the atoms at their equilibrium positions, and vibrations only modify the absorbing atom position in the initial state. In practice, the  $1s$  initial wave function is no more centered on the equilibrium position of the absorbing atom. This shifted  $1s$  wave function is expanded over spherical harmonics centered at the equilibrium position and the  $\ell=1$  component allows for dipole transition to  $3s$  states. This method does not create (or increase) hybridization in the final state on the absorbing atom site.

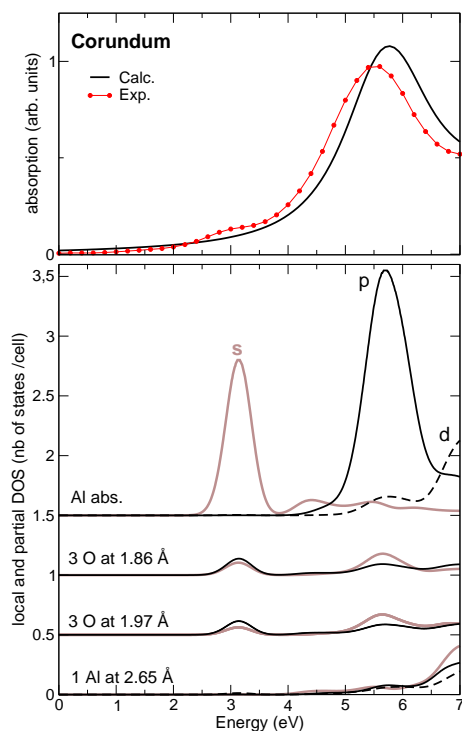


Figure 1.33: Partial DOS projected on the absorbing Al atom and its first neighbors in the supercell of corundum including the Al 1s core-hole. The *s*, *p* and *d* empty DOS are represented by light-colored solid line, black solid line and black dashed line, respectively. The top panel reproduces the pre-edge region of the experimental and calculated spectra in order to make easier the identification of the empty orbitals that are involved in the experimental Al *K* pre-edge peak, labeled P. The role of the Al 3s of the absorbing atom is found to be prominent. Figure extracted from Ref. [39].

der to support our preliminary theoretical results, we also carried out temperature-dependent XANES measurements at the Al *K* edge in corundum and beryl ( $\text{Be}_3\text{Si}_6\text{Al}_2\text{O}_{18}$ ), which also presents a pre-edge feature not reproduced without taking vibrations into account [153]. Results obtained for corundum are shown in Fig. 1.34. The pre-edge peak is found very sensitive to thermal fluctuations: its intensity grows and its position shifts to lower energy as temperature increases. Thermal fluctuations are also visible above the pre-edge region, through an intensity decrease of the main features and through a slight shift to lower energy of the first main peak. Our method developed in Refs. [39, 32] has nearly no impact on the peak intensity above the edge, and is unable to produce any shift of the features.<sup>31</sup> Thus, the development of a the-

<sup>31</sup>This last result was expected because of the use of the crude Born-Oppenheimer approximation. Within this approximation, the transition energies are evaluated for the atoms at their equi-

oretical approach that fully accounts for the thermal fluctuations observed in XANES is of first importance.

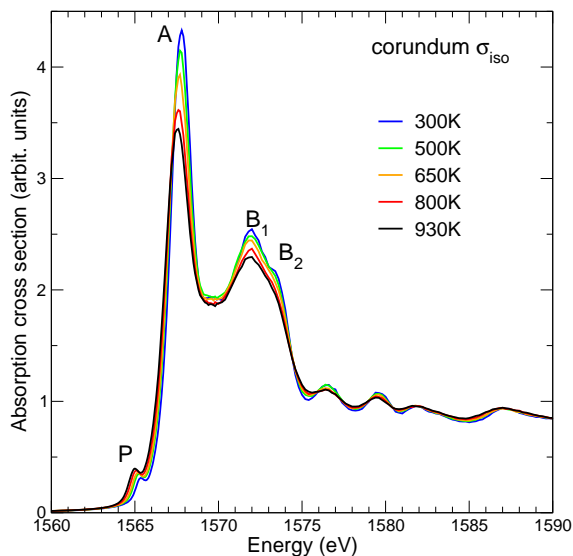


Figure 1.34: Experimental Al *K*-edge XANES spectra of corundum recorded at several temperatures from 300K to 930K, on the LUCIA beamline at SOLEIL synchrotron [153].

The NMR parameters, as well as the XANES cross section, are not linear functions of the atomic coordinates and are therefore sensitive to harmonic and anharmonic fluctuations.<sup>32</sup> The purpose of this project is to describe these quantum harmonic and anharmonic thermal fluctuations, using methods based on DFT. In the case of non-quantum nuclear motion, the method of choice would be molecular dynamics (MD), either classical or *ab initio*. However, MD simulations are appropriate only if  $k_B T > \hbar \omega_{\text{vib}}$ . Thus MD methods are not suitable for systems containing light elements,

librium positions; hence the spectral features remain at the same energy positions as in ‘equil.’ spectrum.

<sup>32</sup>The atomic position can be represented by the coordinate:

$$x(t) = x_0 + \underbrace{A \cos \omega t}_{\text{harmonic term}} + \text{anharmonic term},$$

where  $x_0$  is the equilibrium position. Near  $x_0$ , a property  $\mathcal{O}$  depending on  $x(t)$  is written:

$$\begin{aligned} \mathcal{O}(x(t)) = \mathcal{O}(x_0) &+ \underbrace{(x(t) - x_0) \frac{\partial \mathcal{O}(x_0)}{\partial x}}_{\text{linear function of coordinate}} \\ &+ \underbrace{(x(t) - x_0)^2 \frac{\partial^2 \mathcal{O}(x_0)}{\partial x^2}}_{\text{quadratic function of coordinate}} + \dots \end{aligned}$$

such as corundum and beryl. Therefore, a quantum treatment of vibrations is crucial for this project. A great improvement would be to use path-integral MD, which enables to treat the quantum nature of nuclear motion. For instance, it was successfully used to model the N  $K$ -edge absorption spectrum of N<sub>2</sub> gas [196]. But the computational cost of path-integral MD simulations in solids, such as corundum or beryl, would be a serious limiting factor.

### Description of the project

In this project, we plan to treat the harmonic and anharmonic quantum thermal fluctuations in two steps. First, the harmonic effects will be modeled by generating atomic position configurations that obey quantum statistics at finite temperature. Specifically, the objective is to set up a computing platform for the generation of these structural configurations for any compound. This platform will be integrated in Quantum-Espresso suite of codes. The atom position configurations so obtained will be used as input for the calculation of XANES cross-section and NMR parameters. An equivalent methodology was experienced for the modeling of <sup>17</sup>O and <sup>25</sup>Mg  $\delta_{\text{iso}}$  in MgO by Rossano *et al.* [192], and has proven to be an effective instrument. Second, the anharmonic terms will be evaluated by perturbative methods such as the quasi-harmonic approximation and the self-consistent harmonic approximation [72], which is under development in our group for electron-phonon coupling calculations occurring in superconductivity.

This theoretical work will be coupled to temperature-dependent NMR, XANES and X-ray diffraction experiments for a series of compounds, selected from their XANES spectral signature in the pre-edge region at the Al or Si  $K$ -edge. X-ray diffraction data will be used to characterize the sample and to determine the thermal expansion of the selected materials. XANES experiments will be performed on the LUCIA beamline in the SOLEIL synchrotron in collaboration with Nicolas Trcera. NMR experiments

The expectation value of  $\mathcal{O}$  is then given by:

$$\langle \mathcal{O}(x(t)) \rangle = \mathcal{O}(x_0) + \underbrace{\text{harmonic term}}_{\text{into linear function}} + \underbrace{\text{harmonic term}}_{\text{into quadratic function}} + \underbrace{\text{anharmonic term}}_{\text{into linear function}} + \dots$$

$\underbrace{\hspace{10em}}_{=0}$   
 $\underbrace{\hspace{10em}}_{\text{harmonic fluctuation}}$   
 $\underbrace{\hspace{10em}}_{\text{anharmonic fluctuation}}$

The harmonic and anharmonic fluctuations that we want to model in this project correspond to the third and the fourth terms of  $\langle \mathcal{O}(x(t)) \rangle$ , respectively.

will be realized at the CEMHTI in Orléans with Christel Gervais (LCMCP, UPMC). The quantum thermal fluctuations will be investigated from low temperature (around 10 K) to high temperature (around 900 K). The selected compounds are listed in Table 1.11. As mentioned above, corundum and beryl exhibit a well-defined pre-edge peak, signature of the symmetry violation due to nuclear motion. The pre-edge peak at the Al  $K$ -edge is a constant feature in oxides containing hexa-coordinated aluminum (<sup>6</sup>Al) [116]. Similarly, when Si lies in a six-fold coordinated site (that is rather uncommon), the Si  $K$ -edge displays a well-defined pre-edge peak [147, 149]. That is why we decide to study stishovite, the high-pressure crystalline polymorph of SiO<sub>2</sub>, which has a rutile-type structure, and SiP<sub>2</sub>O<sub>7</sub> polymorphs, where Si is also six-fold coordinated to oxygen atoms. Besides, the polymorphs of SiP<sub>2</sub>O<sub>7</sub> has been already extensively studied in NMR (experiments and calculations) by Christel Gervais and Christian Bonhomme [25], but without taking thermal fluctuations into account, yet. When Al and Si are in four-fold coordinated sites (<sup>4</sup>Al, <sup>4</sup>Si), a pre-edge feature is sometimes detectable but often hidden by the intense white line, which characterizes the corresponding Al  $K$ -edge and Si  $K$ -edge XANES spectra. However, compounds with <sup>4</sup>Al or <sup>4</sup>Si (like berlinite, natrolite and quartz) also are good candidates for our purpose. Indeed, when increasing the temperature, we expect that thermal vibrations make a pre-edge emerge at the left side of the white line. Such a result could lead to a reinterpretation of the appearance of a pre-edge peak observed at the Al  $K$  edge in zeolites when temperature is increased, initially interpreted as the signature of threefold coordinated Al [224, 223, 174].

This pluridisciplinary project is the subject of a PhD work fully-funded by LabEx MATISSE, within a collaboration between us (Francesco Mauri, Christian Brouder and me) and Christel Gervais and Christian Bonhomme from the LCMCP.

## 1.5.2 The modeling of ELNES spectra

### Scientific context and aim of the project

A technique analogous to XANES spectroscopy is the electron energy-loss near-edge structure (ELNES) spectroscopy, which is also a technique currently used at the IMPMC, due to the specific investment made in STEM equipment [20, 175]. More generally, this last decade, Electron Energy Loss Spectroscopy (EELS) has undergone an extensive expansion due to the technical advances of scanning transmission electron microscopy (STEM). The development in correcting electron optical aberrations permits to obtain electron-probe size smaller than 0.1 nm. The electron sources have been improved in terms of current and energy

Table 1.11: List of the compounds that will be investigated in the temperature-dependent NMR/XANES project.

Compound	XANES	NMR
corundum $\alpha$ -Al <sub>2</sub> O <sub>3</sub>	Al <i>K</i> edge (done from 300K to 930K [153])	<sup>27</sup> Al
beryl Be <sub>3</sub> Si <sub>6</sub> Al <sub>2</sub> O <sub>18</sub>	Al <i>K</i> edge (done from 300K to 800K [153])	<sup>27</sup> Al, <sup>29</sup> Si
stishovite SiO <sub>2</sub>	Si <i>K</i> -edge	<sup>29</sup> Si,
SiP <sub>2</sub> O <sub>7</sub> polymorphs	Si <i>K</i> -edge	<sup>29</sup> Si, <sup>31</sup> P
berlinite AlPO <sub>4</sub>	Al <i>K</i> -edge	<sup>27</sup> Al, <sup>31</sup> P
natrolite Na <sub>2</sub> (Al <sub>2</sub> Si <sub>3</sub> O <sub>10</sub> ).2H <sub>2</sub> O	Al <i>K</i> -edge	<sup>23</sup> Na, <sup>27</sup> Al, <sup>29</sup> Si
quartz $\alpha$ -SiO <sub>2</sub>	Si <i>K</i> -edge	<sup>29</sup> Si, <sup>17</sup> O

resolution. For instance, cold-field emission guns provide energy resolution of about 0.3 eV, and the high-brilliance guns combined with monochromator improve the energy resolution up to 0.07-0.1 eV (see Ref. [157] for a comparison of ELNES spectra of 3d transition metal oxides obtained with and without the use of an electron monochromator). Consequently, it is now possible to observe variations on ELNES spectra at the edge of a given element as a function of its spatial localization at the atomic scale. For instance, Haruta *et al.* [104] measured site-resolved oxygen *K*-edge ELNES spectra in La<sub>2</sub>CuSnO<sub>6</sub> (LSCO). The layered structure of the LSCO perovskite is suitable for examining the site-resolved ELNES (see Fig. 1.35 for explanation). The ELNES spectra are reproduced in Fig. 1.36, and clearly exhibit different shapes. Another example is the paper of Suenaga and Koshino [207], who realized site-resolved ELNES measurements in graphene (see Fig. 1.37 for an illustration).

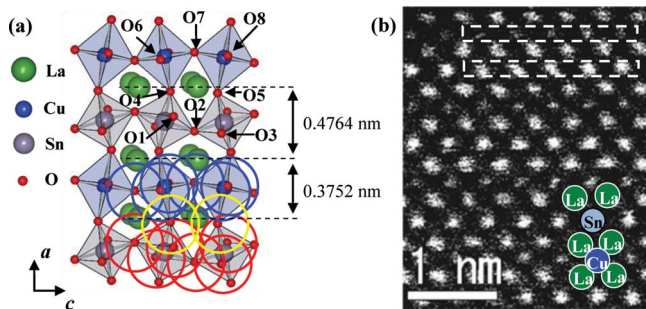


Figure 1.35: (a) Crystalline structure of LSCO, which contains eight non-equivalent sites for oxygen, labeled O1 to O8. The O1, O2 and O3 atoms belong to Sn layer, and are bound to Sn only. Similarly, O6, O7 and O8 belong to the Cu layer and are bound to Cu only. In contrast, O4 and O5 are common to CuO<sub>6</sub> and SnO<sub>6</sub> octahedra. (b) Atomic resolution high-angle annular dark field image of LSCO. The scanning area for site-resolved O *K*-edge ELNES spectra are indicated by the rectangles. The electron probe is successively placed at the Cu site and Sn site, in order to excite the oxygen atoms coordinated to Cu and then those to Sn. Figure extracted from Ref. [104].

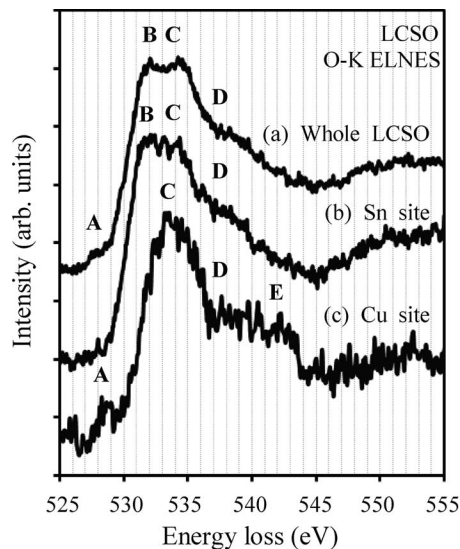


Figure 1.36: O *K*-edge ELNES spectra recorded by scanning an electron probe over a whole unit cell of LSCO, only from the Sn site, and only from the Cu site. Figure extracted from Ref. [104].

In these two examples, experimental spectra are interpreted with the help of DFT calculations. To my knowledge, four available codes based on DFT offer the possibility to calculate ELNES<sup>33</sup>: CASTEP [85], WIEN2K-TELNES.2 [170, 121, 112], FEFF9 [121, 122], ELK ([elk.sourceforge.net](http://elk.sourceforge.net)). Some of their specificities are given in Tab. 1.12. CASTEP, based on the same methods as Quantum-Espresso, seems to be the pioneer code that calculates ELNES spectra, due to the PhD work of Chris Pickard [180]. WIEN2K seems to be the most used code for ELNES spectra modeling

<sup>33</sup>Here I list the codes especially dedicated to core-loss spectra. For low-loss spectra simulations, several *beyond DFT* codes exist: DP (Dielectric Properties) based on TDDFT, EXC (Exciton) and YAMBO (Yet Another Many-Body cOde) based on the BSE formalism. Actually, these codes are able to calculate the whole electron-energy-loss spectrum (including plasmon peak and ionization edge) but are essentially used for the low-loss energy-range modeling.

Table 1.12: List of codes available for ELNES modeling. The indicated authors are the persons who coded the ELNES part.

Name	Methods	Distribution	Authors
CASTEP	DFT, plane-wave basis set, pseudopotentials, PAW periodic boundary conditions (supercell)	commercial (Univ. Cambridge)	Ch. Pickard
WIEN2K-TELNES.2	DFT, FP-LAPW/APW+lo, all-electron periodic boundary conditions (supercell) relativistic effects (anisotropic materials)	commercial (TU Vienna)	K. Jorissen C. Hébert M. Nelhiebel
FEFF9	self-consistent multiple scattering real space (cluster) relativistic effects (anisotropic materials)	commercial (Univ. Washington)	K. Jorissen J. J. Rehr
ELK	DFT, FP-LAPW, all-electron periodic boundary conditions (supercell)	GNU public license	J. K. Dewhurst S. Sharma C. Draxl

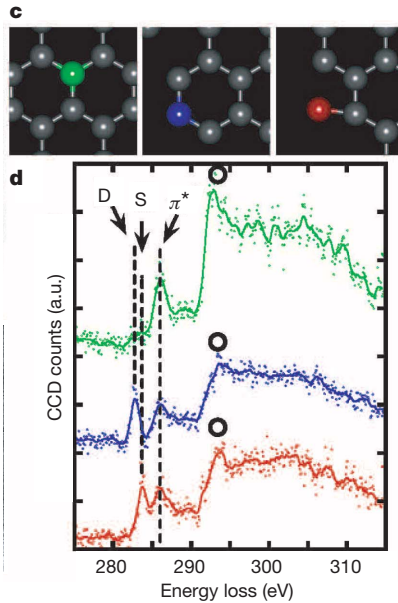


Figure 1.37: Three site-resolved C  $K$ -edge ELNES spectra in graphene. Figure extracted from Ref. [207].

(see Ref. [112] for a review of the ELNES calculations performed using WIEN2K up to 2007). Ref. [161] is dedicated to ELNES calculations using FEFF, which has been recently modified to consider fully relativistic effects within the double differential scattering cross section for inelastic electrons [122]. The ELK code is based on the same method as WIEN2K, but I did not find any publication that reports ELK ELNES calculations. Except ELK, ELNES codes are distributed under general public license. Moreover, the method used in WIEN2K and ELK is time-consuming, so that the treatment of complex systems (defects, surfaces, interfaces), which requires large supercell, is a bottleneck. Hence it appears that an ELNES package (with

a reasonable computational cost) within Quantum-Espresso could be greatly appreciated. Besides, very recently, Tamura *et al.* [213] have presented PAW calculations of ELNES spectra of Ti-bearing oxide crystals and TiO-SiO glasses performed using the QMAS code, already mentioned in Sec. 1.3.1. QMAS is another DFT code that uses periodic boundary conditions and plane-wave basis set, and seems to now incorporate an ELNES package. This emphasizes the importance of adding new features (like ELNES) in electronic structure DFT codes (like Quantum-Espresso) in order to enlarge their application fields.

### Project description

This second project consists in writing an ELNES computational code dedicated to the edges observable in EELS (i.e., for ionization energies that rarely exceed 2 keV) that can be modeled in a single-particle approach. As XSPECTRA, this ELNES code will be incorporated within the Quantum-Espresso distribution. The method of XANES calculation (comprising PAW all-electron wave-function reconstruction, Lanczos basis set, continued fraction) will be adapted to the case of ELNES, including the following specificities:

(i) *The relativistic expression of the double differential electron inelastic scattering cross section*

The modeling of an ELNES spectrum is achieved by the computation of the double differential cross section for the inelastic scattering of fast electrons,

$$\frac{\partial^2 \sigma(\mathbf{q}, E)}{\partial \Omega \partial E}, \quad (1.24)$$

which gives the probability of detecting an electron that has lost energy  $E$  and transferred momentum  $\mathbf{q}$  by scattering into the solid angle  $d\Omega$ . The momentum transfer is  $\mathbf{q} = \mathbf{k} - \mathbf{k}'$ , under the assumption that the

incoming and outgoing fast electrons are plane waves with wave vectors  $\mathbf{k}$  and  $\mathbf{k}'$ , respectively. Since in a (S)TEM, the energy of the incoming electron can reach 300 keV (corresponding to  $v_0/c = 0.77$  where  $\mathbf{v}_0$  is the velocity of the incoming electron and  $c$  the velocity of light), relativistic effects have to be taken into account. Schattschneider *et al.* in 2005 [195], started from the Bethe's theory [22] to derive a relativistic expression of Eq. (1.24) within the Born-Oppenheimer approximation in a single-particle approach. Later, this derivation was revisited by K. Jorissen [121] and Sorini *et al.* [204], who showed that a term of order  $\hbar\omega/mc^2$  in the transition matrix element was omitted by Schattschneider *et al.* ( $\hbar\omega = E$  is the energy lost by the probe). According to Sorini *et al.*, this term is not always negligible. Finally, the relativistic expression of Eq. (1.24) is:

$$\begin{aligned} \frac{\partial^2 \sigma}{\partial \Omega \partial E} &= \frac{4\gamma^2}{a_0^2} \frac{1}{\left[q^2 - q_z^2 \left(\frac{v_0}{c}\right)^2\right]^2} \frac{k_f}{k_i} \\ &\times \sum_{i,f} \left| \langle f | e^{i\mathbf{q}\cdot\mathbf{r}} \left[ 1 - \frac{\mathbf{v}_0}{mc^2} \cdot \left( \mathbf{p} + \frac{\mathbf{q}}{2} \right) \right] | i \rangle \right|^2 \\ &\times \delta(E_f - E_i - E), \end{aligned} \quad (1.25)$$

where  $\gamma = \sqrt{1 - v_0^2/c^2}$  is the relativistic factor,  $a_0$  is the Bohr radius,  $q_z$  is the momentum transfer projected onto the direction of  $\mathbf{v}_0$ ,  $\mathbf{p}$  is the momentum operator,  $m$  is the electron rest mass,  $|i\rangle$  and  $|f\rangle$  are the one-electron initial and final states in the probed material, with energy  $E_i$  and  $E_f$ , respectively.<sup>34</sup>

The relativistic corrections, as given in Eq. (1.25), act differently in the direction of the incident electron beam and in the direction perpendicular to it. Thus the relativistic effects are dramatic for anisotropic materials [195, 122] and compensate for isotropic ones. For isotropic systems, the following expression Eq. (1.24) can be used [112]:

$$\begin{aligned} \frac{\partial^2 \sigma}{\partial \Omega \partial E} &= \frac{4\gamma^2}{a_0^2} \frac{1}{q^4} \frac{k_f}{k_i} \\ &\times \sum_{i,f} \left| \langle f | e^{i\mathbf{q}\cdot\mathbf{r}} | i \rangle \right|^2 \\ &\times \delta(E_f - E_i - E). \end{aligned} \quad (1.26)$$

The relativistic effects concern the scalar and vector potential in the Hamiltonian of the system that are added by the probe fast electron. They only intervene in the prefactor term and in the transition matrix Hamiltonian. Therefore the computation of Eq. (1.25) does not require the calculation of relativistic initial and final states in SCF calculation.

(ii) *The nature of the electronic transitions observed in ELNES spectroscopy*

<sup>34</sup>Actually the term neglected by Schattschneider *et al.* is  $\frac{\mathbf{q}\cdot\mathbf{v}_0}{2mc^2}$ .

For medium acceleration voltages less than 400 keV, the observable momentum transfer in electron inelastic scattering does not exceed  $10^9 \text{ m}^{-1}$  [195]. In this condition,  $qa_0 \ll 1$  that allows a Taylor expansion of  $e^{i\mathbf{q}\cdot\mathbf{r}}$  (done here up to the second order):

$$\left[ 1 + i\mathbf{q}\cdot\mathbf{r} - \frac{1}{2}(\mathbf{q}\cdot\mathbf{r})^2 \right] \left[ 1 - \frac{\mathbf{v}_0}{mc^2} \cdot \left( \mathbf{p} + \frac{\mathbf{q}}{2} \right) \right] = \left( 1 - \frac{\mathbf{v}_0 \cdot \mathbf{q}}{2mc^2} \right) \quad (1.27)$$

$$+ \left( i\mathbf{q}\cdot\mathbf{r} - \frac{\mathbf{v}_0 \cdot \mathbf{p}}{mc^2} - i\mathbf{q}\cdot\mathbf{r} \frac{\mathbf{v}_0 \cdot \mathbf{q}}{2mc^2} \right) \quad (1.28)$$

$$+ \left[ -\frac{1}{2}(\mathbf{q}\cdot\mathbf{r})^2 - i\mathbf{q}\cdot\mathbf{r} \frac{\mathbf{v}_0 \cdot \mathbf{p}}{mc^2} + \frac{1}{2}(\mathbf{q}\cdot\mathbf{r})^2 \frac{\mathbf{v}_0 \cdot \mathbf{q}}{2mc^2} \right] \quad (1.29)$$

$$+ \left[ \frac{1}{2}(\mathbf{q}\cdot\mathbf{r})^2 \frac{\mathbf{v}_0 \cdot \mathbf{p}}{mc^2} \right] \quad (1.30)$$

Term (1.27) is constant and does not contribute to the transition matrix element since  $\langle f | i \rangle = 0$ .

Using  $\mathbf{p} = \frac{m}{i\hbar} [\mathbf{r}, H_0]$  [31], it can be shown that

$$\langle f | \mathbf{p} | i \rangle = i m \frac{E}{\hbar} \langle f | \mathbf{r} | i \rangle = i m (\mathbf{v}_0 \cdot \mathbf{q}) \langle f | \mathbf{r} | i \rangle. \quad (1.31)$$

Hence, term (1.28) is of order  $r$  and leads to the dipole transition matrix element:

$$i \langle f | \left[ \mathbf{q} - \frac{(\mathbf{v}_0 \cdot \mathbf{q}) \mathbf{v}_0}{c^2} - \frac{(\mathbf{v}_0 \cdot \mathbf{q}) \mathbf{q}}{2mc^2} \right] \cdot \mathbf{r} | i \rangle \quad (1.32)$$

Term (1.29) is of order  $r^2$  and leads to both monopole and quadrupole matrix elements (not explicitated here). This differs from x-ray absorption spectroscopy, where the  $r^2$ -order term only corresponds to electric quadrupole transitions. Indeed, the  $r^2$ -order transition operator of XAS is  $\frac{1}{2} \mathbf{k} \cdot \mathbf{r} \boldsymbol{\varepsilon} \cdot \mathbf{r}$  (instead of  $(\mathbf{q} \cdot \mathbf{r})^2$  in ELNES), and the orthogonality between the wave vector  $\mathbf{k}$  and the polarization vector  $\boldsymbol{\varepsilon}$  of the x-ray incident beam cancels the monopole matrix element (see appendix 4.2.2 of Ref. [31] for more details). Term (1.30) is of order  $r^3$  and will be neglected.

Although electronic transitions observed in ELNES are essentially dipolar, the monopole, dipole and quadrupole transition matrix elements will be included in the ELNES code that we want to write, and their angular dependence will be investigated.

(iii) *The specific geometry of an ELNES experiment in a STEM*

Unlike the case of XAS, where the photon beam is polarized, and although different experimental setups were proposed in the literature to record momentum-resolved ELNES (see the review of Keast *et al.* [131]), the accurate selection of incident and scattered electron wave vectors is limited by the use of finite convergence and collection angles. This is particularly true when operating the microscope in STEM mode (see Fig. 1.38) to obtain the finest possible electron probe: the incident wave vector  $\mathbf{k}$  is included in a convergence cone of semi-angle  $\alpha$ . Similarly, the detector

integrates the signal over a certain range of outgoing beam directions so that  $\mathbf{k}'$  is included in a collection cone of semi-angle  $\beta$ . Both  $\alpha$  and  $\beta$  usually are of the order of few to few tens of millirad. Assuming

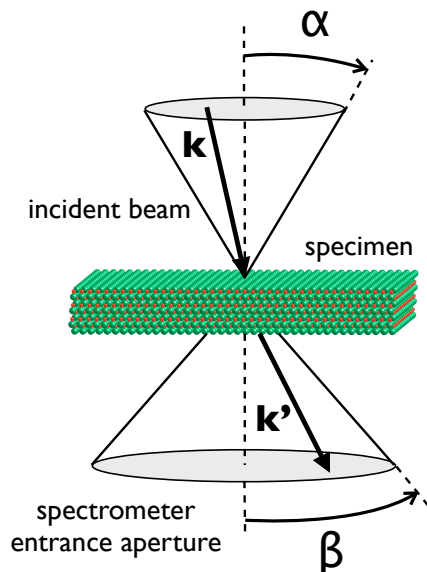


Figure 1.38: Schematic drawing of the scattering geometry including integration over collection and convergence angle (image kindly provided by G. Radtke).

that the incoming electron beam is monochromatic, the measured ELNES signal is given by:

$$\frac{\partial\sigma(E)}{\partial E} = \int_{\alpha,\beta} \frac{\partial^2\sigma(\mathbf{q}, E)}{\partial\Omega\partial E} d^3\mathbf{q}. \quad (1.33)$$

A special care will be paid on the integration over the  $\alpha$  and  $\beta$  angular domains. Besides, the influence of probe convergence, collector aperture and electron-beam incidence angle on the angular-dependence of ELNES spectra will be investigated and confronted to the study of Le Bossé *et al.* [143].

This second project will be carried out in collaboration with Guillaume Radtke, who has joined our laboratory in October 2012. Guillaume Radtke is CNRS researcher; experimentalist specialized in STEM and EELS measurements and expert user of WIEN2K for ELNES calculations. Hence, his skills will be of first importance for the achievement of this project.

## 1.6 and what else?... beyond DFT

In the conclusion of Sec. 1.4, I have discussed the two main deficiencies of DFT-LDA approach, when used to calculate  $K$ -XANES spectra: the modeling of (i) the core-hole-electron interaction, (ii) the electron-electron repulsion.

The second deficiency actually is not too disabling and can be circumvented while remaining in the DFT framework. I confess that, up to now, I have limited my  $K$  XANES calculations to systems that are fairly-well suited to single-particle methods (only  $\text{Ca}_3\text{Al}_2\text{Si}_3\text{O}_{12}:\text{V}^{3+}$  and  $\text{MbcN}$  were borderline cases). Nevertheless, a better strategy than restricting the applications of a method because of its limitations, is to improve it, to find solutions that allow the treatment of a wider variety of systems. For instance, the incorporation of the Hubbard parameter has permitted the calculation of the pre-edge features at the transition metal  $K$  edge in several correlated materials with a good precision (see for instance Refs. [98, 127]). Moreover, very recently, Calandra *et al.* have proposed a simple method to account for the shake-up many-body excitations, which arise from a valence electron excitation following the creation of a core-hole by the incident photon [48]. The method consists of including the shake-up effects in  $K$ -XANES spectra by a simple convolution of the single-particle DFT+ $U$  calculated XANES spectrum with the corresponding  $1s$  photoemission experimental spectrum. Ref. [48] presents successful applications of the method at the metal  $K$ -edge of NiO, CoO and CuO.

On the contrary, the modeling of the core-hole-electron interaction is a more serious issue and certainly requires going beyond DFT. In single-particle DFT schemes, the core-hole effects are statically treated by the electronic relaxation of a supercell of atoms including a  $1s$  core-hole on the absorber. To ensure neutrality of the system, a background charge is added during the SCF procedure of the total energy minimization. By doing so, the results are not always satisfactory. Sec. 1.4 has repeatedly shown that the core-hole screening is too pronounced in the case of  $K$  edge of  $3d$  elements, leading to electric-quadrupole and local electric-dipole pre-edge features at too high energy, compared to experiment. However, at the Al  $K$ -edge, especially when Al is in sixfold coordination, I have observed the opposite effect, i.e., the core-hole screening (by the valence electrons) is not effective enough and leads to a too strong white line (see for instance the Al  $K$ -edge isotropic spectrum of corundum displayed in Fig. 1.1a).<sup>35</sup> Similar underestimation of the core-hole screening was found at the Mg  $K$ -edge in the case of  $^{61}\text{Mg}$ - and  $^{81}\text{Mg}$ -bearing minerals (see Fig. 1.8). To face the problem of the underestimation of the core-hole screening, a half core-hole is sometimes used, notably at the O  $K$ -edge [234, 183].

These observations are not so surprising since DFT is a ground state theory. For the calculation of electronic excitations, *beyond DFT* theories, such as TDDFT and many-body Green's function approaches,

<sup>35</sup>The fact that the core-hole screening is more important for  $^{61}\text{Al}$  than for  $^{41}\text{Al}$  was supposed by using *muffin-tin parameterized* multiple scattering calculations, during my PhD (see the discussion of Ref. [46]).

have undergone a remarkable development since the nineties (see the useful review by G. Onida, L. Reining and A. Rubio, dated 2002 [176]). Unlike DFT, TDDFT is able to describe the evolution of the system instead of its ground state. In many-body Green's function approaches, the key ingredients are the electron self energy  $\Sigma$  and the electron-hole interaction. A good approximation for  $\Sigma$  is given by the Hedin's *GW* approach [113], where  $G$  is the one-electron Green's function and  $W$  the screened Coulomb interaction. The electron-hole interaction is well described by the Bethe Salpeter equation (BSE). Many codes, based on these two methods, were developed for the modeling of optical properties.<sup>36</sup> Nevertheless, at present one observes a formidable emergence of the TDDFT and *GW*/BSE methods for core-level spectroscopy calculations. The *FDMNES* package has recently included TDDFT [4, 36, 35]. The *ORCA* real-space quantum-chemistry code also calculates XANES spectra using TDDFT [59, 190]. Another code, which uses TDDFT for XANES modeling (in the electric-dipole approximation), is becoming an interesting alternative to, on the one hand, solid state codes that use plane-wave basis sets and, on the other hand, quantum-chemistry codes that use localized basis set. Indeed, the *GPW* code (Grid-based Projector Augmented Wave), developed by J. Mortensen and coworkers and written mostly in *Python*, uses uniform real-space grids, which can flexibly treat both free and periodic boundary conditions [163, 71, 151]. Parallel to these TDDFT developments for XANES, there is the *GW*/BSE code developed many years ago by E. Shirley and coworkers, called *NBSE* (N standing for NIST) [201, 18, 203, 202]. Recently (2011), Shirley and the Rehr's group have finalized the *OCEAN* interface, which permits to Obtain Core Excitations using *ABINIT*<sup>37</sup> and *NBSE* [226]. The *OCEAN* interface incorporates advances of the *FEFF9* code, such as the calculation of inelastic mean free paths [187, 188]. Indeed, in both *OCEAN* and *FEFF9*, the intrinsic broadening of the spectra is not a parameter, i.e., the final-state self-energy shifts and damping effects observed in experimental spectra are calculated using the efficient many-pole *GW* self-energy model,<sup>38</sup> developed by Kas *et al.* [129] (see Ref. [130] for an evaluation of these effects on our Mg *K*-edge calculated spectrum of spinel).

*And what about the QUANTUM-ESPRESSO project?*  
As a well-developed electronic structure suite of codes,

<sup>36</sup>Since TDDFT leads to a screening equation similar to the BSE, but with a two-point, rather a four-point, interaction kernel, usually *GW*/BSE approaches also incorporate TDDFT.

<sup>37</sup>*ABINIT* is plane-wave DFT code, distributed under GNU licence, whose full documentation is available on [abinit.org](http://abinit.org).

<sup>38</sup>The many-pole *GW* self-energy model developed by Kas *et al.* is a straightforward extension of the Hedin and Lundqvist single plasmon-pole *GW* self-energy model.

*QUANTUM-ESPRESSO* also includes several *beyond DFT* packages dedicated to the electronic excitation modeling:

- TD-DFPT, standing for Time-Dependent Density Function Perturbation Theory, developed by Walker *et al.* [229],
- *GW*, meaning (*GW* + Wannier + Lanczos), developed by P. Umari *et al.* [220, 221] and able to calculate optical spectra of molecules containing more than 300 atoms in the TDDFT framework,
- *YAMBO* (Yet Another Many-Body cODE) developed by A. Marini *et al.* [154], based on *GW*/BSE formalism, including TDDFT,<sup>39</sup>
- *SAX*, standing for Self-Energy and eXcitation, a *GW* program developed by L. Martin-Samos and G. Bussi [155].

Therefore, it clearly appears from what precedes, that a combination of our DFT scheme, namely *XSPEC*TRA that also belongs to the *QUANTUM-ESPRESSO* distribution, and at least one the *beyond DFT* code (listed below) would be a challenging and promising project, in which I am greatly interested. However, using TDDFT or *GW*/BSE does not necessarily solve the core-hole-electron interaction issue. For instance, in the case of small-gap compounds, the electron-hole interaction as calculated using *GW*/BSE can lead to the fall of the first unoccupied states into the valence band (as in DFT), and then compromise the modeling of the pre-edge structure. Moreover the use of full core-hole *vs* half core-hole is debated not only in DFT, but also in the BSE formalism. Hence, it still remains instructive to compare the core-hole effects when statically treated using a supercell (*XSPEC*TRA) and when dynamically treated using either BSE or TDDFT (via the linear response in the perturbation theory).

To conclude this thesis, my goals are twofold. On the one hand, I plan to further develop the *XSPEC*TRA package by adding the computation of *ELNES* spectra and by incorporating the effects of the electron-phonon interaction. On the other hand, I would like to establish a collaboration with the authors of the *beyond DFT* codes in order to transpose the XAS (E1 and E2 transitions) and EELS transition matrix elements into TDDFT and *GW*/BSE formalisms.

<sup>39</sup>*YAMBO* is also interfaced with *ABINIT*.

## Appendix: Technical details of the calculations

This appendix contains the computational details of the most of the calculations presented in this thesis.

### A1- Structure of the studied compounds

#### Periodic systems

Table 1.13 summarizes the crystallographic structures that were used to calculate the XANES spectra of the minerals and other periodic systems, shown in this thesis.

Table 1.13: Description of the crystallographic structures of the compounds studied. For the absorbing atom,  $I$  indicate its coordination number and, in parenthesis, the point group and multiplicity of its crystallographic site within the conventional cell. The  $Z$  value is the number of formula units per cell. The compounds are listed in alphabetic order, separating the pure minerals from the doped minerals. For the latter (i.e., emerald, pyrope, ruby, sapphires, spinel and tsavorite), the  $Z$  value is the one of the corresponding undoped minerals.

Compounds	Chem. formula	Lattice syst.	Space group	Abs. atom	Cell param.	$Z$	Ref.
anatase	TiO <sub>2</sub>	tetragonal	$I4_1/amd$ (No. 141)	<sup>[6]</sup> Ti ( $\bar{4}m2$ )	$a = 3.7845 \text{ \AA}$ $c = 9.5153 \text{ \AA}$	4	[115]
corundum	$\alpha$ -Al <sub>2</sub> O <sub>3</sub>	trigonal	$R\bar{3}c$ (No. 167)	<sup>[6]</sup> Al (3)	$a_H = 4.7589 \text{ \AA}$ $c_H = 12.991 \text{ \AA}$ $a = 5.128 \text{ \AA}$ $\alpha = 55.3^\circ$	2	[172]
diopside	CaMgSi <sub>2</sub> O <sub>6</sub>	monoclinic	$C2/c$ (No. 15)	<sup>[6]</sup> Mg (2)	$a = 9.746 \text{ \AA}$ $b = 8.899 \text{ \AA}$ $c = 5.251 \text{ \AA}$ $\beta = 105.63^\circ$	4	[49]
enstatite	Mg <sub>2</sub> Si <sub>2</sub> O <sub>6</sub>	orthorhombic	$Pbca$ (No. 61)	<sup>[6]</sup> Mg1 (1, m=8) <sup>[6]</sup> Mg2 (1, m=8)	$a = 18.216 \text{ \AA}$ $b = 8.813 \text{ \AA}$ $c = 5.177 \text{ \AA}$	16	[107]
farringtonite	Mg <sub>3</sub> P <sub>2</sub> O <sub>8</sub>	monoclinic	$P2_1/n$ (No. 14)	<sup>[4]</sup> Mg (1, m=4) <sup>[6]</sup> Mg ( $\bar{1}$ , m=2)	$a = 7.596 \text{ \AA}$ $b = 8.231 \text{ \AA}$ $c = 5.078 \text{ \AA}$ $\beta = 94.05^\circ$	2	[173]
forsterite	Mg <sub>2</sub> SiO <sub>4</sub>	orthorhombic	$Pbnm$ (No. 62)	<sup>[6]</sup> Mg1 ( $\bar{1}$ , m=4) <sup>[6]</sup> Mg2 ( $m$ , m=4)	$a = 4.755 \text{ \AA}$ $b = 10.198 \text{ \AA}$ $c = 5.979 \text{ \AA}$	4	[30]
grandidierite	(Mg,Fe)Al <sub>3</sub> SiBO <sub>9</sub>	orthorhombic	$Pbnm$ (No. 62)	<sup>[5]</sup> Mg ( $m$ )	$a = 10.340 \text{ \AA}$ $b = 10.980 \text{ \AA}$ $c = 5.750 \text{ \AA}$	4	[205]
K <sub>2</sub> Ge <sub>8</sub> O <sub>17</sub>	K <sub>2</sub> Ge <sub>8</sub> O <sub>17</sub>	orthorhombic	$Pnma$ (No. 62)	<sup>[2]</sup> O1 ( $m$ , m=4) <sup>[2]</sup> O2 ( $m$ , m=4) <sup>[2]</sup> O3 ( $m$ , m=4) <sup>[2]</sup> O4 ( $m$ , m=4) <sup>[2]</sup> O5 ( $m$ , m=4) <sup>[2]</sup> O6 (1, m=8) <sup>[2]</sup> O7 (1, m=8) <sup>[2]</sup> O8 (1, m=8) <sup>[2]</sup> O9 (1, m=8) <sup>[2]</sup> O10 (1, m=8) <sup>[2]</sup> O11 (1, m=8)	$a = 13.371 \text{ \AA}$ $b = 8.800 \text{ \AA}$ $c = 13.372 \text{ \AA}$	4	[103]

pyrite	FeS <sub>2</sub>	cubic	$Pa\bar{3}$ (No. 205)	<sup>[6]</sup> Fe ( $\bar{3}$ )	$a = 5.1175 \text{ \AA}$	4	[206]
pyrope	Mg <sub>3</sub> Al <sub>2</sub> Si <sub>3</sub> O <sub>12</sub>	cubic	$Ia\bar{3}d$ (No. 230)	<sup>[8]</sup> Mg (222)	$a = 11.548 \text{ \AA}$	8	[111]
q-GeO <sub>2</sub>	GeO <sub>2</sub>	trigonal	$P3_121$ (No. 152)	<sup>[2]</sup> O (1)	$a = 4.985 \text{ \AA}$ $c = 5.648 \text{ \AA}$	3	[97]
r-GeO <sub>2</sub>	GeO <sub>2</sub>	tetragonal	$P4_2/mnm$ (No. 136)	<sup>[3]</sup> O ( $m2m$ )	$a = 4.395 \text{ \AA}$ $c = 2.860 \text{ \AA}$	2	[15]
rutile	TiO <sub>2</sub>	tetragonal	$P4_2/mnm$ (No. 136)	<sup>[6]</sup> Ti ( $mmm$ )	$a = 4.5937 \text{ \AA}$ $c = 2.9587 \text{ \AA}$	2	[115]
spinel	MgAl <sub>2</sub> O <sub>4</sub>	cubic	$Fd\bar{3}m$ (No. 227)	<sup>[4]</sup> Mg( $\bar{4}3m$ )	$a = 8.080 \text{ \AA}$	8	[242]
emerald	Be <sub>3</sub> Si <sub>6</sub> Al <sub>2</sub> O <sub>18</sub> :Cr <sup>3+</sup>	hexagonal	$P6/mcc$ (No. 192)	<sup>[6]</sup> Cr (32)	$a = 9.21 \text{ \AA}$ $c = 9.19 \text{ \AA}$	2	[162]
red pyrope	Mg <sub>3</sub> Al <sub>2</sub> Si <sub>3</sub> O <sub>12</sub> :Cr <sup>3+</sup>	cubic	$Ia\bar{3}d$ (No. 230)	<sup>[6]</sup> Cr ( $\bar{3}$ )	$a = 11.454 \text{ \AA}$	8	[2]
ruby	$\alpha$ -Al <sub>2</sub> O <sub>3</sub> :Cr <sup>3+</sup>	trigonal	$R\bar{3}c$ (No. 167)	<sup>[6]</sup> Cr (3)	$a = 5.11 \text{ \AA}$ $\alpha = 55.41^\circ$	2	[69]
blue sapphire	$\alpha$ -Al <sub>2</sub> O <sub>3</sub> :Fe-Ti	trigonal	$R\bar{3}c$ (No. 167)	<sup>[6]</sup> Fe (3)	$a = 5.11 \text{ \AA}$ $\alpha = 55.41^\circ$	2	[69]
pink sapphire	$\alpha$ -Al <sub>2</sub> O <sub>3</sub> :Ti <sup>3+</sup>	trigonal	$R\bar{3}c$ (No. 167)	<sup>[6]</sup> Ti (3)	$a = 5.11 \text{ \AA}$ $\alpha = 55.41^\circ$	2	[69]
red spinel	MgAl <sub>2</sub> O <sub>4</sub> :Cr <sup>3+</sup>	cubic	$Fd\bar{3}m$ (No. 227)	<sup>[6]</sup> Cr ( $\bar{3}m$ )	$a = 8.0806 \text{ \AA}$	4	[242]
tsavorite	Ca <sub>3</sub> Al <sub>2</sub> Si <sub>3</sub> O <sub>12</sub> :V <sup>3+</sup>	cubic	$Ia\bar{3}d$ (No. 230)	<sup>[6]</sup> V ( $\bar{3}$ )	$a = 11.847 \text{ \AA}$	8	[94]

### Structural relaxation of the doped minerals

In order to simulate the  $3d$  defect in allochromatic minerals, supercells were built using the DFT optimized crystal structure of the pure phases (corundum for ruby and sapphires, beryl for emerald, spinel for red spinel, pyrope for red pyrope), and the experimental crystal structure of grossular for tsavorite. The supercells were chosen large enough to minimize the interaction between two paramagnetic ions. Moreover, the  $3d$  impurity concentration is estimated to be low enough (<1.7 at %) not to modify the mean cell parameter. While the size of the supercell was kept fixed, all atomic positions were relaxed in order to investigate long-range relaxation. The symmetry of the trivalent ion site is let free to relax. The resulting atomic forces were lower than 0.3 mRy/Bohr radius.<sup>40</sup>

The calculations were performed in the local density approximation (LDA), using the pseudopotentials described in Table 1.15. The code used for the structural relaxation of emerald, ruby and sapphires was CPMD,<sup>41</sup> using a simulated annealing. The wave functions and the charge density were extended in plane waves using 80 Ry and 320 Ry energy-cutoff, respectively. The code used for the structural relaxation of spinel, red-pyrope and tsavorite was PARATEC, using energy cutoff of 90 Ry for spinel and 70 Ry for red-pyrope and tsavorite. In each case, the Brillouin zone was sampled at the  $\Gamma$  point.

## Non-periodic systems

### KMS3 glass

The numerical structure of the KMS3 glass (K<sub>2</sub>O-MgO-3SiO<sub>2</sub>) was obtained from the first-principles relaxation of a 112 atom cubic box (24Si, 64O, 8Mg and 16K), first generated by classical MD simulation. The MD simulation was performed using Born-Mayer-Huggins interatomic pair potentials and three-body terms to constrain the Si-O-Si and O-Si-O angles, using the parameters of Ref. [62, 63] for Si and O, the parameters of

<sup>40</sup>In order to compare directly the theoretical bond distances to those obtained by EXAFS spectroscopy, the initial slight underestimation of the lattice constant of the pure phases (systematic within LDA) was removed by rescaling the lattice parameter by 1.6%. This rescaling is homothetic and does not affect the reduced atomic positions.

<sup>41</sup>CPMD V3.7 Copyright IBM Corp 1990-2003, Copyright MPI fuer Festkoerperforschung Stuttgart 1997-2001. For more information see <http://www.cpmid.org>

Ref. [17] for Mg, and those of Ref. [88] for K.<sup>42</sup> The glass structure was obtained by quenching a relaxed liquid from 4000 K down to room temperature using two quench rates ( $10^{15}$  Ks<sup>-1</sup> from 4000 down to 1400 K and  $4 \times 10^{14}$  Ks<sup>-1</sup> down to 293 K). The first-principles relaxation was then performed using PARATEC and the pseudopotentials described in Table 1.15. Energy minimization was carried out at the  $\Gamma$  point of the Brillouin zone of the cubic cell (i.e., the MD simulation box) in the LDA approximation [51]. While the cell size was kept fixed ( $a=12.54$  Å), all the atomic positions were allowed to relax. Convergence was achieved for a 120 Ry plane-wave energy cutoff, the discrepancies in the atomic forces being lower than 0.3 mRy per Bohr radius unit.

The structural model so obtained was characterized using bond-valence theory following the procedure described in Ref. [191]. Among the 8 Mg distinct sites, 3 presents an Mg unusual environment, in total disagreement with the Pauling's second rule. Consequently, these 3 Mg sites were not considered in the calculation of the Mg *K*-edge spectrum of KMS3. The resulting theoretical spectrum to be compared to experiment is the mean average of 5 individual spectra, all shown in Fig. 1.10.

### The MbCO and MbCN proteins

Table 1.14 gives the structural characteristics of the Fe environment for the MbCO and MbCN clusters used to calculate the Fe *K* pre-edge structures (Sec. 1.4.3). These clusters were embedded in large cubic cell (35 Bohr $\times$ 35 Bohr $\times$ 35 Bohr) in such a way that Fe sits at the center, the  $N_p$  atoms lie along the *x* and *y* direction, and the  $N_{his}$  atom lies along the *z* direction.

Table 1.14: Structural characteristics of the local surrounding of Fe in the MbCO and MbCN clusters used for XANES calculation. Distances are in Å and angles in degrees.

MbCX	$\langle d_{Fe-N_p} \rangle$	$d_{Fe-N_{his}}$	$d_{Fe-C}$	$d_{C-X}$	$\alpha$	$\beta$	PDB code	Ref.	Fig.
MbCO	2.00	2.06	1.83	1.07	6	14	/	[152]	1.22
MbCN	2.04	2.08	1.92	1.11	4	13	2JHO	[10]	1.29

## A2- Pseudopotentials

All the pseudopotentials used for the calculations presented here are norm-conserving Troullier-Martins [218]. Their parameters are described in Table 1.15.

## A3- XANES calculation parameters

The computational details of the single-particle XANES calculations performed within plane-wave pseudopotential formalism and shown in this thesis are gathered in Table 1.16. The calculation of the absorption cross section comprises two steps: (i) the calculation of the self-consistent charge density of the supercell including a 1s core-hole on the absorbing atom, (ii) the calculation of the XANES spectrum (Eq. 1.15). All the reciprocal space integrations are performed using a Monkhorst-Pack *k*-point grid [160]. The charge density calculation can be done either in the local density approximation (LDA) or in the generalized gradient approximation (GGA), and can include spin polarization. The convergence parameters of a XANES calculation are: the energy cutoff of the plane wave basis set and the number of *k*-points in the Brillouin zone for step (i), the dimension of the Lanczos basis and, again, the number of *k*-points for step (ii). It should be noted that the number of computed Lanczos vectors depends on the value of the broadening parameter  $\gamma$  (Eq. 1.15), which can be energy-dependent (but constant across the Fermi level).

<sup>42</sup>In the case of the MgO pair, the value of the short distance repulsive term  $A_{ij}$  was slightly modified and set to  $0.23062 \cdot 10^{-8}$ .

Table 1.15: Parameterization used for the generation of the norm-conserving Troullier-Martins pseudopotentials. The core radii of the valence states are indicated in parentheses in Bohr units. The Mg and K pseudopotentials include non-linear core corrections. The asterisk indicates that the pseudopotential has been generated with only one 1s electron (absorbing atom).

Atom	At. No.	Valence states	Local part	used for
H	1	$1s^1(1.00)$	<i>s</i>	MbCN, MbCO
Be	4	$2s^{0.2}(2.00) 2p^0(2.00)$	<i>p</i>	emerald
B	5	$2s^2(1.80) 2p^1(1.80)$	<i>p</i>	grandidierite
C	6	$2s^2(1.50) 2p^{1.5}(1.50)$	<i>p</i>	MbCN, MbCO
N	7	$2s^2(1.45) 2p^3(1.45)$	<i>s</i>	MbCN, MbCO
O	8	$2s^2(1.45) 2p^4(1.45)$	<i>p</i>	all compounds
O*	8	$2s^2(1.40) 2p^4(1.40) 3d^0(1.40)$	<i>d</i>	q-GeO <sub>2</sub> , r-GeO <sub>2</sub> , K <sub>2</sub> Ge <sub>8</sub> O <sub>17</sub>
Mg	12	$3s^2(2.00) 3p^0(2.00) 3d^0(2.00)$	<i>d</i>	red spinel
Mg	12	$3s^{0.1}(2.00) 3p^0(2.00) 3d^0(2.00)$	<i>d</i>	diopside, enstatite, farringtonite, forsterite, grandidierite, spinel, pyrope
Mg*	12	$3s^{0.1}(2.00) 3p^0(2.00) 3d^0(2.00)$	<i>d</i>	diopside, enstatite, farringtonite, forsterite, grandidierite, spinel, pyrope
Al	13	$3s^2(2.00) 3p^0(2.00) 3d^0(2.00)$	<i>d</i>	spinel, red spinel, ruby, blue sapphire, pink sapphire, emerald, red pyrope, tsavorite
Al	13	$3s^2(2.00) 3p^{0.3}(2.00) 3d^{0.2}(2.00)$	<i>d</i>	corundum
Al*	13	$3s^2(2.00) 3p^{0.3}(2.00) 3d^{0.2}(2.00)$	<i>d</i>	corundum
Si	14	$3s^2(2.00) 3p^{1.3}(2.00) 3d^{0.2}(2.00)$	<i>d</i>	diopside, enstatite, forsterite, grandidierite, pyrope, red pyrope, tsavorite
Si	14	$3s^2(2.00) 3p^1(2.00) 3d^{0.5}(2.00)$	<i>d</i>	emerald
P	15	$3s^2(2.00) 3p^{1.8}(2.00) 3d^{0.2}(2.00)$	<i>d</i>	farringtonite
K	19	$3s^2(1.20) 3p^6(1.30) 3d^0(1.60)$	<i>s</i>	K <sub>2</sub> Ge <sub>8</sub> O <sub>17</sub> , KMS3
Ca	20	$3s^2(1.45) 3p^6(2.00) 3d^0(1.45)$	<i>d</i>	diopside, tsavorite
Ti	22	$3s^2(1.00) 3p^6(1.60) 3d^0(1.50)$	<i>s</i>	anatase, rutile
Ti*	22	$3s^2(1.00) 3p^6(1.60) 3d^0(1.50)$	<i>s</i>	anatase, rutile
Ti*	22	$3s^2(1.10) 3p^6(1.70) 3d^0(1.70)$	<i>d</i>	pink sapphire
V	23	$3s^2(1.00) 3p^6(1.60) 3d^2(1.50)$	<i>s</i>	tsavorite
Cr	24	$3s^2(1.00) 3p^6(1.70) 3d^3(1.70)$	<i>d</i>	emerald, ruby, red spinel, red pyrope
Fe*	26	$3s^2(1.00) 3p^6(1.20) 3d^6(1.20)$	<i>p</i>	MbCO, MbCN
Fe*	26	$3s^2(0.90) 3p^6(1.50) 3d^5(1.50)$	<i>d</i>	blue sapphire
Ge	32	$4s^2(1.70) 4p^{1.8}(2.10) 4d^{0.2}(3.00)$	<i>s</i>	q-GeO <sub>2</sub> , r-GeO <sub>2</sub> , K <sub>2</sub> Ge <sub>8</sub> O <sub>17</sub>

Table 1.16: Computational details of the XANES calculations presented in this report and performed using the plane-wave pseudopotential scheme described in Sec. 1.2.3. Upper part: periodic systems. Middle part: allochromatic minerals with 3d impurities. Lower part: non-periodic systems (molecules and glasses). All categories are listed in alphabetic order. In the case of non periodic systems (MbCO, MbCN and KMS3), the size of the supercell is given in Bohr radius cubed. In the case of spin-polarized calculation (Spin pol.), the value of  $S_{\text{total}}$  imposed to the supercell is given. PBE and CA refer to as the exchange and correlation density functional formulation of Perdew-Burke-Ernzerhof [179] and Ceperley-Alder [51], respectively. The broadening parameter  $\gamma$  (see Eq. 1.15) is constant in most cases, except when the value has an asterisk. In such cases, the indicated value is the one used across the Fermi level and in the pre-edge-region. QE means QUANTUM-ESPRESSO and implies the use of both PWSCF and XSPECTRA.

Compounds	$K$ edge	Supercell		Spin pol.	$E_{xc}$	Cut-off	$k$ -point grid		$\gamma$ (eV)	Code	Fig.
		Size	Nb of atoms				SCF	XANES			
anatase	Ti	3×3×1 tetragonal	108 atoms	none	GGA-PBE	90 Ry	1×1×1	4×4×4	0.47	QE	1.16
corundum	Al	2×2×1 hexagonal	120 atoms	none	LDA-CA	64 Ry	1×1×1	3×3×3	0.7	paraTEC	1.1
	Al	2×2×2 trigonal	80 atoms	none	GGA-PBE	80 Ry	1×1×1	4×4×4	0.7	QE	1.32
diopside	Mg	1×1×2 monoclinic	80 atoms	none	LDA-CA	60 Ry	2×2×2	4×4×4	0.5	paraTEC	1.2
enstatite	Mg	1×1×2 orthorhombic	160 atoms	none	LDA-CA	60 Ry	1×1×1	3×3×3	0.5	paraTEC	1.8
farringtonite	Mg	2×1×2 monoclinic	104 atoms	none	LDA-CA	60 Ry	2×2×2	3×3×3	0.5	paraTEC	1.8
forsterite	Mg	2×1×2 orthorhombic	112 atoms	none	LDA-CA	60 Ry	2×2×2	3×3×3	0.5	paraTEC	1.8
grandidierite	Mg	1×1×2 orthorhombic	120 atoms	none	LDA-CA	60 Ry	2×2×2	4×4×4	0.5	paraTEC	1.2
K <sub>2</sub> Ge <sub>8</sub> O <sub>17</sub>	O	1×1×1 orthorhombic	108 atoms	none	LDA-CA	70 Ry	1×1×1	2×2×2	0.5	paraTEC	1.6
pyrope	Mg	1×1×1 cubic	160 atoms	none	LDA-CA	60 Ry	2×2×2	4×4×4	0.5	paraTEC	1.8
q-GeO <sub>2</sub>	O	2×2×2 hexagonal	72 atoms	none	LDA-CA	70 Ry	1×1×1	3×3×3	0.5	paraTEC	1.6
r-GeO <sub>2</sub>	O	2×2×3 tetragonal	72 atoms	none	LDA-CA	70 Ry	1×1×1	3×3×3	0.5	paraTEC	
rutile	Ti	2×2×3 tetragonal	72 atoms	none	GGA-PBE	80 Ry	1×1×1	4×4×4	0.7	QE	1.15
spinel	Mg	2×2×2 trigonal	112 atoms	none	LDA-CA	60 Ry	2×2×2	4×4×4	0.5	paraTEC	1.2
emerald	Cr	1×1×1 hexagonal	58 atoms	3/2	LDA-CA	80 Ry	1×1×1	4×4×4	0.54*	paraTEC	1.27
red pyrope	Cr	1×1×1 cubic	160 atoms	3/2	LDA-CA	70 Ry	1×1×1	2×2×2	1.1	paraTEC	1.4
ruby	Cr	2×2×2 trigonal	80 atoms	3/2	LDA-CA	64 Ry	1×1×1	4×4×4	0.54*	paraTEC	1.3, 1.25, 1.26
blue sapphire	Fe	2×2×2 trigonal	80 atoms	5/2	LDA-CA	64 Ry	1×1×1	4×4×4	0.62*	paraTEC	1.3
pink sapphire	Ti	2×2×2 trigonal	80 atoms	1/2	LDA-CA	64 Ry	1×1×1	4×4×4	0.47*	paraTEC	1.3
red spinel	Cr	2×2×2 trigonal	112 atoms	3/2	LDA-CA	70 Ry	1×1×1	3×3×3	1.1	paraTEC	1.4
	Cr	2×2×2 trigonal	112 atoms	3/2	LDA-CA	70 Ry	1×1×1	3×3×3	0.54*	paraTEC	1.24
tsavorite	V	1×1×1 cubic	160 atoms	1	LDA-CA	90 Ry	1×1×1	4×4×4	0.5*	QE	1.4, 1.28
KMS3	Mg	23.7×23.7×23.7	112 atoms	none	LDA-CA	90 Ry	1×1×1	2×2×2	0.54	paraTEC	1.10
MbCN	Fe	35×35×35	48 atoms	1/2	GGA-PBE	90 Ry	1×1×1	4×4×4	0.625	QE	1.29
MbCO	Fe	35×35×35	48 atoms	none	GGA-PBE	90 Ry	1×1×1	4×4×4	0.625	QE	1.22



# Bibliography

- [1] J. A., Aramburu, P. Garcia-Fernandez, J. M. García-Lastra, M. T. Barriuso, and M. Moreno. Internal electric fields and color shift in Cr<sup>3+</sup>-based gemstones. *Phys. Rev. B*, 85:245118, 2012.
- [2] G. Artioli A. Pavese and M. Prencipe. X-ray single-crystal diffraction study of pyrope in the temperature range 30-973 K. *Am. Mineral.*, 80:457–464, 1995.
- [3] H. Agren, V. Carravetta, O. Vhatras, and L. G. M. Pettersson. Direct, atomic orbital, static exchange calculations of photoabsorption spectra of large molecules and clusters. *Chem. Phys. Lett.*, 222:75–81, 1994.
- [4] A. L. Ankudinov, A. I. Nesvizhskii, and J. J. Rehr. Dynamic screening effects in x-ray absorption spectra. *Phys. Rev. B*, 67:115120, 2003.
- [5] A. L. Ankudinov, B. Ravel, J. J. Rehr, and S. D. Conradson. Real-space multiple-scattering calculation and interpretation of x-ray-absorption near-edge structure. *Phys. Rev. B*, 58:7565–7576, 1998.
- [6] A. L. Ankudinov and J. J. Rehr. Relativistic calculations of spin-dependent x-ray-absorption spectra. *Phys. Rev. B*, 56:R1712–R1716, 1997.
- [7] A. L. Ankudinov and J. J. Rehr. Theory of solid-state contributions to the x-ray elastic scattering amplitude. *Phys. Rev. B*, 62:2437–2445, 2000.
- [8] A. L. Ankudinov and J. J. Rehr. Nonspherical potential, vibronic and local field effects in X-ray absorption. *Phys. Scr.*, T115:24–27, 2005.
- [9] V. N. Antonov, B. N. Harmon, and A. N. Yaresko. Electronic structure and x-ray magnetic circular dichroism in Cu<sub>3</sub>Au-type transition metal platinum alloys. *Phys. Rev. B*, 64:024402, 2001.
- [10] A. Arcovito, M. Benfatto, M. Cianci, S. S. Hasnain, K. Nienhaus, G. U. Nienhaus, C. Savino, R. W. Strange, B. Vallone, and S. Della Longa. X-ray structure analysis of a metalloprotein with enhanced active-site resolution using in situ x-ray absorption near edge structure spectroscopy. *PNAS*, 104:6211–6216, 2007.
- [11] M. Arfaoui. *Étude structurale et électronique des sites de fixation de bio-molécules par modélisation ab-initio de spectres d'absorption des rayons X*. PhD thesis, Université Pierre et Marie Curie, Paris 6, 2008.
- [12] M.-A. Arrio, S. Rossano, Ch. Brouder, L. Galois L, and G. Calas. Calculation of multipole transitions at the Fe *K* pre-edge through *p-d* hybridization in the Ligand Field Multiplet model. *Europhys. Lett.*, 51:454–460, 2000.
- [13] R. Bacewicz, A. Wolska, K. Lawniczak-Jablonska, and Ph. Saintavit. X-ray absorption near edge structure of CuInSe<sub>2</sub> crystals. *J. Phys.: Condens. Matter*, 12:7371–7379, 2000.
- [14] E. Balan, J. P. R. de Villiers, S. G. Eeckhout, P. Glatzel, M. J. Toplis, E. Fritsch, T. Allard, L. Galois, and G. Calas. The oxidation state of vanadium in titanomagnetite from layered basic intrusions. *Amer. Mineral.*, 91:953–956, 2006.
- [15] W. H. Baur and A. A. Khan. Rutile-type compounds. IV. SiO<sub>2</sub>, GeO<sub>2</sub> and a comparison with other rutile-type structures. *Acta Crystallogr.*, B 27:2133–2139, 1971.
- [16] H. Bayer. Zur theorie der spin-gitterrelaxation in molekiilkristallen. *Z. Physik*, 130:227, 1951.
- [17] D. K. Belashchenko. Computer simulation of non-crystalline oxides MeO and Me<sub>2</sub>O<sub>3</sub>. *J. Non-Cryst. Solids*, 205-207:212–215, 1996.
- [18] L. X. Benedict and E. L. Shirley. *Ab initio* calculation of  $\epsilon_2(\omega)$  including electron-hole interaction: Application to GaN and CaF<sub>2</sub>. *Phys. Rev. B*, 59:5441–5451, 1999.
- [19] M. Benfatto, S. Della Longa, and C. R. Natoli. The MXAN procedure: a new method for analysing the XANES spectra of metalloproteins to obtain structural quantitative information. *J. Synchrotron Rad.*, 10:51–57, 2003.
- [20] K. Benzerara, N. Menguy, F. Guyot, Ch. Vanni, and Ph. Gillet. TEM study of a silicatecarbonatemicrobe interface prepared by focused ion beam milling. *Geochim. Cosmochim. Acta*, 69:1413–1422, 2005.

- [21] A. J. Berry, G. M. Yaxley, A. B. Woodland, and G. J. Foran. A XANES calibration for determining the oxidation state of iron in mantle garnet. *Chem. Geol.*, 278:31–37, 2010.
- [22] H. Bethe. Zur theorie des durchgangs schneller korpuskularstrahlen durch materie. *Ann. Phys.*, 397:325–400, 1930.
- [23] P. Blaha, K. Schwarz, P. Sorantin, and S. B. Trickey. Full-potential, linearized augmented plane-wave programs for crystalline systems. *Comput. Phys. Commun.*, 59:399, 1990.
- [24] P. E. Blöchl. Projector augmented-wave method. *Phys. Rev. B*, 50:17953–17979, 1994.
- [25] C. Bonhomme, C. Gervais, C. Coelho, F. Pourpoint, T. Azaïs, L. Bonhomme-Coury, F. Babonneau, G. Jacob, M. Ferrari, D. Canet, J. R. Yates, C. J. Pickard, S. A. Joyce, F. Mauri, and D. Massiot. New perspectives in the PAW/GIPAW approach:  $J_{P-O-Si}$  coupling constants, antisymmetric parts of shift tensors and NQR predictions. *Magn. Reson. Chem.*, 48:S86–S102, 2010.
- [26] A. Bordage. *Vanadium spectroscopic properties and electronic structure in complex materials: Geological and technological implications*. PhD thesis, Université Pierre et Marie Curie, Paris 6, 2009.
- [27] A. Bordage, E. Balan, J. P. R. de Villiers, R. Cromarty, A. Juhin, C. Carvallo, G. Calas, P. V. Sunder Raju, and P. Glatzel. V oxidation state in Fe-Ti oxides by high-energy resolution fluorescence-detected X-ray absorption spectroscopy. *Phys Chem Minerals*, 38:449–458, 2011.
- [28] A. Bordage, Ch. Brouder, E. Balan, D. Cabaret, A. Juhin, M.-A. Arrio, Ph. Saintavit, G. Calas, and P. Glatzel. Electronic structure and local environment of substitutional  $V^{3+}$  in grossular garnet  $Ca_3Al_2(SiO_4)_3$ :  $K$ -edge x-ray absorption spectroscopy and first-principles modeling. *Amer. Mineral.*, 95:1161–1171, 2010.
- [29] A. Bordage, S. Rossano, A. Heinrich Horn, and Y. Fuchs. Site partitioning of  $Cr^{3+}$  in the trichroic alexandrite  $BeAl_2O_4:Cr^{3+}$  crystal: contribution from x-ray absorption spectroscopy. *J. Phys.: Condens. Matter*, 24:225401, 2012.
- [30] D. Boström. Single-crystal X-ray diffraction studies of synthetic Ni-Mg olivine solid solutions. *Am. Mineral.*, 72:965–972, 1987.
- [31] Ch. Brouder. Angular dependence of x-ray absorption spectra. *J. Phys.: Condens. Matter*, 2:701–738, 1990.
- [32] Ch. Brouder, D. Cabaret, A. Juhin, and Ph. Saintavit. Effect of atomic vibrations on the x-ray absorption spectra at the  $K$  edge of Al in  $\alpha$ - $Al_2O_3$  and of Ti in  $TiO_2$  rutile. *Phys. Rev. B*, 81:115125, 2010.
- [33] Ch. Brouder, D. Cabaret, Ph. Saintavit, A. Kiratisin, J. Goulon, and A. Rogalev. X-ray absorption spectroscopy of impurities in single-crystals. In *Radiation Effects and Defects in Solids*, volume 155, pages 89–93, 2001. Proc. of the 14th International Conference on Defects in Insulating Materials, Johannesburg-Midrand (South-Africa), April 2000.
- [34] O. Bunau and Y. Joly. Self-consistent aspects of x-ray absorption calculations. *J. Phys.: Condens. Matter*, 21:345501, 2009.
- [35] O. Bunau and Y. Joly. Full potential x-ray absorption calculations using time dependent density functional theory. *J. Phys.: Condens. Matter*, 24:215502, 2012.
- [36] O. Bunau and Y. Joly. Time-dependent density functional theory applied to x-ray absorption spectroscopy. *Phys. Rev. B*, 85:155121, 2012.
- [37] R. G. Burns. *Mineralogical Applications of Crystal Field Theory*, volume 5 of *Cambridge Topics in Mineral Physics and Chemistry*. Cambridge University Press, 2nd edition, 1993.
- [38] D. Cabaret, A. Bordage, A. Juhin, M. Arfaoui, and E. Gaudry. First-principles calculations of x-ray absorption spectra at the  $K$ -edge of 3d transition metals: an electronic structure analysis of the pre-edge. *Phys. Chem. Chem. Phys.*, 12:5619–5633, 2010.
- [39] D. Cabaret and Ch. Brouder. Origin of the pre-edge structure at the Al  $K$ -edge: the role of atomic vibrations. *J. Phys.: Conf. Ser.*, 190:012003, 2009. Proc. of the XAFS-14 conference, Camerino, Italie, July 2009.
- [40] D. Cabaret, Ch. Brouder, M. A. Arrio, Ph. Saintavit, Y. Joly, A. Rogalev, and J. Goulon. Natural linear dichroism in pyrite ( $FeS_2$ ): experiments and calculations. *J. Synchrotron Rad.*, 8:460–462, 2001. Proc. of the XAFS-11 conference, Ako (Japan), July 2000.
- [41] D. Cabaret, N. Emery, Ch. Bellin, C. Hérold, Ph. Lagrange, F. Wilhelm, A. Rogalev, and G. Loupias. Nature of empty states in superconducting  $CaC_6$  and related Li-Ca ternary graphite intercalation compounds, using polarized x-ray absorption near-edge structure at the Ca  $K$  edge. *Submitted to Phys. Rev. B*, 2012.

- [42] D. Cabaret, E. Gaudry, M. Taillefumier, Ph. Sainctavit, and F. Mauri. XANES calculation with an efficient “non muffin-tin” method: application to the angular dependence of the Al  $K$ -edge in corundum. *Phys. Scr.*, T115:131–133, 2005. Proc. of the XAFS-12 conference, Malmö, Sweden, June 2003.
- [43] D. Cabaret, M. Le Grand, A. Ramos, A.-M. Flank, S. Rossano, L. Galois, G. Calas, and D. Ghaleb. Medium range structure in borosilicate glasses from Si  $K$ -edge XANES: a combined approach based on multiple scattering and molecular dynamics calculations. *J. Non-Cryst. Solids*, 289:1–8, 2001.
- [44] D. Cabaret, Y. Joly, H. Renevier, and C. R. Natoli. Pre-edge structure analysis of Ti  $K$ -edge polarized x-ray absorption spectra in  $\text{TiO}_2$  by full-potential XANES calculations. *J. Synchrotron Rad.*, 6:258–260, 1999. Proc. of the XAFS-10 conference, Chicago (USA), August 1998.
- [45] D. Cabaret, F. Mauri, and G. S. Henderson. Oxygen  $K$ -edge XANES of germanates investigated using first-principles calculations. *Phys. Rev. B*, 75:184205, 2007.
- [46] D. Cabaret, Ph. Sainctavit, Ph. Ildefonse, and A.-M. Flank. Full multiple-scattering calculations on silicates and oxides at the Al  $K$  edge. *J. Phys.: Condens. Matter*, 8:3691–3704, 1996.
- [47] D. Cabaret, Ph. Sainctavit, Ph. Ildefonse, and A.-M. Flank. Full multiple scattering calculations of the X-ray absorption near edge structure at the magnesium  $K$ -edge in pyroxene. *Amer. Mineral.*, 83:300–304, 1998.
- [48] M. Calandra, J.-P. Rueff, C. Gougoussis, D. Céolin, M. Gorgoi, S. Benedetti, P. Torelli, A. Shukla, D. Chandesaris, and Ch. Brouder.  $k$ -edge x-ray absorption spectra in transition metal oxides beyond the single-particle approximation: shake-up many body effects. *Phys. Rev. B*, 86:165102, 2012.
- [49] M. Cameron, S. Sueno, C. T. Prewitt, and J. J. Papike. High-temperature crystal chemistry of acmite, diopside, hedenbergite, jadeite, spodumene and ureyite. *Am. Mineral.*, 58:594–618, 1973.
- [50] R. Car and M. Parrinello. Unified approach for molecular dynamics and density-functional theory. *Phys. Rev. Lett.*, 55:2471–2474, 1985.
- [51] D. M. Ceperley and B. J. Alder. Ground state of the electron gas by a stochastic method. *Phys. Rev. Lett.*, 45:566–569, 1980.
- [52] M. Cococcioni and S. de Gironcoli. Linear response to the calculation of the effective interaction parameters in the LDA+ $U$  method. *Phys. Rev. B*, 71:035105, 2005.
- [53] M. T. Czyżyk, R. Potze, and G. A. Sawatzky. Band-theory description of high-energy spectroscopy and the electronic structure of  $\text{LiCoO}_2$ . *Phys. Rev. B*, 46:3729–3735, 1992.
- [54] R. de Francesco, M. Stener, M. Causà, D. Toiliac, and G. Fronzoni. Time dependent density functional investigation of the near-edge absorption spectra of  $\text{V}_2\text{O}_5$ . *Phys. Chem. Chem. Phys.*, 8:4300–4310, 2006.
- [55] F. de Groot, G. Vankò, and P. Glatzel. The  $1s$  x-ray absorption pre-edge structures in transition metal oxides. *J. Phys.: Condens. Matter*, 21:104207(7pp), 2009.
- [56] F. M. F. de Groot. Novel techniques and approaches to unravel the nature of X-ray absorption spectra. In B. Hedman and P. Pianetta, editors, *X-ray Absorption Fine Structure—XAFS13*, volume 882 of *AIP conference proceedings*, pages 37–43, 2007.
- [57] F. M. F. de Groot, J. Faber, J. J. M. Michiels, M. T. Czyżyk, M. Abbate, and J. C. Fuggle. Oxygen  $1s$  x-ray absorption of tetravalent titanium oxides: A comparison with single-particle calculations. *Phys. Rev. B*, 48:2074–2080, 1993.
- [58] S. de Wispelaere, D. Cabaret, C. Levelut, S. Rossano, A.-M. Flank, Ph. Parent, and F. Farges. Na-, Al-, and Si  $K$ -edge XANES study of sodium silicate and sodium aluminosilicate glasses: influence of the glass surface. *Chem. Geol.*, 213(1-3):63–70, 2004.
- [59] S. DeBeer George, T. Petrenko, and F. Neese. Prediction of iron  $K$ -edge absorption spectra using time-dependent density functional theory. *J. Phys. Chem. A*, 112:12936–12943, 2008.
- [60] J. L. Dehmer and D. Dill. Shape resonances in  $K$ -shell photoionization of diatomic molecules. *Phys. Rev. Lett.*, 35:213–215, 1975.
- [61] J. L. Dehmer and D. Dill. Molecular effects on inner shell photoabsorption.  $K$  shell spectrum of  $\text{N}_2$ . *J. Phys. Chem.*, 65:5327–5334, 1976.
- [62] J.-M. Delaie and D. Ghaleb. Molecular dynamics simulation of a nuclear waste glass matrix. *Mater. Sci. Eng. B*, 37:232–236, 1996.
- [63] J.-M. Delaie and D. Ghaleb. Molecular dynamics simulation of  $\text{SiO}_2+\text{B}_2\text{O}_3+\text{Na}_2\text{O}+\text{ZrO}_2$  glass. *J. Non-Cryst. Solids*, 195:239–248, 1996.

- [64] S. Della Longa, A. Arcovito, B. Vallone, A. Congiu Castellano, R. Kahn, J. Vicat, Y. Soldo, and J.-L. Hazemann. Polarized X-ray absorption spectroscopy of the low-temperature photoproduct of carbomonoxy-myoglobin. *J. Synchrotron Rad.*, 6:1138–1147, 1999.
- [65] S. Della Longa, A. Soldatov, M. Pompa, and A. Bianconi. Atomic and electronic structure probed by X-ray absorption spectroscopy: full multiple scattering analysis with the G4XANES package. *Comput. Mat. Sci.*, 4:199–210, 1995.
- [66] F. Di Benedetto, F. D'Acapito, G. Fornaciai, M. Innocenti, G. Montegrossi, L. A. Pardi, S. Tesi, and M. Romanelli. A Fe *K*-edge XAS study of amethyst. *Phys Chem Minerals*, 37:283–289, 2010.
- [67] D. B. Dingwell. Relaxation in silicate melts: some applications. *Rev. Mineral.*, 32:21–66, 1995.
- [68] D. B. Dingwell, E. Paris, F. Seifert, A. Mottana, and C. Romano. X-ray absorption study of Ti-bearing silicate glasses. *Phys Chem Minerals*, 21:501–509, 1994.
- [69] W. Duan, R. M. Wentzcovitch, and K. T. Thomson. First-principles study of high-pressure alumina polymorphs. *Phys. Rev. B*, 57:10363:10369, 1998.
- [70] O. Durmeyer, E. Beaupaire, J.-P. Kappler, Ch. Brouder, and F. Baudelet. Temperature dependence of the pre-edge structure in the Ti *K*-edge x-ray absorption spectrum of rutile. *J. Phys.: Condens. Matter*, 22:125504, 2010.
- [71] J. Enkovaara, C. Rostgaard, J. J. Mortensen, J. Chen, M. Dulak, L. Ferrighi, J. Gavnholt, C. Glinsvad, V. Haikola, H. A. Hansen, H. H. Kristoffersen, M. Kuisma, A. H. Larsen, L. Lehtovaara, M. Ljungberg O. Lopez-Acevedo, P. G. Moses, J. Ojanen, T. Olsen, V. Petzold, N. A. Romero, J. Stausholm-Møller, M. Strange, G. A. Tritsarlis, M. Vanin, M. Walter, B. Hammer, H. Häkkinen, G. K. H. Madsen, R. M. Nieminen, J. K. Nørskov, M. Puska, T. T. Rantala, J. Schiøtz, K. S. Thygesen, and K. W. Jacobsen. Electronic structure calculations with GPAW: a real-space implementation of the projector augmented-wave method. *J. Phys.: Condens. Matter*, 22:253202, 2010.
- [72] I. Errea, B. Rousseau, and A. Bergara. Anharmonic stabilization of the high-pressure simple cubic phase of calcium. *Phys. Rev. Lett.*, 106:165501, 2011.
- [73] F. Farges. *Ab initio* and experimental pre-edge investigations of the Mn *K*-edge XANES in oxide-type materials. *Phys. Rev. B*, 71:155109, 2005.
- [74] F. Farges. Chromium speciation in oxide-type compounds: application to minerals, gems, aqueous solutions and silicate glasses. *Phys Chem Minerals*, 36:463–481, 2009.
- [75] F. Farges, G. E. Brown Jr., A. Navrotsky, H. Gan, and J. J. Rehr. Coordination chemistry of Ti (IV) in silicate glasses and melts: II. glasses at ambient temperature and pressure. *Geochim. Cosmochim. Acta*, 60:3039–3053, 1996.
- [76] F. Farges, G. E. Brown Jr., and J. J. Rehr. Coordination chemistry of Ti (IV) in silicate glasses and melts: I. XAFS study of titanium coordination in oxide model compounds. *Geochim. Cosmochim. Acta*, 60:3023–3038, 1996.
- [77] F. Farges, G. E. Brown Jr., and J. J. Rehr. Ti *K*-edge XANES studies of Ti coordination and disorder in oxide compounds: Comparison between theory and experiment. *Phys. Rev. B*, 56:1809–1819, 1997.
- [78] F. Farges, Y. Lefrère, S. Rossano, A. Berthureau, G. Calas, and G. E. Brown Jr. The effect of redox state on the local structural environment of iron in silicate glasses: a combined XAFS spectroscopy, molecular dynamics, and bond valence study. *J. Non-Cryst. Solids*, 344:176–188, 2004.
- [79] P. Le Fèvre, H. Magnan, D. Chandèsris, J. Jupille, S. Bourgeois, A. Barbier, W. Drube, T. Uozumi, and A. Kotani. Hard X-ray resonant electronic spectroscopy in transition metal oxides. *Nucl. Instr. Meth. Phys. Res. A*, 547:176–186, 2005.
- [80] A. Filipponi, A. Di Cicco, and C. R. Natoli. X-ray-absorption spectroscopy and *n*-body distribution functions in condensed matter. I. Theory. *Phys. Rev. B*, 52:15122–15134, 1995.
- [81] A. Filipponi, A. Di Cicco, T. A. Tyson, and C. R. Natoli. *Ab initio* modeling of x-ray absorption spectra. *Solid State Comm.*, 78:265–268, 1991.
- [82] M. E. Fleet, S. Muthupari, M. Kasrai, and S. Prabakar. Sixfold coordinated Si in alkali and alkali-CaO silicophosphate glasses by Si *K*-edge XANES spectroscopy. *J. Non-cryst. Solids*, 220:85–92, 1997.
- [83] D. L. Foulis, R. F. Pettifer, C. R. Natoli, and M. Benfatto. Full-potential scattered-wave calculations for molecules and clusters: Fundamental tests of the method. *Phys. Rev. A*, 41:6922–6927, 1990.

- [84] L. Galois, G. Calas, and M.-A. Arrio. High-resolution XANES spectra of iron in minerals and glasses: structural information from the pre-edge region. *Chemical Geol.*, 174:307–319, 2001. 6th International Silicate Melt Workshop.
- [85] S.-P. Gao, C. J. Pickard, M. C. Payne, J. Zhu, and J. Yuan. Theory of core-hole effects in 1s core-level spectroscopy of the first-row elements. *Phys. Rev. B*, 77:115122, 2008.
- [86] J. M. García-Lastra, M. T. Barriuso, J. A. Aramburu, and M. Moreno. Origin of the different color of ruby and emerald. *Phys. Rev. B*, 72:113104, 2005.
- [87] J. M. García-Lastra, M. T. Barriuso, J. A. Aramburu, and M. Moreno. Microscopic origin of the different colors displayed by  $\text{MgAl}_2\text{O}_4:\text{Cr}^{3+}$  and emerald. *Phys. Rev. B*, 78:085117, 2008.
- [88] S. H. Garofalini. Behavior of atoms at the surface of  $\text{K}_2\text{O}-3\text{SiO}_2$  glass. A molecular dynamics simulation. *J. Am. Ceram. Soc.*, 67:133–136, 1984.
- [89] E. Gaudry. *Structure locale autour des impuretés dans les gemmes, étudiée par spectroscopie et calculs ab initio*. PhD thesis, Université Pierre et Marie Curie, Paris 6, 2004.
- [90] E. Gaudry, D. Cabaret, Ch. Brouder, I. Letard, A. Rogalev, F. Wilhelm, N. Jaouen, and Ph. Sainctavit. Relaxations around the substitutional chromium site in emerald: X-ray absorption experiments and density functional calculations. *Phys. Rev. B*, 76:094110, 2007.
- [91] E. Gaudry, D. Cabaret, Ph. Sainctavit, Ch. Brouder, F. Mauri, J. Goulon, and A. Rogalev. Structural relaxations around Ti, Cr and Fe impurities in  $\alpha\text{-Al}_2\text{O}_3$  probed by x-ray absorption near edge structure combined with first-principles calculations. *J. Phys.: Condens. Matter*, 17:5467–5480, 2005.
- [92] E. Gaudry, D. Cabaret, Ph. Sainctavit, Ch. Brouder, F. Mauri, A. Rogalev, and J. Goulon. *Ab initio* calculation of the Cr  $K$  edge in  $\alpha\text{-Al}_2\text{O}_3:\text{Cr}^{3+}$ . *Phys. Scr.*, T115:191–192, 2005. Proc. of the XAFS-12 conference, Malmö, Sweden, June 2003.
- [93] E. Gaudry, A. Kiratisin, Ph. Sainctavit, Ch. Brouder, F. Mauri, A. Ramos, A. Rogalev, and J. Goulon. Structural and electronic relaxations around substitutional  $\text{Cr}^{3+}$  and  $\text{Fe}^{3+}$  ions in corundum. *Phys. Rev. B*, 67:094108, 2003.
- [94] C. A. Geiger and T. Armbruster.  $\text{Mn}_3\text{Al}_2\text{Si}_3\text{O}_{12}$  spessartine and  $\text{Ca}_3\text{Al}_2\text{Si}_3\text{O}_{12}$  grossular garnet: Structural dynamic and thermodynamic properties. *Amer. Mineral.*, 82:740–747, 1997.
- [95] P. Giannozzi, S. Baroni, N. Bonini, M. Calandra, R. Car, C. Cavazzoni, D. Ceresoli, G. L. Chiarotti, M. Cococcioni, I. Dabo, A. Dal Corso, S. de Gironcoli, S. Fabris, G. Fratesi, R. Gebauer, U. Gerstmann, Ch. Gougoussis, A. Kokalj, M. Lazzeri, L. Martin-Samos, N. Marzari, F. Mauri, R. Mazzarello, S. Paolini, A. Pasquarello, L. Paulatto, C. Sbraccia, S. Scandolo, G. Sclauzero, A. P. Seitsonen, A. Smogunov, P. Umari, and R. M. Wentzcovitch. Quantum espresso: a modular and open-source software project for quantum simulations of materials. *Journal of Physics: Condensed Matter*, 21(39):395502 (19pp), 2009.
- [96] P. Glatzel, M. Sikora, and M. Fernandez-García. Resonant x-ray spectroscopy to study  $K$  absorption pre-edges in 3d transition metal compounds. *Eur. Phys. J. Special Topics*, 169:207–214, 2009.
- [97] J. Glinnemann, H. King, H. Schulz, T. Hahn, S. J. Laplaca, and F. Dacol. Crystal-structures of the low-temperature quartz-type phases of  $\text{SiO}_2$  and  $\text{GeO}_2$  at elevated pressure. *Z. Kristallogr.*, 198:177–212, 1992.
- [98] C. Gougoussis, M. Calandra, A. P. Seitsonen, C. Brouder, A. Shukla, and F. Mauri. Intrinsic charge transfer gap in NiO from Ni  $K$ -edge x-ray absorption spectroscopy. *Phys. Rev. B*, 79:045118, 2009.
- [99] C. Gougoussis, M. Calandra, A. P. Seitsonen, and F. Mauri. First-principles calculations of x-ray absorption in a scheme based on ultra-soft pseudopotentials: From  $\alpha$ -quartz to high- $T_c$  compounds. *Phys. Rev. B*, 80:075102, 2009.
- [100] C. Gougoussis, J.-P. Rueff, M. Calandra, M. d’Astuto, I. Jarrige, H. Ishii, A. Shukla, I. Yamada, M. Azuma, and M. Takano. Multiple pre-edge structures in Cu  $K$ -edge x-ray absorption spectra of high- $T_c$  cuprates revealed by high-resolution x-ray absorption spectroscopy. *Phys. Rev. B*, 81:224519, 2010.
- [101] Ch. Gougoussis. *Excitations électroniques et magnétisme des matériaux : calcul ab initio de l’absorption X et du dichroïsme circulaire magnétique au seuil K*. PhD thesis, Université Pierre et Marie Curie, Paris 6, 2004.
- [102] U. Halenius, G. B. Andreozzi, and H. Skogby. Structural relaxation around  $\text{Cr}^{3+}$  and the red-green color change in the spinel (sensu stricto)-magnesiochromite ( $\text{MgAl}_2\text{O}_4\text{-MgCr}_2\text{O}_4$ ) and gahnite-zincochromite ( $\text{ZnAl}_2\text{O}_4\text{-ZnCr}_2\text{O}_4$ ) solid-solution series. *Am. Mineral.*, 95:456–462, 2010.

- [103] B. Harbrecht, J. Kushauer, and H.-J. Weber.  $K_2Ge_8O_{17}$ : structure determination, optical properties, phase transition. *Eur. J. Solid State Inorg. Chem.*, 27:831–843, 1990.
- [104] M. Haruta, H. Kurata, H. Komatsu, Y. Shimakawa, and S. Isoda. Site-resolved oxygen  $K$ -edge ELNES of the layered double perovskite  $La_2CuSnO_6$ . *Phys. Rev. B*, 80:165123, 2009.
- [105] K. Hatada, K. Hayakawa, M. Benfatto, and C. R. Natoli. Full-potential multiple scattering for x-ray spectroscopies. *Phys. Rev. B*, 76:060102, 2007.
- [106] K. Hatada, K. Hayakawa, M. Benfatto, and C. R. Natoli. Full-potential multiple scattering theory with space-filling cells for bound and continuum states. *J. Phys.: Condens. Matter*, 22:185501, 2010.
- [107] R. M. Hawthorne and J. Ito. Synthesis and crystal-structure refinement of transition-metal orthopyroxenes I: Orthoenstatite and (Mg, Mn, Co) orthopyroxene. *Can. Mineral.*, 15:321–338, 1977.
- [108] R. Haydock. The recursive solution of the Schrödinger equation. *Solid State Physics*, 35:215–294, 1980.
- [109] R. Haydock, V. Heine, and M. J. Kelly. Electronic structure based on the local atomic environment for tight-binding bands. *J. Phys. C: Solid State Phys.*, 5:2845–2858, 1972.
- [110] R. Haydock, V. Heine, and M. J. Kelly. Electronic structure based on the local atomic environment for tight-binding bands: II. *J. Phys. C: Solid State Phys.*, 8:2591–2605, 1975.
- [111] R. M. Hazen and L. W. Finger. High-pressure crystal chemistry of andradite and pyrope: Revised procedures for high-pressure diffraction experiments. *Am. Mineral.*, 74:352–359, 1989.
- [112] C. Hébert. Practical aspects of running the WIEN2K code for electron spectroscopy. *Micron*, 38:12–28, 2007.
- [113] L. Hedin. New method for calculating the one-particle green's function with application to the electron-gas problem. *Phys. Rev.*, 139:A796–A823, 1965.
- [114] G. S. Henderson, X. Liu, and M. E. Fleet. An O  $K$ -edge X-ray absorption study of Ti-silicate glasses. *Mineral. Mag.*, 67:597–607, 2003.
- [115] C. J. Howard, T. M. Sabine, and F. Dickson. Structural and thermal parameters for rutile and anatase. *Acta Cryst.*, B47:462–468, 1991.
- [116] Ph. Ildefonse, D. Cabaret, Ph. Saintavit, G. Calas, and A.-M. Flank. Local aluminium environment in Earth's surface minerals. *Phys Chem Minerals*, 25:112–121, 1998.
- [117] Ph. Ildefonse, G. Calas, A.-M. Flank, and P. Lagarde. Low  $Z$  elements (Mg, Al, and Si)  $K$ -edge X-ray absorption spectroscopy in minerals and disordered systems. *Nucl. Instr. and Meth. B*, 97:172–175, 1995.
- [118] D. N. Jayawardane, Ch. J. Pickard, L. M. Brown, and M. C. Payne. Cubic boron nitride: Experimental and theoretical energy-loss near-edge structure. *Phys. Rev. B*, 64:115107, 2001.
- [119] Y. Joly. X-ray absorption near edge structure calculations beyond the muffin-tin approximation. *Phys. Rev. B*, 63:125120–125129, 2001.
- [120] Y. Joly, D. Cabaret, H. Renevier, and C. R. Natoli. Electron population analysis by full potential x-ray absorption simulations. *Phys. Rev. Lett.*, 82:2398, 1999.
- [121] K. Jorissen. *The ab initio calculation of relativistic electron energy loss spectra*. PhD thesis, Universiteit Antwerpen, Belgium, 2007.
- [122] K. Jorissen, J. J. Rehr, and J. Verbeeck. Multiple scattering calculations of relativistic electron energy loss spectra. *Phys. Rev. B*, 81:155108, 2010.
- [123] A. Juhin. *Propriétés électroniques et structurales du chrome en impureté dans les cristaux. Approche expérimentale et théorique*. PhD thesis, Université Pierre et Marie Curie, Paris 6, 2008.
- [124] A. Juhin, Ch. Brouder, M.-A. Arrio, D. Cabaret, Ph. Saintavit, E. Balan, A. Bordage, A. P. Seitsonen, G. Calas, S. G. Eeckhout, and P. Glatzel. X-ray linear dichroism in cubic compounds: the case of  $Cr^{3+}$  in  $MgAl_2O_4$ . *Phys. Rev. B*, 78:195103, 2008.
- [125] A. Juhin, G. Calas, D. Cabaret, L. Galois, and J.-L. Hazemann. Structural relaxation around substitutional  $Cr^{3+}$  in  $MgAl_2O_4$ . *Phys. Rev. B*, 76:054105, 2007.
- [126] A. Juhin, G. Calas, D. Cabaret, L. Galois, and J.-L. Hazemann. Structural relaxation around substitutional  $Cr^{3+}$  in pyrope garnet. *Amer. Mineral.*, 93:800–805, 2008.
- [127] A. Juhin, F.M.F. de Groot, G. Vankó, M. Clandra, and Ch. Brouder. Angular dependence of core hole screening in  $LiCoO_2$ : A DFT+ $U$  calculation of the oxygen and cobalt  $K$ -edge x-ray absorption spectra. *Phys. Rev. B*, 81:115115, 2010.

- [128] G. S. Kachalova, A. N. Popov, and H. D. Bartunik. A steric mechanism for inhibition of CO binding heme to proteins. *Science*, 284:473–476, 1999.
- [129] J. J. Kas, A. P. Sorini, M. P. Prange, L. W. Cambell, J. A. Soininen, and J. J. Rehr. Many-pole model of inelastic losses in x-ray absorption spectra. *Phys. Rev. B*, 76:195116, 2007.
- [130] J. J. Kas, J. Vinson, N. Trcera, D. Cabaret, E. L. Shirley, and J. J. Rehr. Many-pole model of inelastic losses applied to calculations of XANES. *J. Phys.: Conf. Ser.*, 190:012009, 2009. Proc. of the XAFS-14 conference, Camerino, Italie, July 2009.
- [131] V. J. Keast, A. J. Scott, R. Brydson, D. B. Williams, and J. Bruley. Electron energy-loss near-edge structure - a tool for the investigation of electronic structure on the nanometre scale. *J. Microsc.*, 203:135–175, 2001.
- [132] A. Kokalj. Computer graphics and graphical user interfaces as tools in simulations of matter at the atomic scale. *Comp. Mater. Sci.*, 28:155–168, 2003. Code available from <http://www.xcrysden.org/>.
- [133] J. Kokubun, K. Ishida, D. Cabaret, F. Mauri, R. V. Vedrinskii, V. L. Kraizman, A. A. Novakovitch, E. V. Krivitskii, and V. E. Dmitrienko. Resonant diffraction in FeS<sub>2</sub>: Determination of the x-ray polarization anisotropy of iron atoms. *Phys. Rev. B*, 69:245103, 2004.
- [134] J. Kokubun, K. Ishida, D. Cabaret, R. V. Vedrinskii, V. L. Kraizman, A. A. Novakovich, E. V. Krivitskii, and V. E. Dmitrienko. Real and imaginary parts of the anisotropic atomic factor near the Fe *K*-edge: comparison between two theories and experiment for pyrite. *Phys. Scr.*, T115:1062–1063, 2005. Proc. of the XAFS-12 conference, Malmö, Sweden, June 2003.
- [135] Y. A. Kozinkin, A. A. Novakovich, A. V. Kozinkin, R. V. Vedrinskii, Y. V. Zubavichus, and A. A. Veligzhanin. Mechanisms of formation of near-edge fine structure of *K* X-ray absorption spectra of metallic Cu, Ni, Co (HCP and FCC phases), and Cr. *Phys. Solid State*, 53:1–5, 2011.
- [136] S. Kroeker and J. F. Stebbins. Magnesium coordination environments in glasses and minerals: New insight from high-field magnesium-25 MAS NMR. *Am. Mineral.*, 85:1459–1464, 2000.
- [137] P. Krüger and C. R. Natoli. X-ray absorption spectra at the Ca *L*<sub>2</sub>,*L*<sub>3</sub> edge calculated within multichannel multiple scattering theory. *Phys. Rev. B*, 70:245120, 2004.
- [138] P. Krüger and C. R. Natoli. Theory of Ca *L*<sub>2,3</sub>-edge XAS using a novel multi-channel multiple-scattering method. *J. Synchrotron Rad.*, 12:80–84, 2005.
- [139] J. D. Kubicki and A. C. Lasaga. Molecular dynamics simulation of pressure and temperature effects on MgSiO<sub>3</sub> and Mg<sub>2</sub>SiO<sub>3</sub> melts and glasses. *Phys. Chem. Minerals*, 17:661–673, 1991.
- [140] H. J. Kulik, M. Cococcioni, D. A. Scherlis, and N. Marzari. Density functional theory in transition-metal chemistry: A self-consistent Hubbard *U* approach. *Phys. Rev. Lett.*, 97:103001, 2006.
- [141] C. Lanczos. An iterative method for the solution of eigenvalue problem of linear differential and integral operators. *J. Res. National Bureau. Stand.*, 45:255–282, 1950.
- [142] C. Lanczos. Solution of systems of linear equations by minimized iterations. *J. Res. National Bureau. Stand.*, 49:33–53, 1952.
- [143] J.-C. Le Bossé, T. Épicier, and B. Jouffrey. Polarization dependence in ELNES: Influence of probe convergence, collector aperture and electron beam incidence angle. *Ultramicroscopy*, 106:449–460, 2006.
- [144] M. Le Grand. *Les platinoïdes et le molybdène dans des verres d'intérêt nucléaire. Étude structurale*. PhD thesis, Université Denis Diderot, Paris 7, 1999.
- [145] G. Lelong, L. Cormier, G. Ferlat, V. Giordano, G. S. Henderson, A. Shukla, and G. Calas. Evidence of fivefold-coordinated Ge atoms in amorphous GeO<sub>2</sub> under pressure using inelastic x-ray scattering. *Phys. Rev. B*, 85:134202, 2012.
- [146] C. Levelut, D. Cabaret, M. Benoit, P. Jund, and A.-M. Flank. Multiple scattering calculations of the XANES Si *K*-edge in amorphous silica. *J. Non-Cryst. Solids*, 293-295:100–104, 2001. Proc. of the NCM 8 conference, Wales (UK), August 2000.
- [147] D. Li, G. M. Bancroft, M. E. Fleet, X. H. Feng, and Y. Pan. Al *K*-edge XANES spectra of aluminosilicate minerals. *Am. Mineral.*, 80:432–440, 1995.
- [148] D. Li, G. M. Bancroft, M. E. Fleet, P. C. Hess, and Z. F. Yin. Coordination of B in K<sub>2</sub>O-SiO<sub>2</sub>-B<sub>2</sub>O<sub>3</sub>-P<sub>2</sub>O<sub>5</sub> glasses using B *K*-edge XANES. *Am. Mineral.*, 80:873–877, 1995.

- [149] D. Li, G. M. Bancroft, M. Kasrai, M. E. Fleet, X. H. Feng, and K. H. Tan. High-resolution Si and P  $K$ - and  $L$ -edge XANES spectra of crystalline  $\text{SiP}_2\text{O}_7$  and amorphous  $\text{SiO}_2\text{-P}_2\text{O}_5$ . *Am. Mineral.*, 79:785–788, 1994.
- [150] D. Li, M. Peng, and T. Murata. Coordination and local structure of magnesium in silicate minerals and glasses: Mg  $K$ -edge XANES study. *Can. Mineral.*, 37:199–206, 1999.
- [151] M. P. Ljungberg, J. J. Mortensen, and L. G. M. Pettersson. An implementation of core level spectroscopies in a real space projector augmented wave density functional theory code. *J. Electr. Spectr. Rel. Phenom.*, 184:427–439, 2011.
- [152] S. Della Longa, A. Arcovito, M. Girasole, J.-L. Hazemann, and M. Benfatto. Quantitative analysis of x-ray absorption near-edge structure data by a full multiple scattering procedure: the Fe-CO geometry in photolyzed carbonmonoxymyoglobin single crystal. *Phys. Rev. Lett.*, 87:155501, 2001.
- [153] D. Manuel, D. Cabaret, Ch. Brouder, Ph. Sainctavit, A. Bordage, and N. Trcera. Experimental evidence of thermal fluctuations on the x-ray absorption near-edge structure at the Al  $K$  edge. *Phys. Rev. B*, 85:224108, 2012.
- [154] A. Marini, C. Hogan, M. Grüning, and D. Varsano. An *ab initio* tool for excited state calculations. *Comput. Phys. Comm.*, 180:1392–1403, 2009.
- [155] L. Martin-Samos and G. Bussi. SaX: An open source package for electronic-structure and optical-properties calculations in the  $GW$  approximation. *Comput. Phys. Comm.*, 180:1416–1425, 2009.
- [156] C. Maurizio, F. d’Acapito, M. Benfatto, S. Mobilio, E. Cattaruzza, and F. Gonella. Local coordination geometry around  $\text{Cu}^+$  and  $\text{Cu}^{2+}$  ions in silicate glasses: an X-ray absorption near edge structure investigation. *Eur. Phys. J. B*, 14:211–216, 2000.
- [157] C. Mitterbauer, G. Kothleitner, W. Grogger, H. Zandbergen, B. Freitag, P. Tiemeijer, and F. Hofer. Electron energy-loss near-edge structures of  $3d$  transition metal oxides recorded at high-energy resolution. *Ultramicroscopy*, 96:469–480, 2003.
- [158] S.-D. Mo and W. Y. Ching. *Ab initio* calculation of the core-hole effect in the electron energy-loss near-edge structure. *Phys. Rev. B*, 62:7901–7907, 2000.
- [159] S.-D. Mo and W. Y. Ching. X-ray absorption near-edge structure in  $\alpha$  quartz and stishovite: *Ab initio* calculation with core-hole interaction. *Appl. Phys. Lett.*, 78:3809–3811, 2001.
- [160] H. J. Monkhorst and J. D. Pack. Special points for Brillouin-zone integrations. *Phys. Rev. B*, 13:5188–5192, 1976.
- [161] M. S. Moreno, K. Jorissen, and J. J. Rehr. Practical aspects of electron energy-loss spectroscopy (EELS) calculations using FEFF8. *Micron*, 38:1–11, 2007.
- [162] B. Morosin. Structure and thermal expansion of beryl. *Acta Cryst.*, B28:1899, 1972.
- [163] J. J. Mortensen, L. B. Hansen, and K. W. Jacobsen. Real-space grid implementation of the projector augmented wave method. *Phys. Rev. B*, 71:035109, 2005.
- [164] J. Mustre de Leon, J. J. Rehr, S. I. Zabinsky, and R. C. Albers. *Ab initio* curved-wave x-ray-absorption fine structure. *Phys. Rev. B*, 44:4146–4156, 1991.
- [165] C. R. Natoli and M. Benfatto. A unifying scheme of interpretation of x-ray absorption spectra based on the multiple-scattering theory. *J. Phys. Coll. C8*, 47:11–23, 1986.
- [166] C. R. Natoli, M. Benfatto, C. Brouder, M. F. Ruiz López, and D. L. Foulis. Multichannel multiple-scattering theory with general potentials. *Phys. Rev. B*, 42:1944–1968, 1990.
- [167] C. R. Natoli, M. Benfatto, S. Della Longa, and K. Hatada. X-ray absorption spectroscopy: state-of-the-art analysis. *J. Synchrotron Rad.*, 10:26–42, 2003.
- [168] C. R. Natoli, M. Benfatto, and S. Doniach. Use of general potentials in multiple-scattering theory. *Phys. Rev. A*, 34:4682–4694, 1986.
- [169] C. R. Natoli, D. K. Misemer, S. Doniach, and F. W. Kutzler. First-principles calculation of x-ray absorption-edge structure in molecular clusters. *Phys. Rev. A*, 22:1104–1108, 1980.
- [170] M. Nelhiebel, P.-H. Louf, P. Schattschneider, P. Blaha, K. Schwarz, and B. Joffrey. Theory of orientation-sensitive near-edge fine-structure core-level spectroscopy. *Phys. Rev. B*, 59:12807–12814, 1999.
- [171] D. R. Neuville, D. de Ligny, L. Cormier, G. S. Henderson, J. Roux, A.-M. Flank, and P. Lagarde. The crystal and melt structure of spinel and alumina at high temperature: An *in-situ* XANES study at the Al and Mg  $K$ -edge. *Geoch. Cosmoch. Acta*, 73:3410–3422, 2009.

- [172] R. E. Newnham and Y. M. de Haan. Refinement of the  $\alpha$   $\text{Al}_2\text{O}_3$ ,  $\text{Ti}_2\text{O}_3$ ,  $\text{V}_2\text{O}_3$  and  $\text{Cr}_2\text{O}_3$  structures. *Z. Kristallogr.*, 117:235–237, 1962.
- [173] A. G. Nord and P. Kierkegaard. The crystal structure of  $\text{Mg}_3(\text{PO}_4)_2$ . *Acta Chem. Scan.*, 22:1466–1474, 1968.
- [174] A. Omegna, R. Prins, and J. A. van Bokhoven. Effect of temperature on aluminum coordination in zeolites H-Y and H-USY and amorphous silica-alumina: an in-situ Al K edge XANES study. *J. Phys. Chem. B*, 109:9280–9283, 2005.
- [175] G. Ona-Nguema, G. Morin, Y. Wang, N. Menguy, F. Juillot, L. Olivi, G. Aquilanti, M. Abdelmoula, Ch. Ruby, J. R. Bargar, F. Guyot, G. Calas, and G. E. Brown Jr. Arsenite sequestration at the surface of nano- $\text{Fe}(\text{OH})_2$ , ferrous-carbonate hydroxide, and green-rust after bioreduction of arsenic-sorbed lepidocrocite by *Shewanella putrefaciens*. *Geochim. Cosmochim. Acta*, 73:1359–1381, 2009.
- [176] G. Onida, L. Reining, and A. Rubio. Electronic excitations: density functional versus many body Green’s function approaches. *Rev. Mod. Phys.*, 74:601–659, 2002.
- [177] M. Ostafin and B. Nogaj.  $^{14}\text{N}$ -NQR based device for detection of explosives in landmines. *Measurement*, 40:43–54, 2007.
- [178] S. Pagès-Camagna, I. Reiche, Ch. Brouder, D. Cabaret, S. Rossano, B. Kanngiesser, and A. Erko. New insights into the colour origin of archaeological Egyptian Blue and Green by XAFS at the Cu K edge. *X-Ray Spectrometry*, 35:141–145, 2006.
- [179] J. P. Perdew, S. Burke, and M. Ernzerhof. Generalized gradient approximation made simple. *Phys. Rev. Lett.*, 77:3865, 1996.
- [180] Ch. Pickard. *Ab initio Electron Energy Loss Spectroscopy*. PhD thesis, Christ’s College, Cambridge, 1997.
- [181] Ch. J. Pickard and F. Mauri. All-electron magnetic response with pseudopotentials: NMR chemical shifts. *Phys. Rev. B*, 63:245101, 2001.
- [182] B. Poumellec, R. Cortes, G. Tourillon, and J. Berthon. Angular-dependence of the Ti K-edge in rutile  $\text{TiO}_2$ . *Phys. Stat. Solidi B*, 164:319–326, 1991.
- [183] D. Prendergast and G. Galli. X-ray absorption spectra of water from first principles calculations. *Phys. Rev. Lett.*, 96:215502, 2006.
- [184] M. Profeta, F. Mauri, and Ch. J. Pickard. Accurate first principles prediction of  $^{17}\text{O}$  NMR parameters in  $\text{SiO}_2$ : Assignment of the zeolite ferrierite spectrum. *J. Am. Chem. Soc.*, 125:541–548, 2003.
- [185] J. J. Rehr and R. C. Albers. Scattering-matrix formulation of curved-wave multiple-scattering theory: Application to x-ray-absorption fine structure. *Phys. Rev. B*, 41:8139–8149, 1990.
- [186] J. J. Rehr, R. C. Albers, and S. I. Zabinsky. High-order multiple-scattering calculations of x-ray-absorption fine structure. *Phys. Rev. Lett.*, 69:3397–3400, 1992.
- [187] J. J. Rehr, J. J. Kas, M. P. Prange, A. P. Sorini, Y. Takimoto, and F. Vila. *Ab initio* theory and calculations of X-ray spectra. *C. R. Physique*, 10:548–559, 2009.
- [188] J. J. Rehr, J. J. Kas, F. D. Vila, M. P. Prange, and K. Jorissen. Parameter-free calculations of x-ray spectra with FEFF9. *Phys. Chem. Chem. Phys.*, 12:5503–5513, 2010.
- [189] K. Robinson, G. V. Gibbs, and P. H. Ribbe. Quadratic elongation: A quantitative measure of distortion in coordination polyhedra. *Science*, 172:567–570, 1971.
- [190] M. Roemelt, M. A. Beckwith, C. Duboc, M.-N. Collomb, F. Neese, and S. DeBeer. Manganese K-edge x-ray absorption spectroscopy as a probe of the metalligand interactions in coordination compounds. *Inorg. Chem.*, 51:680–687, 2012.
- [191] S. Rossano, F. Farges, A. Ramos, J.-M. Delaye, and G. E. Brown Jr. Bond valence in silicate glasses. *J. Non-Cryst. Solids*, 304:16773, 2002.
- [192] S. Rossano, F. Mauri, C. J. Pickard, and I. Farnan. First-principles calculation of  $^{17}\text{O}$  and  $^{25}\text{Mg}$  NMR shieldings in  $\text{MgO}$  at finite temperature: Rovibrational effect in solids. *J. Phys. Chem. B*, 109:7245–7250, 2005.
- [193] M. F. Ruiz-Lopez and A. Muñoz-Páez. A theoretical study of the XANES spectra of rutile and anatase. *J. Phys.: Condens. Matter*, 3:8981–8990, 1991.
- [194] Ph. Saintavrit, D. Cabaret, and V. Briois. *Multiple scattering theory applied to X-ray absorption near-edge structure*, pages 67–101. F. Hipert and E. Geissler and J. L. Hodeaux and E. Lelièvre-Berna and J. R. Regnard, springer edition, 2006. ISBN-13 978-1-4020-3336-0.
- [195] P. Schattschneider, C. Hébert, H. Franco, and B. Jouffrey. Anisotropic relativistic cross sections for inelastic electron scattering, and the magic angle. *Phys. Rev. B*, 72:045142, 2005.

- [196] C. P. Schwartz, J. S. Uejio, R. J. Saykally, and D. Prendergast. On the importance of nuclear quantum motions in near edge x-ray absorption fine structure spectroscopy of molecules. *J. Chem. Phys.*, 130:184109, 2009.
- [197] D. Sébilleau, C. Natoli, G. M. Gavaza, H. Zhao, F. Da Pieve, and K. Hatada. MsSpec-1.0: A multiple scattering package for electron spectroscopies in material science. *Comp. Phys. Comm.*, 182:2567–2579, 2011.
- [198] T. Seuthe, M. Höfner, F. Reinhardt, W. J. Tsai, J. Bonse, M. Eberstein, H. J. Eichler, and M. Grehn. Femtosecond laser-induced modification of potassium-magnesium silicate glasses: An analysis of structural changes by near edge x-ray absorption spectroscopy. *Appl. Phys. Lett.*, 100:224101, 2012.
- [199] R. D. Shannon. Revised effective ionic radii and systematic studies of interatomic distances in halides and chalcogenides. *Acta. Cryst.*, A32:751–767, 1976.
- [200] K. Shimoda and M. Okuno. Molecular dynamics study of  $\text{CaSiO}_3$ - $\text{MgSiO}_3$  glasses under high pressure. *J. Phys.: Condens. Matter*, 18:6531–6544, 2006.
- [201] E. L. Shirley. *Ab initio* inclusion of electron-hole attraction: Application to x-ray absorption and resonant inelastic x-ray scattering. *Phys. Rev. Lett.*, 80:794, 1998.
- [202] E. L. Shirley. Ti 1s pre-edge features in rutile: a Bethe-Salpeter calculation. *J. Electr. Spectr. Rel. Phen.*, 136:77–83, 2004.
- [203] J. A. Soininen and E. L. Shirley. Scheme to calculate core hole-electron interactions in solids. *Phys. Rev. B*, 64:165112, 2001.
- [204] A. P. Sorini, J. J. Rehr, and Z. H. Levine. Magic angle in electron energy loss spectra: Relativistic and dielectric corrections. *Phys. Rev. B*, 77:115126, 2008.
- [205] D. A. Stephenson and P. B. Moore. The crystal structure of grandidierite,  $(\text{Mg,Fe})\text{Al}_3\text{SiO}_9$ . *Acta Cryst. B*, 24:1518–1522, 1968.
- [206] E. D. Stevens, M. L. DeLucia, and P. Coppens. Experimental observation of the effect of crystal field splitting on the electron density distribution of iron pyrite. *Inorg. Chem.*, 19:813–820, 1980.
- [207] K. Suenaga and M. Koshino. Atom-by-atom spectroscopy at graphene edge. *Nature*, 468:13–30, 2010.
- [208] K. Suenaga, E. Sandré, C. Colliex, Ch. J. Pickard, and S. Iijima. Electron energy-loss spectroscopy of electron states in isolated carbon nanostructures. *Phys. Rev. B*, 63:165408:1–4, 2001.
- [209] S. R. Sutton, J. Karner, J. Papike, J. S. Shearer, M. Newville, P. Eng, M. Rivers, and M. D. Dyar. Vanadium *K* edge XANES of synthetic and natural basaltic glasses and application to microscale oxygen barometry. *Geochem. Cosmochem. Acta*, 69:2333–3348, 2005.
- [210] Y. Tabira. Local structure around oxygen atoms in  $\text{CaMgSi}_2\text{O}_6$  glass by O *K*-edge EXELFS. *Mater. Sci. Eng. B*, 41:63–66, 1996.
- [211] M. TAILLEFUMIER, D. Cabaret, A.-M. Flank, and F. Mauri. X-ray absorption near-edge structure calculations with the pseudopotentials: application to the *K* edge in diamond and  $\alpha$ -quartz. *Phys. Rev. B*, 66:195107, 2002.
- [212] T. Tamura, T. Ohwaki, A. Ito, Y. Ohsawa, R. Kobayashi, and S. Ogata. Theoretical Mn *K*-edge XANES for  $\text{Li}_2\text{MnO}_3$ : DFT+*U* study. *Modelling Simul. Mater. Sci. Eng.*, 20:045006, 2012.
- [213] T. Tamura S. Tanaka and M. Kohyama. Full-PAW calculations of XANES/ELNES spectra of Ti-bearing oxide crystals and TiO-SiO glasses: Relation between pre-edge peaks and Ti coordination. *Phys. Rev. B*, 85:205210, 2012.
- [214] N. Trcera. *Étude de la structure de verres magnésio-silicatés : approche expérimentale et modélisation*. PhD thesis, Université Paris-Est Marne-la-Vallée, 2008.
- [215] N. Trcera, D. Cabaret, F. Farges, A.-M. Flank, P. Lagarde, and S. Rossano. Mg *K*-edge XANES spectra in crystals and oxide glasses: experimental vs. theoretical approaches. *AIP Conference Proceedings*, 882:226–228, 2007. Proc. of the XAFS-13 conference, Stanford, USA, July 2006.
- [216] N. Trcera, D. Cabaret, S. Rossano, F. Farges, A.-M. Flank, and P. Lagarde. Experimental and theoretical study of the structural environment of magnesium in minerals and silicate glasses using x-ray absorption near-edge structure. *Phys Chem Minerals*, 36:241–257, 2009.
- [217] N. Trcera, S. Rossano, K. Madjer, and D. Cabaret. Contribution of molecular dynamics simulations and *ab initio* calculations to the interpretation of Mg *K*-edge experimental XANES in  $\text{K}_2\text{O}$ - $\text{MgO}$ - $3\text{SiO}_2$  glass. *J. Phys.: Condens. Matter*, 23:255401 (9pp), 2011.

- [218] N. Troullier and J. L. Martins. Efficient pseudopotentials for plane-wave calculations. *Phys. Rev. B*, 43:1993–2006, 1991.
- [219] T. A. Tyson, K. O. Hodgson, C. R. Natoli, and M. Benfatto. General multiple-scattering scheme for the computation and interpretation of x-ray-absorption fine structure in atomic clusters with applications to SF<sub>6</sub>, GeCl<sub>4</sub>, and Br<sub>2</sub> molecules. *Phys. Rev. B*, 46:5997–6019, 1992.
- [220] P. Umari, G. Stenuit, and S. Baroni. Optimal representation of the polarization propagator for large-scale *GW* calculations. *Phys. Rev. B*, 79:201104, 2009.
- [221] P. Umari, G. Stenuit, and S. Baroni. *GW* quasi-particle spectra from occupied states only. *Phys. Rev. B*, 81:115104, 2010.
- [222] J. Vaara, J. Lounila, K. Ruud, and T. Helgaker. Rovibrational effects, temperature dependence, and isotope effects on the nuclear shielding tensors of water: A new <sup>17</sup>O absolute shielding scale. *J. Chem. Phys.*, 109:8388–8397, 1998.
- [223] J. A. van Bokhoven. *In-situ* Al *K*-edge spectroscopy in zeolites: instrumentation, data-interpretation and catalytic consequences. *Phys. Scr.*, T115:76–79, 2005.
- [224] J. A. van Bokhoven, A. M. J. van der Eerden, and D. C. Koningsberger. Three-coordinate aluminum in zeolites observed with *in situ* x-ray absorption near-edge spectroscopy at the Al *K*-edge: flexibility of aluminum coordinations in zeolites. *J. Am. Chem. Soc.*, 125:7435–7442, 2003.
- [225] R. V. Vedrinskii and A. A. Novakovich. Green-function method in one-electron theory of x-ray-spectra of disordered alloys. *Fiz. Met. Metalloved.*, 39:7–15, 1975.
- [226] J. Vinson, J. J. Rehr, J. J. Kas, and E. L. Shirley. Bethe-Salpeter equation calculations of core excitation spectra. *Phys. Rev. B*, 83:115106, 2011.
- [227] J. Vojtechovsky, K. Chu, J. Berendzen, R. M. Sweet, and I. Schlichting. Crystal structures of myoglobin-ligand complexes at near atomic resolution. *Biophys. J.*, 77:2153–2174, 1999.
- [228] D. D. Vvedensky, D. K. Saldin, and J. B. Pendry. An update of DLXANES, the calculation of X-ray absorption near-edge structure. *Comput. Phys. Comm.*, 40:421–440, 1986.
- [229] B. Walker, A. M. Saitta, R. Gebauer, and S. Baroni. Efficient approach to time-dependent density-functional perturbation theory for optical spectroscopy. *Phys. Rev. Lett.*, 96:113001, 2006.
- [230] H. M. Wang and G. S. Henderson. Investigation of coordination number in silicate and germanate glasses using O *K*-edge X-ray absorption spectroscopy. *Chemical Geology*, 213:17–30, 2004.
- [231] H. M. Wang and G. S. Henderson. The germanate anomaly: Is the presence of 5- or 6-fold Ge important? *Phys. Chem. Glasses*, 46:377–380, 2005.
- [232] H. M. Wang and G. S. Henderson. O *K*-edge XANES studies of alkali germanophosphate glasses. *J. Non-Cryst. Solids*, 354:863–872, 2008.
- [233] X. Weng, P. Rez, and O. F. Sankey. Pseudo-atomic-orbital band theory applied to electron-energy-loss near-edge structures. *Phys. Rev. B*, 40:5694–5704, 1989.
- [234] Ph. Wernet, D. Nordlund, U. Bergmann, M. Cavalleri, M. Odelius, H. Ogasawara, L. Å. Näslund, T. K. Hirsch, L. Ojamäe, P. Glatzel, L. G. M. Pettersson, and A. Nilsson. The structure of the first coordination shell in liquid water. *Science*, 304:995–999, 2004.
- [235] T. E. Westre, A. Di Cicco, A. Filippini, C. R. Natoli, B. Hedman, E. I. Solomon, and K. O. Hodgson. GNXAS, a multiple-scattering approach to EXAFS analysis: methodology and applications to iron complexes. *J. Am. Chem. Soc.*, 117:1566–1583, 1995.
- [236] T. E. Westre, P. Kennepohl, J. G. DeWitt, B. Hedman, K. O. Hodgson, and E. I. Solomon. A multiplet analysis of Fe *K*-edge  $1s \rightarrow 3d$  pre-edge features of iron complexes. *J. Am. Chem. Soc.*, 119:6297–6314, 1997.
- [237] M. C. Wilding, C. J. Benmore, J. A. Tange-man, and S. Sampath. Coordination changes in magnesium silicate glasses. *Europhys. Lett.*, 67(2):212–218, 2004.
- [238] M. Wilke, F. Farges, P.-E. Petit, G. E. Brown Jr., and F. Martin. Oxidation state and coordination of Fe in minerals: An Fe *K*-XANES spectroscopic study. *Amer. Mineral.*, 86:714–730, 2001.
- [239] J. C. Woicik, E. L. Shirley, C. S. Hellberg, K. E. Andersen, S. Sambasivan, D. A. Fischer, B. D. Chapman, E. A. Stern, P. Ryan, D. L. Ederer, and H. Li. Ferroelectric distortion in SrTiO<sub>3</sub> thin films on Si(001) by x-ray absorption fine structure spectroscopy: Experiment and first-principles calculations. *Phys. Rev. B*, 75:140103(R), 2007.
- [240] M. Wu, Y. Liang, J.-Z. Jiang, and J. S. Tse. Structure and properties of dense silica glass. *Sc. Rep.*, 2:398, 2012.

- [241] T. Yamamoto. Assignment of pre-edge peaks in K-edge x-ray absorption spectra of 3d transition metal compounds: electric dipole or quadrupole? *X-ray spectrometry*, 37:572–584, 2008.
- [242] T. Yamanaka and Y. Takeuchi. Order-disorder transition in  $\text{MgAl}_2\text{O}_4$  at high temperature up to  $1700^\circ\text{C}$ . *Z. Kristallogr.*, 165:65–78, 1983.
- [243] S. I. Zabinsky, J. J. Rehr, A. Ankudinov, R. C. Albers, and M. J. Eller. Multiple-scattering calculations of x-ray-absorption spectra. *Phys. Rev. B*, 52:2995–3009, 1995.

## 2 Sélection d'articles

Mes articles les plus significatifs sont les suivants :

*Electron Population Analysis by Full Potential X-Ray Absorption Simulations.*

Yves Joly, Delphine Cabaret, Hubert Renevier, Calogero R. Natoli.

Phys. Rev. Lett. 82, 2398-2401 (1999).

*X-ray absorption near-edge structure calculations with the pseudopotentials: Application to the K edge in diamond and  $\alpha$ -quartz.*

Mathieu Taillefumier, Delphine Cabaret, Anne-Marie Flank, Francesco Mauri.

Phys. Rev. B 66, 195107(8pp) (2002).

*Structural relaxations around Ti, Cr and Fe impurities in  $\alpha$ -Al<sub>2</sub>O<sub>3</sub> probed by x-ray absorption near edge structure combined with first-principles calculations.*

E. Gaudry, D. Cabaret, Ph. Saintavit, Ch. Brouder, F. Mauri, J. Goulon, A. Rogalev.

J. Phys.: Condens. Matter 17, 5467-5480 (2005).

*Oxygen K-edge XANES of germanates investigated using first-principles calculations.* Delphine Cabaret, Francesco Mauri, Grant S. Henderson.

Phys. Rev. B 75, 184205(9pp) (2007).

*Experimental and theoretical study of the structural environment of magnesium in minerals and silicate glasses using X-ray absorption near-edge structure.*

Nicolas Trcera, Delphine Cabaret, Stéphanie Rossano, François Farges, Anne-Marie Flank, Pierre Lagarde.

Phys. Chem. Minerals 36, 241-257 (2009).

*First-principles calculations of x-ray absorption spectra at the K-edge of 3d transition metals: an electronic structure analysis of the pre-edge.*

Delphine Cabaret, Amélie Bordage, Amélie Juhin, Mounir Arfaoui, Emilie Gaudry.

Phys. Chem. Chem. Phys. 12, 5619-5633 (2010).

*Experimental evidence of thermal fluctuations on the x-ray absorption near-edge structure at the aluminum K edge.*

D. Manuel, D. Cabaret, Ch. Brouder, Ph. Saintavit, A. Bordage, N. Trcera.

Phys. Rev. B. 85, 224108(13pp) (2012).

Les principaux résultats des cinq premiers papiers ont été repris dans ce mémoire. Le sixième est intégralement contenu dans la section 1.4.<sup>1</sup> Aussi ai-je décidé de ne joindre à ce mémoire que la publication 7, illustrant l'état d'avancement de notre projet sur l'interaction électron-phonon en spectroscopie XANES...

---

<sup>1</sup>Pour la petite histoire, l'écriture de ce mémoire a démarré en 2009, alors que j'étais en congé de maternité, par la partie sur les préseuils *K* des éléments de transition. Au même moment, j'ai été invitée par J. van Bokhoven à écrire un article pour une collection spécial de Physical Chemistry Chemical Physics intitulée "Recent developments in X-ray absorption spectroscopy". J'ai alors décidé de transformer cette partie de mon mémoire en article, et d'en faire ainsi l'objet de cette publication invitée. *Je me souviendrai longtemps des derniers jours de rédaction de l'article avec mon bébé dans les bras... et je remercie chaleureusement les "Amélie" pour leur aide précieuse en cette période mouvementée.*

## Experimental evidence of thermal fluctuations on the x-ray absorption near-edge structure at the aluminum *K* edge

D. Manuel,<sup>1,\*</sup> D. Cabaret,<sup>1</sup> Ch. Brouder,<sup>1</sup> Ph. Sainctavit,<sup>1</sup> A. Bordage,<sup>2</sup> and N. Trcera<sup>3</sup>

<sup>1</sup>Université Pierre et Marie Curie (UPMC), IMPMC, UMR CNRS 7590, 4 place Jussieu, 75252 Paris Cedex 05, France

<sup>2</sup>Wigner Research Centre for Physics, Hungarian Academy of Sciences, P.O. Box 49, H-1525 Budapest, Hungary

<sup>3</sup>Synchrotron SOLEIL, BP 48, 91192 Gif sur Yvette, France

(Received 19 March 2012; published 14 June 2012)

After a review of temperature-dependent experimental x-ray absorption near-edge structure (XANES) and related theoretical developments, we present the Al *K*-edge XANES spectra of corundum and beryl for temperature ranging from 300 to 930 K. These experimental results provide a first evidence of the role of thermal fluctuation in XANES at the Al *K* edge, especially, in the pre-edge region. The study is carried out by polarized XANES measurements of single crystals. For any orientation of the sample with respect to the x-ray beam, the pre-edge peak grows and shifts to lower energy with temperature. In addition, temperature induces modifications in the position and intensity of the main XANES features. First-principles DFT calculations are performed for both compounds. They show that the pre-edge peak originates from forbidden  $1s \rightarrow 3s$  transitions induced by vibrations. Three existing theoretical models are used to take vibrations into account in the absorption cross-section calculations: (i) an average of the XANES spectra over the thermal displacements of the absorbing atom around its equilibrium position, (ii) a method based on the crude Born-Oppenheimer approximation where only the initial state is averaged over thermal displacements, and (iii) a convolution of the spectra obtained for the atoms at the equilibrium positions with an approximate phonon spectral function. The theoretical spectra so obtained permit to qualitatively understand the origin of the spectral modifications induced by temperature. However, the correct treatment of thermal fluctuation in XANES spectroscopy requires more sophisticated theoretical tools.

DOI: [10.1103/PhysRevB.85.224108](https://doi.org/10.1103/PhysRevB.85.224108)

PACS number(s): 78.70.Dm, 91.60.Ki, 71.15.Mb

### I. INTRODUCTION AND STATE OF THE ART

X-ray absorption near-edge structure (XANES) spectroscopy is a powerful technique to probe the empty states in solids and to determine the local structure around a selected atom. The interpretation of *K*-edge XANES spectra is not straightforward and often requires the use of simulation tools, which are traditionally based on the density functional theory (DFT). XANES calculations for inorganic solids usually consider the atoms at fixed positions, even if in reality atoms are subjected to quantum thermal fluctuations that reduce to the zero point motion at  $T = 0$  K. Recently, it has been theoretically shown that vibrations could have a spectacular effect at the Al *K* edge, allowing  $1s$  to  $3s$  dipole transitions.<sup>1</sup> Such forbidden transitions were previously invoked to be responsible for the pre-edge feature that occurs at the Al *K* edge in several aluminosilicate minerals<sup>2</sup> and at the Si *K* edge in silicon diphosphate.<sup>3</sup> Moreover, Ankudinov and Rehr stated that atomic displacements of order of typical Debye-Waller factors could reveal some forbidden transitions.<sup>4</sup> Consequently, the fact that vibrations may be able to induce additional peaks (in the pre-edge or at higher energies) suggests that XANES could be considered as a relevant probe of quantum thermal fluctuations. It is already the case in organic molecules, the vibronic fine structure of which can be observed in XANES or NEXAFS (near-edge x-ray absorption fine structure) spectra. For instance in the last ten years, XANES spectroscopy has revealed the vibronic structure of naphthalene,<sup>5</sup> biphenyl,<sup>6</sup> and even larger molecules such as naphthalenetetracarboxylic dianhydride<sup>7</sup> at the C *K* edge, the vibronic structure of acetonitrile<sup>8</sup> and

acrylonitrile<sup>9</sup> at the N *K* edge, and more recently the one of halogenated acenaphthenequinone<sup>10</sup> at the O *K* edge. The vibronic component of the lowest core-excited state of OH and OD was observed at the O *K* edge as well.<sup>11</sup>

In this paper, we focus on the thermal effects in two inorganic crystalline solids at the Al *K* edge: corundum ( $\alpha$ -Al<sub>2</sub>O<sub>3</sub>) and beryl (Be<sub>3</sub>Al<sub>2</sub>Si<sub>6</sub>O<sub>18</sub>). Polarized XANES spectra have been measured on single crystals for temperatures ranging from 300 to 930 K. Our purpose is to show that thermal fluctuations induce substantial spectral modifications, especially, in the pre-edge region. Very few studies were carried out in inorganic solids toward the same goal. As far as we know, thermal effects measured in XANES spectroscopy mainly concern the Ti *K* pre-edge region in oxides. Such a temperature dependence was first observed by Durmeyer *et al.*<sup>12</sup> in TiO<sub>2</sub> (rutile), Li<sub>4/3</sub>Ti<sub>5/3</sub>O<sub>4</sub> and LiTi<sub>2</sub>O<sub>4</sub>. The main pre-edge peak was found to grow with temperature, and to slightly shift to lower energy for the first two compounds. Later, the temperature dependence of the polarized pre-edge structure at the Ti *K* edge in rutile was measured at low and room temperature.<sup>13</sup> Thermal effects were essentially visible through an increase of intensity of the first two pre-edge peaks. The temperature dependence of the electric dipole and quadrupole contributions of the Ti *K* edge in rutile was investigated in the 6–698 K range by Collins and Dmitrienko in 2010 at the Diamond Light Source.<sup>14</sup> Nozawa *et al.*<sup>15</sup> measured the temperature dependence of the Ti *K*-edge XANES in SrTiO<sub>3</sub> from 15 to 300K, showing an increase of the first two pre-edge peaks along with a slight shift to lower energy of the second pre-edge peak and of the absorption edge.

These effects were attributed to random thermal vibrations of Ti.<sup>15</sup>

Apart from these last examples at the Ti *K* edge, most of temperature-dependent XANES measurements were carried out in order to study phase transition mechanisms or to determine the local structure below and above the transition temperature. For instance, in some perovskite crystals, significant spectral changes in the *K* pre-edge region are induced by temperature and are interpreted in relation to phase transition. The literature reports temperature-dependent x-ray absorption spectra (including pre-edge) in perovskite titanates at the Ti *K* edge,<sup>16–21</sup> in perovskite manganites at the Mn *K* edge<sup>22,23</sup> and at the O *K* edge,<sup>24,25</sup> in zirconates at the Zr *K* edge,<sup>26</sup> niobates at the Nb *K* edge,<sup>27–31</sup> in the  $\text{La}_{1-x}\text{Sr}_x\text{FeO}_{3-\delta}$  system at the Fe *K* edge,<sup>32</sup> in a  $\text{La}(\text{Fe},\text{Ni})\text{O}_3$  solid oxide fuel cell cathode at the O *K* edge,<sup>33</sup> and more recently in the  $\text{Pr}_{0.5}\text{Ca}_{0.5}\text{CoO}_3$  cobaltite at the Ca  $L_{2,3}$ -edges and the Pr  $L_3$  and  $M_{4,5}$ -edges.<sup>34</sup> Phase transition studies using temperature-dependent XANES are not restricted to the perovskite structure. In particular, Cu *K* and La *L*-edges spectra in  $\text{La}_{2-x}\text{Sr}_x\text{CuO}_4$  cuprates were recorded at room temperature and at 78 K.<sup>35</sup> An angular dependence XANES study was performed at the V *K* edge in  $\text{VO}_2$  for temperatures lower and higher than the metal-insulator transition temperature at 68 °C.<sup>36</sup> Several studies reported in literature deal with oxide glass and melt structures. For instance, the local structural environment of Ti in Na-, K-, and Ca-titanosilicate glasses and melts was determined by Ti *K*-edge x-ray absorption spectroscopy at temperatures ranging from 293–1650 K.<sup>37</sup> The Zr *K* edge in a  $\text{ZrO}_2\text{-MgO-Al}_2\text{O}_3\text{-SiO}_2$  glass was measured for various temperatures around  $T_g$  (1085 K).<sup>38</sup> The crystalline and melt structures of  $\text{Al}_2\text{O}_3$  and  $\text{MgAl}_2\text{O}_4$  were investigated using temperature dependent XANES spectroscopy at the Al and Mg *K* edges.<sup>39</sup> A similar study concerns the crystal, glass, and melt structures in the  $\text{CaO-MgO-Al}_2\text{O}_3\text{-SiO}_2$  system at the Al, Si, and Ca *K* edges.<sup>40</sup> Again at the Si *K* edge, the structure of  $\text{SiO}_2$  polymorphs were studied using XANES spectroscopy from room temperature to 2030 K, above the melting point at 2000 K.<sup>41</sup> Furthermore, at the oxygen *K* edge in liquid water, variations were observed between the room-temperature spectrum and the 90 °C one and found to be related to a change of local environment of a significant amount of molecules.<sup>42</sup>

Temperature-dependent x-ray absorption spectroscopy was also used to study chemical reactions. For instance, in catalysis, the local structure of Al in zeolites was examined to understand the processes that take place during steam activation of these complex cagelike porous compounds. Hence Al *K*-edge measurements in several zeolites were carried out in the range 300–975 K, in vacuum or in a flow of helium saturated with water,<sup>43–46</sup> and in other working conditions of the catalysis.<sup>47</sup> In Refs. 43,44,46 and 47, a pre-edge peak appears when temperature is increased. The presence of this Al *K* pre-edge peak at high temperature is interpreted as the signature of threefold coordinated Al in the zeolite structure. Other temperature effects are observable at higher energies in the XANES region and attributed to the transformation of a given amount of octahedrally coordinated Al to tetrahedrally coordinated Al.<sup>44,45</sup> Recently, in a totally different field, the temperature dependence of Fe *K*-edge XANES spectra of  $\text{FePt/Fe}_3\text{O}_4$  nanoparticles has been measured from 300 to 870 K in

order to understand the annealing process, which enables the building of magnetic nanocomposites with combined magnetic properties.<sup>48</sup> A strong temperature dependence was observed in Fe  $L_{2,3}$ -edges spectra of Fe impurities in MgO thin films in the range 77–500 K; it was attributed to the thermal population of low-lying Fe 3*d* excited states, that are present due to the spin-orbit coupling.<sup>49</sup> At last, the valence state of Yb in  $\text{YbC}_2$ , investigated by Yb  $L_3$  XANES spectroscopy at low and high temperatures, is found to be stable from 15 to 1123 K, so providing new information about this long-known compound.<sup>50</sup>

In all the references cited in the previous two paragraphs, the role of nuclear motion in the temperature-dependent XANES spectra was not investigated. A thorough study of thermal fluctuations could then bring new insights in the interpretation of the temperature-dependent spectral features whatever the purpose of the experiments is (catalysis, phase transition, etc.).

The modeling of nuclear motion in the absorption cross section of solids is a challenging task. In particular, the presence of phonon modes in crystalline solids generates a dynamic disorder, which has a completely different behavior from the static disorder that can be found in glasses. Far from the edge, in the extended x-ray absorption fine structure (EXAFS) region, vibrations are taken into account through a Debye-Waller factor  $\exp(-2k^2\sigma^2)$ .<sup>51,52</sup> Since this factor vanishes for  $k \simeq 0$ , it cannot reproduce well the thermal effects in the XANES region and especially in the pre-edge region. Fujikawa and co-workers showed in a series of papers of increasing sophistication<sup>53–55</sup> that the treatment of vibrations could be achieved by the convolution of the “phononless” x-ray absorption spectrum with the phonon spectral function. To our knowledge, this theoretical work has not been applied to any real case yet. A basic and simple idea to take vibrations into account is to calculate the absorption cross section for a configuration where the absorbing atom is shifted from its equilibrium position.<sup>4,26</sup> For instance, at the B *K* edge of  $\text{ABO}_3$  perovskite structures, the approach used by Vedrinskii *et al.*<sup>26</sup> to treat the temperature effects is based on the assumption that the area of the pre-edge peak is proportional to the mean-square displacements of the B atom along the O-B-O chain. In such a way, the symmetry breaking of the absorbing atom site generates or increases local *p-d* and *p-s* hybridization. Brouder and co-workers<sup>1,56</sup> developed a different approach assuming that vibrational energies are small with respect to the instrumental resolution, and using the crude Born-Oppenheimer approximation, so that only core-hole motion remains. The resulting expression for the absorption cross section shows that, at the *K* edge, vibrations enable electric-dipole transitions to 3*s* and 3*d* final states, that are not due to local hybridization with the *p* states. In the case of organic molecules, more advanced theories are employed to reproduce the vibronic structure observed in XANES spectra. Beyond the Born-Oppenheimer approximation, a vibronic coupling theory was developed and successfully applied to the C-1*s* absorption spectra of ethylene<sup>57</sup> ( $\text{C}_2\text{H}_4$ ), ethyne<sup>58</sup> ( $\text{C}_2\text{H}_2$ ), and isotopomers. Besides, many approaches calculate Franck-Condon factors based on a vibrational eigenmode analysis in the ground and excited states. In particular, the linear coupling model was used to

compute the Franck-Condon factors for NEXAFS spectra at the O *K* edge in formaldehyde,<sup>59</sup> at the C *K* edge in formaldehyde,<sup>60</sup> naphthalene,<sup>5</sup> gaseous cyclopropane,<sup>61</sup> and acetic acid<sup>62</sup> and at the N *K* edge in gaseous pyridine,<sup>63</sup> acetonitrile,<sup>8</sup> and acrylonitrile.<sup>9</sup> In Ref. 9, a direct calculation of the Franck-Condon amplitudes is also performed. However, the Franck-Condon approximation ignores the impact of nuclear motion on the electronic transition amplitude. To first order, this impact is referred to as the Herzberg-Teller effect.<sup>64</sup> To go beyond the Franck-Condon approximation, the nuclear degrees of freedom of molecules was modeled using various molecular dynamics (MD) techniques. In doing so, atomic configurations are generated at finite temperature and then used as input in cross-section calculations. Finally, the individual spectra associated to each sampled atomic configuration are averaged over. Using this methodology, vibrations were included in XANES calculations at the N *K* edge of several prototype molecules: upon classical MD sampling<sup>65-67</sup> and upon path-integral molecular dynamics (PIMD).<sup>66,68</sup> PIMD sampling enables to consider the quantum nature of nuclear motion, which has been found to be of noticeable importance to accurately simulate XANES of N<sub>2</sub>,<sup>66</sup> s-triazine, and glycine.<sup>68</sup> The sensitivity of photoabsorption spectroscopy to a quantum treatment of nuclear motion was also highlighted in the optical range<sup>69</sup> and in the UV range.<sup>70</sup> The MD methodology is not restricted to organic molecules; simulations of the density and temperature dependence of XANES in warm dense aluminum plasmas were achieved using *ab initio*<sup>71,72</sup> and classical<sup>73</sup> MD and, recently, they have been compared to experiments.<sup>74,75</sup>

In the present study, DFT calculations based on plane-wave formalism are performed in order to understand the spectral modifications induced by temperature that are observed experimentally. Reference theoretical Al *K* XANES spectra of corundum and beryl are first obtained considering the atoms at their equilibrium positions. Then three existing methods are used to account for vibrations: (i) a calculation considering thermal displacements of the absorbing atom around its equilibrium position, (ii) the method developed by Brouder *et al.*,<sup>1</sup> and (iii) a convolution of the spectra obtained for the atoms at the equilibrium positions with an approximate phonon spectral function.

The paper is organized as follows. Section II is dedicated to the methods. First, the temperature-dependent XANES experiments at the Al *K* edge of corundum and beryl are described, with a specific attention paid to the self-absorption correction procedure. Second, the three theoretical DFT methods used to take the vibrations into account are detailed. Section III is devoted to the description of the experimental spectra recorded for temperatures ranging from 300 to 930 K. In Sec. IV, the experimental results are analyzed with the help of the DFT calculations and discussed in the context of the temperature-dependent XANES spectra already reported in the literature. The conclusion of this work is given in Sec. V.

## II. METHODS

### A. Experimental setup

Two single-crystalline samples containing aluminum in 6-fold coordination with oxygen are studied. The first is a cylindrical synthetic transparent ruby ( $\alpha$ -Al<sub>2</sub>O<sub>3</sub> with 18 ppm

of Cr and 10 ppm of Ti) of 4.0 mm diameter and 1.0 mm thickness, which will thereafter be denoted as corundum. The second is a parallelepipedic section of a natural green emerald from Colombia (Be<sub>3</sub>Al<sub>2</sub>Si<sub>6</sub>O<sub>18</sub> with 238 ppm of Fe, 78 ppm of Cr, 59 ppm of Sc and 36 ppm of Co) of 10.0 mm length, 3.6 mm width and 1.2 mm thickness, which will be denoted as beryl. The samples were analyzed using the CAMPARIS electronic microprobe at Université Pierre et Marie Curie - Paris 6, France.

X-ray absorption experiments were performed at LUCIA beamline in the French synchrotron facility SOLEIL.<sup>76</sup> The synchrotron was operating in the top-up mode at 2.75 GeV with a current of 400 mA. The beam spot size was set to 1 × 2 mm<sup>2</sup> and the energy range chosen to include the Al *K* edge (1559.6 eV in bulk)<sup>77</sup> was set from 1550 to 1700 eV, hence measuring pre-edge, XANES, and the beginning of EXAFS. Energy selection was performed through the combination of an HU52 “Apple II” type undulator and a double KTP (011) crystal monochromator. The pressure in the experimental chamber was 10<sup>-5</sup> mbar.

The samples were held between a parallelepipedic boron nitride furnace and a punched molybdenum lamella fixed to the furnace, allowing temperatures ranging from 300 to 950 K. This holder was fixed on a mobile stage, allowing translations along a cartesian *xyz* coordinate system plus a *z*-axis rotation, where the *x* axis corresponds to the beam direction and the *y* axis to the (horizontal) linear polarization  $\epsilon$  of the beam. In order to minimize self-absorption effects, the sample surfaces should be orthogonal to the beam axis. For fluorescence detection, the sample holder has been slightly rotated by 15° around *z* axis.

Corundum and beryl point groups are  $\bar{3}m$  and  $\frac{6}{m}mm$ , respectively.<sup>78,79</sup> This implies that both materials are dichroic in the electric dipole approximation.<sup>80</sup> The single crystals were set on the sample holder in order to measure successively  $\sigma_{\parallel}$  and  $\sigma_{\perp}$  spectra, corresponding respectively to  $\epsilon$  parallel and perpendicular to the high symmetry axis, i.e., the threefold symmetry axis for corundum and the sixfold symmetry axis for beryl.

Total fluorescence yield was measured by a four element silicon drift diode (SDD) detector with a total active area of 40 mm<sup>2</sup> protected from infrared and visible radiations by a thin beryllium window. In order to maximize the signal/noise ratio, each point was obtained after a six second acquisition time and five consecutive spectra were measured for each configuration (a configuration consists of a sample, an orientation and a temperature). This system produces five intensity outputs, one for each of the four SDD (*I*<sub>1</sub>, *I*<sub>2</sub>, *I*<sub>3</sub>, *I*<sub>4</sub>) and one for the incident beam (*I*<sub>0</sub>), measured before the sample. For each spectrum, each *I*<sub>*j*</sub> was then divided by *I*<sub>0</sub>, followed with a normalization on the 1590–1700 eV energy range (spectra are divided by their mean values on this region) giving (*I*<sub>*j*</sub>/*I*<sub>0</sub>)<sub>norm</sub>. Then, (*I*<sub>*j*</sub>/*I*<sub>0</sub>)<sub>av</sub> was calculated for each configuration by averaging five consecutive acquisitions of (*I*<sub>*j*</sub>/*I*<sub>0</sub>)<sub>norm</sub>. Since self-absorption effects are angle dependent and since the four SDD were not at the exact same spatial position, the four (*I*<sub>*j*</sub>/*I*<sub>0</sub>)<sub>av</sub> were not directly comparable. Self-absorption correction was performed using the formula<sup>81,82</sup>

$$\sigma_j(\omega) = \frac{\mu_j(\omega)}{\mu_j(\omega_0)} = \frac{N_j(\omega) \left( \beta \frac{\sin \theta_j}{\sin \theta_{f,j}} + \gamma \right)}{\left( \beta \frac{\sin \theta_j}{\sin \theta_{f,j}} + \gamma + 1 \right) - N_j(\omega)} \quad (1)$$

in which  $\mu_j$  is the edge absorption coefficient for detector  $j$ ,  $N_j(\omega) = \frac{(I_j/I_0)_{av}(\omega)}{(I_j/I_0)_{av}(\omega_0)}$  is the measured intensity on silicon drift diode  $j$ , normalized at a fixed pulsation  $\omega_0$  (chosen after the main edge at  $\hbar\omega_0 = 1653$  eV),  $\theta_i = 75^\circ$  is the angle between the beam axis and the sample surface,  $\theta_{f,j}$  is the angle between the sample surface and the outgoing fluorescence beam (which depends on each detector  $j$  position). Coefficient  $\beta$  is equal to  $\frac{\mu_{tot}(\omega_{fluo})}{\mu(\omega_0)}$ , where  $\omega_{fluo}$  is the  $K\alpha_1$ -fluorescence pulsation ( $\hbar\omega_{fluo} = 1486.7$  eV) and  $\mu_{tot}$  is the total absorption coefficient, including edge absorption  $\mu$  and background contribution  $\mu_{bg}$  of other atomic species in the sample. Finally,  $\gamma$  is equal to  $\frac{\mu_{bg}}{\mu}(\omega_0)$ . Values for  $\beta$  and  $\gamma$  are calculated based on crystal stoichiometry, atomic masses, unit cell geometry and using experimental tabulated atomic values.<sup>83</sup> For example,  $\mu_{tot}(\omega) = \sum_{at} \rho_{at} \mu_{at}^{table}(\omega)/M_{at}$  with  $\rho_{at} = N_{at} M_{at} N_A / V_{u.c.}$  where the sum is over all the atoms in the unit cell and for each atom  $\mu_{at}^{table}$  is the tabulated value in Barns/atom,  $M_{at}$  is the molar mass in  $\text{g mol}^{-1}$ ,  $N_{at}$  is the number of atoms ‘‘at’’ in the unit cell,  $V_{u.c.}$  is the unit cell volume in  $\text{cm}^3$ , and  $N_A$  is the Avogadro constant. Such a correction gives comparable values of  $\sigma_j$  for each detector, each one being normalized at the point of energy  $\hbar\omega_0$ . By using such a procedure to perform self-absorption correction, averaging over the four detectors is possible and gives the spectra  $\sigma_{\parallel}$  and  $\sigma_{\perp}$  shown in Sec. III. No smoothing was applied to the spectra.

### B. Theoretical methods

In order to explain the experimental spectral features observed when temperature is increased, first-principles calculations were performed in the density functional theory framework using the QUANTUM-ESPRESSO suite of codes.<sup>84</sup> The  $1s$  core-hole effects were taken into account within a  $2 \times 2 \times 2$  trigonal supercell for corundum, containing 80 atoms,<sup>78</sup> and a  $2 \times 1 \times 1$  hexagonal supercell for beryl, containing 58 atoms.<sup>79</sup> Troullier-Martins<sup>85</sup> norm-conserving pseudopotential were used. The pseudopotentials of Al and Si were generated using the  $3s$ ,  $3p$ , and  $3d$  orbitals as valence states, with 2.00 Bohr cutoff radii and considering the  $d$  states as local. The pseudopotential of the Al absorbing atom was generated with only one  $1s$  electron in the Al electronic configuration. The oxygen and beryllium pseudopotentials were built using the  $2s$  and  $2p$  as valence states (local part  $p$ ) with cutoff radii of 1.46 Bohr for O and of 2.00 Bohr for Be. Self-consistent charge densities were calculated in the generalized gradient approximation of Ref. 86, using the PWscf code, at the  $\Gamma$  point, with plane-wave energy cutoff of 80 Ry. Thereafter local and partial density of states were calculated using Löwdin projections on a  $4 \times 4 \times 4$   $k$ -point grid with a Gaussian broadening parameter of 0.3 eV. XANES cross section calculations were performed using the XSpectra code.<sup>87,88</sup> The all-electron wave function of the Al absorbing atom was reconstructed using the projector augmented wave method,<sup>89</sup> with augmentation region radii of 2.0 Bohr. The spectra were computed on  $4 \times 4 \times 4$   $k$ -point grid with a broadening parameter  $\gamma = 0.6$  eV.

Three methods were used to take into account the effects of vibrations without having to calculate phonon modes. First,

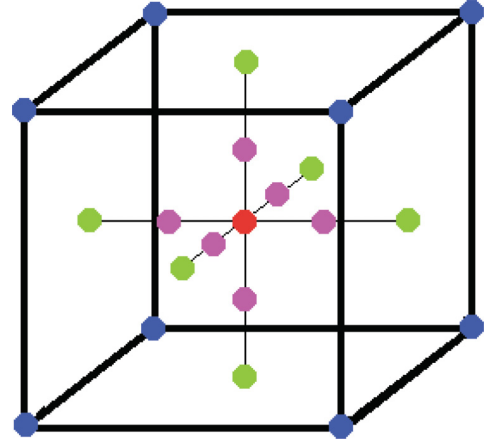


FIG. 1. (Color online) A sketch of the 21-point cubic grid used in Eq. (2).

adapting the idea of Ref. 15 on vibrations, only the absorbing atom was moved in the crystal structure with respect to its equilibrium position. This method will be referred to as method 1 in the following section. As vibrations are concerned, spectra for several absorbing atom displacements  $\mathbf{R}$  were calculated and averaged with a weighting core displacement distribution function  $\rho(\mathbf{R})$ . Within the harmonic approximation, this distribution function is linked to the thermal parameter matrix  $[U_{ij}]$  through  $\rho(\mathbf{R}) = \exp(-\mathbf{R} \cdot \frac{U^{-1}}{2} \cdot \mathbf{R})$ . The components of the rank-2 tensor  $U$  are given by x-ray or neutron scattering measurements. In this approximation, each spectrum is calculated with a static off-center absorbing atom, modifying hybridization between Al valence orbitals and neighboring atoms orbitals, thus changing valence states of the crystal. Vibration modeling comes from averaging spectra over a large number of absorbing atom displacements.

The absorbing atom motion was discretized on a cubic tridimensional grid consisting of 361 points. Equation (2) gives the cubic integral approximation on a grid of 21 points (see Fig. 1).<sup>90</sup>

$$\frac{1}{a^3} \int_{\text{cube}} f(\omega, \mathbf{R}) d\mathbf{R} = \frac{1}{360} \left( -496 f_m + 128 \sum f_r + 8 \sum f_f + 5 \sum f_v \right) + O(a^6), \quad (2)$$

where  $a$  is the length of the cube edge,  $f(\omega, \mathbf{R}) = \sigma_e(\omega, \mathbf{R}) \times \rho(\mathbf{R})$  is the weighted spectrum calculated with absorbing atom displaced of  $\mathbf{R}$ ,  $f_m = f(\omega, \mathbf{0})$  is the value at the center of the cube (red point),  $\sum f_r$  is the sum of the values of  $f$  at the four points halfway between the center of the cube and the center of each face (pink points),  $\sum f_f$  is the sum of the values of  $f$  at the center of each face (green points), and  $\sum f_v$  is the sum of the values of  $f$  at the vertices of the cube (blue points). The 361 point grid is an augmented  $3 \times 3 \times 3$  version of the 21 point one. This discretization would lead to a  $27 \times 21$  point grid, which reduces to only 361 points after avoiding double counting of similar points. The value of the integration cube edge  $a$  is given by  $2\sqrt{U_{\text{eig}}}$ , where  $U_{\text{eig}}$  are the eigenvalues of the  $U$  matrix. For the method 1 calculations,  $a$  was chosen equal to 0.3 Bohr radius, corresponding to  $U_{\text{eig}} = 0.07 \text{ \AA}^2$ , in

agreement with the thermal matrix parameters of corundum and beryl given in Refs. 79 and 91.

The second method, referred to as method 2 in the following, was described and mathematically justified in Refs. 1 and 56. It uses several approximations. First, vibrational energies are considered to be small with respect to the experimental resolution. In other words, this approximation accounts for the fact that the absorption process is much faster than atomic vibrations. Second, the strongly localized character of the  $1s$  initial wave function is used to restrict vibrations in the initial state to the absorbing atom motion only. Third, the crude Born-Oppenheimer approximation is made for the final

state, which assumes that atomic motions do not significantly change the final electronic states. Consequently, in method 2, the final states are determined for the atoms at their equilibrium positions, and only the absorbing atom position in the initial state is modified by vibrations. In practice, the  $1s$  initial wave function is no more centered on the equilibrium position of the absorbing atom. This shifted  $1s$  wave function is expanded over spherical harmonics centered at the equilibrium position and the  $\ell = 1$  component allows for dipole transition to  $3s$  states. Contrary to method 1, method 2 does not create (or increase) hybridization in the final state on the absorbing atom site. In the resulting absorption cross section formula

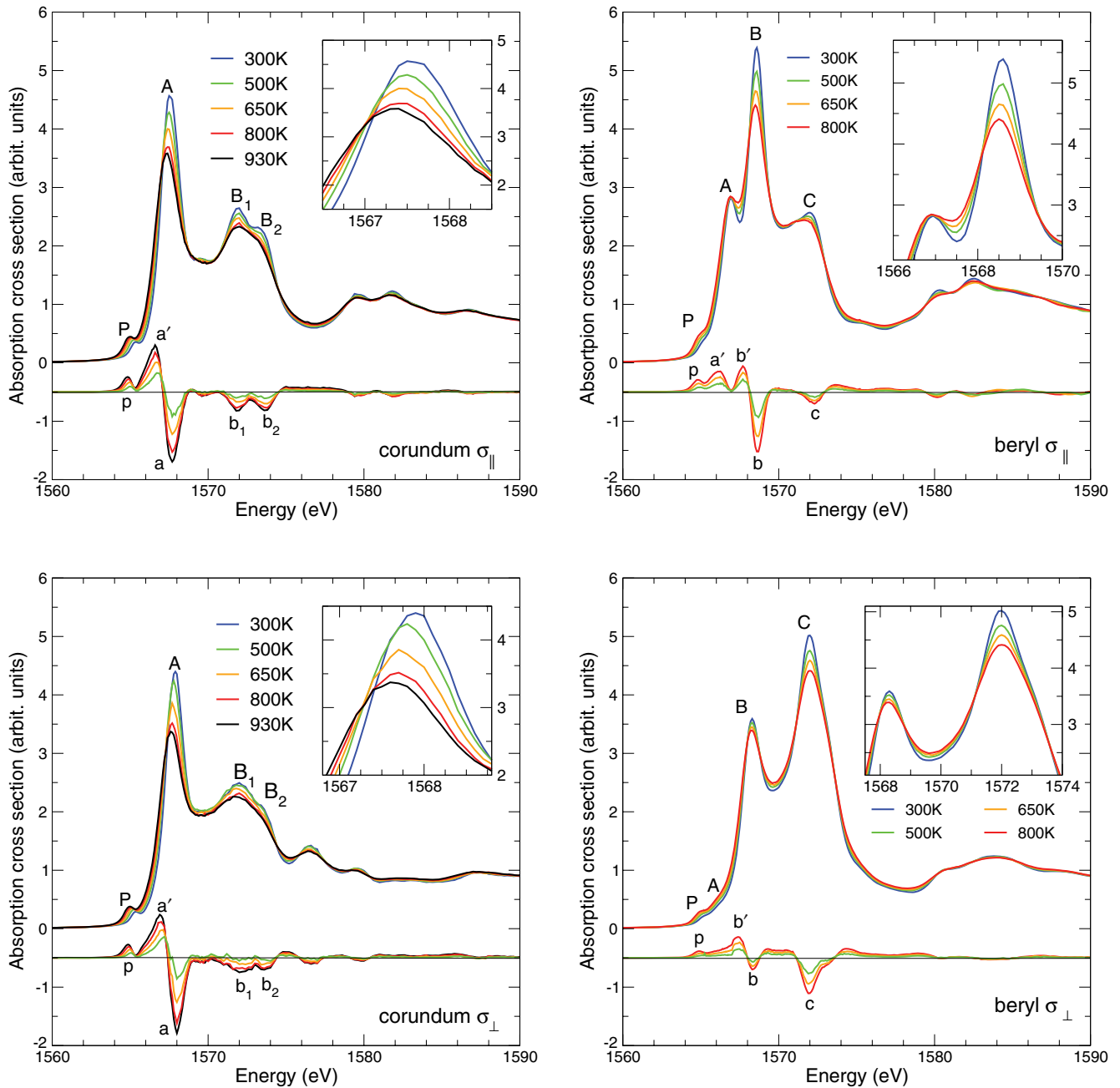


FIG. 2. (Color online) Experimental x-ray absorption polarized spectra of corundum (left) and beryl (right) at the Al  $K$  edge for different temperatures along with difference of each spectrum with respect to the 300 K reference. The top and bottom panels display the  $\sigma_{\parallel}$  and  $\sigma_{\perp}$  spectra, respectively. The upper-right insets use the same legend code and present a zoom on the main peak(s).

[Eq. (9) of Ref. 1], the integral over the absorbing atom displacement (in the initial state) is performed by using the same core displacement distribution and the same 361 point grid as those used in method 1. We used a shorter value for  $a$  ( $a = 0.1$  Bohr radius), corresponding to  $U_{\text{eig}} = 0.007 \text{ \AA}^2$ , as in Ref. 1.

The third method, denoted as method 3, is based on Fujikawa's work.<sup>54</sup> Within the Franck-Condon approximation, the effect of vibrations on x-ray absorption spectroscopy can be represented as the convolution of the phonon spectral function with the x-ray absorption spectrum at equilibrium position. Here, the phonon spectral function is approximated as a Gaussian distribution. Along with the two precedent methods, convoluted spectra are calculated. The convolution is performed between the first-principles equilibrium spectrum for a configuration and a Gaussian. The Gaussian equation is  $1/(\sqrt{2\pi}\sigma) \exp[-x^2/(2\sigma)^2]$ , with parameter  $\sigma$  being chosen for each configuration in order to reproduce the main edge intensity of method 1 spectra. Calculated spectra presented in Sec. IV are all normalized on the high-energy region, as was done for experimental data.

### III. EXPERIMENTAL RESULTS

Figure 2 shows the self-absorption corrected XANES spectra of corundum and beryl recorded at different temperatures for both orientations. Spectra originating at  $y = -0.5$  correspond to the difference  $\sigma(T) - \sigma(300 \text{ K})$ . We observe here for the first time the slow evolution of the Al  $K$  pre-edge feature with temperature. In addition to the expected increase in the peak intensity,<sup>1,56</sup> a shift toward lower energy of the pre-edge structure is observed when temperature increases. Furthermore, this effect appears for each sample and for each orientation and seems to be general as well as the decreasing intensities and broadening of main peaks with temperature.

Corundum  $\sigma_{\parallel}$  and  $\sigma_{\perp}$  spectra are quite similar up to 1575 eV: they both present a well-resolved pre-edge peak P, the main peak A followed by the double feature B<sub>1</sub> and B<sub>2</sub>. The 300-K polarized spectra are in agreement with those recorded in total electron yield shown in Ref. 92. As mentioned before, the intensity of peak P increases with temperature while its position is shifted towards lower energy. This is confirmed by the peak p in the difference spectra. Peak A also varies with temperature: it broadens, its intensity decreases and its position is shifted to lower energy (around 0.2 and 0.3 eV for  $\sigma_{\parallel}$  and  $\sigma_{\perp}$ , respectively). The decrease of peak A intensity corresponds to the difference spectra peak a and the shift to lower energy to a'. Peak a' is also related to the broadening of peak A with temperature. Peaks B<sub>1</sub> and B<sub>2</sub> intensities also diminish and they only form one broad peak at 930 K in  $\sigma_{\parallel}$  and  $\sigma_{\perp}$ .

Beryl  $\sigma_{\parallel}$  and  $\sigma_{\perp}$  spectra present much different shapes, unlike the case of corundum. In the energy range 1560–1575 eV, the  $\sigma_{\parallel}$  spectrum exhibits the pre-edge peak P and three main features A, B, and C, feature B being around twice more intense than A and C at 300 K. On the contrary, the  $\sigma_{\perp}$  spectrum exhibits two main features B and C, preceded by a small shoulder A and the pre-edge P. Peak C is more intense than peak B. Peak A and B of  $\sigma_{\perp}$  are located at 0.7 and 0.3 eV lower than their corresponding peaks in  $\sigma_{\parallel}$ . The pre-edge peak P is less intense in  $\sigma_{\perp}$  than in  $\sigma_{\parallel}$  at 300 K and its intensity

increases more in  $\sigma_{\parallel}$  than in  $\sigma_{\perp}$ . Indeed, the difference peak p appears better resolved and more intense in  $\sigma_{\parallel}$  than in  $\sigma_{\perp}$ . Peak A of  $\sigma_{\parallel}$  has a constant intensity with temperature but creates the difference peak a' due to broadening. The weak peak A of  $\sigma_{\perp}$  decreases in intensity with temperature. The B peak intensity also decreases with temperature as well as a slight shift of 0.1 eV toward lower energy, that creates peaks b and b' in the difference spectra, more pronounced in  $\sigma_{\parallel}$  than in  $\sigma_{\perp}$ . Peak C decreases and broadens with temperature, leading to feature c in the difference spectra.

The x-ray natural linear dichroisms (XNLD) for the various experimental temperatures are plotted in Fig. 3. The XNLD signals of the two samples are large and their variations with temperature do not change their general shape. XNLD on the pre-edge is quite small so that temperature dependence can hardly be seen. One mainly observes that some sharp XNLD maxima are reduced when the temperature increases: A1 and A2 peaks for corundum and B peak for beryl. One also notices that the rising edge and the maximum of the first XNLD feature is shifted to lower energies. This effect is observed for both

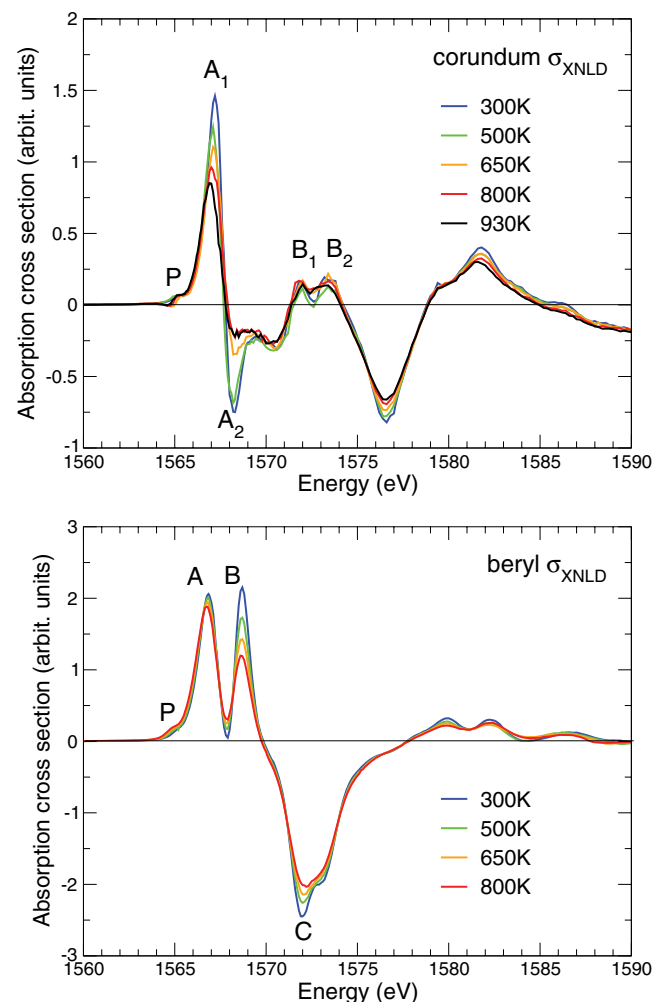


FIG. 3. (Color online) Temperature dependence of the x-ray natural linear dichroism (XNLD) measured at the Al  $K$  edge in corundum (top panel) and beryl (bottom panel). The cross section  $\sigma_{\text{XNLD}}$  is equal to the difference  $\sigma_{\parallel} - \sigma_{\perp}$ . Note that the y-axis range is twice larger for beryl than for corundum.

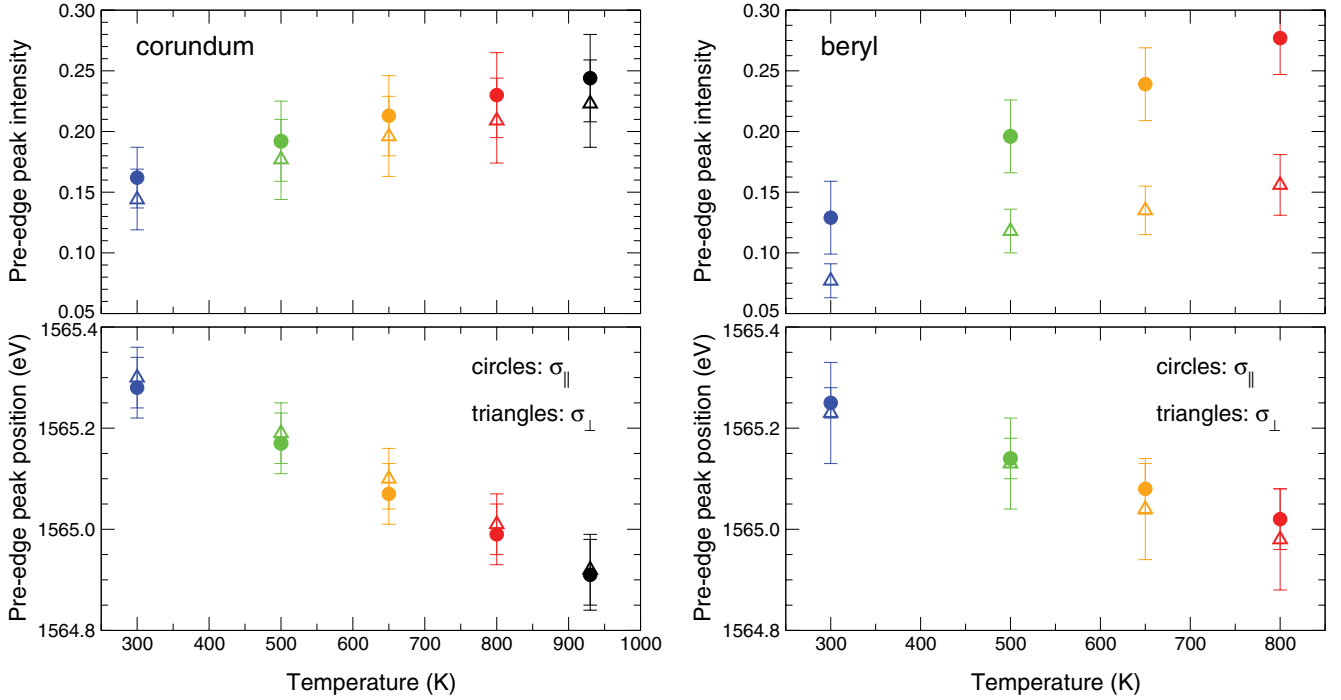


FIG. 4. (Color online) Pre-edge intensity and energy position for both orientations and for both samples as a function of temperature. The y-axis units of the upper panels are consistent with those of Fig. 2. The error bars correspond to an uncertainty of 10% on the best fit value ( $R^2 \simeq 0.9$ ).

corundum and beryl and can also be detected on the parallel and perpendicular cross sections. It is apparently a key feature of the temperature evolution of the spectra. The features at high energies are only slightly modified. Sum rules relates XNLD to the electric quadrupole distribution of the empty DOS with  $p$  symmetry on the aluminum site.<sup>93</sup> The sum rules were first derived in the absence of electron-phonon coupling and it is not yet clear whether the sum rules still hold when temperature is present. A theoretical analysis of the temperature dependence of XNLD sum rules is beyond the scope of the present paper but would eventually give information on the modification of the electronic structure with the temperature.

In order to more quantitatively describe the behavior of the pre-edge peak, extraction was performed using FITYK software,<sup>94</sup> which fits the main edge and pre-edge by the sum of an arctangent and a Gaussian. Figure 4 reports the fitted Gaussian intensities and center energies for each sample and each orientation. These quantitative values are in good agreement with the foregoing observations, a global increase of intensity with temperature is noticeable. While both orientations seem to progress similarly in corundum, it is not the case in beryl where  $\sigma_{\perp}$  intensities grow less rapidly than in  $\sigma_{\parallel}$ . Concerning peak position, both compounds and orientations present a similar shift toward lower energies.

#### IV. INTERPRETATION AND DISCUSSION

In this section, theoretical results are presented and discussed in order to try to understand the effects of temperature observed in the XANES spectra shown in Sec. III. First, a density of states (DOS) analysis is performed for both compounds

showing the involvement of the  $3s$  empty states of the Al absorbing atom in the process of pre-edge peak creation. Then, theoretical spectra obtained by using the three different methods described in Sec. II B are shown and compared together.

##### A. DOS calculations: the nature of the pre-edge peak

The pre-edge peak is not reproduced by purely electric dipole  $1s \rightarrow p$  transitions, as shown in the top panels of Fig. 5. Hence some transition toward non- $p$  states must be at stake. The bottom panels of Fig. 5 present partial and local density of states (DOS) of corundum and beryl. The  $s$ ,  $p$ , and  $d$  partial empty DOS are plotted for the absorbing aluminum atom (with a core hole), only the  $s$  and  $p$  for the first six oxygen neighbors, and again the  $s$ ,  $p$ , and  $d$  for the aluminum next neighbor. The similarity between the absorbing Al  $3p$  local DOS and the XANES spectra shows that the later is a good probe of the former. In the pre-edge region, the role of the absorbing Al atom is clear as the pre-edge position coincides with its  $3s$  projected DOS. In the case of beryl, a certain proportion of absorbing Al  $3d$  states is also present in the pre-edge region. However, the  $3d$  states do not contribute to the absorption coefficient via electric quadrupole ( $1s \rightarrow 3d$ ) transitions. Indeed, the calculated electric quadrupole transitions are negligible in the whole XANES region, since they are found to be lower than  $0.25 \cdot 10^{-4}$  in the normalized units used in the top panels of Fig. 5. Aluminum atoms are in 3 and 32 symmetry point group sites in corundum and beryl, respectively. Thus, according to group theory, a mixing of aluminum  $s$  and  $p_z$  states is allowed (on the contrary, the Al  $p_x$ - $p_y$  states cannot hybridize with the Al  $s$  states). Our calculations are consistent with these

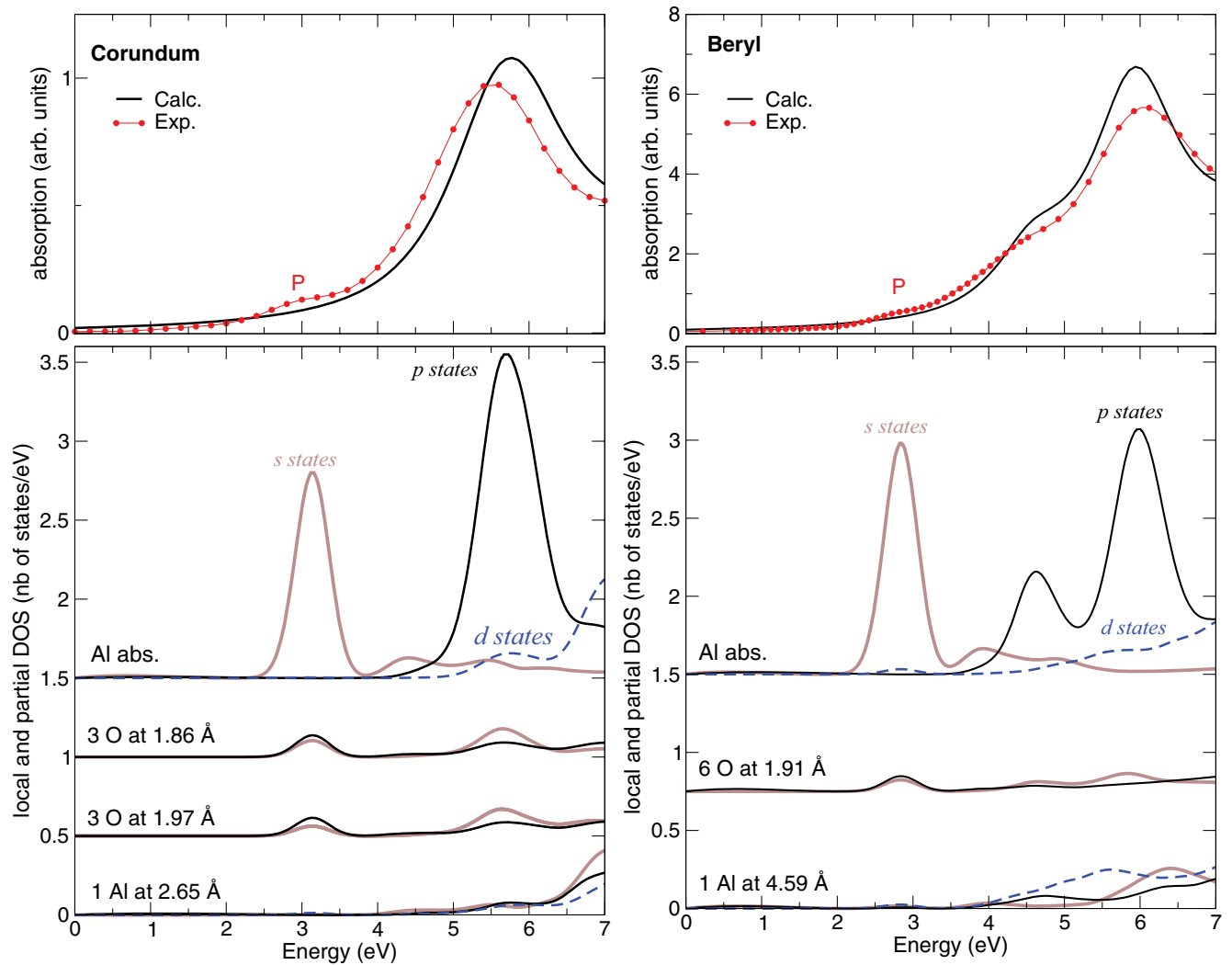


FIG. 5. (Color online) Top: calculated and experimental isotropic  $(2\sigma_{\perp} + \sigma_{\parallel})/3$  spectra at the Al  $K$  edge of corundum (left) and beryl (right). Bottom: partial and local density of states of corundum (left) and beryl (right) calculated for the supercell including a  $1s$  core hole. The role of the Al  $3s$  of the absorbing atom is prominent in the pre-edge region.

predictions. Indeed, the  $p_z$  DOS of the Al absorbing atom, although indistinguishable in Fig. 5, is not zero at the position of the Al  $3s$  peak. Nevertheless the  $s$ - $p_z$  mixing of the Al states is definitely too weak to give rise to a pre-edge peak in the  $\sigma_{\parallel}$  spectrum. The  $3s$  states of the absorber interact with both  $s$  and  $p$  empty states of the oxygen neighbors while the aluminum next neighbors do not contribute to the pre-edge since their DOS are at higher energies. The presence of the  $1s$  core hole on the absorbing atom shifts the first empty states to the bottom of the conduction band and leads to the pre-edge and first peaks of XANES.

### B. Theoretical XANES spectra: vibration modeling

The DOS analysis indicates that the modeling of the experimental Al  $K$ -edge XANES spectra has to allow transitions toward the  $3s$  states of the absorbing Al. Both method 1 and method 2 presented in Sec. II B are able to achieve this

goal. Figure 6 displays the theoretical spectra obtained by the three methods described in Sec. II B, together with the spectra calculated with the atoms at their equilibrium positions (labeled “equil.”). Difference spectra with respect to the equil. reference are also plotted. It should be noted that the equil. spectra do not strictly correspond to the 0-K case since they do not take the zero point motion of nuclei into account. Experimental spectra measured at 20 K on the same samples (not shown here) still exhibit the pre-edge peak, even without active phonon modes, and the pre-edge intensity at 20 K is quite similar to that at 300 K. At room temperature nearly no phonon mode is active,<sup>95,96</sup> thus the pre-edge feature observable in the 20–300K range seems to be essentially due to the quantum zero-point motion effect.

Corundum  $\sigma_{\perp}$  and  $\sigma_{\parallel}$  equil. spectra reproduce well the overall shape of the experimental spectra, except in the pre-edge-region. Switching on method 1 mostly affects the main edge A intensity and shifts its position by 0.2 eV with respect to equil. spectra. Peaks a and a' of the difference

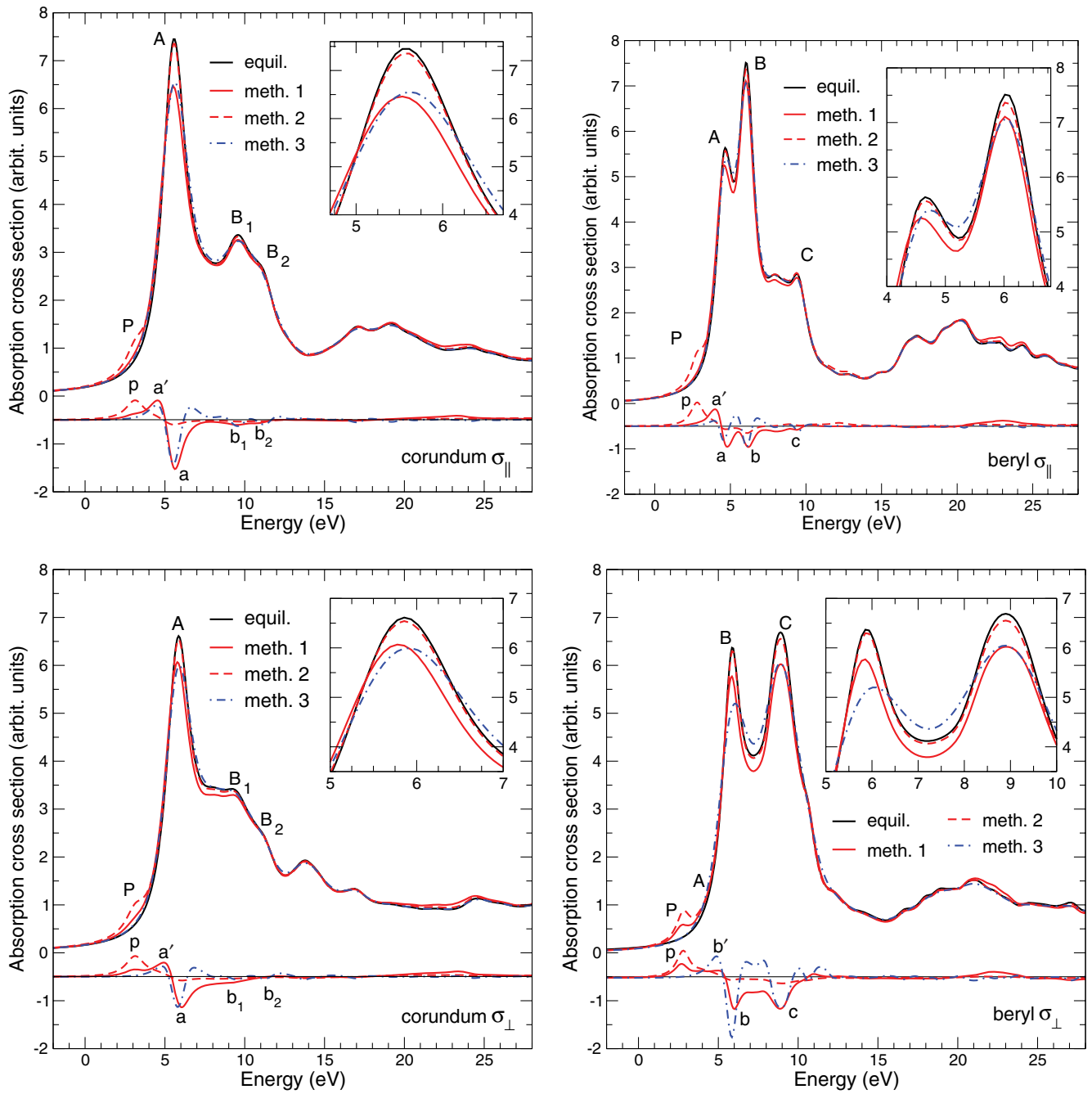


FIG. 6. (Color online) Calculated  $\sigma_{\parallel}$  and  $\sigma_{\perp}$  spectra at the Al K edge of corundum (left) and beryl (right) along with difference of each spectrum with respect to the equil. reference. The “equil.” spectra correspond to DFT calculations performed with the atoms at the equilibrium positions. The spectra labeled “meth. 1,” “meth. 2,” and “meth. 3” refer to the three methods of vibration modeling described in Sec. II. The upper-right insets use the same legend code and present a zoom on the main peak(s).

spectra are the signature of these effects. Peak  $B_1$  intensity slightly decreases for both orientations while peak  $B_2$  is nearly unchanged. Small difference peaks  $b_1$  and  $b_2$  confirm these points. A weak pre-edge peak  $P$  seems to appear for both orientations. Although method 1 is not able to grow a well-resolved pre-edge peak, it provides difference spectra that are very similar to the temperature-dependent experimental difference spectra of Fig. 2 (left panels). On the contrary, method 2 gives rise to a more important pre-edge peak, which

is in better agreement with experiment. The difference peak  $p$  shows a really distinct Gaussian-like shape. The rest of the spectrum is nearly unchanged and this is confirmed by the flat difference spectra. Method 3 spectra do not show a pre-edge but have a visible impact on main edge peak  $A$ , by broadening it, lowering its intensity, and shifting its energy to higher energies by 0.1 eV, i.e., in the opposite direction as compared to temperature-dependent experiments. These effects are visible on difference peaks  $a$  and  $a'$ .

Beryl  $\sigma_{\parallel}$  and  $\sigma_{\perp}$  equil. spectra also reproduce the experimental spectra quite well, except for some of the peak intensities. While peaks A and C are of similar amplitude in  $\sigma_{\parallel}$  experimental spectrum, the intensity of peak A is twice the one of peak C in the equil. spectrum. On the opposite, peaks B and C have similar intensity in  $\sigma_{\perp}$  equil. spectrum while peak B is 1.5 times less intense than peak C in the 300-K experimental spectrum. By using method 1 for  $\sigma_{\parallel}$ , no pre-edge peak seems to arise, peak A is decreased and shifted to lower energy by 0.2 eV, peak B is also decreased, and peak C remains stable. These effects are also visible through the shape of the difference spectrum. Thus vibrations treated within method 1 are not able to well reproduce the temperature-dependence trend observed in the top-right panel of Fig. 2. In the case of  $\sigma_{\perp}$ , method 1 leads to theoretical spectrum in better agreement with the x-ray absorption temperature dependence seen in the bottom-right panel of Fig. 2. Indeed, method 1 enables a well resolved pre-edge peak P to rise (clearly confirmed by difference peak p), and a very weak peak A to appear. It also moves B to lower energy (0.2 eV) and decreases the intensity of peaks B and C. Here again, method 2 has no influence on peak position, it nearly does not change the amplitude of peaks A, B, C in  $\sigma_{\parallel}$  and B, C in  $\sigma_{\perp}$ . However, it creates the pre-edge P at the right energy, but with too high an intensity. The value of the  $U$  parameter used in method 2 might be overestimated for beryl and yielded a too pronounced pre-edge peak. Method 3 decreases the amplitude of main peaks. It also shifts peak A of  $\sigma_{\parallel}$  and B of  $\sigma_{\perp}$  towards higher energies that, as in corundum, is the opposite of what is seen experimentally. A slight broadening appears and is more visible in  $\sigma_{\perp}$ .

To summarize, method 1 leads to difference spectra that reproduce quite well the temperature-dependent trend observed experimentally in most cases. Nevertheless, the impact of vibrations as treated by method 1 is not sufficient to systematically reproduce the experimental pre-edge feature. The  $p$ - $s$  hybridization on the Al site induced by this method is not satisfactory enough. In method 1, the vibration modeling results in integration, over a cubic volume around the absorbing atom, of cross sections calculated for absorbing Al isotropically displaced inside this volume. In other words, this method equally considers the contributions of Al motion along all directions. Some Al displacements would be favored by taking into account the phonon modes of the material, what could substantially improve the agreement between theoretical and experimental spectra at least in the pre-edge region. Method 2 spectra all exhibit a well-defined pre-edge peak, corresponding to dipole  $1s$ - $3s$  transitions, which are allowed by the displacement of the  $1s$  wave function.<sup>1,56</sup> Nevertheless, method 2 has nearly no impact on the peak intensity above the edge, and is unable to produce any shift of the features. This last result was expected because of the use of the crude Born-Oppenheimer approximation in method 2. Within this approximation, the transition energies are evaluated for the atoms at their equilibrium positions, hence the spectral features remain at the same energy positions as in equil. spectra. Method 3 spectra, as expected, do not exhibit any pre-edge peak, and present main-edge peaks less intense and shifted in energy. However, the energy shift goes the wrong way, i.e., to higher energies. Therefore a simple convolution of the equil. spectra seems to be inappropriate to account for

the temperature-dependence of the XANES spectra observed experimentally.

Thermal expansion effects have been evaluated in the case of corundum by performing a XANES calculation for the structural parameters refined at 2170 K (153 K below the melting point).<sup>97</sup> A contraction of the highest energy XANES features has been noticed. Such an effect was expected according to the predictions of the Natoli's rule.<sup>98</sup> However, it is contradictory with what has been experimentally observed when temperature is increased (see Fig. 2). Therefore, the thermal expansion is unable to explain the temperature dependence of the Al  $K$ -edge XANES spectra in corundum and beryl.

The calculations carried out in this study clearly show the crucial role of vibrations in the pre-edge region and partially explain the temperature dependence observed in the whole XANES region. However, none of the three methods used here is fully satisfactory. A great improvement would be to use PIMD as Schwartz *et al.* did in the case of two isolated organic molecules.<sup>66</sup> But the computational cost of PIMD simulations in solids, such as corundum or beryl, would be a serious limiting factor. A more reasonable way to account for the thermal fluctuation of XANES at the Al  $K$  edge would consist of the generation of atomic configurations of the whole crystal from the dynamical matrix of the system. The temperature-dependent XANES theoretical spectrum would then result in an average of cross sections calculated for a large number of configurations. An analogous methodology has been successfully employed to account for the temperature dependence of nuclear magnetic resonance chemical shift in MgO.<sup>99</sup>

## V. CONCLUSION

In this study, temperature-dependent Al  $K$ -edge XANES spectra of corundum and beryl have been presented for temperature ranging from 300 to 930 K. The XANES spectra were measured on single-crystals with the polarization vector of the x-ray beam parallel and perpendicular to the high-symmetry axis of the minerals, allowing the investigation of the temperature dependence of the  $\sigma_{\parallel}$  and  $\sigma_{\perp}$  components. This series of experiments shows that the pre-edge peak is very sensitive to thermal fluctuations: the pre-edge peak intensity grows and its position shifts to lower energy as temperature increases. These variations do not depend much on the x-ray polarization. Thermal fluctuations are also visible above the pre-edge region, through an intensity decrease of the main features and, in the case of corundum, through a slight shift to lower energy of the first main peak.

First-principles DFT calculations have confirmed the Al  $3s$  nature of the pre-edge peak in both minerals, and have shown that the introduction of vibrations within the XANES calculation gives rise to a pre-edge peak. Our experimental and theoretical results on the Al  $K$  pre-edge in corundum and beryl suggest that vibrations (the zero-point motion and also temperature) could be able to induce a pre-edge feature at the Al  $K$  edge in other minerals. This conclusion might bring a reinterpretation of the appearance of a pre-edge peak observed at the Al  $K$  edge in zeolites when temperature is increased, which was interpreted as the signature of threefold coordinated Al.<sup>43,44,46</sup>

We have used three existing methods to take nuclear motion into account in the Al  $K$ -edge XANES modeling. Method 2

permits to account for the existence of the pre-edge peak, which mainly originates from zero point motion in corundum and beryl. Method 2 is therefore acceptable for XANES modeling at low temperature, but it fails to reproduce the spectral energy shifts observed at high temperature. On the contrary, method 1 provides spectra in better agreement with the high temperature experiments, but is not suitable to the XANES calculation at low temperature. Indeed method 1 is unable to give rise to the well-defined pre-edge peak observed experimentally. Finally, method 3 is found to be inappropriate to account for the impact of the thermal fluctuations on XANES at the Al *K*-edge. These theoretical results will be particularly useful for upcoming works, giving insight of what has to be considered in the modeling of temperature-dependent XANES spectra.

#### ACKNOWLEDGMENTS

We are grateful to Steve Collins for showing us the temperature dependence of Ti *K*-edge spectra that he measured on rutile at beamline I16 at Diamond Light Source. This work was granted access to the HPC resources of IDRIS under the allocation 2011-1202 and 2012-100172 made by GENCI (Grand Equipement National de Calcul Intensif). Experiments were performed on the LUCIA beamline at SOLEIL Synchrotron, France (proposal numbers 20100888 and 99110023). We are grateful to the SOLEIL staff for smoothly running the facility. We also acknowledge Pierre Lagarde and Francesco Mauri for fruitful discussions.

\*damien.manuel@impmc.upmc.fr

- <sup>1</sup>C. Brouder, D. Cabaret, A. Juhin, and P. Sainctavit, *Phys. Rev. B* **81**, 115125 (2010).
- <sup>2</sup>D. Li, G. M. Bancroft, M. E. Fleet, X. H. Feng, and Y. Pan, *Am. Mineral.* **80**, 432 (1995).
- <sup>3</sup>D. Li, G. M. Bancroft, M. Kasrai, M. E. Fleet, X. H. Feng, and K. H. Tan, *Am. Mineral.* **79**, 785 (1994).
- <sup>4</sup>A. L. Ankudinov and J. J. Rehr, *Phys. Scr. T* **115**, 24 (2005).
- <sup>5</sup>I. Minkov, F. Gel'mukhanov, R. Friedlein, W. Osikowicz, C. Suess, G. Öhrwall, S. L. Sorensen, S. Braun, R. Murdey, W. R. Salaneck, and H. Ågren, *J. Chem. Phys.* **121**, 5733 (2004).
- <sup>6</sup>I. Minkov, F. Gel'mukhanov, H. Ågren, R. Friedlein, C. Suess, and W. R. Salaneck, *J. Phys. Chem. A* **109**, 1330 (2005).
- <sup>7</sup>A. Schöll, Y. Zou, L. Kilian, D. Hübner, D. Gador, C. Jung, S. G. Urquhart, T. Schmidt, R. Fink, and E. Umbach, *Phys. Rev. Lett.* **93**, 146406 (2004).
- <sup>8</sup>S. Carniato, R. Täieb, E. Kuk, Y. Luo, and B. Brena, *J. Chem. Phys.* **123**, 214301 (2005).
- <sup>9</sup>V. Ilakovac, S. Carniato, J.-J. Gallet, E. Kuk, D. Horvatić, and A. Ilakovac, *Phys. Rev. A* **77**, 012516 (2008).
- <sup>10</sup>N. Schmidt, T. Clark, S. G. Urquhart, and R. H. Fink, *J. Chem. Phys.* **135**, 144301 (2011).
- <sup>11</sup>S. Stranges, R. Richter, and M. Alagia, *J. Chem. Phys.* **116**, 3676 (2002).
- <sup>12</sup>O. Durmeyer, J.-P. Kappler, E. Beaurepaire, J. M. Heintz, and M. Drillon, *J. Phys.: Condens. Matter* **2**, 6127 (1990).
- <sup>13</sup>O. Durmeyer, E. Beaurepaire, J.-P. Kappler, C. Brouder, and F. Baudelet, *J. Phys.: Condens. Matter* **22**, 125504 (2010).
- <sup>14</sup>S. P. Collins and V. E. Dmitrienko (private communication).
- <sup>15</sup>S. Nozawa, T. Iwazumi, and H. Osawa, *Phys. Rev. B* **72**, 121101(R) (2005).
- <sup>16</sup>B. Ravel, E. A. Stern, Y. Yacobi, and F. Dogan, *Jpn. J. Appl. Phys.* **32**, 782 (1993).
- <sup>17</sup>B. Ravel and E. A. Stern, *Physica B* **208/209**, 316 (1995).
- <sup>18</sup>B. Ravel and E. A. Stern, *J. Phys. IV* **7**, C2 1223 (1997).
- <sup>19</sup>R. V. Vedrinskii, V. L. Kraizman, A. A. Novakovich, P. V. Demekhin, S. V. Urzhidin, B. Ravel, and E. A. Stern, *J. Phys. IV* **7**, C2 107 (1997).
- <sup>20</sup>K. Sato, T. Miyanaga, S. Ikeda, and D. Diop, *Phys. Scr. T* **115**, 359 (2005).
- <sup>21</sup>T. Hashimoto, A. Yoshiasa, M. Okube, H. Okudera, and A. Nakatsuka, *AIP Conf. Proc.* **882**, 428 (2007).
- <sup>22</sup>F. Bridges, C. H. Booth, G. H. Kwei, J. J. Neumeier, and G. A. Sawatzky, *Phys. Rev. B* **61**, R9237 (2000).
- <sup>23</sup>Q. Qian, T. A. Tyson, C.-C. Kao, M. Croft, S.-W. Cheong, and M. Greenblatt, *Phys. Rev. B* **62**, 13472 (2000).
- <sup>24</sup>N. Mannella, A. Rosenhahn, M. Watanabe, B. Sell, A. Nambu, S. Ritchey, E. Arenholz, A. Young, Y. Tomioka, and C. S. Fadley, *Phys. Rev. B* **71**, 125117 (2005).
- <sup>25</sup>Y. T. Tsai, W. J. Chang, S. W. Huang, J.-Y. Lin, J. Y. Lee, J. M. Chen, K. H. Wu, T. M. Uen, Y. S. Gou, and J. Y. Juang, *Physica B* **404**, 1404 (2009).
- <sup>26</sup>R. V. Vedrinskii, E. S. Nazarenko, M. P. Lemesko, V. Nassif, O. Proux, A. A. Novakovich, and Y. Joly, *Phys. Rev. B* **73**, 134109 (2006).
- <sup>27</sup>V. A. Shuvaeva, K. Yanagi, K. Yagi, K. Sakaue, and H. Terauchi, *J. Synchrotron Rad.* **6**, 367 (1999).
- <sup>28</sup>V. A. Shuvaeva, Y. Azuma, K. Yagi, K. Sakaue, and H. Terauchi, *J. Synchrotron Rad.* **8**, 833 (2001).
- <sup>29</sup>V. A. Shuvaeva, I. Pirog, Y. Azuma, K. Yagi, K. Sakaue, H. Terauchi, I. P. Raevskii, K. Zhuchkov, and M. Yu. Antipin, *J. Phys.: Condens. Matter* **15**, 2413 (2003).
- <sup>30</sup>V. A. Shuvaeva, Y. Azuma, I. P. Raevskii, K. Yagi, K. Sakaue, and H. Terauchi, *Ferroelectrics* **299**, 103 (2004).
- <sup>31</sup>M. P. Lemesko, E. S. Nazarenko, A. A. Gonchar, L. A. Reznichenko, T. I. Nedoseykina, A. A. Novakovich, O. Mathon, Y. Joly, and R. V. Vedrinskii, *Phys. Rev. B* **76**, 134106 (2007).
- <sup>32</sup>A. Deb, J. M. Ralph, E. J. Cairns, and U. Bergmann, *Phys. Rev. B* **73**, 115114 (2006).
- <sup>33</sup>A. Braun, S. Erat, A. K. Ariffin, R. Manzke, H. Wadati, T. Graule, and L. J. Gauckler, *Appl. Phys. Lett.* **99**, 202112 (2011).
- <sup>34</sup>J. Herrero-Martín, J. L. García-Muñoz, S. Valencia, C. Frontera, J. Blasco, A. J. Barón-González, G. Subías, R. Abrudan, F. Radu, E. Dudzik, and R. Feyerherm, *Phys. Rev. B* **84**, 115131 (2011).
- <sup>35</sup>M. Hidaka, N. Tokiwa, M. Oda, J.-Y. Choi, and J. M. Lee, *Phase Transitions* **76**, 905 (2003).
- <sup>36</sup>B. Poumellec, R. Cortès, E. Loisy, and J. Berthon, *Phys. Status Solidi B* **183**, 335 (1994).
- <sup>37</sup>F. Farges, G. E. Brown Jr., A. Navrotsky, H. Gan, and J. J. Rehr, *Geoch. Cosmoch. Acta* **60**, 3055 (1996).

- <sup>38</sup>O. Dargaud, G. Calas, L. Cormier, L. Galoisy, C. Jousseume, G. Querel, and M. Newville, *J. Am. Ceram. Soc.* **93**, 342 (2010).
- <sup>39</sup>D. R. Neuville, D. de Ligny, L. Cormier, G. S. Henderson, J. Roux, A.-M. Flank, and P. Lagarde, *Geoch. Cosmoch. Acta* **73**, 3410 (2009).
- <sup>40</sup>D. R. Neuville, L. Cormier, D. de Ligny, J. Roux, A.-M. Flank, and P. Lagarde, *Am. Mineral.* **93**, 228 (2008).
- <sup>41</sup>D. de Ligny, D. R. Neuville, L. Cormier, J. Roux, G. S. Henderson, G. Panczer, S. Shoval, A.-M. Flank, and P. Lagarde, *J. Non-Cryst. Solids* **355**, 1099 (2009).
- <sup>42</sup>P. Wernet, D. Nordlund, U. Bergmann, M. Cavalleri, M. Odelius, H. Ogasawara, L. Å. Näslund, T. K. Hirsch, L. Ojamäe, P. Glatzel, L. G. M. Pettersson, and A. Nilsson, *Science* **304**, 995 (2004).
- <sup>43</sup>J. A. van Bokhoven, A. M. J. van der Eerden, and D. C. Koningsberger, *J. Am. Chem. Soc.* **125**, 7435 (2003).
- <sup>44</sup>J. A. van Bokhoven, *Phys. Scr. T* **115**, 76 (2005).
- <sup>45</sup>A. Omegna, R. Prins, and J. A. van Bokhoven, *J. Phys. Chem. B* **109**, 9280 (2005).
- <sup>46</sup>G. Agostini, C. Lamberti, L. Palin, M. Milanesio, N. Danilina, B. Xu, M. Janousch, and J. A. van Bokhoven, *J. Am. Chem. Soc.* **132**, 667 (2010).
- <sup>47</sup>L. R. Aramburo, E. de Smi, B. Arstad, M. M. van Schooneveld, L. Sommer, A. Juhin, T. Yokosawa, H. W. Zandbergen, U. Olsbye, F. de Groot, and B. M. Weckuysen, *Angew. Chem. Int. Ed.* **51**, 3616 (2012).
- <sup>48</sup>S. J. A. Figueroa, S. J. Stewart, T. Rueda, A. Hernando, and P. de la Presa, *J. Phys. Chem. C* **115**, 5500 (2011).
- <sup>49</sup>T. Haupricht, R. Sutarro, M. W. Haverkort, H. Ott, A. Tanaka, H. H. Hsieh, H.-J. Lin, C. T. Chen, Z. Hu, and L. H. Tjeng, *Phys. Rev. B* **82**, 035120 (2010).
- <sup>50</sup>P. Link, P. Glatzel, K. Kvashnina, R. I. Smith, and U. Ruschewitz, *Inorg. Chem.* **50**, 5587 (2011).
- <sup>51</sup>F. D. Vila, J. J. Rehr, H. H. Rossner, and H. J. Krappe, *Phys. Rev. B* **76**, 014301 (2007).
- <sup>52</sup>F. D. Vila, V. E. Lindahl, and J. J. Rehr, *Phys. Rev. B* **85**, 024303 (2012).
- <sup>53</sup>T. Fujikawa, *J. Phys. Soc. Jpn.* **65**, 87 (1996).
- <sup>54</sup>T. Fujikawa, *J. Phys. Soc. Jpn.* **68**, 2444 (1999).
- <sup>55</sup>H. Arai, N. Ueno, and T. Fujikawa, *AIP Conf. Proc.* **882**, 108 (2007).
- <sup>56</sup>D. Cabaret and C. Brouder, *J. Phys.: Conf. Ser.* **190**, 012003 (2009).
- <sup>57</sup>H. Köppel, F. X. Gadea, G. Klatt, J. Schirmer, and L. S. Cederbaum, *J. Chem. Phys.* **106**, 4415 (1997).
- <sup>58</sup>B. Kempgens, B. S. Itchkawitz, J. Feldhaus, A. M. Bradshaw, H. Köppel, M. Döscher, F. X. Gadea, and L. S. Cederbaum, *Chem. Phys. Lett.* **277**, 436 (1997).
- <sup>59</sup>A. B. Trofimov, T. E. Moskovskaya, E. V. Gromov, H. Köppel, and J. Schirmer, *Phys. Rev. A* **64**, 022504 (2001).
- <sup>60</sup>A. B. Trofimov, E. V. Gromov, H. Köppel, J. Schirmer, K. C. Prince, R. Richter, M. de Simone, and M. Coreno, *J. Phys. B* **36**, 3805 (2003).
- <sup>61</sup>D. Duflot, S. Zeggari, and J.-P. Flament, *Chem. Phys.* **327**, 518 (2006).
- <sup>62</sup>D. Duflot, J.-P. Flament, A. Giuliani, J. Heinesch, and M.-J. Hubin-Franskin, *Int. J. Mass Spectrom.* **277**, 70 (2009).
- <sup>63</sup>C. Kolczewski, R. Püttner, O. Plashkevych, H. Ågren, V. Staemmler, M. Martins, G. Snell, A. S. Schlachter, M. Sant'Anna, G. Kaindl, and L. G. M. Pettersson, *J. Chem. Phys.* **115**, 6426 (2001).
- <sup>64</sup>G. Herzberg and E. Teller, *Z. Physik. Chem. B* **21**, 410 (1933).
- <sup>65</sup>J. S. Uejio, C. P. Schwartz, R. J. Saykally, and D. Prendergast, *Chem. Phys. Lett.* **467**, 195 (2008).
- <sup>66</sup>C. P. Schwartz, J. S. Uejio, R. J. Saykally, and D. Prendergast, *J. Chem. Phys.* **130**, 184109 (2009).
- <sup>67</sup>C. P. Schwartz, R. J. Saykally, and D. Prendergast, *J. Chem. Phys.* **133**, 044507 (2010).
- <sup>68</sup>S. Fatehi, C. P. Schwartz, R. J. Saykally, and D. Prendergast, *J. Chem. Phys.* **132**, 094302 (2010).
- <sup>69</sup>F. Della Sala, R. Rousseau, A. Görling, and D. Marx, *Phys. Rev. Lett.* **92**, 183401 (2004).
- <sup>70</sup>A. Kaczmarek, M. Shiga, and D. Marx, *J. Phys. Chem. A* **113**, 1985 (2009).
- <sup>71</sup>S. Mazevet and G. Zérah, *Phys. Rev. Lett.* **101**, 155001 (2008).
- <sup>72</sup>V. Recoules and S. Mazevet, *Phys. Rev. B* **80**, 064110 (2009).
- <sup>73</sup>O. Peyrusse, *High Energy Density Phys.* **6**, 357 (2010).
- <sup>74</sup>A. Benuzzi-Mounaix, F. Dorchie, V. Recoules, F. Festa, O. Peyrusse, A. Levy, A. Ravasio, T. Hall, M. Koenig, N. Amadou, E. Brambrink, and S. Mazevet, *Phys. Rev. Lett.* **107**, 165006 (2011).
- <sup>75</sup>A. Lévy, F. Dorchie, A. Benuzzi-Mounaix, A. Ravasio, F. Festa, V. Recoules, O. Peyrusse, N. Amadou, E. Brambrink, T. Hall, M. Koenig, and S. Mazevet, *Phys. Rev. Lett.* **108**, 055002 (2012).
- <sup>76</sup>A.-M. Flank, G. Cauchon, P. Lagarde, S. Bac, M. Janousch, R. Wetter, J.-M. Dubuisson, M. Idir, F. Langlois, T. Moreno, and D. Vantelon, *Nucl. Instrum. Meth. B* **246**, 269 (2006).
- <sup>77</sup>J. A. Bearden and A. F. Burr, *Rev. Mod. Phys.* **39**, 125 (1967).
- <sup>78</sup>R. E. Newnham and Y. M. de Haan, *Z. Kristallogr.* **117**, 235 (1962).
- <sup>79</sup>R. M. Hazen, A. Y. Au, and L. W. Finger, *Am. Mineral.* **71**, 977 (1986).
- <sup>80</sup>C. Brouder, *J. Phys.: Condens. Matter* **2**, 701 (1990).
- <sup>81</sup>J. Goulon, C. Goulon-Ginet, R. Cortes, and J. M. Dubois, *J. Phys.* **43**, 539 (1982).
- <sup>82</sup>D. Haskel, FLUO: Correcting XANES for self-absorption in fluorescence measurements, 1999, [<http://www.aps.anl.gov/xfd/people/haskel/fluo.html>].
- <sup>83</sup>E. B. Saloman, J. H. Hubbell, and J. H. Scofield, *Atom. Data Nucl. Data Tables* **38**, 1 (1988).
- <sup>84</sup>P. Giannozzi, S. Baroni, N. Bonini, M. Calandra, R. Car, C. Cavazzoni, D. Ceresoli, G. L. Chiarotti, M. Cococcioni, I. Dabo, A. Dal Corso, S. Fabris, G. Fratesi, S. de Gironcoli, R. Gebauer, U. Gerstmann, C. Gougoussis, A. Kokalj, M. Lazzeri, L. Martin-Samos, N. Marzari, F. Mauri, R. Mazzarello, S. Paolini, A. Pasquarello, L. Paulatto, C. Sbraccia, S. Scandolo, G. Sclauzero, A. P. Seitsonen, A. Smogunov, P. Umari, and R. M. Wentzcovitch, *J. Phys.: Condens. Matter* **21**, 395502 (2009).
- <sup>85</sup>N. Troullier and J. L. Martins, *Phys. Rev. B* **43**, 1993 (1991).
- <sup>86</sup>J. P. Perdew, K. Burke, and M. Ernzerhof, *Phys. Rev. Lett.* **77**, 3865 (1996).
- <sup>87</sup>C. Gougoussis, M. Calandra, A. P. Seitsonen, and F. Mauri, *Phys. Rev. B* **80**, 075102 (2009).
- <sup>88</sup>M. Taillefumier, D. Cabaret, A.-M. Flank, and F. Mauri, *Phys. Rev. B* **66**, 195107 (2002).
- <sup>89</sup>P. E. Blöchl, *Phys. Rev. B* **50**, 17953 (1994).
- <sup>90</sup>M. Abramowitz and I. Stegun, *Handbook of Mathematical Functions with formulas, Graphs and Mathematical Tables* (Dover, New York, 1964).
- <sup>91</sup>P. Thompson and I. G. Wood, *J. Appl. Crystallogr.* **16**, 458 (1983).
- <sup>92</sup>D. Cabaret, E. Gaudry, M. Taillefumier, P. Sainctavit, and F. Mauri, *Phys. Scr. T* **115**, 131 (2005).

- <sup>93</sup>P. Carra, H. Koenig, B. T. Thole, and M. Altarelli, *Physica B* **192**, 182 (1993).
- <sup>94</sup>M. Wojdyr, *J. Appl. Cryst.* **43**, 1126 (2010).
- <sup>95</sup>H. Bialas and H. J. Stoltz, *Z. Phys. B* **21**, 319 (1975).
- <sup>96</sup>M. Prencipe, Y. Noel, B. Civalieri, C. Roetti, and R. Doveri, *Phys. Chem. Minerals* **33**, 519 (2006).
- <sup>97</sup>N. Ishizawa, T. Miyata, I. Minato, F. Marumo, and S. Iwai, *Acta Cryst. B* **36**, 228 (1980).
- <sup>98</sup>C. R. Natoli, *EXAFS and Near Edge Structure*, Springer Series in Chemical Physics Vol. 27 (Springer, Berlin, 1983), pp. 43–56.
- <sup>99</sup>S. Rossano, F. Mauri, C. J. Pickard, and I. Farnan, *J. Phys. Chem. B* **109**, 7245 (2005).